DESIGN, SYNTHESIS, AND STUDY OF BIOACTIVE NATURAL PRODUCT CONGENERS

A THESIS SUBMITTED IN PARTIAL FULFILLMENT OF THE REQUIREMENTS FOR THE DEGREE OF DOCTOR OF PHILOSOPHY

BRILLIANT N. MARAK

MZU REGISTRATION NO.: 1600457

Ph.D. REGISTRATION NO.: MZU/Ph.D./1253 of 09.08.2018

DEPARTMENT OF CHEMISTRY

SCHOOL OF PHYSICAL SCIENCES

NOVEMBER, 2025

DESIGN, SYNTHESIS, AND STUDY OF BIOACTIVE NATURAL PRODUCT CONGENERS

BY

BRILLIANT N. MARAK

Department of Chemistry

Under the supervision of

Prof. VED PRAKASH SINGH

Submitted

In partial fulfillment of the requirement of the Degree of Doctor of Philosophy in Chemistry of Mizoram University, Aizawl.

Mizoram University

Department of Industrial Chemistry
School of Physical Science
Mizoram University,
Aizawl- 796004, Mizoram, India

CERTIFICATE

This is to certify that the thesis entitled **"Design, Synthesis, and Study of Bioactive Natural Product Congeners"** submitted by **Mr. Brilliant N. Marak** for the award of the degree of **Doctor of Philosophy** in **Chemistry** of Mizoram University, Aizawl, embodies the record of original investigation carried out by him under my supervision. He has been duly registered and the thesis presented is worthy of being considered for the award of the Ph.D. degree. This work has not been submitted for any degree in any other University.

Date:

Place: Aizawl

(Prof. Ved Prakash Singh)
Supervisor

DECLARATION OF THE CANDIDATE

MIZORAM UNIVERSITY

NOVEMBER, 2025

I **Brilliant N. Marak**, hereby declare that the subject matter of this thesis is the record of work done by me, that the contents of this thesis did not form basis of the award of any previous degree to me or to do the best of my knowledge to anybody else, and that the thesis has not been submitted by me for any research degree in any other University/ Institute.

This is being submitted to the Mizoram University for the **Degree of Doctor of Philosophy in Chemistry.**

Date:

Place: Aizawl

(Brilliant N. Marak)

Candidate

(Prof. N. MOHONDAS SINGH)
Head
Department of Chemistry Mizoram University

(Prof. Ved Prakash Singh)
Supervisor
Department of Industrial Chemistry
Mizoram University

Acknowledgement

The completion of this thesis would not have been possible without the invaluable support, guidance, and encouragement of many individuals, both directly and indirectly. As I write this section, I am filled with a deep sense of gratitude and accomplishment, and I wish to acknowledge all those who have contributed to this important milestone in my academic journey. Although I cannot fully repay the debt of gratitude I owe, I have made every effort to express my sincere appreciation.

First and foremost, I offer my deepest gratitude to Almighty God for blessing me with good health, strength, and wisdom to accomplish this work. Without His grace and constant presence throughout this journey, this achievement would not have been possible.

I would like to express my sincere thanks to my thesis supervisor, **Prof. Ved Prakash Singh**, Department of Industrial Chemistry, Mizoram University, for his invaluable guidance, unwavering support, and endless patience throughout my research. His trust, insightful suggestions, and constant encouragement transformed this work from a vision into reality.

I am deeply grateful to all the faculty members of the Department of Chemistry and Industrial Chemistry, Mizoram University, **Prof. N. Mohondas Singh** (Head of Department), **Prof. Diwakar Tiwari, Prof. Muthukumuran R.**, **Dr. Zodinpuia Pachuau**, **Dr. Lalrempuia**, **Dr. A. Bimolini Devi**, **Dr. Joydeep Das**, **Dr. Manjeet Singh**, **Dr. G. Rajendra Kumar**, **Dr. Lalhmunsiama**, **Dr. Aniket Chowdhury**, **Dr. Soumabha Bag**, **Dr. Sinjan Das**, for their guidance, support, and encouragement. I also extend my sincere thanks to the non-teaching staff, **Dr. Brojendro Singh Shagolsem** (Senior Laboratory Technician) and **Mr. John Vanlalhruaia** (Technical Assistant), for their continuous assistance during my research.

My special thanks go to **Prof. K. Lalchhandama**, Department of Zoology, Pachhunga University College; **Dr. Zothansiama**, Department of Zoology, Mizoram University; and **Prof. Umesh Chand Singh Yadav**, Special Centre for Molecular Medicine, Jawaharlal Nehru University, for their assistance and support in

conducting the biological assays. I also wish to extend my gratitude to **Dr. P.B. Lalthanpuii** (Pachhunga University College), **Dr. F. Nghakliana**, **Ms. Lalfakawmi** (Department of Zoology, Mizoram University), and **Ms. Anupama Dubey** (Jawaharlal Nehru University) for their valuable help in carrying out these assays.

I extend my heartfelt thanks to **Dr. Biswajit Saha**, Principal Scientist, Advanced Materials Group, Materials Sciences & Technology Division, CSIR–North East Institute of Science & Technology, Jorhat, Assam, for his support in collecting the SCXRD data.

I am also grateful to the Central Drug Research Institute (CDRI), Lucknow; Indian Institute of Chemical Technology (IICT), Hyderabad; and Banaras Hindu University (BHU), Varanasi, for providing facilities for spectroscopic analyses, including NMR and High-Resolution Mass Spectrometry.

I sincerely thank my lab mates, **Dr. Jayata Dowarah**, **Dr. Lalhruaizela**, **Dr. Laldingluaia Khiangte**, **Mr. Biki Hazarika**, **Mr. Lalropuia**, **Ms. Lalremruati**, **Mr. Saurabh Chetia**, **Mr. C. Lalrammawia**, and **Ms. Elizabeth Laltluangkimi** for their invaluable assistance, companionship, and encouragement throughout my research. Their support during challenging times has been truly meaningful, and their kindness will always be remembered.

I would also like to extend my heartfelt thanks to my fellow research scholars and friends for their camaraderie, insightful discussions, and continuous encouragement. Their companionship, both inside and outside the laboratory, made this journey more enjoyable and intellectually stimulating. Their presence has been a source of motivation and positivity throughout my academic pursuit.

Finally, I express my deepest gratitude to my family for their unwavering love, endless support, motivation and constant prayers. My parents have been my greatest source of strength, and no words can truly express my appreciation for their unconditional love and sacrifices. I am also profoundly thankful to my siblings for their moral support and infinite love throughout my life.

(Brilliant N. Marak)

CONTENTS

CHAPTER 3

SYNTHESIS AND ANTI-CANCER ACTIVITY OF NOVEL 2,5-DIKETOPIPERAZINE-BASED COUMARIN ANALOGUES

CHAPTER 4

DESIGN AND DEVELOPMENT OF NOVEL HYBRIDS OF BIS-4-HYDROXYCOUMARIN DERIVATIVES AS ANTHELMINTIC AGENTS

CHAPTER 5

LISTS OF TABLES

LIST OF FIGURES

ABBREVIATIONS

5-FU	5-Fluorouracil
A549	Human lung adenocarcinoma (non-small cell) cell line
ADMET	Absorption, Distribution, Metabolism, Excretion, and Toxicity
AO	Acridine Orange
ATCC	American Type Culture Collection
BBB	Blood–Brain Barrier
BxPC-3	Human pancreatic adenocarcinoma cell line
CCK-8	Cell Counting Kit-8
$CDCl_3$	Deuterated Chloroform
CNS	Central Nervous System
CO_2	Carbon Dioxide
DFG	Aspartate–Phenylalanine–Glycine motif
DKP/DKPs	2,5-Diketopiperazine(s)
DMSO	Dimethyl Sulfoxide
DMSO-d_6	Deuterated Dimethyl Sulfoxide
EtBr	Ethidium Bromide
EtOAc	Ethyl Acetate
EtOH	Ethanol
FBS	Fetal Bovine Serum
FDA	United States Food and Drug Administration

HCCLM3	Human hepatocellular carcinoma metastatic cell line
HCT116	Human colorectal carcinoma cell line
HDAC6	Histone Deacetylase 6
HeLa	Human cervical cancer cell line (from Henrietta Lacks)
HepG2	Human hepatocellular carcinoma cell line
HL60	Human promyelocytic leukemia cell line
HRMS	High-Resolution Mass Spectrometry
HuVECs	Human Umbilical Vein Endothelial Cells
IC_{50}	Half Maximal Inhibitory Concentration
K_d	Dissociation Constant
K562	Human chronic myelogenous leukemia cell line
MCF-7	Human breast adenocarcinoma cell line
MIC	Minimum Inhibitory Concentration
MTT	3-(4,5-Dimethylthiazol-2-yl)-2,5-Diphenyltetrazolium Bromide
NCI-H460	Human large-cell lung carcinoma cell line
NMR	Nuclear Magnetic Resonance
^{1}H NMR	Proton Nuclear Magnetic Resonance
^{13}C NMR	Carbon-13 Nuclear Magnetic Resonance
NSCLC	Non-Small Cell Lung Carcinoma
PBS	Phosphate Buffered Saline
QTOF	Quadrupole Time-of-Flight (Mass Spectrometry)

RPMI-1640	Roswell Park Memorial Institute Medium
RPMI-8226	Human multiple myeloma cell line
RT	Room Temperature
SAR	Structure–Activity Relationship
SCXRD	Single-Crystal X-ray Diffraction
SCLC	Small Cell Lung Carcinoma
SEM	Scanning Electron Microscopy
$T_{1/2}$	Half-life
TLC	Thin Layer Chromatography
TMS	Tetramethylsilane
UA159	*Streptococcus mutans* strain identifier
U266	Human multiple myeloma cell line
U937	Human histiocytic lymphoma cell line
UV	Ultraviolet
VEID-pNA	Caspase-6 Colorimetric Substrate (Val-Glu-Ile-Asp–p-Nitroanilide)
β-Tubulin	Beta-Tubulin

CHAPTER 1

INTRODUCTION

CHAPTER 1

INTRODUCTION

1.1. Background

Natural products are substances produced by living organisms. Natural products have long been a rich source of biologically active molecules and have inspired the development of numerous clinically approved drugs (Arora et al., 2020; Huryn & Wipf, 2008; Khan et al., 2015). Most pharmaceutical agents are derived from the core structures of secondary metabolites produced by plants, marine organisms, microbes, and other natural sources. Between 1981 and 2019, the U.S. Food and Drug Administration (FDA) approved 1,881 novel chemical entities, of which 71 (3.8%) were pure natural products, 356 (18.9%) were natural product derivatives, 14 (0.8%) were botanical drugs (defined mixtures), and 65 (3.2%) were synthetic compounds containing natural product pharmacophores. Altogether, this accounted for 506 (26.9%) of all approved drugs derived from natural products (Newman & Cragg, 2020). Furthermore, natural products and their derivatives often exhibit higher success rates in later clinical trial phases and exhibit lower toxicity profiles than purely synthetic compounds, likely due to their intrinsic affinity for biological targets (Newman et al., 2008; Wermuth, 2003). Thus, the design and synthesis of natural products and natural product-inspired molecules remain a major focus in medicinal chemistry and drug development (Harvey et al., 2015; Rodrigues et al., 2016; Shen, 2015).

Despite the historical success of natural products in drug discovery, many bioactive natural compounds remain unexplored. Recognizing the untapped potential of these molecules is crucial, as they may hold significant promise for the development of future therapeutics (Harvey, 2008). To illustrate this, some bioactive natural product derivatives are summarized here in Figure 1.1.

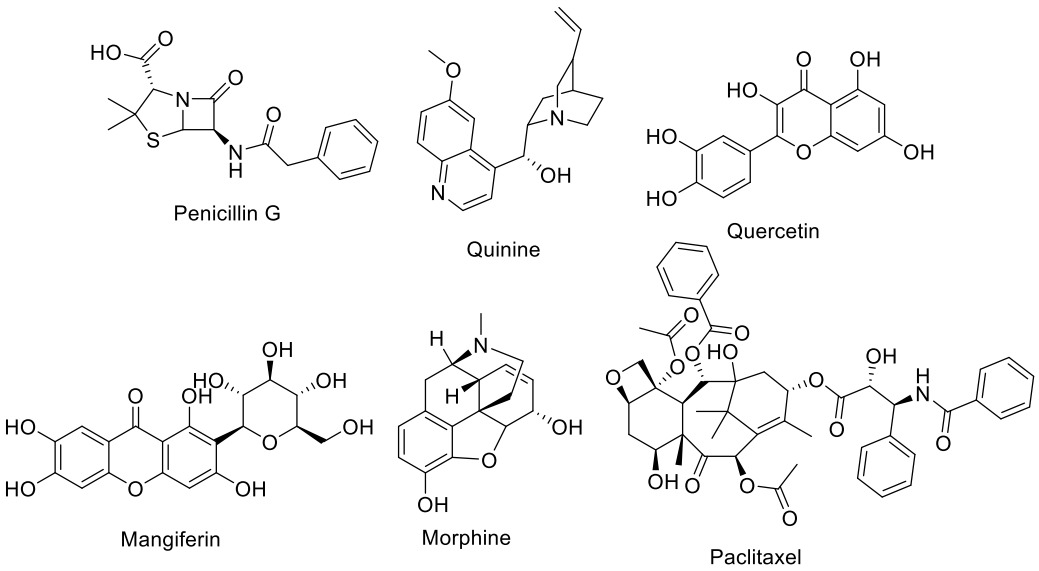

Figure 1.1. Structure of some selected naturally occurring bioactive compounds.

Typically, bioactive natural product compounds are small organic molecules produced by plants, bacteria, and fungi for ecological functions as products of secondary metabolism (Narang et al., 2024; Omokhefe Bruce, 2022). Among the several biological sources, the majority of natural product compounds have been isolated from plants. These natural products encompass various classes, including amino acids, alkaloids, flavonoids, polypeptides, fatty acids, terpenoids, and steroids. Among these classes, alkaloids represent a particularly significant group due to their structural complexity and pharmacological activity (Kurek, 2019; Shi et al., 2014). Notably, alkaloids contain at least one nitrogen atom and are primarily derived from amino acid-based secondary metabolism in plants and some animals. To date, over 3,000 alkaloids have been isolated from approximately 4,000 plant species (Kurek, 2019). Historically, alkaloids have played a pivotal role in medicine due to their potent bioactivities. For example, in the early 19th century (1803–1804), Friedrich Wilhelm Sertürner successfully isolated the first alkaloid, called morphine, from the opium poppy. Morphine is one of the most well-known alkaloids used as a pain reliever; however, its use as a drug is limited because of its addictive properties (Trescot, 2008).

Despite the pharmacological potential of natural products, it is considerably challenging to isolate, purify, and characterize their structures due to their structural complexity. Furthermore, the structure optimization of many natural product

compounds for drug development is complicated by their intricate structures (Harvey, 2008; O' Connor et al., 2011). To address these issues, drugs can be developed that mimic the structures of natural product compounds, thereby yielding fully synthetic or semisynthetic compounds (Wender & Miller, 2009).

1.2. Bioactive 2,5-Diketopiperazine (DKP) Derivatives

2,5-diketopiperazines (DKPs) are an important class of naturally occurring molecules with diverse structures and a wide range of biological activities. DKPs are the smallest cyclic dipeptides, formed through the condensation of two α-amino acids, resulting in a rigid six-membered piperazine ring (Borthwick, 2012). These compounds are abundant in nature and are also frequently produced as degradation products of polypeptides, particularly in processed foods and beverages (Borthwick & Da Costa, 2017; Borthwick, 2012).

DKPs have been isolated from a wide range of natural sources, including plants, fungi, bacteria, and mammals, either as discrete molecules or as components of more complex natural products (Borthwick, 2012). DKPs are regarded as privileged scaffolds as they can bind with numerous biological receptors, making them highly valuable in medicinal chemistry (Huang et al., 2014; Martins & Carvalho, 2007). Moreover, their favorable physicochemical properties, structural stability, and drug-like characteristics enhance their potential as versatile templates for drug design.

Phenylalanyl-based DKP derivative **1.1**, isolated from *Penicillium nigricans* and a marine mangrove endophytic fungus, has displayed potent anthelmintic activity against *Schistosoma mansoni* and *H. nana* in mice (Walchshofer et al., 1997). Its tyrosine analogue, compound **1.3**, obtained from *Cordyceps sinensis* (Berk.) Sacc, acts as a reversible inhibitor of voltage-dependent L-type calcium channels, whereas another tyrosine analogue, compound **1.2**, has been identified as an irreversible inhibitor of the same channels. Moreover, compound **1.3** enhances heart rate and cardiac function in rats, while compound **1.2** exerts the opposite effect, leading to a reduction in these parameters. In addition to its cardiovascular activity, compound **1.2** exhibits significant anticancer activity against HeLa, HT-29, and MCF-7 cancer cell

lines, whereas compound **1.3** shows no anticancer effects (Jia et al., 2005; Kilian et al., 2005).

Phenylalanyl-based DKP derivative **1.1**, isolated from *Penicillium nigricans* and a marine mangrove endophytic fungus, has displayed potent anthelmintic activity against Schistosoma mansoni and H.nana in mice (Walchshofer et al., 1997). Its tyrosine analogue, compound **1.3**, obtained from Cordyceps sinensis (Berk.) Sacc acts as a reversible inhibitor of voltage-dependent L-type calcium channels, whereas another tyrosine analogue, compound **1.2**, has been identified as an irreversible inhibitor of the same channels. Moreover, compound **1.3** increases heart rate and cardiac function in rats, whereas compound **1.2** has the opposite effect, reducing these parameters. In addition to its cardiovascular activity, compound **1.2** exhibits significant anticancer activity against HeLa, HT-29, and MCF-7 cancer cell lines, whereas compound **1.3** shows no anticancer effects (Jia et al., 2005; Kilian et al., 2005).

The 3,4-dihydroxyphenylalanine derivative **1.4** serves as a key intermediate in the biosynthetic pathway of ecteinascidin 743 (ET-743), a class of tetrahydroisoquinoline alkaloids originally isolated from the tunicate *Ecteinascidia turbinate* (Jeedigunta et al., 2000; Wright et al., 1990). ET-743 exhibits potent cytotoxicity against numerous solid tumor cell lines, including those derived from non-small cell lung carcinoma (NSCLC), ovarian, melanoma, and colon cancers (Saleh & Kerr, 2004).

Furthermore, the N-dimethyl analogue **1.5**, isolated from *Streptomyces griseus* (SC488), exhibits potent calpain inhibition with an IC_{50} value of 0.8 μM (Alvarez et al., 1994). The N-methyl analogue **1.6**, obtained from the mycelial solid cultures of G. candidum, demonstrates modest antifungal activity against *P. litchi*. Another N-methyl analogue, compound **1.7**, with hydroxyl groups at the 2- and 6-positions of the phenyl ring, exhibits fungistatic activity against *Candida albicans* (Liu et al., 2007; Lorenz et al., 1998).

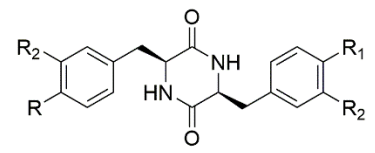

1.1 R=R_1=R_2=H **1.2** R=OH, R_1=R_2=H

1.3 R=R_1=OH, R_2=H **1.4** R=R_1=R_2=OH

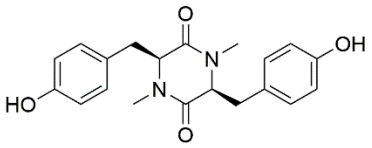

1.5

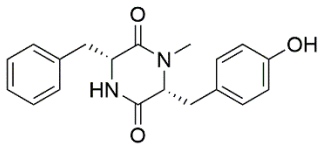

1.6

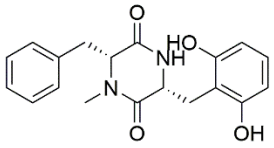

1.7

The N-hydroxy phenylalanyl-based DKP derivative **1.8**, isolated from a red tunicate of the Red Sea, exhibits potent antifungal activity against *C. albicans*, with a MIC value of 3 μg/mL (Hirsch et al., 1989). Compounds **1.9** and **1.10**, obtained as an inseparable mixture from the marine ascidian Didemnum sp. (strain BA99ASCI-05), have moderate antimicrobial activity against *Staphylococcus aureus* (ATCC 6538) and *Streptococcus mutans* (UA159) (Kossuga et al., 2009).

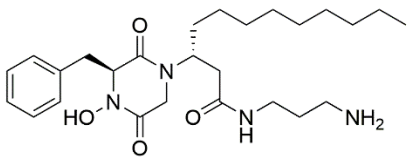

1.8

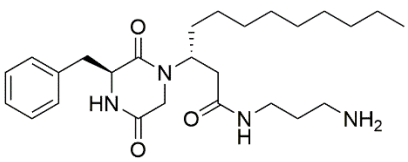

1.9

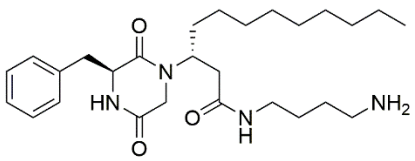

1.10

The ditryptophan-based DKP derivatives, known as fellutanines A−D, are indole alkaloids isolated from cultures of *Penicillium fellutanum* (Kozlovsky et al., 2001). Among this series, fellutanine D (**1.14**) is structurally distinct due to its diannulated scaffold and is the only compound to exhibit cytotoxic activity, with IC_{50} values of 9.5, 11.6, and 19.7 μg/mL, respectively.

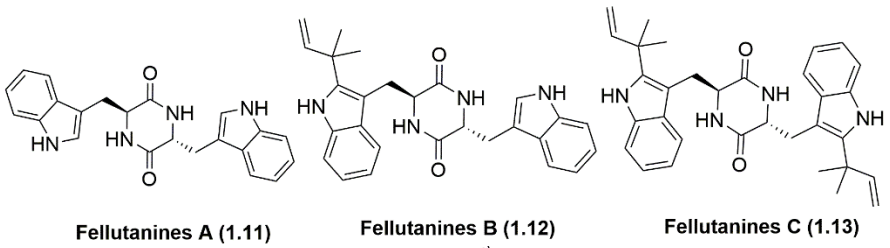

Fellutanines A (1.11) Fellutanines B (1.12) Fellutanines C (1.13)

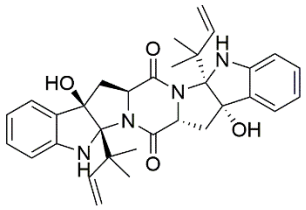

Fellutanines D (1.14)

1.3. 2,5-Diketopiperazines as Anticancer Agents

Purushotham and Paul reported that iodinated DKPs containing varying numbers of iodine atoms exhibited cytotoxicity against three cancer cell lines, i.e., HeLa, MCF-7, and A431, with the activity depending on both the degree of iodination and the presence of a phenolic group within the molecular scaffold (Purushotham & Paul, 2022). Notably, compound **1.15**, which lacks iodine, exhibited no cytotoxic effect across a range of tested concentrations (5, 2.5, and 1.25 mM). In contrast, compounds **1.16** and **1.17**, containing three and four iodine atoms, respectively, significantly reduced cell viability in all three cell lines at the same concentrations.

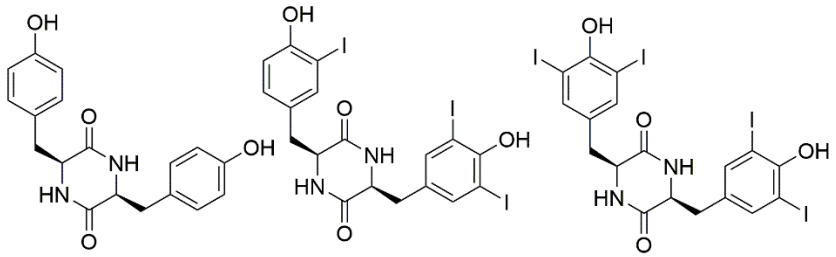

1.15 1.16 1.17

Chen et al. reported the synthesis of a novel series of DKP derivatives as potent and selective inhibitors of histone deacetylase 6 (HDAC6) (Chen et al., 2020). Among these, compound **1.18** exhibited the most potent HDAC6 inhibitory activity, with an IC_{50} value of 0.73 nM. In cytotoxicity assays, compounds **1.19, 1.20**, and **1.21** exhibited strong or comparable efficacy against two multiple myeloma cell lines: U266 (IC_{50} = 25.8 µM, 23.3 µM, and 23.1 µM, respectively) and RPMI-8226 (IC_{50} =

11.6 µM, 12.1 µM, and 13.4 µM, respectively). Additionally, the combination treatment of compound **1.19** with doxorubicin produced a synergistic cytotoxic effect against A549 non-small cell lung cancer cells.

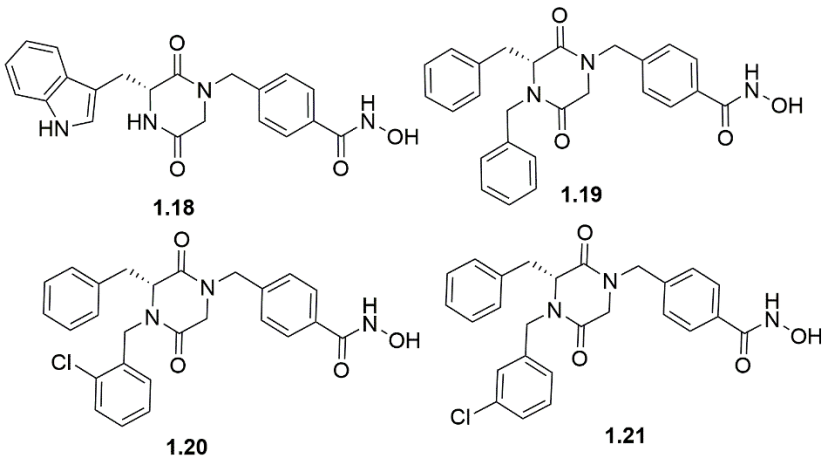

Plinabulin (**1.22**), a potent microtubule-targeting agent, is derived from phenylahistin, a natural cyclic 2,5-diketopiperazine isolated from *Aspergillus ustus*. It exhibits strong microtubule-depolymerizing activity by binding near the colchicine-binding site on tubulin monomers. Plinabulin and its derivatives exhibited a broad spectrum of anticancer properties, including anti-multiple myeloma (A. V. Singh et al., 2011), anti-microtubule (Ding et al., 2020; Honda-Uezono et al., 2012; Mahar et al., 2018), anti-angiogenic (A. V. Singh et al., 2011), anti-pancreatic cancer (Fu et al., 2018), anti-vascular (Nicholson et al., 2006), anti-proliferative,anti-tumor (Bertelsen et al., 2011; Ma et al., 2018), anti-mitotic (Yamazaki, Sumikura, et al., 2012), and cytotoxic effects (Honda-Uezono et al., 2012).

Plinabulin has advanced to phase III clinical trials, notably in combination with docetaxel for the treatment of non-small cell lung cancer (NSCLC). However, its suboptimal pharmacokinetic profile and limited clinical efficacy have posed challenges to FDA approval (Bertelsen et al., 2011; Ding et al., 2017, 2020; Tian et al., 2018). Despite these setbacks, plinabulin remains under active investigation in ongoing clinical trials for metastatic NSCLC (phase I), multiple myeloma (phase II), and recurrent small cell lung cancer (SCLC) (phase II).

In an effort to develop more potent antimicrotubule and cytotoxic agents based on the plinabulin (**1.22**) scaffold, Yamazaki and co-workers designed and synthesized a series of compounds by modifying the tert-butyl and phenyl groups of the plinabulin (Yamazaki et al., 2012). Their structure-activity relationship (SAR) studies identified compounds **1.23** and **1.24** as the most cytotoxic and the most effective inhibitors against the HuVECs cell line, suggesting that their enhanced cytotoxicity is primarily due to their antimicrotubule activity. Among these, compound **1.24** exhibited strong cytotoxicity against HT-29 colorectal cancer cells, with an IC_{50} value of 1.4 nM. Remarkably, compounds **1.23** and **1.24** exhibited 7-fold and 22-fold greater potency than plinabulin, with IC_{50} values of 1.5 nM and 0.5 nM, respectively. These two compounds represent promising second-generation plinabulin derivatives with dual vascular-disrupting and cytotoxic properties, highlighting their potential for treating solid tumors and supporting the further development of novel antimicrotubule agents for cancer therapy.

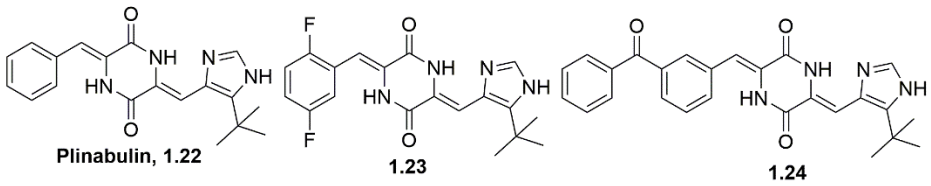

In a related study, Yamazaki et al. developed a series of potent anti-microtubule agents incorporating a benzophenone moiety, derived from the plinabulin (**1.22**) and compound **1.24** scaffolds (Yamazaki, Sumikura, et al., 2012). Structural optimization via 4-fluoro substitution on the benzophenone ring yielded compound **1.25**, which exhibited enhanced *in vitro* cytotoxicity (IC_{50} = 0.5 nM) against HT-29 cancer cells. Structural modification by further substitution at the same position with chlorine improved cytotoxicity, whereas bulkier electron-withdrawing groups, such as bromine and trifluoromethyl, were less effective. Their study also revealed that when tested against HeLa and A549 cancer cell lines, compound **1.25** outperformed compounds **1.24**, with IC_{50} values of 0.8 nM and 1.7 nM, respectively. These findings highlight compound **1.25** as the more potent candidate in cell-based assays. However, compound **1.25** showed slightly reduced microtubule depolymerization activity (IC_{50} = 0.90 µM) and tubulin-binding affinity (K_d = 0.072 µM) compared to compound **1.24**

(K_d = 0.065, IC_{50} =0.76 µM). Moreover, treatment of HeLa cells with 3 nM concentrations of compounds 1.24 and **1.25** partially disrupted the interphase microtubule network. In contrast, combretastatin A-4, a reference compound, exhibited little to no effect at the same concentration, underscoring the superior anti-mitotic potential of compound **1.25**. Currently, compound **1.25** is undergoing clinical trials as a tumor-vascular-disrupting agent for the treatment of solid tumors.

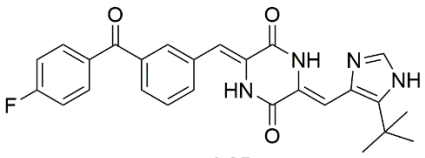

1.25

A study conducted by Ma et al. showed that compound **1.22a**, a deuterium-substituted analog of plinabulin, exhibited improved pharmacokinetic properties compared to its parent compound (**1.22**). Notably, when administered as a single intravenous dose (5 mg/kg) in Wistar rats, compound **1.22a** exhibited a longer half-life ($T_{1/2}$ = 1.47 h) than plinabulin ($T_{1/2}$ = 1.13 h). While both compounds remained stable in rat plasma, compound **1.22a** demonstrated markedly superior metabolic stability in rat liver microsomes. The analysis of the tissue distribution of compound **1.22a** at various time points (0.5, 1, 4, 8, and 12 hours) revealed that it was rapidly and broadly distributed across multiple organs, with the highest concentration in the lungs. Moreover, in pharmacodynamic assessments, co-administration of compound **1.22a** with gefitinib resulted in significantly greater antitumor activity *in vivo* than monotherapy (Ma et al., 2018).

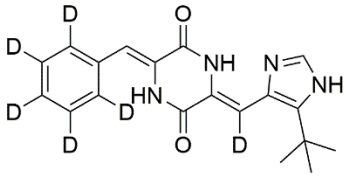

Plinabulin, 1.22a

In a related study, Deng et al. showed that compound **1.22b** has greater *in vitro* anti-proliferative activity than plinabulin **1.22b** against hepatocellular carcinoma cell lines Bel-7402 and HCCLM3. Compound **1.22b** has IC_{50} values of 5.70 nM and 5.58

nM against Bel-7402 and HCCLM3 cells, respectively, while plinabulin exhibited IC_{50} values of 11.73 nM and 7.24 nM for the same cell lines (M. Deng et al., 2018).

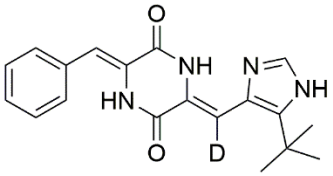

MBRI-001, 1.22b

Ding et al. carried out a structure-based design and synthesis of novel furan-containing plinabulin derivatives as potent microtubule inhibitors, utilizing the co-crystal structure of tubulin bound to compound **1.24** (Ding et al., 2020). Their findings demonstrated that replacing the imidazole core with various moieties, particularly five-membered rings, resulted in greater cytotoxicity than six-membered ring substitutions. Notably, derivatives bearing a 5-methoxymethyl group at the furan ring, i.e., compounds **1.26** and **1.27**, exhibited remarkable cytotoxicity against the human lung cancer NCI-H460 cell line, with IC_{50} values of 14.0 nM and 2.9 nM, respectively. Furthermore, both compounds showed potent activity against HT-29 (IC_{50} = 7.0 nM and 2.2 nM, respectively) and BxPC-3 (IC_{50} = 6.6 nM and 2.0 nM, respectively) cancer cell lines. Moreover, immunofluorescence assays also confirmed their strong inhibition of tubulin polymerization.

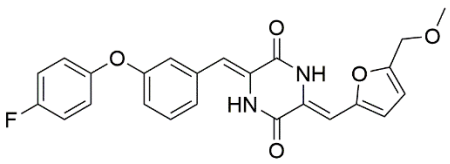

1.26

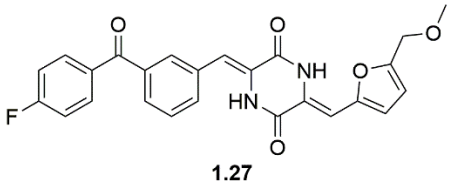

1.27

Tian and co-workers evaluated the bioactivity and interaction mechanisms of a series of plinabulin derivatives containing a benzophenone moiety (compounds **1.28-1.33**) as tubulin polymerization inhibitors (Tian et al., 2018). Among these, compound **1.30**, with a 4-fluoro substituent on the aryl ring, exhibited the highest antiproliferative activity, with IC_{50} values of 3.8 nM and 0.7 nM against NCI-H460 and BxPC-3 cell lines, respectively. In contrast, replacing the tert-butyl group on the imidazole ring

with a methyl group results in a significant reduction in bioactivity. As a result, compound **1.28** exhibited the weakest activity in the series, with IC_{50} values of 306 nM for BxPC-3 and >1000 nM for NCI-H460 cells. Similarly, compound **1.29** with IC_{50} values of 0.9 nM and 4.1 nM (NCI-H460) was more active than compound **1.31** with an IC_{50} value of 56.8 nM (BxPC-3) and 51.7 nM (NCI-H460). Interestingly, replacing the imidazole ring with a pyridine ring in compound **1.32** yielded comparable activity to compound **1.29**, with IC_{50} values of 5.0 nM (BxPC-3) and 27.2 nM (NCI-H460). Conversely, substitution of the imidazole with a benzyl group in compound **1.33** led to a significant decrease in activity, with IC_{50} values of 91.7 nM (BxPC-3) and 388.7 nM (NCI-H460). Moreover, tubulin polymerization assays further showed the inhibitory rates of 12.8%, 72.2%, 92.5%, 66.1%, 61.1%, and 9.9% for compounds **1.28**-**1.33**, respectively.

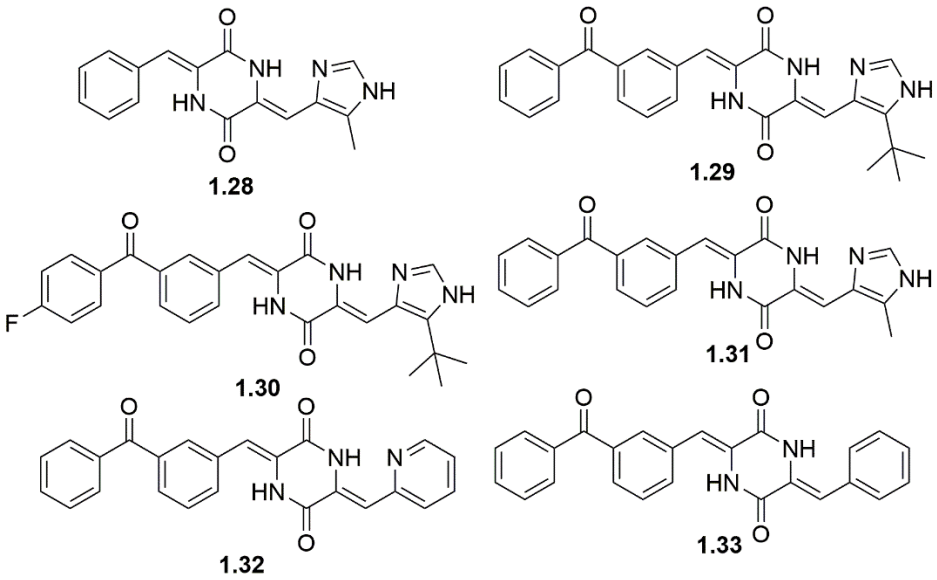

Fu et al. designed and synthesized a series of novel plinabulin derivatives, guided by the co-crystal structure of plinabulin (**1.22**) and compound **1.24** (Fu et al., 2018). The newly developed compounds were evaluated for anticancer activity against the human pancreatic cancer BxPC-3 cell line. Among them, compounds **1.34** and **1.35** demonstrated potent cytotoxicity, with IC_{50} values of 1.56 nM and 1.72 nM, respectively. In contrast, derivatives with a pyrrole substituent (compounds **1.36** and **1.37**) showed significantly reduced activity, with IC_{50} values exceeding 100 nM.

Tubulin polymerization assays confirmed that compounds **1.34** and **1.35** effectively inhibited microtubule assembly, achieving inhibition rates of 39.27% and 46.36%, respectively. Additionally, molecular docking studies revealed that the binding modes of **1.34** and **1.35** closely resembled that of compound **1.24** within the tubulin complex.

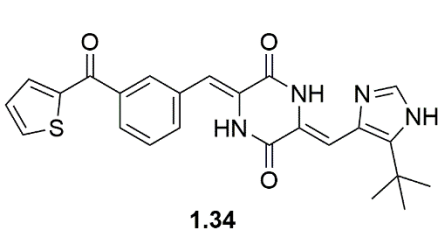

1.34

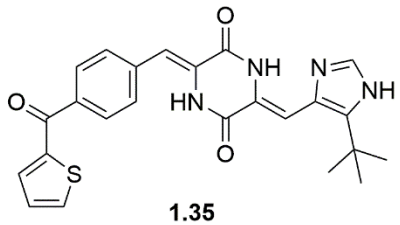

1.35

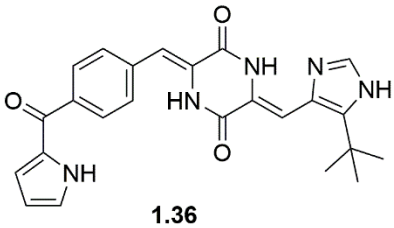

1.36

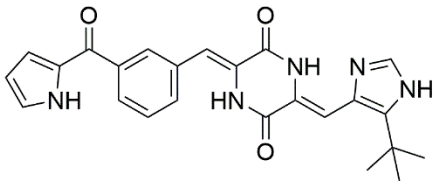

1.37

Chinh et al. synthesized a series of N-propargyl and N-methyl plinabulin-based 4-oxoquinoline derivatives through a one-pot aldol condensation and alkylation reaction (Chinh et al., 2021). The resulting compounds were evaluated for cytotoxicity against the HepG2, Lu, KB, and MCF-7 cancer cell lines. Among them, compounds **1.38, 1.39**, and **1.40** exhibited strong cytotoxicity against HepG2, Lu, and KB cell lines, with IC_{50} values ranging from 3.04 to 10.62 µM.

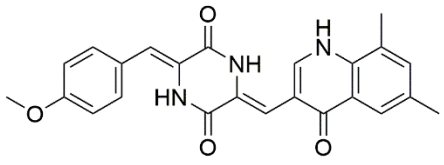

1.38

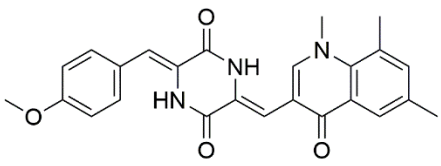

1.39

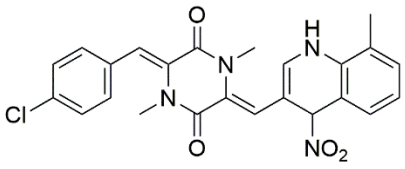

1.40

Liao et al. designed and synthesized a series of N-allyl-protected DKP derivatives and evaluated their anticancer activity against 10 cancer cell lines using the CCK-8 assay (Liao et al., 2014). The results revealed that many of the synthesized

compounds exhibited broad-spectrum anticancer activity. Among them, compound **1.41** showed potent activity against all tested cell lines (IC_{50} = 0.5-4.5 µM). Notably, compound **1.41** was effective against the cancer cell lines U937 and K562, with IC_{50} values of 0.5 µM and 0.9 µM, respectively (Liao et al., 2014).

In another study, Liao et al. synthesized a series of N-allyl protected DKP derivatives (**1.42**) with long alkyl chains (n = 1–10, 14) and evaluated their cytotoxicity against eight cancer cell lines. The results revealed that compound **1.42a**, with a 4-methoxyphenyl group and a pentylidene side chain, displayed potent cytotoxicity against all tested cell lines, with IC_{50} values ranging from 0.36 to 1.9 µM. Moreover, treatment with **1.42a** at 1.0 µM for 48 hours induced apoptosis in the U937 cell line. Similarly, compound **1.42b**, with a 2-methoxyphenyl group and a pentylidene side chain, also showed potent cytotoxicity against all tested cell lines, with the most pronounced effect observed in the HL60 cell line, with an IC_{50} value of 0.5 µM (Liao et al., 2016).

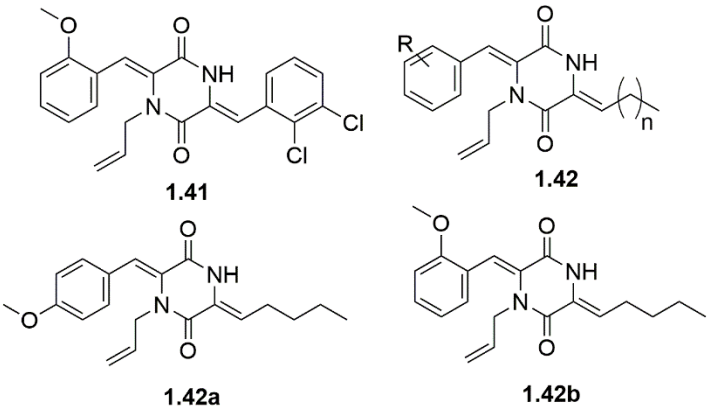

1.4. Bioactive Coumarin Derivatives

Coumarin is a naturally occurring heterocyclic compound with a benzopyrone scaffold that consists of a benzene ring fused to an α-pyrone ring. Coumarin and its derivatives have been identified as secondary metabolites in more than 150 plant species, i.e., over 30 plant families, such as Rutaceae, Umbelliferae, Fabaceae, and Clusiaceae (Dandriyal et al., 2016; Sethna & Shah, 1945). Although coumarin derivatives are mainly found in plants, it has also been extracted from many

microorganisms. For example, novobiocin, an antibacterial agent, was isolated from the actinomycete *S. niveus*. Coumermycin A, which possesses both antibacterial and anticancer properties, was extracted from *S. rishiriensis* (Vanden Broeck et al., 2019).

Several coumarin derivatives have also been extracted from traditionally used medicinal plants. For instance, certain dihydrofuran-fused coumarins and 6-hydroxycoumarin were extracted from the rhizome of *Glaucidium palmatum*. These compounds have also been reported as microtubule-stabilizing agents with potent antimitotic activity and antiproliferative activity against KB cells (Morita et al., 2004). Moreover, 7-dihydroxycoumarin, which was isolated from the bark of *Kayea assamica*, exhibited anticancer as well as antimalarial activity against chloroquine-resistant *Plasmodium falciparum* (Lee et al., 2003). The chemical structures of some bioactive coumarin derivatives are illustrated in Figure 2.

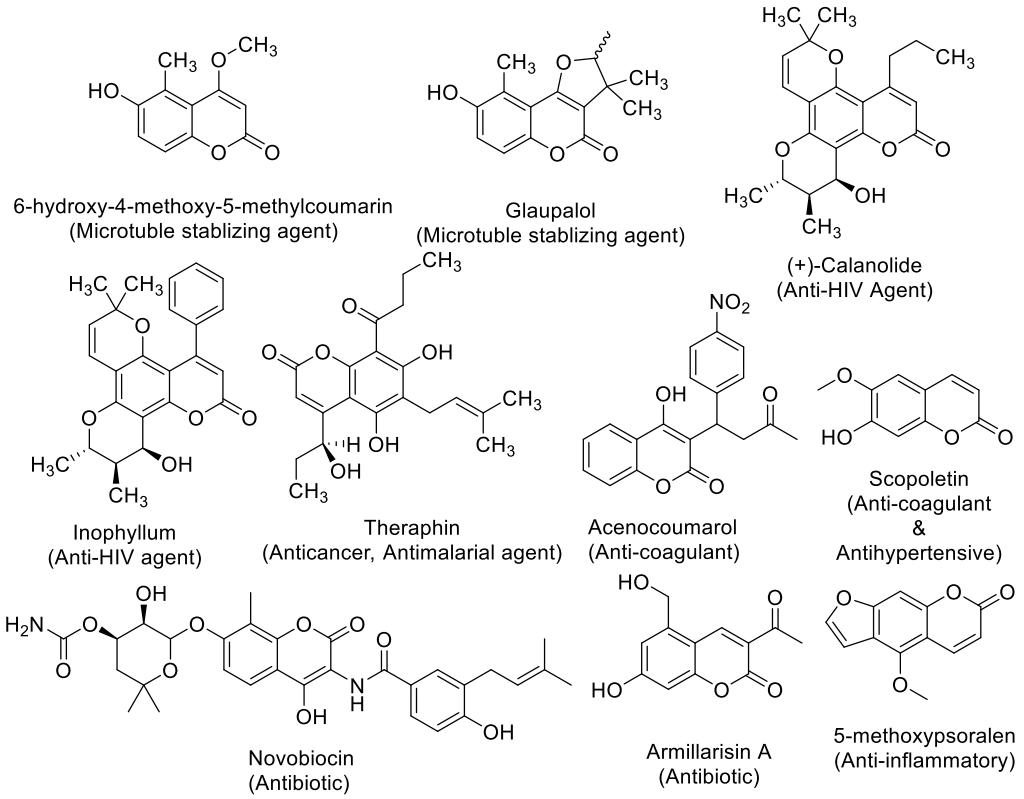

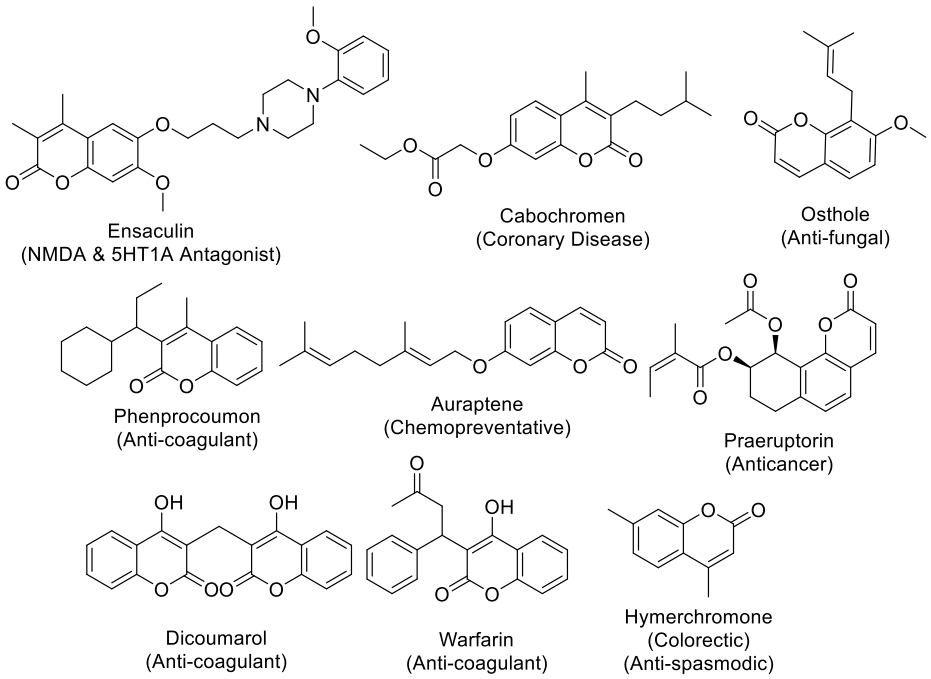

Figure 1.2. Chemical structures of some bioactive coumarin derivatives

1.5. Coumarin Derivatives as Anticancer Agents

Coumarins exhibit a broad spectrum of biological activities, such as anticoagulant, antitumor, anti-inflammatory, antiviral, antioxidant, antimicrobial, and antibacterial activities (Wu et al., 2009). Several studies have shown that coumarins can induce apoptosis by arresting cells at G0, G1, S, and M phases of the cell cycle (N. Singh et al., 2014; Thakur et al., 2015). Coumarins have been reported to exert anticancer effects by targeting kinases, which are key enzymes involved in the initiation and regulation of signalling pathways essential for cell growth and proliferation. These properties of coumarins made them valuable scaffolds in disrupting oncogenic pathways (Bhat et al., 2024). Furthermore, coumarins have also been reported to directly bind to heat shock protein 90 (HSP90), a molecular chaperone frequently overexpressed in cancer cells (Matts et al., 2011; Samadi et al., 2011). Moreover, coumarins have been reported to disrupt many other cancer-related pathways, including inhibition of angiogenesis, mitosis, carbonic anhydrase, telomerase activity, aromatase, monocarboxylate transporters, and sulfatase enzymes (Geisler et al., 2011; Lin et al., 2014; Saidu et al., 2012). Some coumarin derivatives with potent anticancer activity are listed in Table 1.1.

Table 1.1. Overview of some coumarin derivatives exhibiting potent anticancer activity.

Structure	Cancer cell line	Anticancer activity	Enzyme Inhibition/Other activity	Ref.
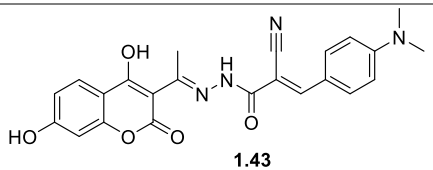 **1.43**	A549, SKNSH, MCF7 and HeLa,	IC_{50} = 4.31, 6.09, 3.42 µM, and 5.14, respectively	IC_{50} = 6.19 µM	(Govindaiah et al., 2019)
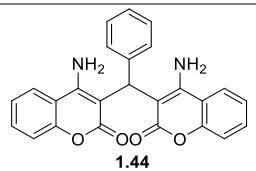 **1.44**	Ehrlich ascites carcinoma cells (EAC)	IC_{50} = 0.10 µM		(Ibrahim et al., 2016)
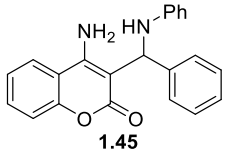 **1.45**	Ehrlich ascites carcinoma cells (EAC)	IC_{50} = 0.13 µM		(Ibrahim et al., 2016)
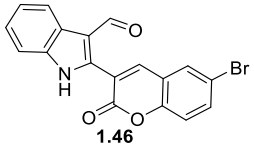 **1.46**	MCF-7 and normal Vero cell lines	IC_{50} = 7.4 µM and >100 µM, respectively		(Kamath et al., 2015)

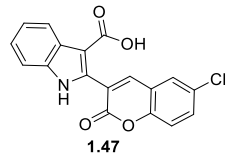 1.47	MCF-7 and normal Vero cell lines	IC_{50} = 5.5 µM and 15.4 µM, respectively	(Kamath et al., 2015)
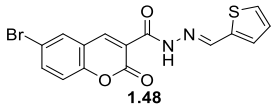 1.48	Panc-1, Hep-G2, CCRF	IC_{50} = 6.50, 3.60, and 5.15, respectively.	(Nasr et al., 2014)
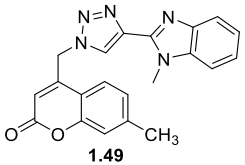 1.49	A549, HepG2, CFPAC-1, HeLa, SW620, 3T3	IC_{50} = 16.85, 0.90, 59.41, 17.48, >100, and 45.33 µM, respectively.	(Kraljević et al., 2016)
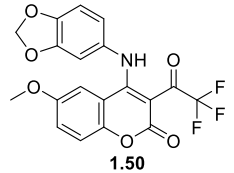 1.50	HCT116, Panc-1, HepG2, and MCF-7	IC_{50} = 4.42, 5.16 µM, 5.45, and 16.57, respectively.	(Luo et al., 2017)
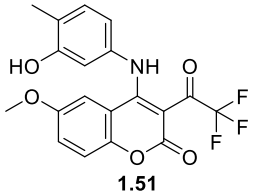 1.51	HCT116, MCF-7, HepG2, and Panc-1	IC_{50} = 4.62, 20.14, 6.71, and 5.62 µM respectively.	(Luo et al., 2017)

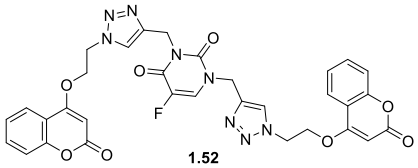 1.52	MCF-7	GI_{50} = 1.55 µM.	Anti-bacterial activity against *Staphylococcus aureus* (MIC = 11.7 µg/ mL).	(Sanduja et al., 2020)
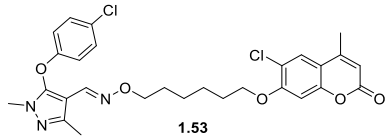 1.53	Hep G2, SMMC-7721, U87, H1299	IC_{50} = 2.96, 2.08, 3.85, and 5.36 µM, respectively.		(Dai et al., 2019)
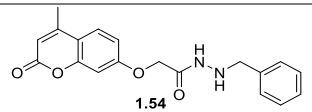 1.54	MCF-7	IC_{50} = 1.24 µM.	VEGFR-2 inhibition IC_{50} = 0.36	(Ahmed et al., 2020)
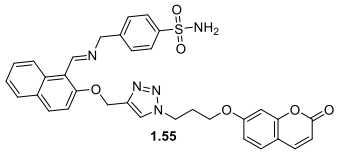 1.55	HT-29 and HEK293T	IC_{50} = 17.01 and 118.73 µM, respectively.		(Zengin Kurt et al., 2019)
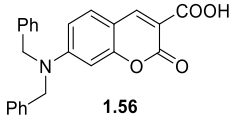 1.56	MDA-MB-231 and GL261-luc2	IC_{50} = 0.24 and >0.25 µM, respectively.	MCT1 inhibition IC_{50}= 0.09 µM.	(Gurrapu et al., 2016)
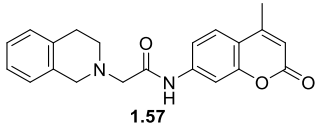 1.57	A549 and MCF-7	IC_{50} = 0.024 and 4.85 µM, respectively.		(Soni & Soman, 2018)

1.6. Other Pharmacological Activity of Coumarin Derivatives

Coumarins possess therapeutic potential to reduce edema by promoting the removal of proteins and excess fluid from damaged tissues through activation of phagocytosis, enzyme secretion, and proteolysis (Chen et al., 2017). Additionally, its derivative, imperatorin (**1.58**), exhibits anti-inflammatory properties by suppressing the expression of nitric oxide synthase (NOS) and cyclooxygenase-2 (COX-2) (Huang et al., 2012). Furthermore, compounds **1.59** and **1.60** have demonstrated both anti-inflammatory and immunomodulatory effects by promoting immune cell proliferation and stimulating the release of interferon-gamma (IFN-γ) and interleukin-4 (IL-4), primarily through COX-2 inhibition (Yildirim et al., 2022; Zamani Taghizadeh Rabe et al., 2016).

Compound **1.61** exhibited potent antifibrotic activity by blocking TGF-β-induced collagen buildup in NRK-49F cells, while causing little toxicity and only limited macrophage migration (D. Deng et al., 2020). Dihydromammea (**1.62**), which was isolated from the seeds of the Mammea africana, exhibited antihypertensive properties, while scopoletin (**1.63**), extracted from the fruits of Tetrapleura tetraptera (Mimosaceae), showed significant hypotensive activities (Crichton & Waterman, 1978; Mead et al., 1958). Visnadine (**1.64**), isolated from the fruit of Ammi visnaga, possesses vasodilatory and coronary therapeutic properties, making it especially effective in the treatment of angina pectoris (Duarte et al., 1997). Scoparone (**1.65**), with reported vasodilatory activities, exerts its action by inhibiting calcium-dependent channels and reducing the contractile activity of aortic rings, thereby interfering with the mechanism of action of various agonists (Huang et al., 1992).

Furthermore, coumarins such as ammoresinol (**1.66**) and ostruthin (**1.67**) have shown antibacterial activity against several Gram-positive bacteria, including B. megaterium, M. luteus, and S. aureus (Dadák & Hoďák, 1966). Umbelliferone (**1.68**) and related derivatives, such as phelodenol (**1.69**), bergaptene (**1.70**), marmesin (**1.71**), rutaretin (**1.72**), and xantholein (**1.73**), isolated from the plant Fatoua pilosa, showed notable activity against M. tuberculosis, with umbelliferone and scopoletin being particularly effective (Chiang et al., 2010; Cunha et al., 2015). Moreover, coumarins,

such as inophyllums and calanolides, extracted from the giant African snail Achatina fulica, exhibited antiviral activity. Notably, inophyllums B and P (**1.74** & **1.75**) inhibited HIV-1 reverse transcriptase activity in cell culture, showing selective action against HIV-1 (Patil et al., 1993).

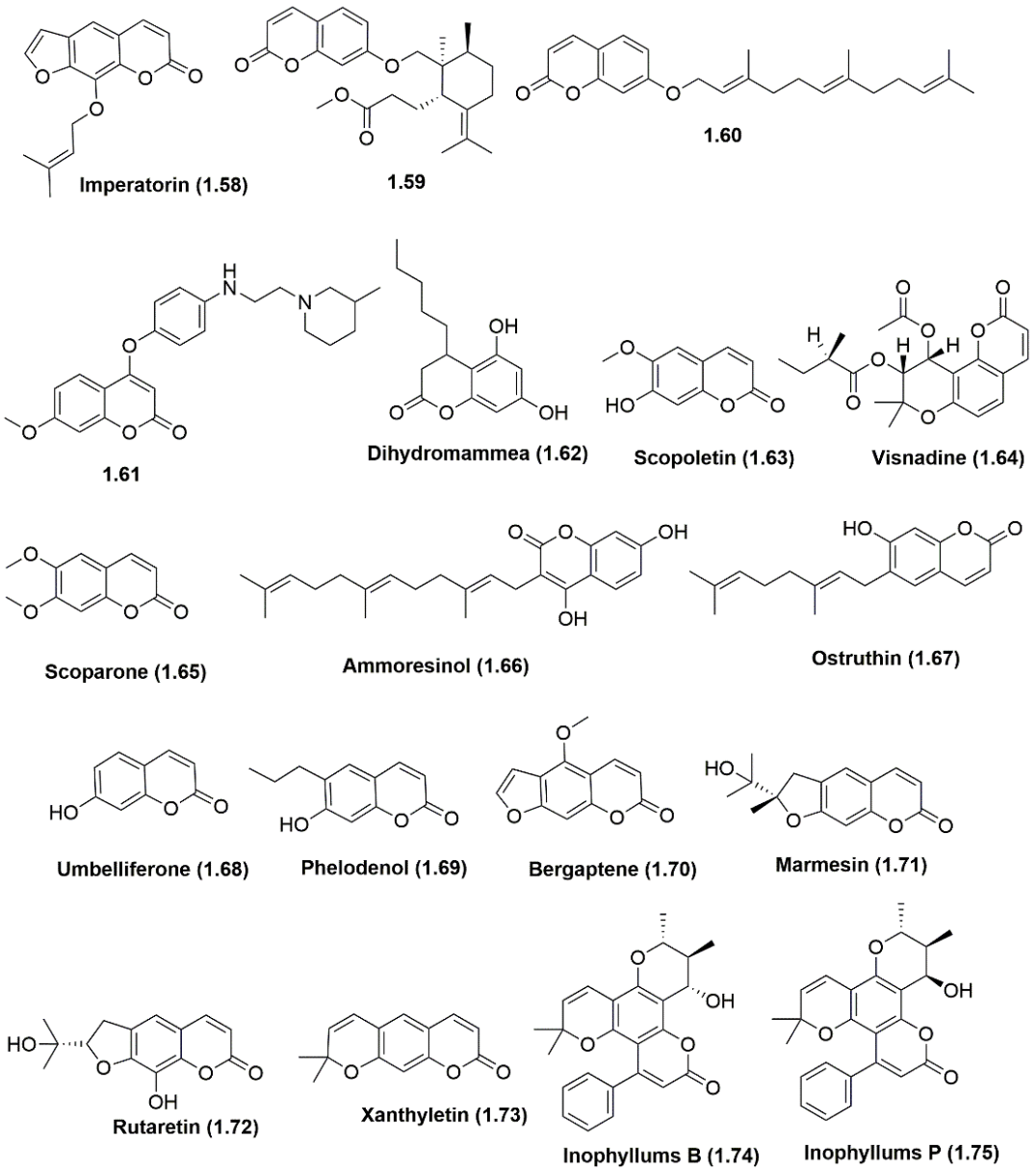

1.7. Bioactive Bis-Coumarin Derivatives

Similar to coumarins, bis-coumarins with a characteristic benzopyrone core are commonly found in nature as integral subunits of intricate natural products (Fonseca et al., 2017; Hu et al., 2017). Bis-coumarins exhibit a broad spectrum of biological activities, such as anti-cancer (M.-M. Liu et al., 2014), anti-bacterial (Hu et al., 2017; Li et al., 2012), anti-fungal (Puttaraju et al., 2013), anti-HCV (Neyts et al., 2009), anti-inflammatory (Kontogiorgis & Hadjipavlou-Litina, 2005), anti-HIV (Kamiyama et al., 2011), anti-malarial (Hu et al., 2017; Pingaew et al., 2014), anti-tuberculosis (Hu et al., 2017; Xu et al., 2017; Zhang et al., 2017), anti-alzheimer (Hamulakova et al., 2014), anti-parasitic (Basumatary et al., 2020)and antipsychotics (Y. Chen et al., 2013). Notably, dicoumarol, a prominent bis-coumarin derivative, is currently used as an anticoagulant because it disrupts vitamin K metabolism. Given their pharmacological diversity and established clinical relevance, bis-coumarins have recently become the focus of intensified research efforts.

1.8. Anticoagulant Activity of Bis-Coumarin Derivatives

The bis-coumarins isolated from *Viola yedoensis Makino* (Violaceae), namely dimeresculetin (**1.76**) and euphorbetin (**1.77**), have been reported to exhibit anticoagulant activity, as evidenced by their effects on activated partial prothrombin time, thromboplastin time, and thrombin time (Zhou et al., 2009). Moreover, among the series of bis-coumarins synthesized by Manolov et al., compound **1.78** has been reported to exhibit a notable anticoagulant effect, markedly prolonging blood coagulation time at doses ranging from 1/120 to 1/20 of its LD_{50} (Manolov et al., 2006). The most notable effect was reported at a dose equivalent to 1/40 of the LD_{50}, resulting in a 6.6-fold increase in coagulation time.

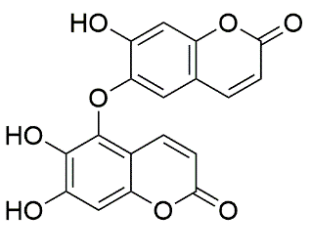

1.76

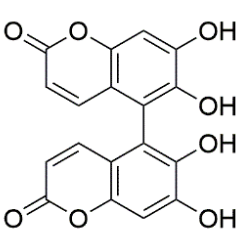

1.77

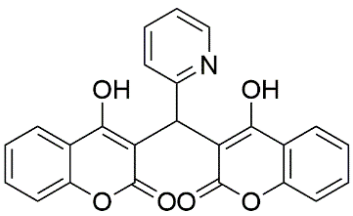

1.78

1.9. Antiparasitic Activity of Bis-Coumarin Derivatives

Helminth infections rank among the most prevalent gastrointestinal diseases in humans, often transmitted through air, food, and water. These parasitic worms cause illness by releasing toxins and depleting essential nutrients from their hosts (Basumatary et al., 2020).In a study by Baruah et al., coumarin-based unsymmetrical trisubstituted methanes (**1.79**) were found to exhibit acetylcholinesterase inhibitory activity, highlighting their potential as therapeutic agents for Alzheimer's disease (Baruah et al., 2019). Given that acetylcholine receptor inhibition is also a key mechanism of action for many anthelmintic drugs, the same research group further explored the anthelmintic potential of these compounds. Their findings revealed significant activity of the trisubstituted methanes (**1.79**) against helminth parasites *Raillietina echinobothrida* and *Syphacia obvelata*, with some compounds outperforming the commonly used drug albendazole. Expanding upon these findings, Kharrngi et al. from the same laboratory developed an efficient synthesis method for biscoumarins and evaluated their anthelmintic efficacy against the same parasites (Kharrngi et al., 2021). Their study showed that compounds **1.80, 1.81, 1.82,** and **1.83** exhibited markedly superior activity against *R. echinobothrida* compared to the standard drug praziquantel, inducing paralysis and death in nearly half the time required by praziquantel.

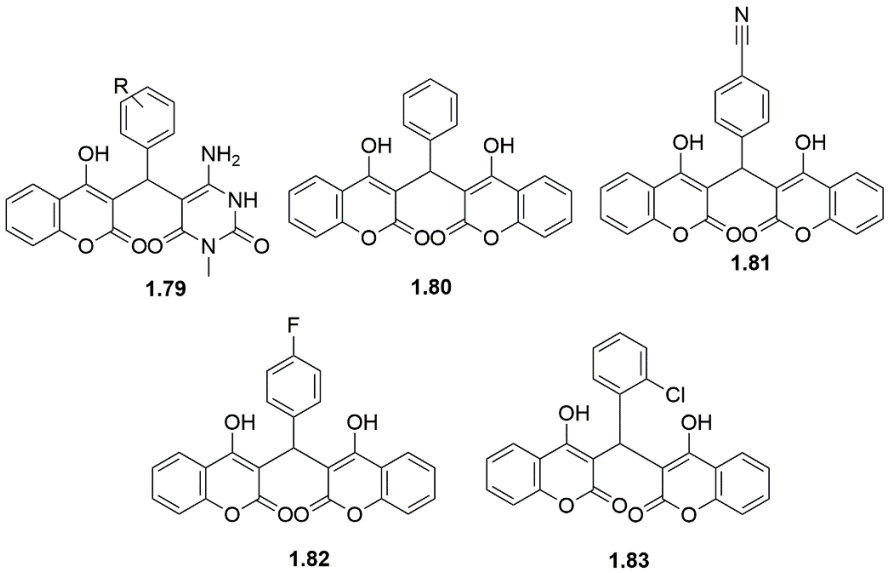

Leishmaniasis is a prevalent parasitic disease caused by protozoan parasites of the Leishmania genus. Coumarin derivatives have shown promising anti-leishmanial properties. In this context, Ibrar et al. designed and synthesized a novel series of bis-coumarin–iminothiazole hybrids, among which compound **1.84** demonstrated significant anti-leishmanial activity, achieving 70.4% inhibition at a concentration of 100 μM, which is comparable to the standard drug amphotericin B (79.8% inhibition) (Ibrar et al., 2015). Additionally, compound **1.84** demonstrated notable anticancer potential, inhibiting the growth of BHK-21 and H-157 cell lines by 57.2% and 54.4%, respectively, at 100 μM. In a separate study, Rahim et al. reported the synthesis and evaluation of a series of biscoumarin derivatives. Among these, biscoumarin **1.85** emerged as the most potent anti-leishmanial agent, exhibiting an IC_{50} value of 35.62 μM (Rahim et al., 2017).

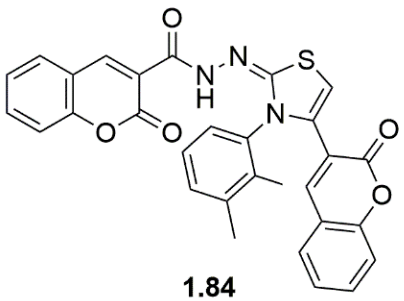

1.84

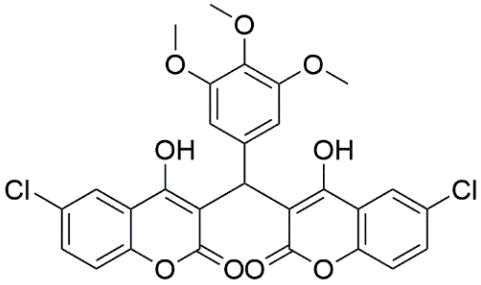

1.85

Plant-parasitic nematodes are among the most destructive plant pathogens globally (Ntalli & Caboni, 2012). Certain simple coumarins, furocoumarins, and dicoumarol derivatives have demonstrated excellent nematicidal activity, making their chemical scaffolds attractive for the development of effective nematicides (Cui et al., 2014; Pan et al., 2016). In a study by Pan et al., a series of novel coumarin and bis-coumarin derivatives were designed and synthesized, among which compounds **1.86–1.89** exhibited strong, broad-spectrum nematicidal activity against all tested nematode species (Pan et al., 2016). Notably, compound **1.88** exhibited the most potent activity against *D. destructor*, *M. incognita*, *B. xylophilus*, *B. mucronatus*, and *A. besseyi* with LC_{50} values of 3.7, 5.1, 2.5, 6.4, and 3.1 mmol/L, respectively. Similarly, Liu et al. reported that coumarin hybrids (**1.90–1.93**) exhibited potent anthelmintic activity against *Dactylogyrus intermedius* at concentrations ranging from 1 to 10 mg/L, with

compound **1.90** showing the highest activity, displaying an EC_{50} value of 0.85 mg/L (Liu et al, 2016).

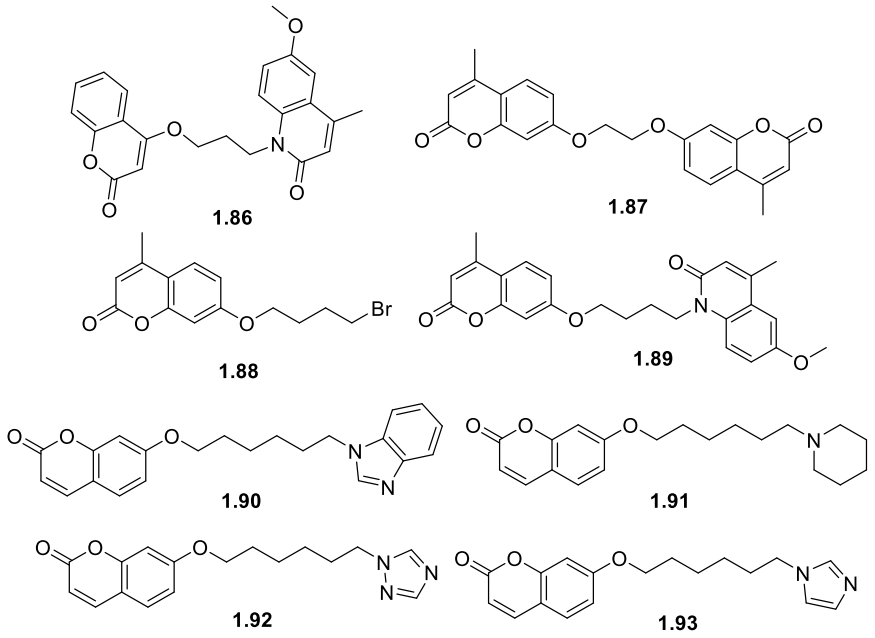

1.10. Objectives of the present work

The objectives of the present studies are:

(i) To design and synthesize novel compounds based on natural product scaffolds.

(ii) To evaluate the biological activity of the synthesized compounds.

(iii) To perform *in silico* analyses of the synthesized compounds to understand their interactions with target receptors.

CHAPTER 2

DESIGN, SYNTHESIS AND ANTI-CANCER ACTIVITY OF NOVEL PLINABULIN-BASED 2,5-DIKETOPIPERAZINE ANALOGUES

CHAPTER 2

DESIGN, SYNTHESIS AND ANTI-CANCER ACTIVITY OF NOVEL PLINABULIN-BASED 2,5-DIKETOPIPERAZINE ANALOGUES

2.1. Background

Cancer is a life-threatening condition and continues to be a significant global health challenge, ranking as the second most common disease after cardiovascular disorders (Kong et al., 2023). Among various cancer types, colorectal cancer accounts for 9.6% of cases and is the third leading cause of cancer-related deaths, contributing to 9.3% of mortality (Bray et al., 2024). Conventional chemotherapy primarily relies on inducing cytotoxic effects to destroy cancer cells. However, these drugs often lack specificity, affecting both cancerous and healthy cells, which can lead to severe side effects, especially with prolonged use, and may eventually result in drug resistance (Kong et al., 2023). Such limitations significantly hinder effective cancer treatment. Therefore, there is an urgent need to develop novel anticancer agents that are safer, less toxic, and more effective, a need that remains a central focus in pharmaceutical research.

As discussed in Chapter 1 (section 1.2), the 2,5-diketopiperazine (DKP) scaffold is abundant in numerous natural and synthetic bioactive compounds. DKPs are privileged structures because they can exhibit a broad range of biological activities, most notably anticancer properties.

Microtubules are essential components of the cytoskeleton and are involved in critical cellular functions, such as maintaining cell shape, intracellular transport, and cell division (Nogales, 2000). Given their pivotal role in mitosis, microtubules have been targeted extensively in cancer therapy (Gupton et al., 2017; Xiang et al., 2018). For example, plinabulin, a synthetic derivative of the marine natural product phenylahistin, inhibits microtubule polymerization (Kanoh et al., 1999; Yamazaki et al., 2010). Plinabulin, in combination with Docetaxel, is currently undergoing phase III clinical trials for the treatment of non-small cell lung cancer (NSCLC) (Han et al.,

2024). Structural modifications of Plinabulin derivatives at the aromatic moieties have also yielded analogues with improved efficacy (Yamazaki, Sumikura, et al., 2012; Yamazaki, Tanaka, et al., 2012). However, many non-protected DKP derivatives, i.e., those bearing an unprotected amide nitrogen, suffer from poor solubility, likely due to extensive intermolecular hydrogen bonding and π–π stacking interactions that form linear or network-like assemblies within the DKP framework, thereby hindering their pharmaceutical applications (Figure 2.1) (Ando et al., 2011; Borthwick, 2012; Liao et al., 2014; Ressurreição et al., 2011).

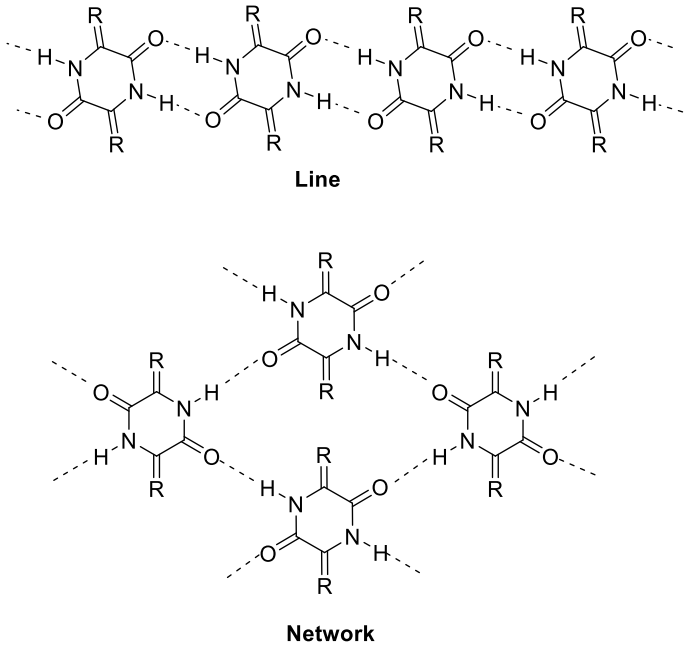

Figure 2.1. Schematic view of H-bonding patterns for DKP derivatives.

Gefitinib and Canertinib (Figure 2.2), both epidermal growth factor receptor (EGFR) inhibitors with potent anticancer activity, exemplify the importance of incorporating hydrophilic moieties. Gefitinib, approved by the FDA (Cohen et al., 2004), contains a 3-(morpholino or 4-methylpiperazin-1-yl)propoxy side chain, which improves water solubility and cellular potency (El-Damasy et al., 2016). Compound **2.11** (Figure 2.2), a 2-anilinoquinoline derivative bearing a morpholino-propoxy group, inhibits a broad range of cancer cell lines, including NSCLC, leukemia, ovarian, melanoma, CNS, renal, prostate, colon, and breast cancer, with GI_{50} values ranging from 1.85 to 3.01 μM (El-Damasy et al., 2016).

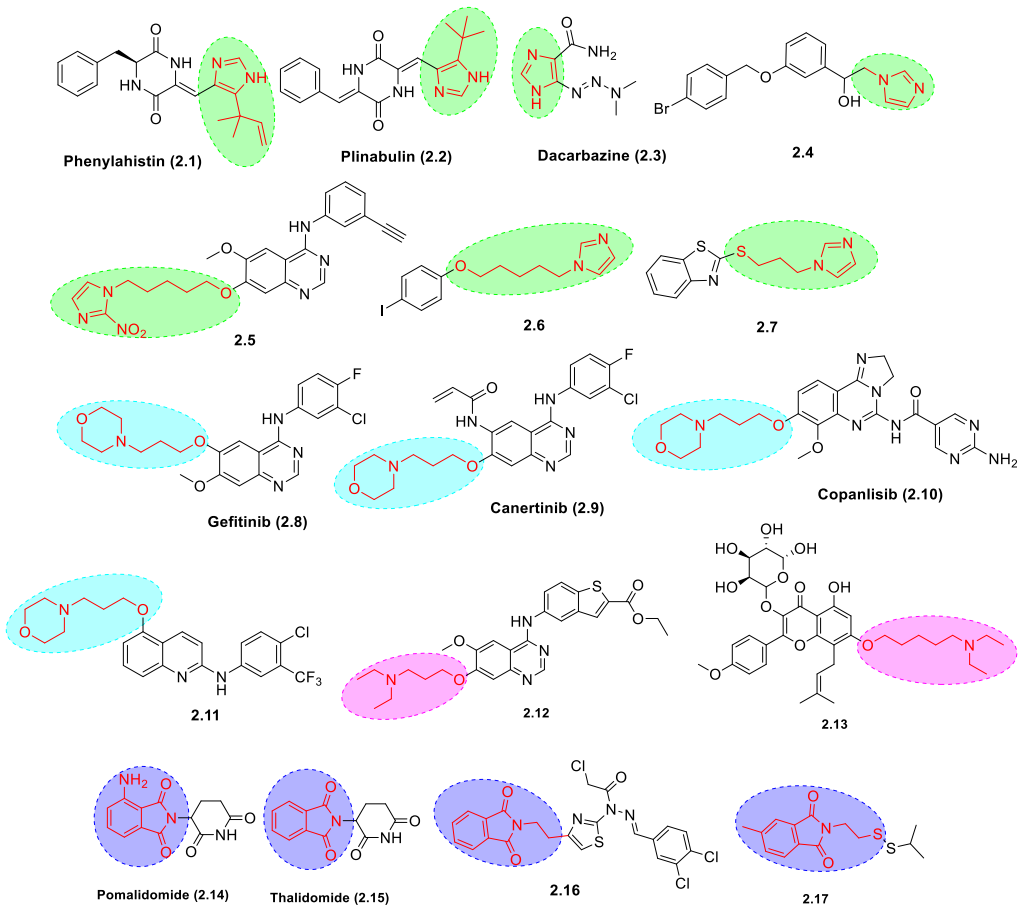

Figure 2.2. Chemical structures of anticancer drugs and compounds with potent anticancer activity, highlighting morpholino, imidazolo, diethylamino and phthalimido moieties connected directly or through flexible alkyl linkers.

Imidazole-based derivatives have also garnered attention for their anticancer potential. Several imidazole-containing agents, including Dacarbazine, Zoledronic acid, Mercaptopurine, Tipifarnib, and Temozolomide, are currently in clinical use for the treatment of various cancers (Ali et al., 2017). Compounds **2.6** and **2.7** (Figure 2.2), featuring imidazole rings linked to aryloxy and benzothiazole moieties, exhibited promising anticancer activity against MCF-7 cells, with IC_{50} values of 10.98 µM and 27.51 µM, respectively (Salerno et al., 2015). Similarly, compound **2.5** (Figure 2.2), a 4-anilinoquinazoline incorporating a 2-nitroimidazole group, demonstrated exceptional EGFR inhibition (IC_{50} = 0.47 nM), alongside strong antiproliferative effects on A549 and HT-29 cells under both normoxic and hypoxic conditions,

outperforming established drugs such as gefitinib and erlotinib (Cheng et al., 2014). Furthermore, another imidazole derivative, compound **2.4** (Figure 2.2), displayed moderate cytotoxic activity against MCF-7 cells (IC_{50} = 47.36 µM) (Ciaffaglione et al., 2020).

Studies by Wu et al. have shown that the incorporation of secondary alkyl amine side chains into Icariside II (ICA II) significantly enhances anticancer potency. Notably, compound 2.13, a modified derivative of ICA II, exhibited potent inhibitory effects on MCF-7, HepG2, HCCLM3-LUC, and MDA-MB-231 cell lines, with IC_{50} values ranging from 2.44 to 13.28 µM, substantially surpassing the activity of the parent molecule (T. Wu et al., 2018). Furthermore, a related study demonstrated that 4-benzothienylaminoquinazolines with secondary amino-substituted side chains, such as compound **2.12** (Figure 2.2) with a diethyl amino chain, not only inhibited HER2-positive tumor cells with 86% efficiency but also induced apoptosis and suppressed tumor growth *in vivo*, outperforming the reference compound gefitinib (X. Wu et al., 2010).

Phthalimide derivatives are also well-established in the field of anticancer pharmacology. Thalidomide (Figure 2.2), one of the most prominent phthalimide-based drugs, possesses anti-inflammatory, anti-angiogenic, and immunomodulatory properties and is used clinically in the treatment of multiple myeloma (Singhal et al., 1999). Compound **2.16** (Figure 2.2), containing a phthalimide moiety linked via an alkyl-thiazole moiety to a dichloro-substituted phenyl ring, exhibited notable anticancer activity against A549 cells (IC_{50} = 10.41 µM), as well as significant elastase inhibition and a 16-fold increase in caspase 3/7 activity (Donarska et al., 2021). Additionally, compound **2.17** (Figure 2.2), a phthalimide derivative with disulfide bonds, demonstrated selective cytotoxicity against MCF-7 cells (IC_{50} = 3.21 µM) while exhibiting low toxicity towards normal L929 fibroblasts (Chi et al., 2022).

2.2. Present Work

Building on the substantial evidence supporting the anticancer activity of 2,5-diketopiperazine (DKP) scaffolds and the beneficial role of alkyl-substituted secondary amines, the present study focuses on the design and synthesis of novel DKP-

based derivatives. Specifically, we propose the development of allyl-protected DKPanalogues functionalized with nitrogen-containing hydrophilic secondary amines, either directly appended to the aromatic ring or introduced via flexible alkyl chain linkers.

The introduction of alkyl chains offers several pharmacological advantages. Their small size and conformational flexibility allow for efficient spatial orientation between interacting pharmacophores, thereby enhancing the binding affinity of drug candidates to their biological targets (X. Wu et al., 2022). Furthermore, the literature survey shows that nitrogen atoms in the form of amine groups are prevalent in bioactive compounds due to their ability to form hydrogen bonds and engage in electrostatic interactions, thereby improving solubility and bioavailability. The presence of amine functionalities also enhances molecular reactivity, offering multiple sites for electrophilic attack and potentially promoting cytotoxicity against cancer cells (Joshi et al., 2013; Li et al., 2012).

As discussed, and illustrated (Figure 2.1), the clinical applications of DKP derivatives have been limited by poor solubility, despite their promising potential, particularly in non-protected analogues. To address this, one viable strategy is to substitute amide hydrogen atoms with protective groups, thereby disrupting strong intermolecular hydrogen-bond and π–π stacking interactions. Therefore, in this study, we have employed allyl groups to replace one of the amide hydrogens in the DKP core. This modification is expected to not only reduce intermolecular hydrogen bonding but also enhance lipophilicity. Interestingly, allyl-containing molecules such as S-allylcysteine have demonstrated broad-spectrum anticancer activity (Knowles & Milner, 2001; Ng et al., 2012; Xu et al., 2014). The presence of the allyl group has been shown to contribute significantly to their therapeutic effects, underscoring the rationale for its inclusion in the present design.

Therefore, based on these considerations, we report the design and synthesis of a novel series of allyl-protected DKP derivatives featuring hydrophilic secondary amines, either directly connected or introduced via alkyl spacers onto the aromatic ring of the DKP scaffold (Figure 2.3). This strategy aims to synergistically combine

solubility, potency, and pharmacokinetic advantages to develop new lead compounds with enhanced anticancer activity.

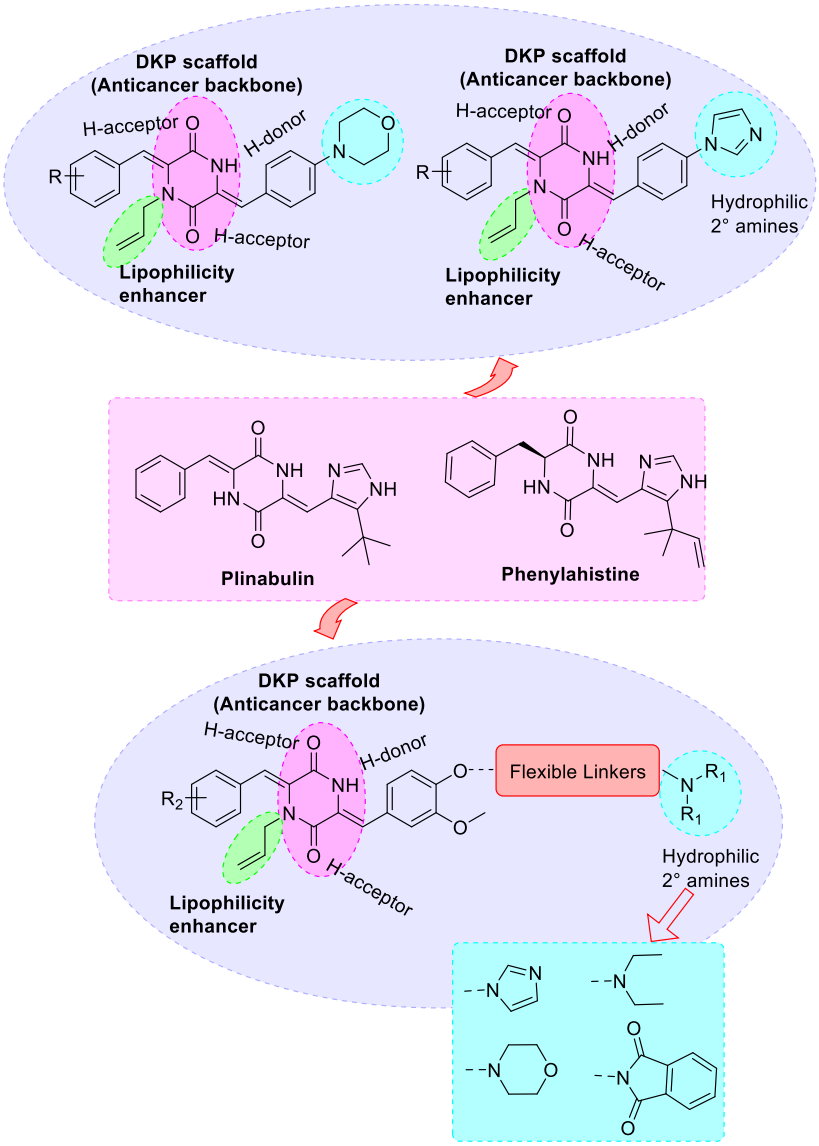

Figure 2.3. Schematic illustration of the design strategy for the development of novel Plinabulin-based DKP derivatives.

2.3. Materials and Methods

Unless otherwise specified, all chemicals and reagents were obtained from commercial suppliers and used as received, without further purification. Product characterization was performed using ^{1}H NMR, ^{13}C NMR, and High-Resolution Mass

Spectrometry (HRMS). HRMS spectra were recorded on a SCIEX Model X500R QTOF in positive-ion mode with internal calibration. NMR spectra were collected in DMSO-d_6 or $CDCl_3$ using a Bruker Avance spectrometer, operating at 500 or 600 MHz for ^{1}H NMR and 125 MHz for ^{13}C NMR, with tetramethylsilane (TMS) as the internal standard. Chemical shifts (δ) are reported in ppm relative to residual $CDCl_3$ (δ 7.26) and DMSO-d_6 (δ 2.50) for ^{1}H NMR, and $CDCl_3$ (δ 77.16) and DMSO-d_6 (δ 39.52) for ^{13}C NMR. Melting points were determined in open capillaries using a melting point apparatus and are uncorrected. Reaction progress was monitored by thin-layer chromatography (TLC) on Merck 60G F254 precoated aluminum plates, visualized under UV light or by staining with iodine vapors or with a potassium permanganate solution ($KMnO_4$, Na_4CO_4, deionized water). Flash chromatography separation was performed with silica gel (230-400 mesh). All solvents were of analytical grade. DMF was dried in CaH_2 and distilled. Glycine anhydride was purchased from Tokyo Chemicals Limited (TCI).

2.3.1. Schemes for the Synthesis of Novel Plinabulin-Based 2,5-Diketopiperazine Analogues

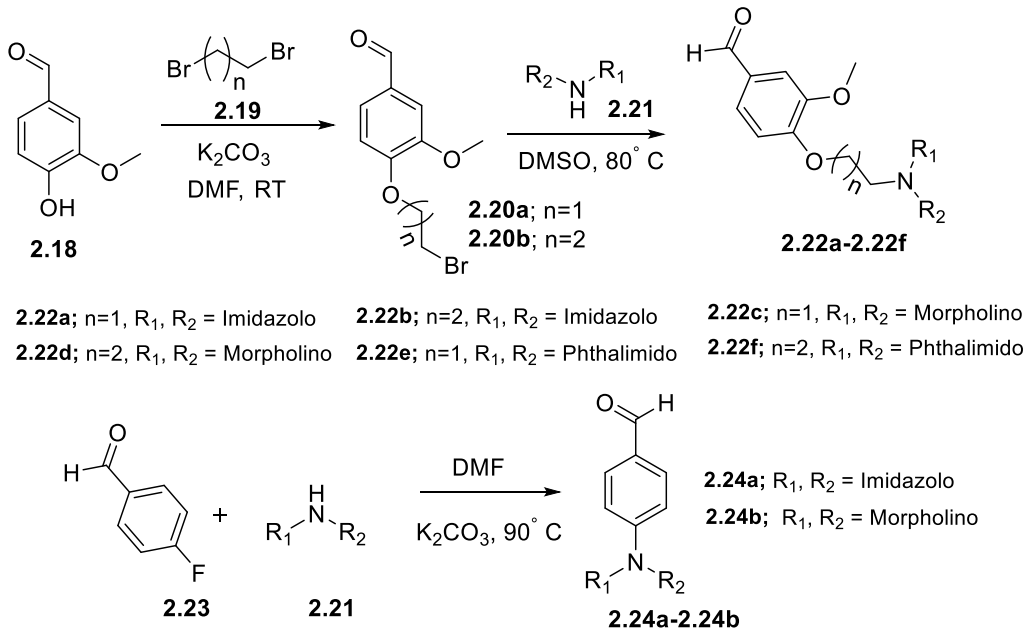

Scheme 2.1.

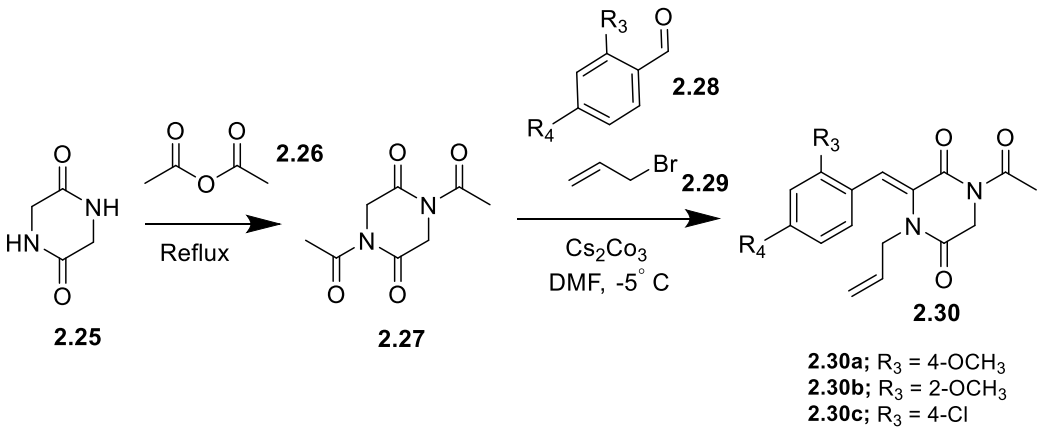

Scheme 2.2.

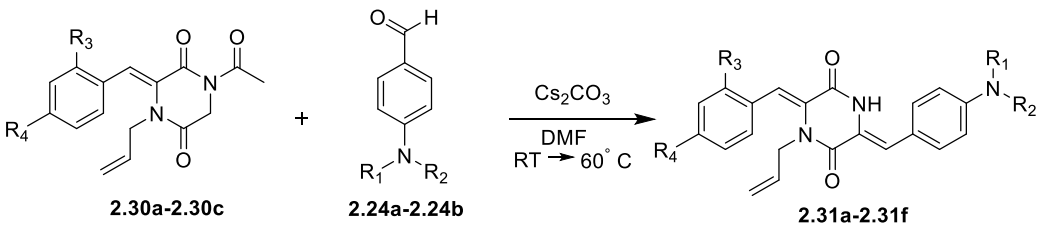

2.31a; R_3= H; R_4= 4-OCH_3, R_1, R_2 = Imidazolo
2.31b; R_3= H; R_4= 4-OCH_3, R_1, R_2 = Morpholino
2.31c; R_3= 2-OCH_3; R_4= H; R_1, R_2 = Imidazolo
2.31d; R_3= 2-OCH_3; R_4= H; R_1, R_2 = Morpholino
2.31e; R_3= H; R_4= 4-Cl, R_1, R_2 = Imidazolo
2.31f; R_3= H; R_4= 4-Cl, R_1, R_2 = Morpholino

Scheme 2.3.

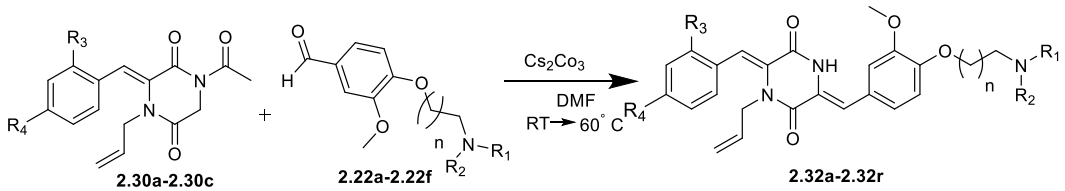

2.32a; n= 1, R_3= H; R_4= 4-OCH_3; R_1, R_2 = Imidazolo
2.32b; n= 2, R_3= H; R_4= 4-OCH_3, R_1, R_2 = Imidazolo
2.32c; n= 1, R_3= H; R_4= 4-OCH_3, R_1, R_2 = Morpholino
2.32d; n= 2, R_3= H; R_4= 4-OCH_3, R_1, R_2 = Morpholino
2.32e; n= 1, R_3= H; R_4= 4-OCH_3, R_1, R_2 = Phthalimido
2.32f; n= 2, R_3= H; R_4= 4-OCH_3, R_1, R_2 = Phthalimido
2.32g; n= 1, R_3= 2-OCH_3; R_4= H; R_1, R_2 = Imidazolo
2.32h; n= 2, R_3= 2-OCH_3; R_4= H; R_1, R_2 = Imidazolo
2.32i; n= 1, R_3= 2-OCH_3; R_4= H; R_1, R_2 = Morpholino
2.32j; n= 2, R_3= 2-OCH_3; R_4= H; R_1, R_2 = Morpholino
2.32k; n= 1, R_3= 2-OCH_3; R_4= H; R_1, R_2 = Phthalimido
2.32l; n= 2, R_3= 2-OCH_3; R_4= H; R_1, R_2 = Phthalimido
2.32m; n= 1, R_3= H; R_4= 4-Cl, R_1, R_2 = Imidazolo
2.32n; n= 2, R_3= H; R_4= 4-Cl, R_1, R_2 = Imidazolo
2.32o; n= 1, R_3= H; R_4= 4-Cl, R_1, R_2 = Morpholino
2.32p; n= 2, R_3= H; R_4= 4-Cl, R_1, R_2 = Morpholino
2.32q; n= 1, R_3= H; R_4= 4-Cl, R_1, R_2 = Phthalimido
2.32r; n= 2, R_3= H; R_4= 4-Cl, R_1, R_2 = Phthalimido

Scheme 2.4.

2.3.2. General Procedure for the Synthesis of 4-(Bromoalkoxy)-3-methoxybenzaldehyde (2.20a & 2.20b)

To a stirred solution of 4-Hydroxy-3-methoxybenzaldehyde (**2.18**) (32.86 mmol) and anhydrous potassium carbonate (92.58 mmol) in 60 mL DMF, aliphatic

dibromoalkanes (92.58 mmol) were added. The reaction mixture was stirred overnight at room temperature. After completion of the reaction, as indicated by TLC, the reaction mixture was poured into cold water and extracted with EtOAc (5 × 30 mL). The organic layers were then combined, dried over anhydrous Na_2SO_4, and evaporated under reduced pressure in a rotary evaporator. The crude product is purified by flash column chromatography over silica gel using hexane and EtOAc as eluents to obtain the desired product.

2.3.2.1. 4-(2-Bromoethoxy)-3-methoxybenzaldehyde (2.20a)

White solid; Yield: 49%; ^{1}H NMR (500 MHz, $CDCl_3$) δ 9.88 (s, 1H), 7.44 (dd, *J* = 5.9, 2.1 Hz, 2H), 7.01 (d, *J* = 8.6 Hz, 1H), 4.42 (t, *J* = 6.9 Hz, 2H), 3.95 (s, 3H), 3.70 (t, *J* = 7.1 Hz, 2H); ^{13}C·NMR (125 MHz, $CDCl_3$) δ 191.11, 153.05, 150.03, 130.84, 126.55, 112.35, 109.72, 68.77, 56.29, 29.65.

2.3.2.2. 4-(3-Bromopropoxy)-3-methoxybenzaldehyde (2.20b)

White solid; Yield: 56%; ^{1}H NMR (600 MHz, $CDCl_3$) δ 9.86 (s, 1H), 7.47 – 7.39 (m, 2H), 7.01 (d, *J* = 8.1 Hz, 1H), 4.25 (t, *J* = 5.9 Hz, 2H), 3.91 (s, 3H), 3.64 (t, *J* = 6.3 Hz, 2H), 2.42 (p, *J* = 6.1 Hz, 2H). ^{13}C·NMR (125 MHz, $CDCl_3$) δ 191.11, 153.63, 149.86, 130.25, 127.14, 111.79, 109.09, 66.79, 56.36, 32.38, 30.13.

2.3.3. General Procedure for the Synthesis of Amino Substituted Aldehydes (2.22a–2.22d)

Compound **2.20** (5.49 mmol), anhydrous K_2CO_3 (10.98 mmol), and desired secondary amines (6.59 mmol) were stirred in 20 mL DMF at 80 °C for 7 hours. After completion of the reaction, as indicated by TLC, the reaction mixture was poured into ice-cold water (60 mL) and extracted with EtOAc (4 × 30 mL). The organic layer was washed with brine (3 × 30 mL) and dried over Na_2SO_4. The solvent was then evaporated under reduced pressure using a rotary evaporator to obtain an oily residue of aldehydes substituted with secondary amines (**20.22a–20.22d**). The obtained product was used without further purification for subsequent reactions.

2.3.4. General Procedure for the Synthesis of Phthalimide substituted aldehydes (2.22e–2.22f)

Compound **2.20** (5.49 mmol), anhydrous K_2CO_3 (10.98 mmol), and phthalimide (6.59 mmol) were stirred in 20 mL DMF at room temperature overnight. Upon completion of the reaction, as indicated by TLC, the reaction mixture was poured into ice-cold water (60 mL), and the resulting solids were filtered. The solids obtained were then recrystallized using EtOH to afford the pure compound as white solids.

2.3.5. General procedure for the synthesis of 4-amino benzaldehydes (2.24a & 2.24b).

4-Fluorobenzaldehyde (16.11 mmol) was taken in a round-bottom flask, and 50 mL of DMF was added. To this solution, morpholine or imidazole (32.22 mmol) was added, and the reaction mixture was stirred at 90 °C overnight. Upon completion of the reaction, as indicated by TLC, the mixture was poured into ice-cold water and stored in a freezer overnight. The resulting solids were then filtered and recrystallized from ethanol to afford the desired product.

2.3.5.1. 4-(1H-imidazol-1-yl)benzaldehyde (2.24a)

Yellow solid; Yield: 90%; ^{1}H NMR (500 MHz, $CDCl_3$) δ 9.22 (s, 1H), 8.10 (d, *J* = 8.5 Hz, 2H), 7.98 (s, 1H), 7.57 (d, *J* = 8.40 Hz, 2H), 7.43 (s, 1H), 7.26 (s, 1H). ^{13}C NMR (125 MHz, $CDCl_3$) δ 190.43, 141.71, 135.62, 131.45, 131.29, 130.87, 121.16, 118.41.

2.3.5.2. 4-Morpholinobenzaldehyde (2.24b)

Yellow solid; Yield: 84%; ^{1}H NMR (500 MHz, $CDCl_3$) δ 9.21 (s, 1H), 7.52 (d, *J* = 8.1 Hz, 2H), 6.78 (d, *J = 8.0* Hz, 2H), 3.95-3.89 (m, 4H), 3.39-3.45 (m, 4H). ^{13}C NMR (125 MHz, $CDCl_3$) δ 190.46, 155.71, 132.52, 125.84, 114.87, 66.46, 48.38.

2.3.6. Procedure for Synthesis of 1,4-Diacetylpiperazine-2,5-dione (2.27)

A mixture of glycine anhydride (**2.25**) (17.5 mmol) and acetic anhydride (80 mL) was refluxed at 140°C for 18 hours. Upon completion, the excess acetic anhydride was removed under reduced pressure, and the obtained crude solid was purified by flash column chromatography over silica gel using hexane and EtOAc as eluent to obtain compound **2.27** as a Light yellowish solid.

Light yellowish Solid; Yield: 96%; ^{1}H NMR (500 MHz, $CDCl_3$) δ 4.56 (s, 4H), 2.54 (s, 6H); ^{13}C NMR (125 MHz, $CDCl_3$) δ 170.65, 165.83, 47.04, 26.58.

2.3.7. General procedure for the synthesis of compounds (2.30a–2.30c)

To a stirred solution of 1,4-diacetyl-2,5-diketopiperazine (5 mmol), allyl bromide (12.5 mmol), and aromatic aldehydes (12.5 mmol) in dry DMF (10 mL) was added Cs_2CO_3 (12.6 mmol) and stirred at -5°C for around 6 hours. The progress of the reaction was monitored by TLC, and after completion, the mixture was poured into cold water (30 mL) and extracted with EtOAc (4 × 30 mL). The extracted organic layers were combined and dried over Na_2SO_4. The excess solvent was removed under reduced pressure using a rotary evaporator, and the residue was purified by flash column chromatography over silica gel using hexane and EtOAc as the eluent to obtain the target compounds as white solids.

2.3.7.1. (Z)-1-acetyl-4-allyl-3-(4-methoxybenzylidene)piperazine-2,5-dione (2.30a)

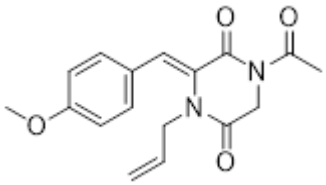

White solid; Yield: 61%; ^{1}H NMR (500 MHz, $CDCl_3$) δ 7.32 (d, *J* = 5.0 Hz, 2H), 7.24 (s, 1H), 6.93 (d, *J* = 10.0 Hz, 2H), 5.56-5.50 (m, 1H), 5.03 (d, *J* = 10.0 Hz, 1H), 4.78 (d, *J* = 15.0 Hz, 1H), 4.50 (s, 2H), 4.13 (d, *J* = 5.0 Hz, 2H), 3.85 (s, 3H), 2.60 (s, 3H); ^{13}C NMR (125 MHz, $CDCl_3$) δ 171.42, 165.14, 164.91, 160.81, 131.60, 131.33, 127.54, 126.9, 124.91, 118.86, 114.37, 55.42, 46.41, 45.34, 26.62; HRMS (ESI-TOF) m/z: calcd for $C_{17}H_{18}N_2O_4$, 314.1344 found, 315.1347 [M+H]+.

2.3.7.2. (Z)-1-acetyl-4-allyl-3-(2-methoxybenzylidene)piperazine-2,5-dione (2.30b)

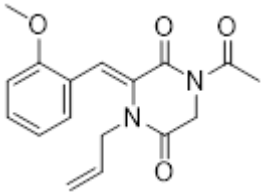

White solid; Yield: 62%; ^{1}H NMR (500 MHz, $CDCl_3$) δ 7.45 (s, 1H), 7.39 (t, *J* = 10.0 Hz, 1H), 7.25 (d, *J* = 10.0 Hz, 1H), 6.98 (t, *J* = 10.0 Hz, 1H), 6.94 (d, *J* = 10.0 Hz, 1H), 5.56-5.48 (m, 1H), 5.02 (d, *J* = 10.0 Hz, 1H), 4.73 (d, *J* = 15.0 Hz, 1H), 4.52 (s, 2H), 4.03 (d, *J* = 5.0 Hz, 2H), 3.86 (s, 3H), 2.64 (s, 3H); ^{13}C NMR (125 MHz, $CDCl_3$) δ 171.51, 164.72, 164.54, 157.83, 131.46, 131.12, 130.17, 129.41, 122.52,

121.81, 120.51, 118.73, 110.94, 55.64, 45.80, 45.35, 26.78; HRMS (ES-TOF) m/z: calcd for $C_{17}H_{18}N_2O_4$, 314.1344 found 315.1349 [M+H]+.

2.3.7.3. (Z)-1-acetyl-4-allyl-3-(4-chlorobenzylidene)piperazine-2,5-dione (2.30c)

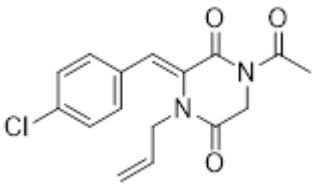

White solid; Yield: 60%; ^{1}H NMR (500 MHz, $CDCl_3$) δ 7.36 (d, *J* = 5.0 Hz, 2H), 7.24 (s, 1H), 7.21 (d, *J* = 12.0 Hz, 2H), 5.53-5.43 (m, 1H), 5.01 (d, *J* = 10.0 Hz, 1H), 4.73 (d, *J* = 17.0 Hz, 1H), 4.49 (s, 2H), 4.06 (d, *J* = 6.5 Hz, 2H), 2.58 (s, 3H); ^{13}C NMR (125 MHz, $CDCl_3$) δ 170.89, 164.26, 163.71, 160.01, 130.49, 131.01, 126.11, 125.23, 123.64, 117.72, 113.37, 55.57, 45.59, 26.71; HRMS (ESI-TOF) m/z: calcd for $C_{16}H_{15}ClN_2O_3$, 318.0771 found 319.1123 [M+H]+.

2.3.8. General procedure for the Synthesis of 2,5-Diketopiperazine Derivatives (2.31a-2.31f)

To a solution of intermediates (**2.30a–2.30c**) (1.6 mmol) and amino-substituted aldehydes (**2.24a & 2.24b**) (1.6 mmol) in dry DMF (3 mL), Cs_2CO_3 (2.4 mmol) was added. The reaction mixture was stirred at room temperature, then heated to 60 °C and stirred for 6 hours. Upon completion of the reaction, as indicated by TLC, the reaction mixture was poured into an ice-cold brine solution, and the organic compound was extracted with EtOAc (4 × 20 mL). The organic layers were then combined, dried over Na_2SO_4, and evaporated under reduced pressure using a rotary evaporator. The crude product was purified by flash column chromatography over silica gel using $CHCl_3$/MeOH as the eluent, affording the target compounds.

2.3.8.1. 3-((Z)-4-(1H-imidazol-1-yl)benzylidene)-1-allyl-6-((Z)-4-methoxybenzylidene)piperazine-2,5-dione (2.31a)

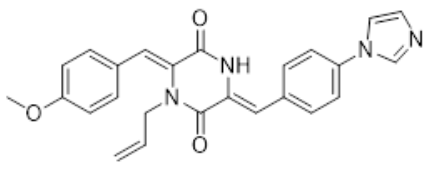

Yellowish Solid: Yield; 50%; M.p.: 302-304 °C; ^{1}H NMR (500 MHz, DMSO-d_6) δ 10.57 (s, 1H), 8.32 (s, 1H), 7.82 – 7.65 (m, 5H), 7.31 (d, *J* = 8.2 Hz, 2H), 7.09 (s, 1H), 7.06 – 6.91 (m, 3H), 6.82 (s, 1H), 5.63 – 5.50 (m, 1H), 4.97 (d, *J* = 10.4 Hz, 1H), 4.67 (d, *J* = 17.2 Hz, 1H), 4.16 (d, *J* = 5.5 Hz, 2H), 3.77 (s, 3H). ^{13}C NMR (125 MHz, $CDCl_3$) δ 160.80, 160.34, 159.72, 137.14, 135.46, 132.49, 131.57, 131.30, 130.72, 130.38, 127.11, 126.72, 125.83,

123.00, 122.01, 118.48, 117.97, 115.75, 114.17, 55.46, 48.18. HRMS (ESI-TOF) m/z: calcd for $C_{25}H_{22}N_4O_3$, 426.1691, found 427.1743 $[M+H]^+$.

2.3.8.2. 1-allyl-6-((Z)-4-methoxybenzylidene)-3-((Z)-4-morpholinobenzylidene) piperazine-2,5-dione (2.31b)

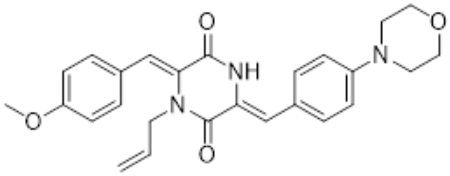

Yellowish Solid; Yield: 53%; ^{1}H NMR (500 MHz, $CDCl_3$) δ 7.92 (s, 1H), 7.39 – 7.29 (m, 4H), 7.21 (d, *J* = 8.0 Hz, 1H), 7.01 – 6.87 (m, 5H), 5.63 – 5.45 (m, 1H), 4.98 (d, *J* = 10.5 Hz, 1H), 4.75 (d, *J* = 17.0 Hz, 1H), 4.22 (d, *J* = 6.0 Hz, 2H), 3.90 – 3.81 (m, 7H), 3.26 – 3.18 (m, 4H). ^{13}C NMR (125 MHz, $CDCl_3$) δ 160.23, 159.73, 157.48, 151.27, 131.74, 130.54, 130.50, 130.04, 128.79, 124.24, 123.97, 123.11, 120.33, 118.01, 117.90, 117.77, 115.46, 110.75, 66.75, 55.57, 48.34, 47.42. HRMS (ESI-TOF) m/z: calcd for $C_{26}H_{27}N_3O_4$, 445.2001, found 446.2531 $[M+H]^+$.

2.3.8.3. 3-((Z)-4-(1H-imidazol-1-yl)benzylidene)-1-allyl-6-((Z)-2-methoxybenzyli dene)piperazine-2,5-dione (2.31c)

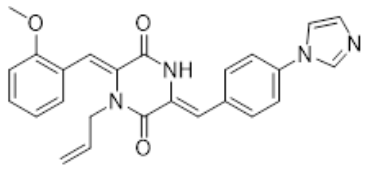

Yellowish Solid; Yield: 58%; ^{1}H NMR (500 MHz, DMSO-d_6) δ 10.61 (s, 1H), 8.32 (s, 1H), 7.79 (s, 1H), 7.73 – 7.68 (m, 4H), 7.36 (t, *J* = 8.0 Hz, 1H), 7.22 (d, *J* = 7.9 Hz, 1H), 7.10 (s, 1H), 7.08 – 7.02 (m, 2H), 6.98 (t, *J* = 7.4 Hz, 1H), 6.84 (s, 1H), 5.58 – 5.44 (m, 1H), 4.94 (d, *J* = 10.0 Hz, 1H), 4.59 (d, *J* = 17.0 Hz, 1H), 4.08 (d, *J* = 5.9 Hz, 2H), 3.80 (s, 3H). ^{13}C NMR (125 MHz, $CDCl_3$) δ 160.99, 160.30, 159.85, 137.07, 135.39, 132.51, 131.77, 131.60, 131.26, 130.75, 130.52, 127.15, 126.83, 125.83, 122.80, 121.80, 118.44, 117.88, 115.90, 114.16, 77.41, 77.15, 76.90, 55.47, 48.13. HRMS (ESI-TOF) m/z: calcd for $C_{25}H_{22}N_4O_3$, 426.1691, found 427.1739 $[M+H]^+$.

2.3.8.4. 1-allyl-6-((Z)-2-methoxybenzylidene)-3-((Z)-4-morpholinobenzylidene)

piperazine-2,5-dione (2.31d)

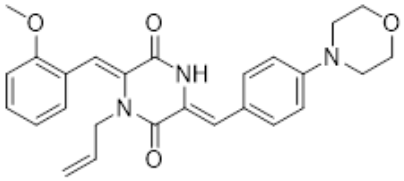

Yellowish Solid; Yield: 57%; ^{1}H NMR (500 MHz, DMSO-d_6) 10.32 (s, 1H), 7.46 (d, J = 8.5 Hz, 2H), 7.34 (t, J = 8.0 Hz, 1H), 7.19 (d, J = 7.5 Hz, 1H), 7.05 (d, J = 8.5 Hz, 1H), 7.01 – 6.90 (m, 4H), 6.74 (s, 1H), 5.55 – 5.44 (m, 1H), 4.92 (d, J = 10.0 Hz, 1H), 4.58 (d, J = 17.0 Hz, 1H), 4.05 (d, J = 5.5 Hz, 2H), 3.78 (s, 3H), 3.76 – 3.65 (m, 4H), 3.23 – 3.09 (m, 4H). ^{13}C NMR (125 MHz, $CDCl_3$) δ 160.21, 159.73, 157.48, 151.27, 131.74, 130.54, 130.50, 130.04, 128.77, 124.22, 123.09, 120.33, 118.02, 117.92, 117.77, 115.47, 110.74, 66.76, 55.57, 48.34, 47.43. HRMS (ESI-TOF) m/z: calcd for $C_{26}H_{27}N_3O_4$, 445.2001, found 446.2048 $[M+H]^+$.

2.3.8.5. 3-((Z)-4-(1H-imidazol-1-yl)benzylidene)-1-allyl-6-((Z)-4-chlorobenzyli dene)piperazine-2,5-dione (2.31e)

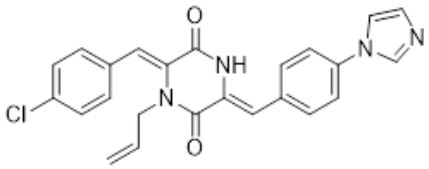

Yellowish Solid; Yield: 59%; ^{1}H NMR (500 MHz, $CDCl_3$) δ 8.02 (s, 1H), 7.94 (s, 1H), 7.57 (d, J = 9.0 Hz, 2H), 7.50 (d, J = 8.0 Hz, 2H), 7.39 (d, J = 8.5 Hz, 2H), 7.34 (s, 1H), 7.28 (d, J = 9.6 Hz, 3H), 7.23 (s, 1H), 7.08 (s, 1H), 5.61 – 5.50 (m, 1H), 5.06 (d, J = 10.0 Hz, 1H), 4.81 (d, J = 17.0 Hz, 1H), 4.29 (d, J = 6.5 Hz, 2H). ^{13}C NMR (125 MHz, $CDCl_3$) δ 160.31, 159.65, 136.58, 135.90, 134.88, 132.88, 132.29, 131.30, 130.73, 130.66, 130.00, 128.92, 128.86, 126.90, 121.98, 120.79, 118.47, 116.32, 48.07. HRMS (ESI-TOF) m/z: calcd for $C_{24}H_{19}ClN_4O_2$, 430.1196, found 431.1236 $[M+H]^+$.

2.3.8.6. 1-allyl-6-((Z)-4-chlorobenzylidene)-3-((Z)-4-morpholinobenzylidene)pi perazine-2,5-dione (2.31f)

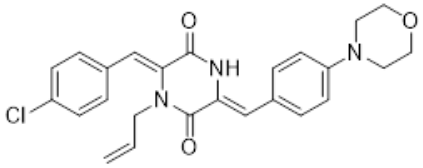

Yellowish Solid: Yield: 56% ^{1}H NMR (500 MHz, $CDCl_3$) δ 7.91 (s, 1H), 7.40 – 7.34 (m, 4H), 7.25 (d, J = 8.0 Hz, 2H), 7.19 (s, 1H), 7.02 (s, 1H), 6.93 (d, J = 8.0 Hz, 2H), 5.58 – 5.48 (m, 1H), 5.02 (d, J = 10.0 Hz, 1H), 4.79 (d, J = 17.0 Hz, 1H), 4.26 (d, J = 5.0 Hz, 2H), 3.88 – 3.85 (m, 4H), 3.24 (t, J = 5.5 Hz, 4H). ^{13}C NMR (125 MHz, $CDCl_3$) δ 160.02, 159.95, 151.40,

134.79, 132.57, 131.55, 130.78, 130.12, 129.16, 128.84, 123.78, 123.65, 120.17, 118.69, 118.32, 115.40, 66.72, 48.24, 48.09. HRMS (ESI-TOF) m/z: calcd for $C_{25}H_{24}ClN_3O_3$, 449.1506, found 450.1559 $[M+H]^+$.

2.3.9. General procedure for the synthesis of 2,5-Diketopiperazine derivatives (2.32a-2.32r)

To a solution of intermediates (**2.30a–2.30c**) (1.6 mmol) and amino-substituted aldehydes (**2.24a–2.24f**) (1.6 mmol) in dry DMF (3 mL), Cs_2CO_3 (2.4 mmol) was added. The reaction mixture was stirred at room temperature, then heated to 60 °C and stirred for 6 hours. Upon completion of the reaction, as indicated by TLC, the reaction mixture was poured into an ice-cold brine solution, and the organic compound was extracted with EtOAc (4 × 20 mL). The organic layers were then combined, dried over Na_2SO_4, and evaporated under reduced pressure using a rotary evaporator. The crude product was purified by flash column chromatography over silica gel using $CHCl_3$/MeOH as the eluent, affording the target compounds.

2.3.9.1. 3-((Z)-4-(2-(1H-imidazol-1-yl)ethoxy)-3-methoxybenzylidene)-1-allyl-6-((Z)-4-methoxybenzylidene)piperazine-2,5-dione (2.32a)

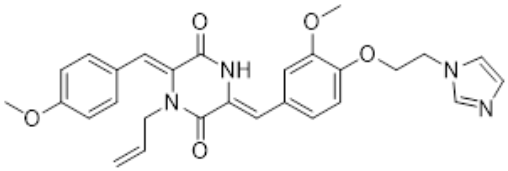

Yellowish Solid; Yield: 52%; ^{1}H NMR (500 MHz, $CDCl_3$) δ 7.94 (s, 1H), 7.64 (s, 1H), 7.28 (d, *J* = 7.9 Hz, 2H), 7.21 (s, 1H), 7.08 (d, *J* = 12.1 Hz, 2H), 7.02 – 6.94 (m, 2H), 6.95 – 6.88 (m, 3H), 6.82 (d, *J* = 8.0 Hz, 1H), 5.63 – 5.51 (m, 1H), 5.02 (d, *J* = 10.5 Hz, 1H), 4.82 (d, *J* = 17.2 Hz, 1H), 4.37 (t, *J* = 4.9 Hz, 2H), 4.34 – 4.25 (m, 4H), 3.87 (s, 3H), 3.85 (s, 3H). ^{13}C NMR (125 MHz, $CDCl_3$) δ 160.78, 160.19, 160.12, 150.30, 148.08, 137.75, 131.72, 131.24, 129.46, 127.27, 127.11, 126.05, 125.70, 122.30, 121.23, 119.59, 118.25, 117.43, 114.36, 114.09, 112.85, 68.76, 56.11, 55.44, 48.02, 46.53. HRMS (ESI-TOF) m/z: calcd for $C_{28}H_{28}N_4O_5$, 500.2059, found 501.2634 $[M+H]^+$.

2.3.9.2. 3-((Z)-4-(3-(1H-imidazol-1-yl)propoxy)-3-methoxybenzylidene)-1-allyl-6-((Z)-4-methoxybenzylidene)piperazine-2,5-dione (2.32b)

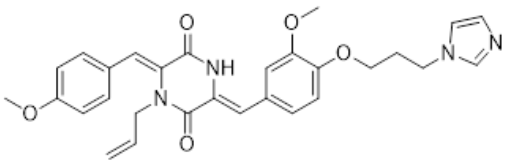

Yellowish Solid; Yield: 47%; ^{1}H NMR (500 MHz, $CDCl_3$) δ 7.92 (s, 1H), 7.53 – 7.49 (m, 1H), 7.28 (d, *J* = 8.2 Hz, 2H), 7.07 (s, 1H), 7.02 – 6.98 (m, 2H), 6.95 – 6.85 (m, 6H), 5.58 (m, 1H), 5.03 (d, *J* = 9.7 Hz, 1H), 4.83 (d, *J* = 17.2 Hz, 1H), 4.31 (d, *J* = 5.6 Hz, 2H), 4.24 (t, *J* = 6.6 Hz, 2H), 3.98 (t, *J* = 6.0 Hz, 2H), 3.90 (s, 3H), 3.86 (s, 3H), 2.28 (m, 2H). ^{13}C NMR (125 MHz, $CDCl_3$) δ 160.64, 160.21, 160.05, 150.23, 148.51, 137.47, 131.71, 131.26, 129.58, 127.04, 126.68, 126.04, 125.57, 122.41, 121.18, 119.05, 118.30, 117.48, 114.10, 114.06, 112.49, 65.19, 56.08, 55.44, 48.08, 43.46, 30.72. HRMS (ESI-TOF) m/z: calcd for $C_{29}H_{30}N_4O_5$, 514.2216, found 515.2799 $[M+H]^+$.

2.3.9.3. 1-allyl-3-((Z)-3-methoxy-4-(2-morpholinoethoxy)benzylidene)-6-((Z)-4-methoxybenzylidene)piperazine-2,5-dione (2.32c)

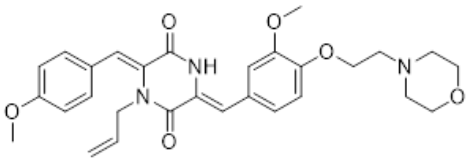

Yellowish Solid; Yield: 60%; ^{1}H NMR (600 MHz, $CDCl_3$) δ 7.89 (s, 1H), 7.28 (d, *J* = 8.6 Hz, 2H), 7.22 (s, 1H), 7.04 – 6.97 (m, 2H), 6.95 – 6.85 (m, 4H), 5.62 – 5.53 (m, 1H), 5.03 (dd, *J* = 10.2, 1.3 Hz, 1H), 4.83 (dd, *J* = 17.1, 1.4 Hz, 1H), 4.31 (d, *J* = 6.0 Hz, 2H), 4.20 (t, *J* = 5.8 Hz, 2H), 3.88 (s, 3H), 3.86 (s, 3H), 3.75 (t, *J* = 4.6 Hz, 4H), 2.88 (t, *J* = 5.8 Hz, 2H), 2.62 (t, *J* = 4.8 Hz, 4H). ^{13}C NMR (125 MHz, $CDCl_3$) δ 160.57, 160.20, 150.18, 148.87, 144.73, 131.73, 131.25, 127.04, 126.32, 126.05, 125.49, 122.36, 121.18, 118.26, 117.62, 114.10, 113.81, 112.58, 66.98, 57.45, 56.15, 55.44, 54.18, 48.07. HRMS (ESI-TOF) m/z: calcd for $C_{29}H_{33}N_3O_6$, 519.2369, found 520.2389 $[M+H]^+$.

2.3.9.4. 1-allyl-3-((Z)-3-methoxy-4-(3-morpholinopropoxy)benzylidene)-6-((Z)-4-methoxybenzylidene)piperazine-2,5-dione (2.32d)

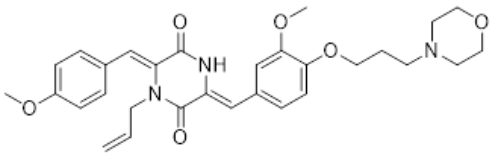

Yellowish Solid; Yield: 52%; ^{1}H NMR (600 MHz, $CDCl_3$) δ 7.89 (s, 1H), 7.28 (d, *J* = 8.1 Hz, 2H), 7.22 (s, 1H), 7.02 (d, *J* = 8.3 Hz, 1H), 6.99 (s, 1H), 6.96 – 6.88 (m, 4H), 5.62 – 5.53 (m, 1H), 5.03 (d, *J* = 10.0 Hz, 1H), 4.83 (d, *J* = 17.4 Hz, 1H), 4.31 (d, *J* = 5.9 Hz, 2H), 4.13 (t, *J* = 6.6 Hz, 2H), 3.88 (s,

3H), 3.86 (s, 3H), 3.72 (t, *J* = 4.7 Hz, 4H), 2.54 (t, *J* = 7.2 Hz, 2H), 2.51 – 2.44 (m, 4H), 2.05 (p, *J* = 6.9 Hz, 2H). ^{13}C NMR (126 MHz, $CDCl_3$) δ 160.52, 159.79, 157.69, 150.21, 149.32, 131.87, 130.85, 130.71, 128.87, 126.17, 125.37, 123.22, 121.54, 120.57, 118.41, 118.30, 117.88, 113.62, 112.76, 110.99, 77.67, 77.41, 67.57, 67.17, 56.38, 55.81, 55.66, 53.96, 47.63, 26.46. HRMS (ESI-TOF) m/z: calcd for $C_{30}H_{35}N_3O_6$, 533.2525, found 534.576 $[M+H]^+$.

2.3.9.5 2-(2-(4-((Z)-(4-allyl-5-((Z)-4-methoxybenzylidene)-3,6-dioxopiperazin-2-ylidene)methyl)-2-methoxyphenoxy)ethyl)isoindoline-1,3-dione (2.32e)

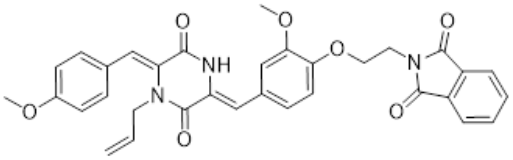

Yellowish Solid; Yield: 70%; ^{1}H NMR (600 MHz, $CDCl_3$) δ 7.88 (dd, *J* = 5.4, 3.1 Hz, 2H), 7.85 (s, 1H), 7.73 (dd, *J* = 5.4, 3.0 Hz, 2H), 7.27 (d, *J* = 8.6 Hz, 2H), 7.21 (s, 1H), 7.00 – 6.96 (m, 2H), 6.96 (s, 1H), 6.92 (d, *J* = 8.8 Hz, 2H), 6.85 (s, 1H), 5.63 – 5.51 (m, 1H), 5.02 (dd, *J* = 10.2, 1.3 Hz, 1H), 4.82 (dd, *J* = 17.1, 1.4 Hz, 1H), 4.33 (t, *J* = 6.1 Hz, 2H), 4.30 (dt, *J* = 6.0, 1.4 Hz, 2H), 4.15 (t, *J* = 6.1 Hz, 2H), 3.85 (s, 3H), 3.78 (s, 3H). ^{13}C NMR (125 MHz, $CDCl_3$) ^{13}C NMR (125 MHz, $CDCl_3$) δ 168.15, 160.61, 160.19, 160.05, 150.42, 148.46, 134.13, 132.19, 131.73, 131.25, 127.03, 126.83, 126.06, 125.42, 123.42, 122.36, 121.19, 118.25, 117.57, 114.78, 114.09, 112.88, 66.06, 56.14, 55.43, 48.06, 37.13. HRMS (ESI-TOF) m/z: calcd for $C_{33}H_{29}N_3O_7$, 579.2005, found 580.2060 $[M+H]^+$.

2.3.9.6. 2-(3-(4-((Z)-(4-allyl-5-((Z)-4-methoxybenzylidene)-3,6-dioxopiperazin-2-ylidene)methyl)-2-methoxyphenoxy)propyl)isoindoline-1,3-dione (2.32f)

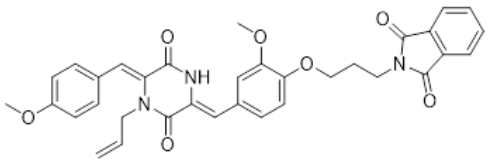

Yellowish Solid; Yield; 69%. ^{1}H NMR (600 MHz, $CDCl_3$) δ 7.92 (s, 1H), 7.84 (dd, *J* = 4.4, 3.1 Hz, 2H), 7.72 (dd, *J* = 4.7, 2.7 Hz, 2H), 7.28 (d, *J* = 8.4 Hz, 2H), 7.21 (s, 1H), 7.00 (d, *J* = 8.8 Hz, 1H), 6.97 (s, 1H), 6.92 (d, *J* = 7.4 Hz, 2H), 6.89 (d, *J* = 8.2 Hz, 1H), 6.82 (s, 1H), 5.62 – 5.52 (m, 1H), 5.02 (dd, *J* = 10.2, 1.3 Hz, 1H), 4.82 (dd, *J* = 17.1, 1.4 Hz, 1H), 4.31 (d, *J* = 6.0 Hz, 2H), 4.13 (t, *J* = 6.1 Hz, 2H), 3.93 (t, *J* = 6.6 Hz, 2H), 3.86 (s, 3H), 3.69 (s, 3H), 2.26 (p, *J* = 6.4 Hz, 2H). ^{13}C NMR (125 MHz, $CDCl_3$) δ 168.43, 160.61, 160.15, 150.03, 148.93, 133.94, 132.33, 131.77, 131.25, 127.11, 126.09, 126.05, 125.21, 123.28, 122.24,

121.24, 118.22, 117.81, 114.07, 113.55, 112.42, 67.07, 55.94, 55.43, 48.04, 35.61, 28.39. HRMS (ESI-TOF) m/z: calcd for $C_{34}H_{31}N_3O_7$, 593.2162, found 594.2272 $[M+H]^+$.

2.3.9.7. 3-((Z)-4-(2-(1H-imidazol-1-yl)ethoxy)-3-methoxybenzylidene)-1-allyl-6-((Z)-2-methoxybenzylidene)piperazine-2,5-dione (2.32g)

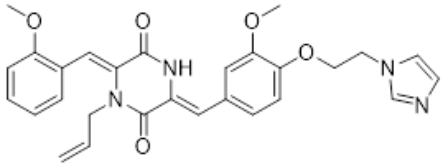

Yellowish Solid; Yield: 56%; ^{1}H NMR (600 MHz, $CDCl_3$) δ 8.22 (s, 1H), 7.66 (s, 1H), 7.34 (td, *J* = 7.7, 1.7 Hz, 1H), 7.30 (s, 1H), 7.21 (dd, *J* = 8.1, 1.5 Hz, 1H), 7.09 (s, 1H), 7.04 (s, 1H), 7.01 – 6.88 (m, 5H), 6.81 (d, *J* = 8.3 Hz, 1H), 5.58 – 5.48 (m, 1H), 4.98 (dd, *J* = 10.2, 1.4 Hz, 1H), 4.74 (dd, *J* = 17.1, 1.4 Hz, 1H), 4.35 (t, *J* = 5.1 Hz, 2H), 4.25 (t, *J* = 5.1 Hz, 2H), 4.21 (d, *J* = 6.0 Hz, 2H), 3.86 (s, 3H), 3.84 (s, 3H). ^{13}C NMR (125 MHz, $CDCl_3$) δ 160.24, 159.43, 157.47, 150.39, 148.07, 137.74, 131.59, 130.66, 130.49, 129.35, 128.59, 127.32, 125.65, 122.97, 121.07, 120.35, 119.64, 118.32, 118.13, 117.13, 114.46, 112.78, 110.77, 68.78, 56.14, 55.59, 47.43, 46.59. HRMS (ESI-TOF) m/z: calcd for $C_{28}H_{28}N_4O_5$, 500.2059, found 501.2133 $[M+H]^+$.

2.3.9.8. 3-((Z)-4-(3-(1H-imidazol-1-yl)propoxy)-3-methoxybenzylidene)-1-allyl-6-((Z)-2-methoxybenzylidene)piperazine-2,5-dione (2.32h)

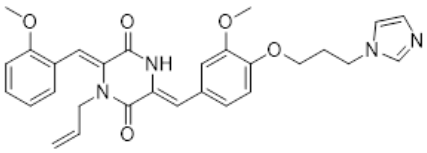

Yellowish Solid; Yield: 47%; ^{1}H NMR (600 MHz, $CDCl_3$) δ 7.98 (s, 1H), 7.51 (s, 1H), 7.39 – 7.31 (m, 2H), 7.23 (d, *J* = 6.8 Hz, 1H), 7.08 – 7.05 (m, 1H), 7.00 (m, 2H), 6.95 – 6.90 (m, 3H), 6.90 – 6.83 (m, 2H), 5.59 – 5.51 (m, 1H), 5.00 (dd, *J* = 10.1, 1.5 Hz, 1H), 4.77 (dd, *J* = 17.0, 1.5 Hz, 1H), 4.28 – 4.18 (m, 4H), 3.98 (t, *J* = 5.7 Hz, 2H), 3.91 (s, 3H), 3.86 (s, 3H), 2.29 (p, *J* = 6.4 Hz, 2H). ^{13}C NMR (125 MHz, $CDCl_3$) δ 160.24, 157.48, 150.23, 148.38, 137.50, 131.66, 130.65, 130.51, 129.72, 129.64, 126.79, 125.53, 123.01, 121.23, 120.38, 119.11, 118.27, 118.20, 117.30, 114.13, 112.55, 110.78, 65.24, 56.12, 55.62, 47.47, 43.48, 30.77. HRMS (ESI-TOF) m/z: calcd for $C_{29}H_{30}N_4O_5$, 514.2216, found 515.2249 $[M+H]^+$.

2.3.9.9. 1-allyl-3-((Z)-3-methoxy-4-(2-morpholinoethoxy)benzylidene)-6-((Z)-2-methoxybenzylidene)piperazine-2,5-dione (2.32i)

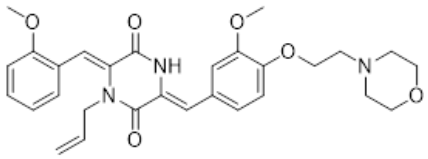

Yellowish Solid; Yield: 44%; ^{1}H NMR (600 MHz, $CDCl_3$) δ 7.96 (s, 1H), 7.37 – 7.34 (m, 1H), 7.33 (s, 1H), 7.22 (dt, *J* = 7.5, 1.4 Hz, 1H), 7.04 – 6.89 (m, 6H), 5.59 – 5.51 (m, 1H), 5.00 (dd, *J* = 10.2, 1.3 Hz, 1H), 4.77 (dd, *J* = 17.1, 1.5 Hz, 1H), 4.24 (d, *J* = 6.0 Hz, 2H), 4.20 (t, *J* = 6.0 Hz, 2H), 3.88 (s, 3H), 3.86 (s, 3H), 3.75 (t, *J* = 4.7 Hz, 4H), 2.87 (t, *J* = 6.0 Hz, 2H), 2.62 (t, *J* = 4.8 Hz, 4H). ^{13}C NMR (125 MHz, $CDCl_3$) δ 160.23, 159.51, 157.46, 150.13, 148.86, 131.65, 130.60, 130.48, 128.65, 126.33, 125.29, 123.01, 121.26, 120.34, 118.14, 118.04, 117.45, 113.78, 112.64, 110.76, 66.95, 57.45, 56.13, 55.57, 54.16, 47.38. HRMS (ESI-TOF) m/z: calcd for $C_{29}H_{33}N_3O_6$, 519.2369, found 520.2446 $[M+H]^+$.

2.3.9.10. 1-allyl-3-((Z)-3-methoxy-4-(3-morpholinopropoxy)benzylidene)-6-((Z)-2-methoxybenzylidene)piperazine-2,5-dione (2.32j)

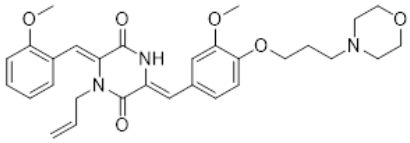

Yellowish Solid; Yield: 55%; ^{1}H NMR (600 MHz, $CDCl_3$) δ 7.93 (s, 1H), 7.38 – 7.32 (m, 2H), 7.23 (d, *J* = 7.0 Hz, 1H), 7.05 – 6.88 (m, 6H), 5.61 – 5.49 (m, 1H), 5.00 (dd, *J* = 10.2, 1.3 Hz, 1H), 4.77 (dd, *J* = 17.1, 1.4 Hz, 1H), 4.24 (d, *J* = 6.1 Hz, 2H), 4.13 (t, *J* = 6.6 Hz, 2H), 3.88 (s, 3H), 3.86 (s, 3H), 3.73 (t, *J* = 4.7 Hz, 4H), 2.59 – 2.39 (m, 6H), 2.05 (p, *J* = 6.9 Hz, 2H). ^{13}C NMR (126 MHz, $CDCl_3$) δ 160.29, 159.56, 157.46, 149.98, 149.09, 131.63, 130.62, 130.48, 128.64, 125.94, 125.14, 122.99, 121.31, 120.34, 118.18, 118.06, 117.65, 113.39, 112.53, 110.76, 67.33, 66.94, 56.15, 55.57, 55.43, 53.72, 47.40, 26.22. HRMS (ESI-TOF) m/z: calcd for $C_{30}H_{35}N_3O_6$, 533.2525, found 534.2560 $[M+H]^+$.

2.3.9.11. 2-(2-(4-((Z)-(4-allyl-5-((Z)-2-methoxybenzylidene)-3,6-dioxopiperazin-2-ylidene)methyl)-2-methoxyphenoxy)ethyl)isoindoline-1,3-dione (2.32k)

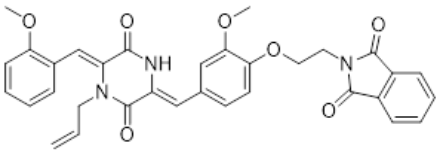

Yellowish Solid; Yield: 68%; ^{1}H NMR (600 MHz, $CDCl_3$) δ 7.90 (s, 1H), 7.91 – 7.84 (m, 2H), 7.76 – 7.70 (m, 2H), 7.38 – 7.32 (m, 1H),

7.32 (s, 1H), 7.24 – 7.19 (m, 1H), 7.01 – 6.97 (m, 3H), 6.96 (s, 1H), 6.94 – 6.89 (m, 1H), 6.85 (d, *J* = 1.7 Hz, 1H), 5.59 – 5.50 (m, 1H), 5.00 (dd, *J* = 10.2, 1.3 Hz, 1H), 4.76 (dd, *J* = 17.1, 1.3 Hz, 1H), 4.33 (t, *J* = 6.1 Hz, 2H), 4.23 (dt, *J* = 6.0, 1.4 Hz, 2H), 4.15 (t, *J* = 6.1 Hz, 2H), 3.85 (s, 3H), 3.78 (s, 3H). ^{13}C NMR (125 MHz, $CDCl_3$) δ 168.17, 160.13, 159.43, 157.48, 150.47, 148.44, 134.14, 132.20, 131.63, 130.56, 128.59, 126.90, 125.38, 123.43, 123.00, 121.10, 120.35, 118.32, 118.24, 117.36, 114.82, 112.86, 110.77, 66.08, 56.15, 55.57, 47.44, 37.16. HRMS (ESI-TOF) m/z: calcd for $C_{33}H_{29}N_3O_7$, 579.2005, found 580.2139 $[M+H]^+$.

2.3.9.12. 2-(3-(4-((Z)-(4-allyl-5-((Z)-2-methoxybenzylidene)-3,6-dioxopiperazin-2-ylidene)methyl)-2-methoxyphenoxy)propyl)isoindoline-1,3-dione (2.32l)

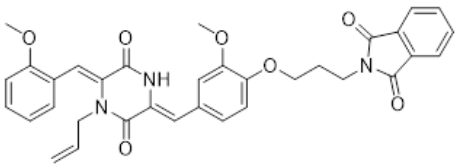

Yellowish Solid; Yield: 64%; ^{1}H NMR (600 MHz, $CDCl_3$) δ 8.02 (s, 1H), 7.85 (dd, *J* = 5.5, 3.1 Hz, 2H), 7.72 (dd, *J* = 5.6, 3.1 Hz, 2H), 7.38 – 7.30 (m, 2H), 7.22 (d, *J* = 7.5 Hz, 1H), 7.03 – 6.95 (m, 3H), 6.96 – 6.86 (m, 2H), 6.83 (s, 1H), 5.61 – 5.49 (m, 1H), 5.00 (dd, *J* = 10.3, 1.7 Hz, 1H), 4.76 (dd, *J* = 17.2, 1.8 Hz, 1H), 4.23 (d, *J* = 6.0 Hz, 2H), 4.13 (t, *J* = 6.2 Hz, 2H), 3.93 (t, *J* = 6.6 Hz, 2H), 3.86 (s, 3H), 3.70 (s, 3H), 2.26 (p, *J* = 6.5 Hz, 2H). ^{13}C NMR (125 MHz, $CDCl_3$) δ 168.42, 160.84, 160.17, 149.99, 148.94, 133.94, 132.32, 131.76, 131.26, 127.08, 126.07, 126.02, 125.12, 123.27, 122.28, 121.38, 118.23, 118.05, 114.07, 113.53, 112.46, 67.07, 55.92, 55.43, 48.04, 35.61, 28.39. HRMS (ESI-TOF) m/z: calcd for $C_{34}H_{31}N_3O_7$, 593.2162, found 594.2240 $[M+H]^+$.

2.3.9.13. 3-((Z)-4-(2-(1H-imidazol-1-yl)ethoxy)-3-methoxybenzylidene)-1-allyl-6-((Z)-4-chlorobenzylidene)piperazine-2,5-dione (2.32m)

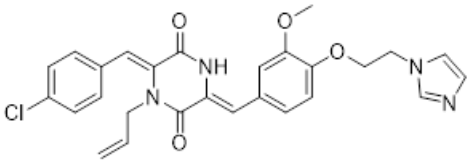

Light Brownish Solid; Yield: 53%; ^{1}H NMR (600 MHz, $CDCl_3$) δ 7.96 (s, 1H), 7.68 (s, 1H), 7.38 (d, *J* = 8.1 Hz, 2H), 7.26 – 7.23 (m, 2H), 7.20 (s, 1H), 7.10 (d, *J* = 11.8 Hz, 2H), 7.02 – 6.95 (m, 2H), 6.89 (s, 1H), 6.83 (d, *J* = 8.3 Hz, 1H), 5.59 – 5.48 (m, 1H), 5.03 (d, *J* = 10.2 Hz, 1H), 4.79 (d, *J* = 17.0 Hz, 1H), 4.39 (t, *J* = 5.2 Hz, 2H), 4.35 – 4.17 (m, 4H), 3.88 (s, 3H). ^{13}C NMR (125 MHz,

$CDCl_3$) δ 160.25, 159.95, 150.18, 148.14, 137.73, 134.79, 132.47, 131.45, 130.78, 129.32, 129.13, 128.84, 127.10, 125.27, 121.44, 120.37, 119.62, 118.36, 118.18, 114.19, 112.84, 77.49, 77.23, 76.98, 68.69, 56.08, 48.04, 46.52. HRMS (ESI-TOF) m/z: calcd for $C_{27}H_{25}ClN_4O_4$, 504.1564, found 505.1604 $[M+H]^+$.

2.3.9.14. 3-((Z)-4-(3-(1H-imidazol-1-yl)propoxy)-3-methoxybenzylidene)-1-allyl-6-((Z)-4-chlorobenzylidene)piperazine-2,5-dione (2.32n)

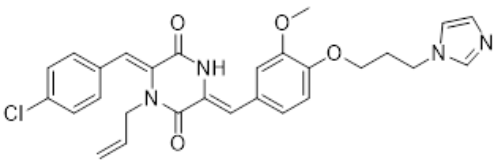

Yellowish Yellowish Solid; Yield: 58%; ^{1}H NMR (600 MHz, $CDCl_3$) δ 8.16 (s, 1H), 7.54 (s, 1H), 7.37 (d, *J* = 8.3 Hz, 2H), 7.26 – 7.22 (m, 2H), 7.19 (s, 1H), 7.06 (s, 1H), 7.02 – 6.98 (m, 2H), 6.93 (d, *J* = 13.2 Hz, 2H), 6.86 (d, *J* = 8.2 Hz, 1H), 5.59 – 5.49 (m, 1H), 5.03 (dd, *J* = 10.2, 1.4 Hz, 1H), 4.79 (dd, *J* = 17.1, 1.4 Hz, 1H), 4.28 – 4.21 (m, 4H), 3.97 (t, *J* = 5.7 Hz, 2H), 3.90 (s, 3H), 2.28 (p, *J* = 6.3 Hz, 2H). ^{13}C NMR (125 MHz, $CDCl_3$) δ 160.08, 159.87, 150.15, 148.60, 137.50, 134.84, 132.49, 131.46, 130.81, 129.57, 129.08, 128.88, 126.51, 125.14, 122.44, 121.41, 120.49, 119.07, 118.35, 113.95, 112.56, 109.54, 65.14, 56.07, 48.10, 43.41, 30.68. HRMS (ESI-TOF) m/z: calcd for $C_{28}H_{27}ClN_4O_4$, 518.1720, found 519.1739 $[M+H]^+$.

2.3.9.15. 1-allyl-6-((Z)-4-chlorobenzylidene)-3-((Z)-3-methoxy-4-(2-morpholino ethoxy)benzylidene)piperazine-2,5-dione (2.32o)

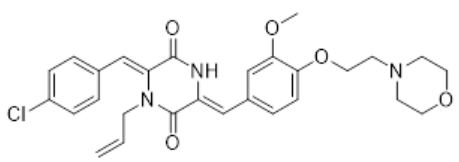

Yellowish Solid; Yield: 57%; ^{1}H NMR (500 MHz, $CDCl_3$) δ 7.99 (s, 1H), 7.38 (d, *J* = 8.1 Hz, 2H), 7.25 (d, *J* = 8.0 Hz, 2H), 7.19 (s, 1H), 7.02 (d, *J* = 7.4 Hz, 2H), 6.94 (d, *J* = 8.1 Hz, 1H), 6.89 (s, 1H), 5.61 – 5.48 (m, 1H), 5.03 (d, *J* = 10.2 Hz, 1H), 4.79 (d, *J* = 16.5 Hz, 1H), 4.26 (d, *J* = 5.5 Hz, 2H), 4.19 (t, *J* = 6.0 Hz, 2H), 3.87 (s, 3H), 3.73 (t, *J* = 5.3 Hz, 4H), 2.86 (t, *J* = 6.7 Hz, 2H), 2.60 (t, *J* = 5.0 Hz, 4H). ^{13}C NMR (125 MHz, $CDCl_3$) δ 160.05, 159.84, 150.12, 149.05, 134.83, 132.50, 131.47, 130.80, 129.04, 128.85, 126.07, 124.90, 121.39, 120.40, 118.42, 118.35, 113.73, 112.68, 67.06, 66.99, 57.43, 56.13, 54.20, 48.07. HRMS (ESI-TOF) m/z: calcd for $C_{28}H_{30}ClN_3O_5$, 523.1874, found 524.2477 $[M+H]^+$.

2.3.9.16. 1-allyl-6-((Z)-4-chlorobenzylidene)-3-((Z)-3-methoxy-4-(3-morpholino propoxy)benzylidene)piperazine-2,5-dione (2.32p)

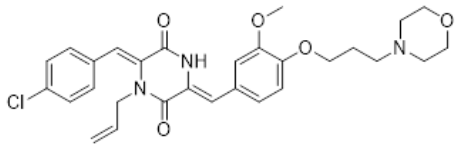

Yellowish Solid; Yield: 49%; ^{1}H NMR (500 MHz, $CDCl_3$) δ 7.99 (s, 1H), 7.38 (d, *J* = 8.0 Hz, 2H), 7.25 (d, *J* = 8.0 Hz, 2H), 7.19 (s, 1H), 7.05 – 7.00 (m, 2H), 6.94 (d, *J* = 8.1 Hz, 1H), 6.89 (s, 1H), 5.59 – 5.49 (m, 1H), 5.03 (d, *J* = 10.2 Hz, 1H), 4.79 (d, *J* = 16.7 Hz, 1H), 4.26 (d, *J* = 5.4 Hz, 2H), 4.13 (t, *J* = 6.6 Hz, 2H), 3.88 (s, 3H), 3.72 (t, *J* = 4.7 Hz, 4H), 2.54 (t, *J* = 7.3 Hz, 2H), 2.48 (t, *J* = 4.5 Hz, 4H), 2.04 (p, *J* = 6.7 Hz, 2H). ^{13}C NMR (125 MHz, $CDCl_3$) δ 160.00, 159.83, 150.01, 149.29, 134.85, 132.49, 131.45, 131.29, 130.80, 129.00, 128.86, 125.65, 124.78, 121.31, 120.46, 118.52, 118.38, 113.30, 112.50, 77.41, 77.16, 76.90, 67.36, 67.02, 56.16, 55.41, 53.77, 48.11, 29.78. HRMS (ESI-TOF) m/z: calcd for $C_{29}H_{32}ClN_3O_5$, 537.2030, found 538.2083 $[M+H]^+$.

2.3.9.17. 2-(2-(4-((Z)-(4-allyl-5-((Z)-4-chlorobenzylidene)-3,6-dioxopiperazin-2-ylidene)methyl)-2-methoxyphenoxy)ethyl)isoindoline-1,3-dione (2.32q)

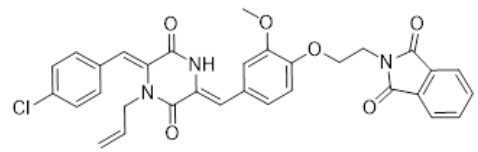

Yellowish Solid; Yield: 63%; ^{1}H NMR (600 MHz, $CDCl_3$) δ 7.92 (s, 1H), 7.88 (dd, *J* = 5.4, 3.1 Hz, 2H), 7.74 (dd, *J* = 5.4, 3.1 Hz, 2H), 7.38 (d, *J* = 8.3 Hz, 2H), 7.25 (d, *J* = 8.1 Hz, 2H), 7.19 (s, 1H), 7.03 – 6.95 (m, 3H), 6.85 (s, 1H), 5.59 – 5.48 (m, 1H), 5.03 (d, *J* = 10.2 Hz, 1H), 4.79 (d, *J* = 17.1 Hz, 1H), 4.33 (t, *J* = 6.1 Hz, 2H), 4.26 (d, *J* = 5.9 Hz, 2H), 4.15 (t, *J* = 6.1 Hz, 2H), 3.78 (s, 3H). ^{13}C NMR (125 MHz, $CDCl_3$) δ 168.15, 159.87, 159.75, 150.46, 148.58, 134.85, 134.15, 132.49, 132.18, 131.45, 130.78, 128.97, 128.85, 126.65, 125.01, 123.43, 121.20, 120.50, 118.37, 118.19, 114.75, 112.90, 66.05, 56.16, 48.11, 37.11. HRMS (ESI-TOF) m/z: calcd for $C_{32}H_{26}ClN_3O_6$, 583.1510, found 584.1601 $[M+H]^+$.

2.3.9.18. 2-(3-(4-((Z)-(4-allyl-5-((Z)-4-chlorobenzylidene)-3,6-dioxopiperazin-2-ylidene)methyl)-2-methoxyphenoxy)propyl)isoindoline-1,3-dione (2.32r)

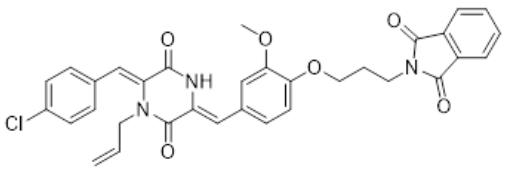

Yellowish Solid; Yield: 66%; ^{1}H NMR (600 MHz, $CDCl_3$) δ 7.96 (s, 1H), 7.84 (dd, *J* = 5.4, 3.1 Hz, 2H), 7.72 (dd, *J* = 5.5, 3.0 Hz, 2H), 7.38 (d, *J* = 8.4 Hz, 2H), 7.25 (d, *J* = 7.9 Hz, 2H), 7.19 (s, 1H), 7.02 – 6.95 (m, 2H), 6.90 (d, *J* = 8.4 Hz, 1H), 6.82 (s, 1H), 5.59 – 5.49 (m, 1H), 5.03 (dd, *J* = 10.1, 1.4 Hz, 1H), 4.79 (dd, *J* = 17.1, 1.5 Hz, 1H), 4.26 (d, *J* = 5.8 Hz, 2H), 4.13 (t, *J* = 6.1 Hz, 2H), 3.93 (t, *J* = 6.6 Hz, 2H), 3.69 (s, 3H), 2.26 (p, *J* = 6.4 Hz, 2H). ^{13}C NMR (126 MHz, $CDCl_3$) δ 168.42, 159.96, 159.84, 150.05, 149.08, 134.81, 133.94, 132.52, 132.32, 131.49, 130.79, 129.04, 128.84, 125.86, 124.77, 123.28, 121.33, 120.39, 118.53, 118.34, 113.55, 112.47, 67.08, 55.95, 48.08, 35.60, 28.38. HRMS (ESI-TOF) m/z: calcd for $C_{33}H_{28}ClN_3O_6$, 597.1666, found 598.1755 $[M+H]^+$.

2.3.10. Single Crystal X-ray Diffraction

The obtained single crystals were collected and analysed using a Bruker Smart APEX-II CCD diffractometer with monochromated Mo Kα radiation (λ = 0.71073 Å). The structures were solved with SHELXT, and refinements were performed by full-matrix least-squares on F2 (Sheldrick, 2015). All non-hydrogen atoms were refined anisotropically. Nitrogen-bound hydrogen atoms were located from difference Fourier maps and refined isotropically. The remaining hydrogen atoms were placed in geometrically idealized positions with fixed isotropic displacement parameters (Uiso) set to 1.5 times those of their parent methyl carbons and 1.2 times those of methine, methylene, and phenylene carbons. These hydrogen atoms were treated as riding on their respective carbon atoms during refinement.

2.3.11. Hirshfeld Surface analysis

The Hirshfeld surface and corresponding 2D fingerprint plots were generated from a CIF file using CrystalExplorer 21.5 (Wolff et al., 2012). On the Hirshfeld isosurface, two distances, i.e., di and de, are used to characterize intermolecular contacts, where di measures the distance from a surface point to the nearest atom inside the surface, and de measures the distance to the nearest atom outside it. The normalized contact distance (dnorm) depends on both di and de, and is expressed as:

$$d_{norm} = \frac{(d_i - r_i^{vdw})}{r_i^{vdw}} + \frac{(d_e - r_e^{vdw})}{r_e^{vdw}} \quad (1)$$

where, r_i^{vdw} and r_e^{vdw} represent the van der Waals radii of the internal and external atoms, respectively.

The enrichment ratio (Jelsch et al., 2014) is derived from the percentage contribution of specific interatomic contacts on the Hirshfeld surface, providing insight into favorable and unfavorable intermolecular interactions. The proportion of an atom type Y on the molecular surface (SY) is defined as:

$$S_Y = C_{YY} + \frac{1}{2} \sum_{Z \neq Y} C_{YZ} \quad (2)$$

where C_{YZ} denotes the proportion of Hirshfeld surface contacts involving atoms Y and Z.

Assuming all types of Y···Z contacts are randomly distributed, the ratio of random contacts (R_{AB}) between atoms A and B can be calculated as:

$$R_{YY} = S_Y S_Y \text{ and } R_{YZ} = 2 S_Y S_Z \quad (3)$$

The enrichment ratio E_{YZ} for the interacting atom pair Y···Z is then defined as:

$$E_{YZ} = \frac{C_{YZ}}{R_{YZ}} \quad (4)$$

2.3.12. Materials and Methods for *in vitro* Studies

2.3.12.1. Chemicals and reagents

3-(4,5-dimethylthiazole-2-yl)−2,5-diphenyltetrazolium bromide (MTT),fetal bovine serum (FBS), Trypsin-EDTA, sodium bicarbonate,RPMI-1640 media, Triton X-100, ethidium bromide, acridine orange, and DMSO were purchased from HiMedia Laboratories Pvt. Ltd. Ethylenediaminetetraacetic acid (EDTA),phenol red, L-Glutamine, Trizma hydrochloride, trichloroacetic acid (TCA), Trizma base, and agarose (low gelling temperature) were purchased from Sigma Chemicals. The other chemicals were purchased from Sisco Research Laboratories Pvt. Ltd., Spectrochem, and Merck Specialities Pvt. Ltd.

2.3.12.2. Cell lines and Culture

The human colorectal carcinoma cell line HCT116 and the human hepatocellular carcinoma cell line HepG2 were obtained from the National Centre for Cell Sciences (NCCS), Pune, India. The cells were cultured in RPMI-1640 medium supplemented with 0.2% sodium bicarbonate, 0.03% L-glutamine, and 10% fetal bovine serum (FBS), and maintained in a humidified incubator at 37 °C with 5% CO_2 (Eppendorf, Hamburg, Germany).

2.3.12.3. Cytotoxicity Assay (MTT assay)

The cytotoxic potential of compounds **2.31a-2.31f** and **2.32a-2.32r** against HCT116 and HepG2 cells was estimated by an MTT reduction assay. It involved seeding 1 × 104 cells into 96-well plates (HiMedia Laboratories Pvt. Ltd.) containing 100 µL of RPMI-1640 medium and incubation for 24 h at 37 °C in a humidified atmosphere with 5% CO2. Subsequently, the cells were treated with various concentrations of the test compounds (**2.31a–2.31f**, **2.32a–2.32r**) for 24 h, along with an untreated control. After treatment, the medium was removed, and the cells were washed with FBS-free medium, then incubated with 10 µL of MTT solution (5 mg/mL) for 2 h at 37 °C. The purple formazan crystals formed were dissolved by adding 100 µL of DMSO to each well. The absorbance was then measured at 560 nm using a microplate reader (SpectraMax M2e). Each experiment was performed in triplicate across three independent trials. The percentage inhibition of cell viability was calculated using the following formula:

$$\%\ Inhibition = \frac{Control - Treatment}{Control} \times 100$$

2.3.12.4. Cell Morphology Analysis Using Dual AO/EtBr Staining

The apoptosis-inducing potential of compound **2.32q** was studied using the dual fluorescent staining technique. 1 × 105 cells were seeded into each well of a six-well plate and allowed to adhere for 24 h. Subsequently, the cells were treated with different concentrations (25, 50, and 80 µM) of compound **2.32q** and incubated for an additional 24 h. 5-Fluorouracil (5-FU, 80 µM) was used as a positive control. Following treatment, the cells were harvested by trypsinization and stained with a mixture containing 2.5 µL of acridine orange (AO, 100 µg/mL) and ethidium bromide

(EtBr, 100 µg/mL), incubated for 2 min. The morphological features of apoptotic and viable cells were then examined under a fluorescence microscope (Thermo Fisher Scientific, EVOSR FL, AMEP-4615). At least 300 cells were scored, and the apoptotic index was subsequently determined as follows.

$$Apoptotic\ Index\ (\%) = \frac{Number\ of\ apoptotic\ cells\ scored}{Total\ number\ of\ cells\ counted} \times 100$$

2.3.12.5. Caspase-6 Activity Assay

A quantitative enzymatic activity assay for caspase-6 was conducted according to the manufacturer's protocol (BioVision Inc., USA). 2×10^6 cells were seeded in a T-25 flask containing 5 mL of culture medium and subsequently treated with 25 µg/mL of compound **2.32q**. 5-FU (50 µM) was used as a positive control. After 24 hours of treatment, the cells were harvested and lysed with 50 µL chilled lysis buffer, then incubated on ice for 10 minutes. The resulting lysate was centrifuged at 15000 × g for 1 minute at 4 °C, and the supernatant was collected for further analysis. The protein concentration in each sample was determined using the Bradford method (Bradford, 1976). A specific colorimetric substrate, VEID-pNA, was used to measure enzyme activity using 150 µg of total protein from each sample. The assay was performed in 96-well plates with a total volume of 100 µL and incubated for 2 hours at 37 °C. The release of p-nitroanilide (pNA), resulting from the cleavage of the respective substrates by active caspase-6, was quantified by measuring the absorbance at 405 nm using a microplate reader (SpectraMax M2e).

2.3.13. Molecular docking

The crystal structures of β-tubulin (PDB id: 5YL4) and c-Met (PDB id: 3U6I) were retrieved from the Protein Data Bank (www.rcsb.org) in PDB format. Prior to docking, the protein structure was refined by removing co-crystallized ligands, cofactors, and water molecules. Missing residues were modelled, and polar hydrogens were added to complete the structures. The binding pocket coordinates for β-tubulin and c-Met were defined based on their respective native ligands. For β-tubulin, the binding site was centered at x = -15.868, y = -64.554, z = 35.133 with grid box dimensions of 20 Å × 20 Å × 27 Å, while for c-Met, it was centered at x = 23.711, y

= -2.497, z = 17.912 with grid box dimensions of 25 Å × 25 Å × 30 Å. Docking simulation was carried out using AutoDock Vina with the exhaustiveness parameter set to 20. The docking results were visualized with PyMOL, UCSF Chimera, and Discovery Studio. The docking protocol was validated by redocking the native ligands and comparing the predicted binding orientations with the crystallographic conformations through structural superimposition.

2.3.14. Statistical Analysis

Experimental results were expressed as mean ± standard error of the mean (SEM). Data were analyzed using one-way analysis of variance (ANOVA), followed by Tukey's post hoc test. All statistical analyses were performed using SPSS (ver. 16.0) and OriginPro 25.

2.4. Results and Discussion

2.4.1. Synthesis and Characterization of the Compounds

A series of novel DKP derivatives was synthesized through multi-step procedures, as illustrated in Schemes 2.1–2.4. In scheme 2.1, the synthesis began with the commercially available compound 4-hydroxy-3-methoxybenzaldehyde (**2.18**), which underwent a nucleophilic substitution reaction with an excess of linear aliphatic dibromoalkanes (**2.19**) in the presence of anhydrous K_2CO_3 in N,N-dimethylformamide (DMF) at room temperature. This reaction afforded aldehydes (**2.20a** & **2.20b**) bearing terminal bromo groups. These intermediates were subsequently subjected to nucleophilic substitution with various secondary amines to yield the corresponding amino-substituted aldehydes (**2.22a–2.22f**). Similarly, a commercially available compound 4-fluorobenzaldehyde (**2.23**) was reacted with morpholine and imidazole at 90°C in DMF to furnish amino-substituted aldehydes (**2.24a** & **2.24b**).

In Scheme 2.2, glycine anhydride (**2.25**) was acetyl-protected using excess acetic anhydride to obtain intermediate compound **2.27**. Compound **2.27** was then subjected to a one-pot reaction involving aldol condensation and nucleophilic substitution with various aromatic aldehydes and allyl bromide in dry DMF using Cs_2CO_3 under a nitrogen atmosphere at -5 °C, affording intermediates **2.30a–2.30c**

(Scheme 2.3). These intermediates were further reacted with the amino-substituted aldehydes (**2.22a–2.22f, 2.24a**, & **2.24b**) via aldol condensation in the presence of Cs_2CO_3 in dry DMF under a nitrogen atmosphere at 60–90 °C, yielding the final products (**2.31a–2.31f** and **2.32a–2.32r**) (Scheme 2.4) (Figure 2.4). Solubility tests of the final compounds confirmed their solubility in common organic solvents, including ethyl acetate, acetone, DMF, dimethyl sulfoxide, chloroform, and dichloromethane, with solubilities exceeding 1.0 mg/mL at room temperature.

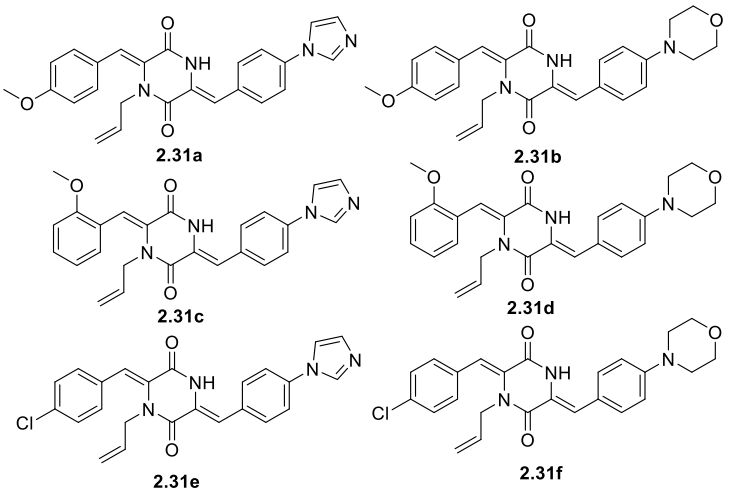

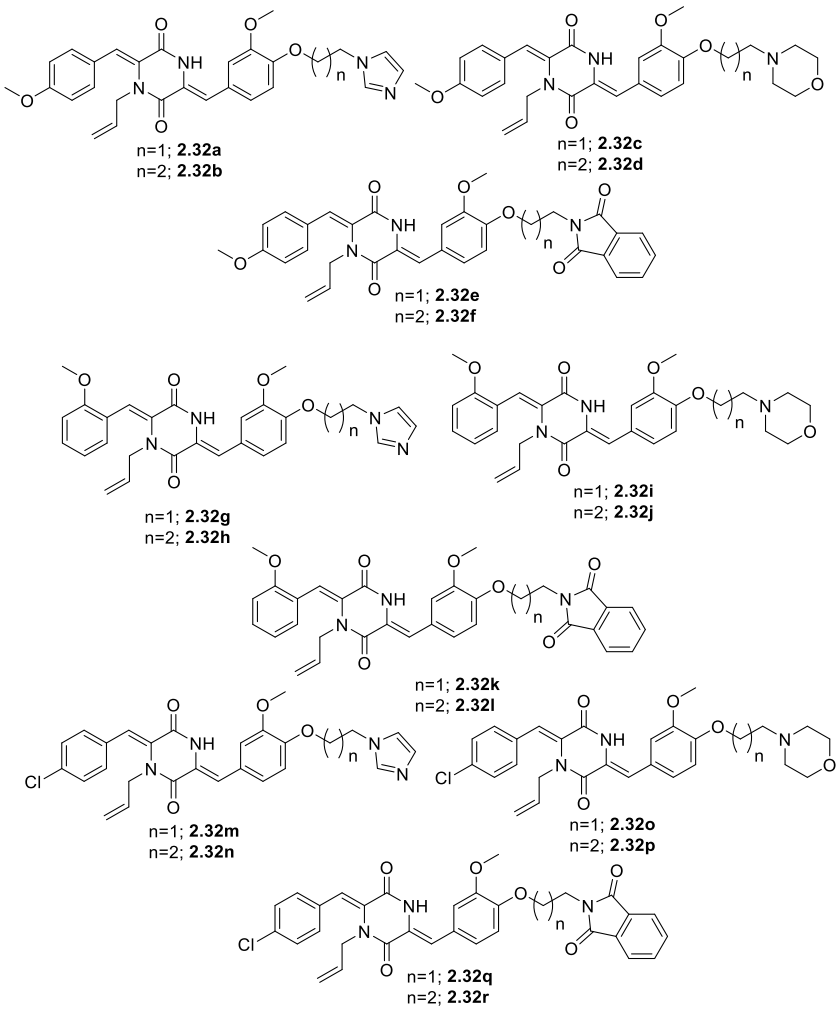

Figure 2.4. Chemical structures of novel Plinabulin-based DKP derivatives (**2.31a–2.31f** and **2.32a–2.32f**) designed and synthesized as potential anticancer agents.

The NMR spectra (^{1}H NMR and ^{13}C NMR) of one of the final DKP-derivatives, **2.32f**, recorded in $CDCl_3$, were selected to illustrate the characteristic chemical shifts and are shown in Figure 2.5 and 2.6. In the ^{1}H NMR spectrum, a pentet at δ 2.26 ppm of two protons and a triplet at δ 3.93 ppm and δ 4.13 ppm of two proton each correspond to the propylene linker. The singlet peaks at δ 3.69 ppm and δ 3.86 ppm of three protons each are assigned to the methoxy protons. A doublet at δ 4.31 ppm of two protons corresponds to the allylic CH_2 group attached to nitrogen. The doublets of doublets at δ 4.82 ppm and δ 5.02 ppm of one proton each are attributed to the two diastereotopic protons of the terminal vinylic CH_2 in the allyl group, where the dd pattern arises from geminal and vicinal cis/trans couplings. The multiplet at δ 5.62–

5.52 ppm of one proton corresponds to the internal vinylic (CH=) proton of the allyl group. The singlet at δ 7.92 ppm of one proton is assigned to the amide NH proton.

The NMR spectra (^{1}H NMR and ^{13}C NMR) of one of the final DKP-derivatives, **2.32f,** recorded in $CDCl_3$, were selected to illustrate the characteristic chemical shifts and are shown in Figures 2.5 and 2.6. In the ^{1}H NMR spectrum, a pentet at δ 2.26 ppm of two protons and a triplet at δ 3.93 ppm and δ 4.13 ppm of two protons each correspond to the propylene linker. The singlet peaks at δ 3.69 ppm and δ 3.86 ppm, each corresponding to three protons, are assigned to the methoxy protons. A doublet at δ 4.31 ppm of two protons corresponds to the allylic CH_2 group attached to nitrogen. The doublets of doublets at δ 4.82 ppm and δ 5.02 ppm of one proton each are attributed to the two diastereotopic protons of the terminal vinylic CH_2 in the allyl group, where the dd pattern arises from geminal and vicinal cis/trans couplings. The multiplet at δ 5.62–5.52 ppm of one proton corresponds to the internal vinylic (CH=) proton of the allyl group. The singlet at δ 7.92 ppm of one proton is assigned to the amide NH proton.

The ^{13}C NMR spectrum of compound **2.32f** exhibits twenty-seven distinct carbon resonances (Figure 2.6). The signals at δ 28.39, 35.61, and 67.07 ppm correspond to the three carbon atoms of the propylene linker, while the signals at δ 55.94 and 55.43 ppm arise from the methoxy carbons. The allylic CH_2 carbon attached to nitrogen resonates at δ 48.04 ppm. The phthalimide carbonyl carbons appear downfield at δ 168.43 ppm, while the remaining sp^2 carbons resonate at δ 160.61, 160.15, 150.03, 148.93, 133.94, 132.33, 131.77, 131.25, 127.11, 126.09, 126.05, 125.21, 123.28, 122.24, 121.24, 118.22, 117.81, 114.07, 113.55, and 112.42 ppm. HRMS of **2.32f** (Figure 2.7) shows three significant peaks at m/z 594.2272 $[M+H]^+$, 595.2292 $[M+2H]^{2+}$, and 595.2286 $[M+3H]^{3+}$, consistent with the calculated value for $C_{34}H_{31}N_3O_7$ (m/z 593.2162 $[M]^+$), further confirming its molecular structure.

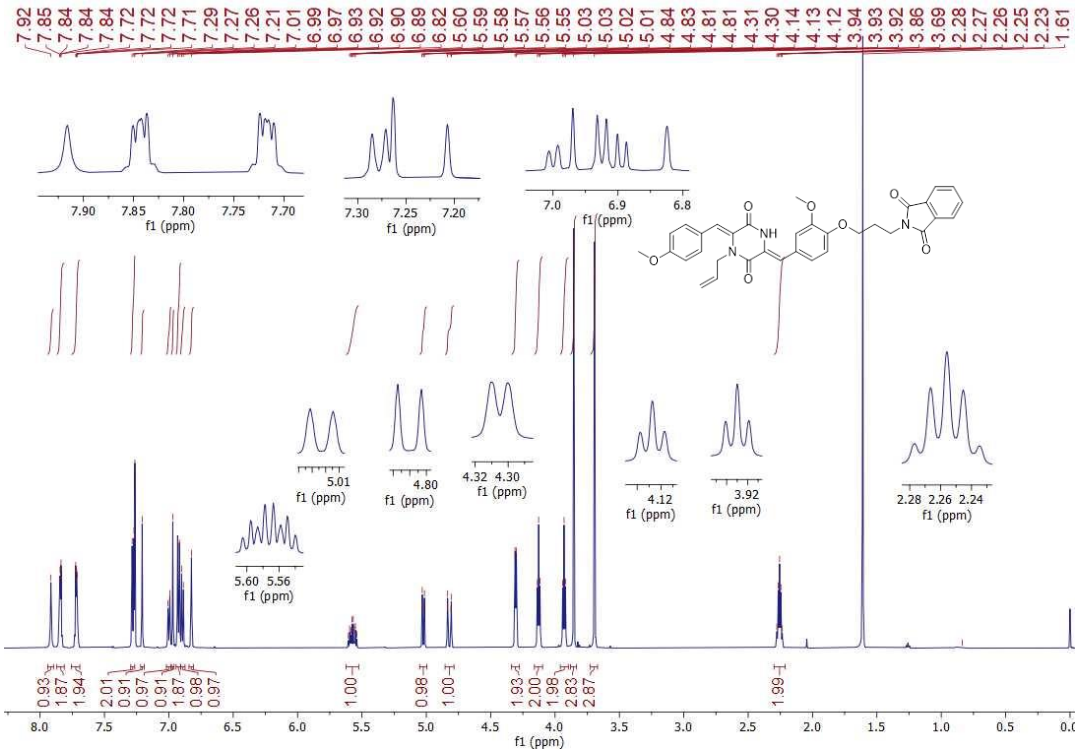

Figure 2.5. ^{1}H NMR spectrum of **2.32f.**

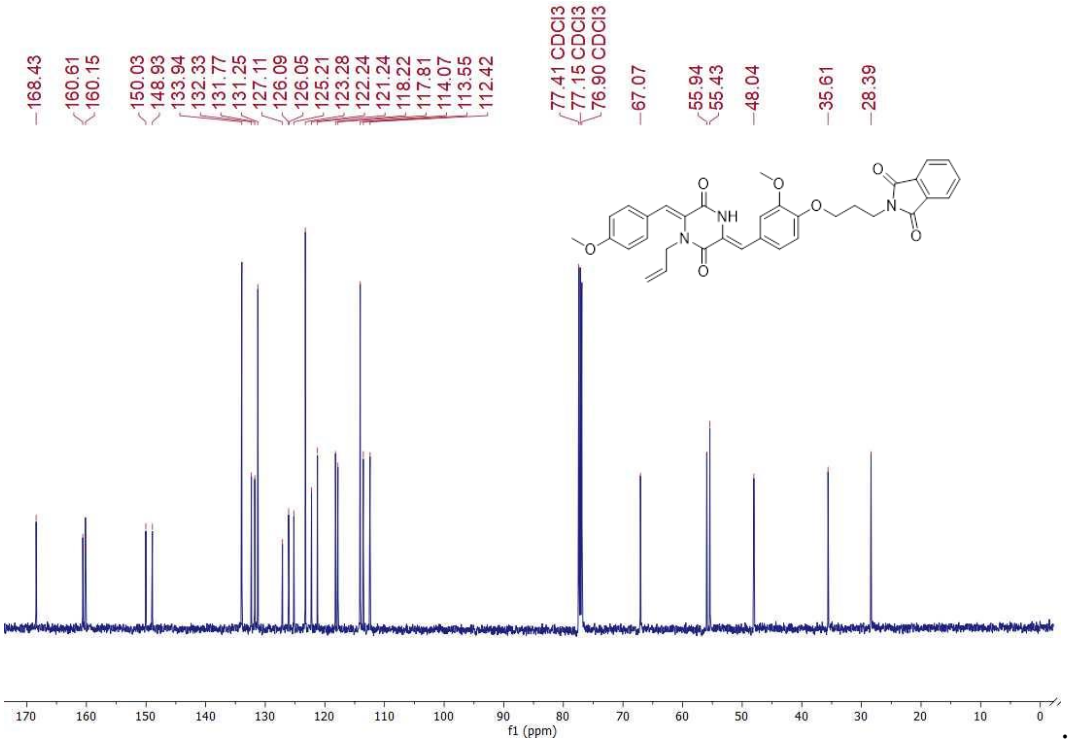

Figure 2.6. ^{13}C NMR spectrum of **2.32f**.

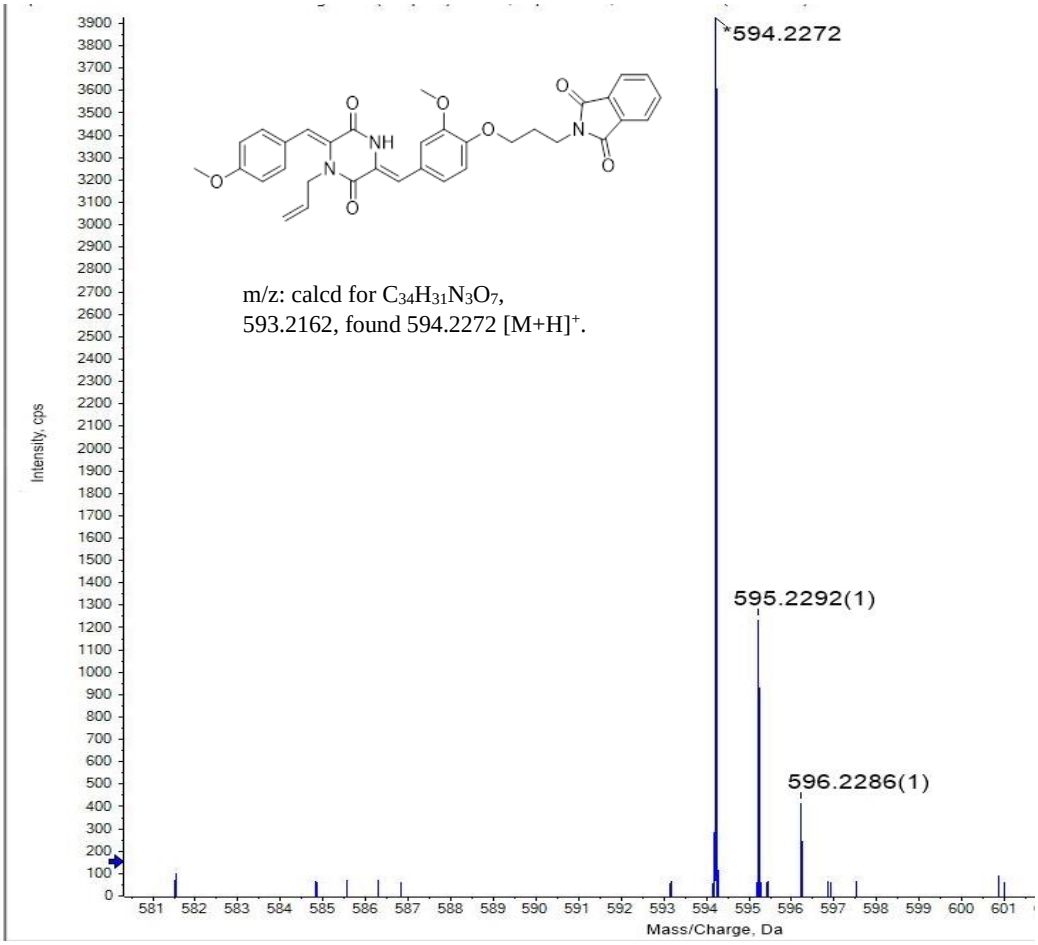

Figure 2.7. HRMS spectrum of **2.32f**.

2.4.2. Single Crystal X-ray Diffraction Analysis of Compound 2.31f

To gain a deeper understanding of the molecular conformation, crystal packing, and intermolecular interactions of the synthesized DKP derivatives, single-crystal X-ray diffraction (SCXRD) analysis was carried out on compound **2.31f**. This compound was selected as a representative model due to its structural similarity to other synthesized analogs, all of which feature a central DKP scaffold N-linked to an allyl group and substituted with various secondary amines. Although compounds **2.32a-2.32r** contains secondary amines tethered via alkyl chains, they share the core DKP pharmacophore, making **2.31f** a suitable reference.

In addition to SCXRD, Hirshfeld surface analysis and energy framework calculations were performed to visualize and quantify intermolecular interactions, and to elucidate their contributions to crystal packing and supramolecular stability. These

methods are useful for establishing correlations between molecular interactions and potential biological activity, as they provide insight into how structural features influence molecular recognition processes such as protein binding, membrane permeability, and interactions with biomolecules.

Crystals of compound **2.31f** were grown by slow evaporation of ethyl acetate in a two-neck round-bottom flask kept in the dark at room temperature for six days. High-quality single crystals were harvested and analyzed by SCXRD. Compound **2.31f** crystallizes in the monoclinic crystal system with the $P2_1/c$ space group and contains four molecules per unit cell in the asymmetric unit. The ORTEP diagram, shown at 50% probability ellipsoids, is depicted in Figure 2.8, and the crystallographic parameters are summarized in Table 2.1.

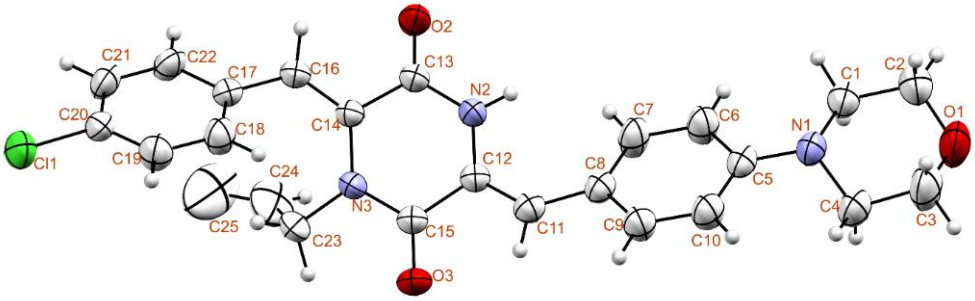

Figure 2.8. X-ray structure of **2.31f** highlighting Z,Z stereochemistry at C2 and C14 (crystallographic numbering). The Ortep diagram has been depicted at 50% probability ellipsoids.

Table 2.1. Crystal Data and Structure Refinement Parameters of compound **2.31f**.

Chemical formula	$C_{25}H_{24}ClN_3O_3$
Formula weight	449.1506
Crystal system	Monoclinic
space group	$P2_1/c$
a (Å)	14.3575 (15)
b (Å)	15.3187 (17)
c (Å)	10.2940 (11)
α (°)	90

β (°)	90.927 (3)
γ (°)	90
Volume ($Å^3$)	2263.7 (4)
Z	4
Temperature (K)	302
F(000)	936
Radiation type	Mo Kα (λ = 0.71073 Å)
μ (mm^{-1})	0.20
No. of measured, independent and observed [I > 2σ(I)] reflections	43851, 5191, 4478
R_{int}	0.030
$(\sin \theta/\lambda)_{max}$ ($Å^{-1}$)	0.651
Θ range (°)	27.5–1.9
Refinement $R[F^2 > 2\sigma(F^2)]$, $wR(F^2)$, S	0.067, 0.210, 1.07
No. of reflections	5191
No. of parameters	290
$\Delta\rho_{max}$, $\Delta\rho_{min}$ (e $Å^{-3}$)	1.34, -0.61

2.4.3. Structural Features of Compound 2.31f

Structural analysis revealed that the central DKP ring is not perfectly planar but exhibits a slight puckering at atoms C12 and C14, adopting a boat-like conformation. The atoms N2, N3, C13, and C15 lie nearly in the same plane, whereas C12 and C14 deviate from this mean plane (N2, N3, C13, C15) by 0.247 Å and 0.286 Å, respectively. Since the lone pair in the nitrogen atom is not involved in intramolecular interactions, it will be oriented either above or below the ring plane. This facilitates π-resonance between N2 and the C13–O2 carbonyl group, imparting partial double-bond character to the N2–C13 bond, which has a shortened bond length of 1.347(3) Å. This also supports the co-planarity of N2 and C13. In contrast, the N3–C15 bond is slightly longer (1.375(3) Å) due to the absence of a hydrogen atom on N3,

limiting π-resonance with the adjacent C15–O3 carbonyl. As a result, N3 deviates marginally (by 0.015 Å) from the mean plane defined by C13, N2, and C15. Furthermore, since no π-resonance is possible with the adjacent carbonyl groups in C13–C14 and C12–C15, the bond lengths C13–C14 and C12–C15 are relatively longer (1.490(3) Å), compared to the partially double-bonded N2–C13 and N3–C15. This bond-length asymmetry likely contributes to the slight ring puckering and to the DKP ring adopting a distorted chair-like conformation.

Notably, the two aryl substituents at the opposite ends of the DKP ring adopt significantly different orientations. The dihedral angle between the DKP plane and the 4-chlorophenyl ring is 141.96°, while that with the 4-morpholinophenyl ring is 148.47°. This difference is likely induced by steric repulsion from the allyl group, which displaces the 4-chlorophenyl moiety from its ideal orientation.

In the crystal self-assembly of compound **2.31f**, molecular organization is predominantly governed by strong classical hydrogen bonds (N–H···O) and non-classical hydrogen bonds (C–H···O). The most significant interaction involves an N2–H2···O2 hydrogen bond with a donor–acceptor distance of 2.115 Å, forming a graph-set motif $R_2^2(8)$ (Figure 2.9). Interestingly, the O2 atom acts as a trifurcated hydrogen bond acceptor, participating in two additional non-classical hydrogen bonds, i.e., C7-H7···O2 and C4-H4A···O2, with the bond distances of 2.289 Å and 2.649 Å, respectively. The C7-H7···O2 interactions along with N2-H2···O2 interactions formed a graph set of $R_2^1(8)$, while, the C21-H21···O3 (2.562 Å) and C4-H4A···O2 interactions together formed a graph set of $R_2^2(19)$ (Figure 2.9b). Additional stabilization within the crystal lattice is provided by weak C–H···π interactions. Notably, C4–H4B···π and C18–H18···π interactions are observed with contact distances of 2.922 Å and 3.534 Å, respectively (Figure 2.9c). These interactions collectively reinforce the three-dimensional supramolecular architecture and contribute to the overall crystal stability of compound **2.31f**. The distances involved in the intermolecular interactions of compound **2.31f** is summarized in Table 2.2.

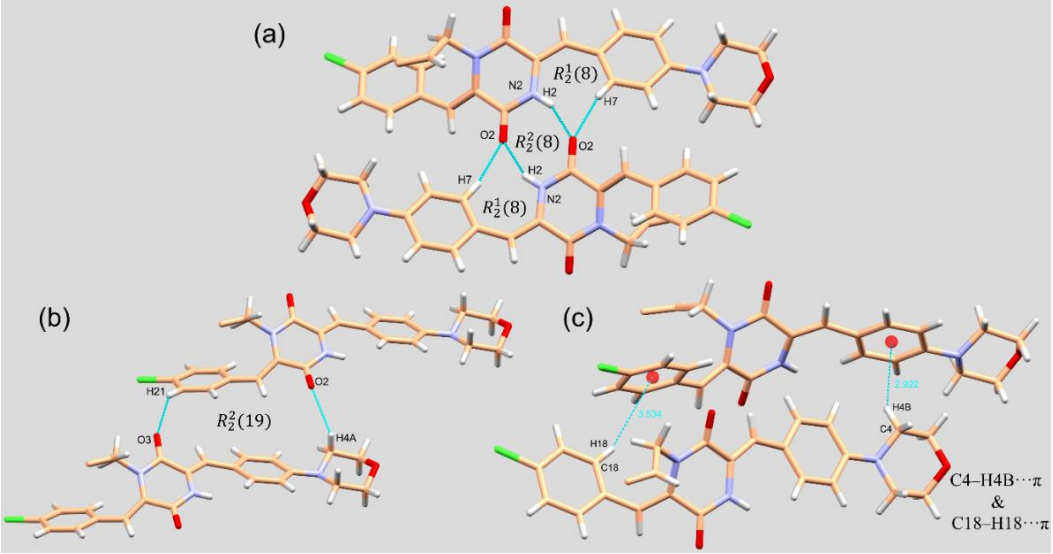

Figure 2.9. (a) N–H···O interactions that formed $R_2^2(8)$ & $R_2^1(8)$ graph sets. (b) C–H···O interactions that formed $R_2^2(19)$ graph set. (c) Depiction of C–H···π interactions.

Table 2.2. Intermolecular interactions in the packing of compound **2.31f**.

D-H···A	D–H, Å	H···A, Å	D···A, Å	D-H···A, º
N2-H2···O2	0.860	2.115	2.893	150.10
C7-H7···O2	0.930	2.289	3.205	168.33
C21-H21···O3	0.930	2.562	3.351	142.90
C4-H4A···O2	0.970	2.649	3.522	149.98
C4–H4B···π (C5-C10)		2.922		
C18–H18···π (C17-C22)		3.534		

2.4.4. Hirshfeld Surface analysis

Hirshfeld surface (HS) analysis was employed to investigate the nature and contribution of various intermolecular interactions involved in the self-assembly of **2.31f**. The HS mapped over the normalized contact distance (d_{norm}) provides a visual representation of the relative strength and proximity of intermolecular contacts (Figure

2.10a & 2.10b). Intense red spots on the surface correspond to strong van der Waals contacts, particularly classical N–H···O hydrogen bonds, indicating close donor–acceptor interactions. In contrast, pale red spots are associated with weaker C–H···O hydrogen bonds, representing non-classical interactions. White regions on the surface reflect contacts that are approximately equal to the sum of the van der Waals radii, such as H···H interactions. Blue regions indicate interatomic distances exceeding the sum of the van der Waals radii, suggesting weaker or non-interacting regions.

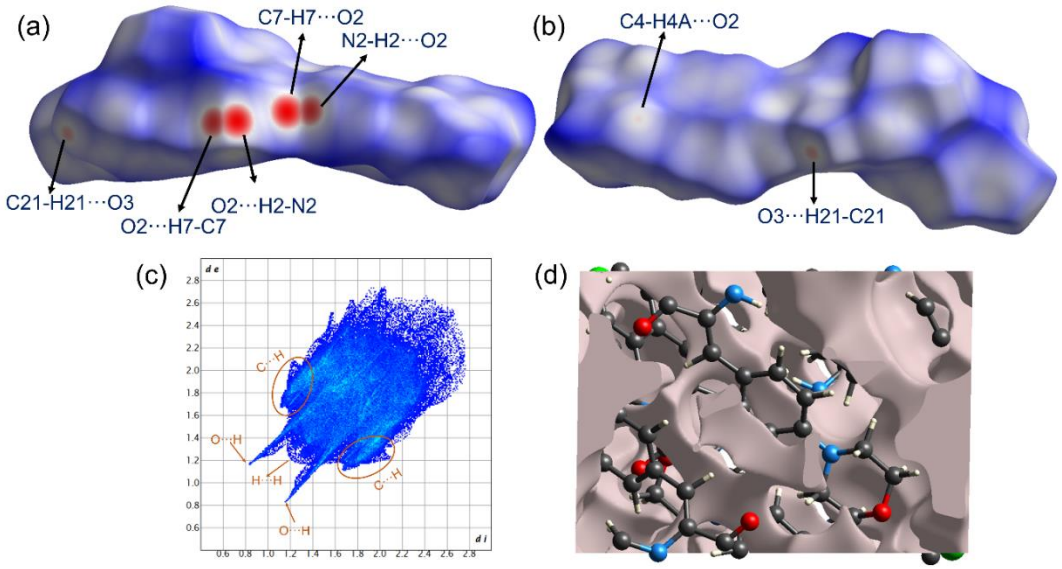

Figure 2.10. (a), (b) Hirshfeld Surface of compound **2.31f** mapped over d_{norm}. (c) Fingerprint plot of compound **2.31f**. (d) Crystal voids of compound **2.31f**.

Further insights were obtained through the analysis of 2D fingerprint plots, which decompose the surface into specific interaction types. In Figure 2.10c, sharp spike-like features in the plots correspond to H···O/O···H, and H···H contacts. The lower spike (where di>de) typically reflects the acceptor character, while the upper spike (where di<de) indicates the donor character. Since hydrogen contributes the highest amount to the Hirshfeld surface (66.45%), interactions such as H···H, O···H, and C···H are the most significant contributors to the crystal packing. The H···O/O···H contacts, which reflect both classical (N–H···O) and non-classical (C–H···O) hydrogen bonds, occur at di + de ≈ 2.0 Å and have the percentage contribution

of 15% in the crystal packing of compound **2.31f**. Additionally, C···H/H···C contacts, indicative of C–H···π interactions, appear as broader spikes in the fingerprint plot and have di+de ≈ 3.4 Å, contributing approximately 28.0% of the total interactions. The overall extension of the crystal structure into a robust three-dimensional supramolecular network is driven by a combination of these strong and weak interactions.

Furthermore, the void domain calculations revealed that the unit cell of the titled crystal compound has a void volume of 342.05 Å3 and a void surface area of 889.67 Å2, which is 15.11% of the unit cell volume (Figure 2.10d). This indicates that the crystal molecules are closely packed and that no large cavities are present.

The Enrichment Ratio (ER) is a valuable metric for evaluating preferential intermolecular interactions, which are crucial to molecular crystal packing. It is derived from Hirshfeld surface analysis, based on the observed proportion of interatomic contacts between pairs of atoms (Y, Z) relative to a theoretical proportion for random, equiprobable contacts. An ER value greater than unity (ER > 1) indicates that a particular contact type (Y···Z) occurs more frequently than expected by chance, suggesting favorable interactions. Conversely, ER values less than unity (ER < 1) imply that such contacts are disfavored or underrepresented. Analysis of the ER values presented in Table 2.3 reveals that O···H/H···O, C···H/H···C, and Cl···H/H···Cl contacts are all enriched (ER > 1) in the self-assembly of compound **2.31f**, signifying their important roles in molecular packing. The enrichment of C···H/H···C contacts is particularly notable and likely arises from C–H···π interactions, which contribute significantly to the stability and organization of the crystal structure. Although the N···H/H···N contacts display ER values above unity, they are considered less significant due to their low absolute proportion in both actual and random contacts (i.e., <2.8%). Furthermore, the C···C contacts exhibit an ER value of 0.49, indicating a disfavored interaction. This suggests the absence of possible π···π stacking interactions in the molecular association of compound **2.31f**.

Table 2.3. Percentage contribution and calculated ER values of intermolecular contacts in **2.31f**.

Actual Contacts (%)		**S_X**		**Random Contacts (%) R_{xx}/R_{xy}**	
H···H	38.3	H	66.45	H···H	44.16
N···H/H···N	2.8	O	9.05	N···H/H···N	2.06
O···H/H···O	15.0	C	16.85	O···H/H···O	12.03
C···H/H···C	28.0	N	1.55	C···H/H···C	22.39
Cl···H/H···Cl	10.5	Cl	6.2	Cl···H/H···Cl	8.24
Cl···Cl/Cl···Cl	--			Cl···Cl/Cl···Cl	--
Cl···O/Cl···O	0.9			Cl···O/Cl···O	1.12
Cl···N/Cl···N	--			Cl···N/Cl···N	--
Cl···C/Cl···C	1.0			Cl···C/Cl···C	2.0
O···O	0.1			O···O	0.82
O···C/C···O	1.8			O···C/C···O	3.04
O···N/N···O	0.2			O···N/N···O	0.28
C···C	1.4			C···C	2.83
N···N/N···N	--			N···N/N···N	--
N···C/C···N	0.1			N···C/C···N	0.52
Enrichment ratio E_{xx}/E_{xy}					
H···H	0.87			Cl···C/Cl···C	0.5
N···H/H···N	1.36			O···O	0.12
O···H/H···O	1.25			O···C/C···O	0.59
C···H/H···C	1.25			O···N/N···O	0.71
Cl···H/H···Cl	1.27			C···C	0.49
Cl···Cl/Cl···Cl	--			N···N/N···N	--
Cl···O/Cl···O	0.80			N···C/C···N	0.19
Cl···N/Cl···N	--				

2.4.5. Energy Framework Analysis

The intermolecular interaction energies contributing to the self-assembly of compound **2.31f** were calculated using CrystalExplorer21, employing the scale factors k_ele = 1.057, k_pol = 0.74, k_rep = 0.618, and k_disp = 0.871. The calculations were

performed at the B3LYP/6-31G(d,p) level of theory. A molecular cluster comprising all molecules within a 3.8 Å radius of a reference molecule was considered to evaluate the interaction energies responsible for the crystal packing of **2.31f**.

The results, including individual contributions from electrostatic (E_{ele}), polarization (E_{pol}), repulsion (E_{rep}), dispersion (E_{disp}), and total interaction energies (Etot), are summarized in Table 2.4. The overall interaction energy for compound **2.31f** was found to be –290.4 kJ/mol. Analysis of the energy framework revealed that dispersion interactions are the predominant stabilizing force in the crystal packing, while polarization contributions were minimal. Specifically, the total dispersion and electrostatic energies were –242.922 kJ/mol and –145.866 kJ/mol, respectively, whereas polarization contributed only –29.01 kJ/mol.

The dominance of dispersion forces in the supramolecular organization of **2.31f** can be attributed to significant contributions from H···H (38.3%) and C···H (28.0%) contacts. Among the molecular pairs (symmetry operation: x, -y+1/2, z+1/2), those exhibiting C4–H4B···π and C18–H18···π interactions displayed the lowest dispersion energy of –66.54 kJ/mol (E_{ele}= –15.01 kJ/mol, E_{pol} = –3.03 kJ/mol, E_{rep} = 27.50 kJ/mol, E_{tot} = –57.0 kJ/mol). In contrast, the strongest intermolecular interaction was observed for molecular pairs (symmetry operation: -x, -y, -z) that formed the graph sets $R_2^2(8)$ due to classical N2–H2···O2 hydrogen bonds, with a total energy of –74.8 kJ/mol. In this case, electrostatic contributions were dominant (E_{ele} = –82.87 kJ/mol), followed by dispersion (E_{dis} = –38.76 kJ/mol), polarization (E_{pol} = –15.17 kJ/mol), and repulsion (E_{rep} = 62.11 kJ/mol). Additionally, the molecular pairs (symmetry operation: x, y, z) that formed a graph sets $R_2^2(19)$ due to C4–H4A···O2 and C21–H21···O3 interactions exhibited a moderate interaction energy of –29.8 kJ/mol (E_{ele} = –13.53 kJ/mol, E_{dis} = –25.17 kJ/mol, E_{pol} = –2.81 kJ/mol, E_{rep} = 11.80 kJ/mol). The corresponding energy framework diagram (Figure 2.11) visually represents the intermolecular interactions, where the tube thickness is proportional to the magnitude of interaction energy.

Table 2.4. Calculated interaction energies (kJ/mol) for the intermolecular interactions of compound **2.31f.**

N	Symmetry operation	R	E_{ele}	E_{pol}	E_{dis}	E_{rep}	E_{tot}
0	x, -y+1/2, z+1/2	21.27	-12.7	-0.2	-5.9	0	-18.7
0	-x, -y, -z	16.28	-2.2	-2.3	-10.2	0	-12.9
0	x, -y+1/2, z+1/2	6.43	-14.2	-4.1	-76.4	44.5	-57
0	-x, -y, -z	10.66	10.9	-1.2	-16.7	7.4	0.7
0	x, y, z	17.53	1.5	-0.7	-10.7	0	-8.2
0	-x, y+1/2, -z+1/2	14.39	-2.5	-0.7	-7.1	0	-9.2
2	x, y, z	10.29	-12.8	-3.8	-28.9	19.1	-29.8
1	-x, -y, -z	6.47	-78.4	-20.5	-44.5	100.5	-74.8
0	-x, -y, -z	9.88	-26.6	-5.4	-72.1	34.3	-73.7
0	-x, y+1/2, -z+1/2	9.36	-1	-0.3	-6.4	0.1	-6.8
		Total	-145.87	-29.01	-242.92	127.25	-290.40

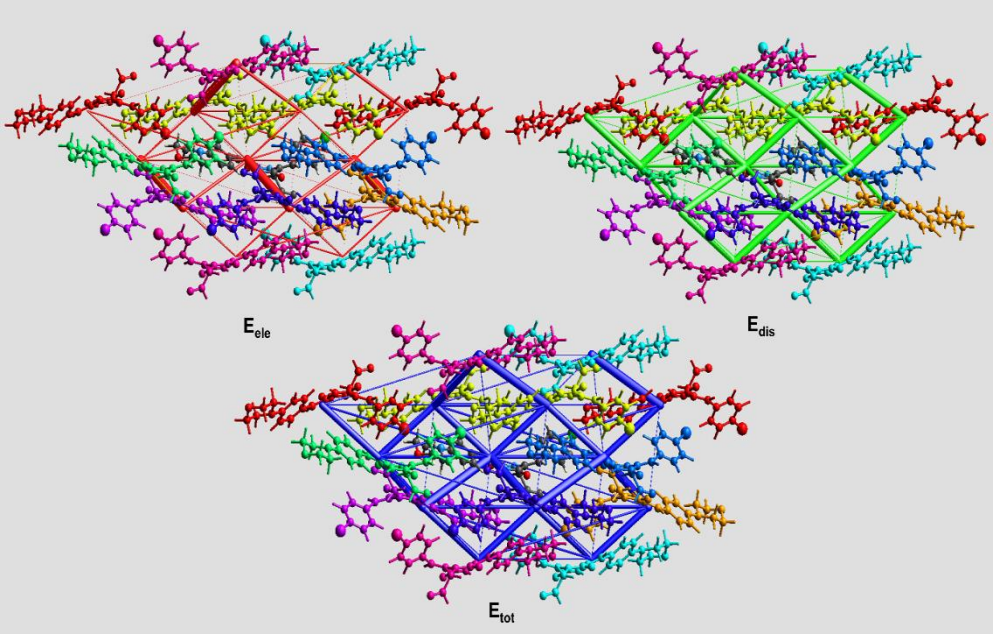

Figure 2.11. Energy Framework diagram of electrostatic energy (E_{ele}), dispersion energy (E_{dis}) and Total energy (E_{tot}) of compound **2.31f**.

2.4.6. *In vitro* Anticancer Activity of Plinabulin-based DKP Analogues and Structural Activity Relationships

In vitro cytotoxicity serves as an important index in drug screening. The cytotoxicity of compounds **2.31a**–**2.31f** and **2.32a–2.32r** was evaluated against HepG2 (human hepatocellular carcinoma) and HCT116 (human colon carcinoma) cell lines using the standard MTT assay.

2.4.6.1. Cytotoxicity of Compounds 2.32a–2.32r Against HepG2 Cancer Cell Lines

Table 2.5. IC_{50} values of compounds **2.31a–2.31f** against HepG2 cancer cell line.

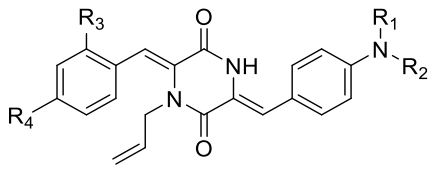

2.31a-2.31f

				IC_{50} values (µM)
Comp	**R_3**	**R_4**	**NR_1R_2**	**HepG2**
2.31a	H	4-OCH_3	Imidazolo	188.2 ± 2.61[d]
2.31b	H	4-OCH_3	Morpholino	91.81 ± 3.90[a]
2.31c	2-OCH_3	H	Imidazolo	154.9 ± 4.72[c]
2.31d	2-OCH_3	H	Morpholino	105.1 ± 4.75[b]
2.31e	H	Cl	Imidazolo	232.1 ± 3.42[e]
2.31f	H	Cl	Morpholino	152.3 ± 2.58[c]
5-Fluorouracil (5-FU)	--	--	--	77.64 ± 0.25[a]

Data are presented as mean ± SEM (n = 3). Different superscript letters indicate significant differences ($p < 0.05$) by Tukey's HSD test following one-way ANOVA. Compounds with the same superscript letter are not statistically different. Lower IC_{50} = higher cytotoxicity.

The cytotoxic effects of compounds **2.31a**–**2.31f** were evaluated against HepG2 cells, and the results were expressed as the percentage inhibition of cell viability. The inhibition data were plotted against the logarithm of compound concentrations to determine IC_{50} values. As summarized in Table 2.5, compounds **2.31a–2.31f** exhibited moderate to potent cytotoxicity against the HepG2 cancer cell line after 24 hours of treatment. Among them, compounds **2.31b** and **2.31d** displayed the strongest inhibitory effects, with IC_{50} values of 91.81 ± 3.90 µM and 105.1 ± 4.75 µM, respectively, indicating promising cytotoxic potency relative to the reference drug 5-fluorouracil (5-FU) (IC_{50} = 77.64 ± 0.25 µM). Treatment with these compounds resulted in a clear dose-dependent increase in cytotoxicity (Figure 2.12 & 2.13). Specifically, at concentrations of 50, 100, 200, and 300 µM, compound **2.31b** inhibited cell growth by 35.2%, 53.4%, 64.6%, and 79.7%, respectively, whereas compound **2.31d** exhibited 30.3%, 49.3%, 65.1%, and 78.2% inhibition at the same concentrations.

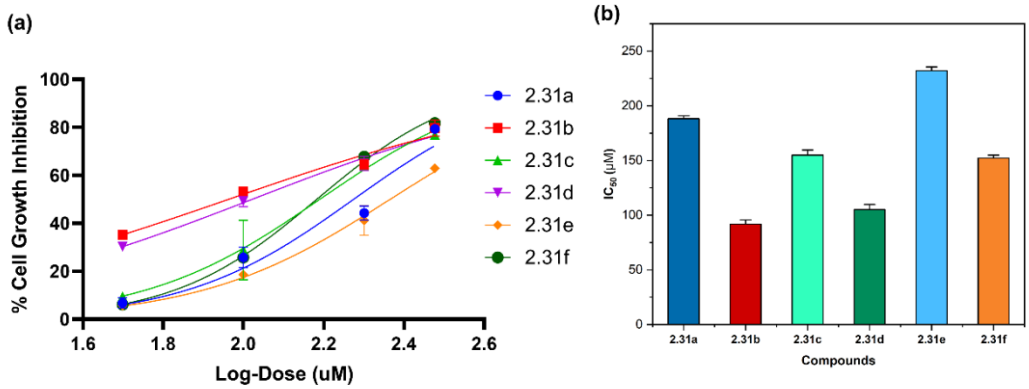

Figure 2.12. (a) Plot of log-dose against percentage cell growth inhibition of different concentrations of compounds **2.31a-2.31f** against HepG2 cancer cells. (b) IC_{50} values of compounds **2.31a-2.31f**. Data are presented as mean ± SEM (n=3).

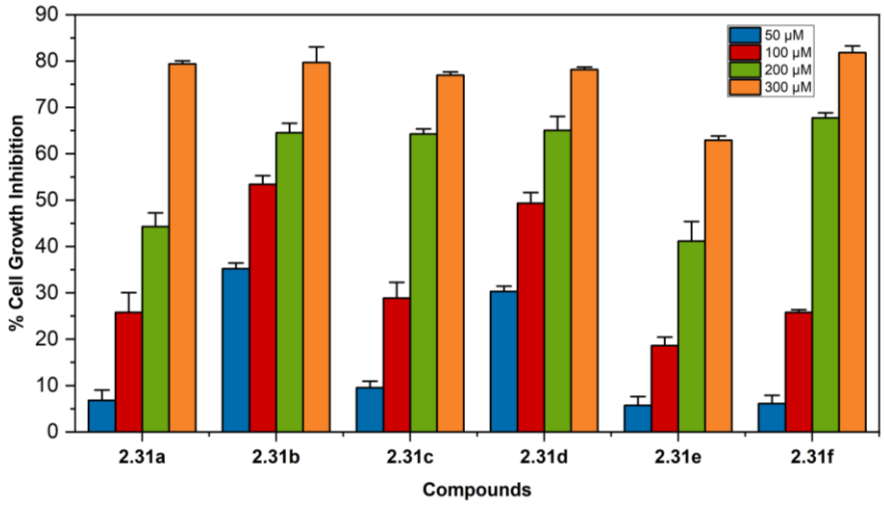

Figure 2.13. Graph showing percentage cell growth inhibition of different concentrations of compounds **2.31a–2.31f**. Data are presented as mean ± SEM (n=3).

The structure-activity relationship (SAR) derived from Table 2.5 indicates that introducing hydrophilic morpholino groups onto phenyl rings enhances the anticancer activity of the compounds, whereas the presence of an imidazole group reduces the activity. Electron-donating methoxy groups at the para position are more favourable than at the ortho position, while electron-withdrawing chlorine substituents at the para position decrease biological activity. This trend is also observed among the imidazole derivatives: **2.31a**, which has a para-methoxy group, is more active than **2.31c** with an ortho-methoxy group, whereas **2.31e**, with a para-chlorine substituent, exhibits the lowest activity in the series. The SAR of compounds **2.31a**–**2.31f** is illustrated in Figure 2.14.

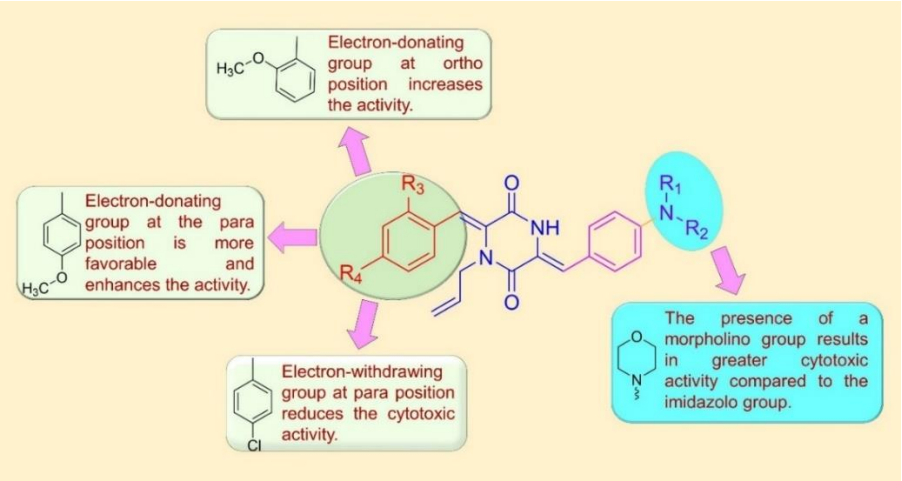

Figure 2.14. Structure activity relationship of compounds **2.31a**–**2.31f**.

2.4.6.2. Cytotoxicity of Compounds 2.32a-2.32r Against HCT116 and HepG2 Cancer Cell Lines

In the subsequent investigation, compounds **2.32a–2.32r**, where amino functionalities were introduced through flexible alkyl linkers, were examined for cytotoxicity. The assessment of these compounds against the HCT116 cancer cell line revealed a broad spectrum of cytotoxic effects, as summarized in Table 2.6 and Figure 2.16. Several compounds displayed notable potency within 24 hours of treatment, with **2.32q, 2.32f**, and **2.32i** emerging as the most active members of this series. Their IC_{50} values were 63.15 ± 1.22 μM, 84.43 ± 1.58 μM, and 109.3 ± 1.23 μM, respectively, demonstrating promising growth-inhibitory potential relative to the reference drug 5-FU (IC_{50} = 61.13 ± 0.29 μM). A clear concentration-dependent increase in cytotoxicity was observed upon treatment (Figure 2.15). Specifically, at concentrations of 50, 100, 200, and 300 μM, compound **2.32q** inhibited cell growth by 43.8%, 61.8%, 78.8%, and 83.2%, respectively (Figure 2.17). Similarly, compound **2.32f** exhibited 34.8%, 54.6%, 75.5%, and 80.7% inhibition, while **2.32i** showed 15.5%, 37.9%, 72.2%, and 80.8% inhibition at the same concentrations (Figures 2.18 and 2.19).

To further evaluate their cytotoxic potential, compounds **2.32q** and **2.32f** were tested against HepG2 cells. Both compounds exhibited strong cytotoxic effects, though their activities were lower than those observed in HCT116 cells, suggesting some degree of cell-line selectivity (Figure 2.20). Compound **2.32f** exhibited slightly greater cytotoxic potency than compound **2.32q** in HepG2 cells (IC_{50} = 96.03 ± 2.33 μM and 105.2 ± 2.50 μM, respectively), opposite to the trend observed in HCT116 cells, where **2.32q** was more active (Figure 2.20b). At concentrations of 50, 100, 200, and 300 μM, compound **2.32f** inhibited cell growth by 33.1%, 50.8%, 68.6%, and 78.7%, respectively, whereas compound **2.32q** showed 29.2%, 48.8%, 66.1%, and 80.2% inhibition at the same concentrations (Figure 2.20).

Table 2.6. IC_{50} values of compounds **2.32a**-**2.32r** against HCT116 and HepG2 cancer cell lines. Data are presented as mean ± SEM (n=3).

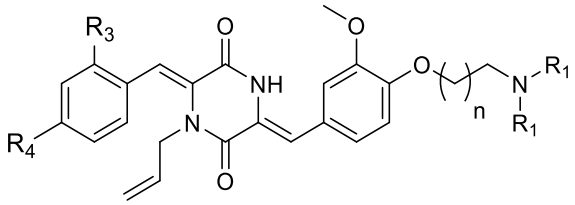

2.32a-2.32r

					IC_{50} values (μM)	
Comp	**n**	**R_3**	**R_4**	**NR_1R_2**	**HCT116**	**HepG2**
2.32a	1	H	4-OCH_3	Imidazolo	252.2 ± 1.48[h]	--
2.32b	2	H	4-OCH_3	Imidazolo	230.7 ± 2.34[g]	--
2.32c	1	H	4-OCH_3	Morpholino	129.4 ± 1.23[d]	--
2.32d	2	H	4-OCH_3	Morpholino	290.9 ± 4.34[i]	--
2.32e	1	H	4-OCH_3	Phthalimido	131.2 ± 1.23[d]	--
2.32f	2	H	4-OCH_3	Phthalimido	84.43 ± 1.58[b]	96.03 ± 3.33[b]
2.32g	1	2-OCH_3	H	Imidazolo	297.5 ± 1.12[i]	--
2.32h	2	2-OCH_3	H	Imidazolo	148.3 ± 2.41[e]	--
2.32i	1	2-OCH_3	H	Morpholino	109.3 ± 1.23[c]	--
2.32j	2	2-OCH_3	H	Morpholino	127.3 ± 1.26[d]	--
2.32k	1	2-OCH_3	H	Phthalimido	362.4 ± 2.11[k]	--
2.32l	2	2-OCH_3	H	Phthalimido	325.5 ± 1.70[j]	--
2.32m	1	H	4-Cl	Imidazolo	179.2 ± 3.72[f]	--

2.32n	2	H	4-Cl	Imidazolo	128.6 ± 1.54[d]	--
2.32o	1	H	4-Cl	Morpholino	126.6 ± 2.97[d]	--
2.32p	2	H	4-Cl	Morpholino	123.1 ± 1.91[d]	--
2.32q	1	H	4-Cl	Phthalimido	63.15 ± 1.22[a]	105.2 ± 3.56[b]
2.32r	2	H	4-Cl	Phthalimido	130.3 ± 2.40[d]	--
5-FU)	--	--	--	--	61.13 ± 0.29[a]	77.64 ± 0.25[a]

Data are presented as mean ± SEM (n = 3). Different superscript letters indicate significant differences ($p < 0.05$) by Tukey's HSD test following one-way ANOVA. Compounds with the same superscript letter are not statistically different. Lower IC_{50} = higher cytotoxicity.

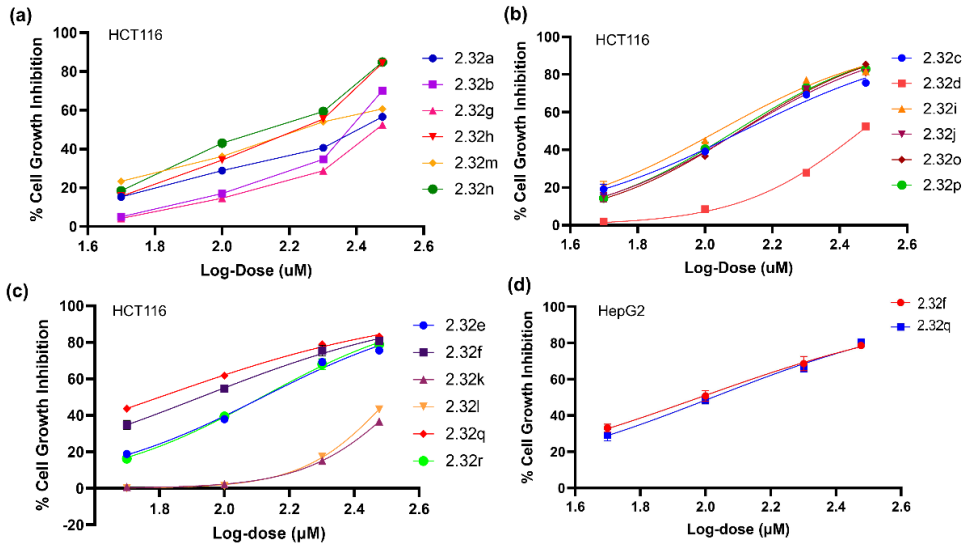

Figure 2.15. Plot of log-dose against percentage cell growth inhibition for different concentrations of compounds **2.32a**-**2.32r**. (a) Imidazole-containing compounds **2.32a**, **2.32b**, **2.32g**, **2.32h**, **2.32m** and **2.32n** against HCT116 cancer cells. (b) Morpholine-containing compounds **2.32c**, **2.32d**, **2.32i**, **2.32j**, **2.32o** and **2.32p** against HCT116 cancer cells. (c) Phthalimide-containing compounds **2.32e**, **2.32f**, **2.32k**, **2.32l**, **2.32q** and **2.32r** against HCT116 cancer cells. (d) compounds **2.32f** and **2.32q** against HepG2 cancer cells.

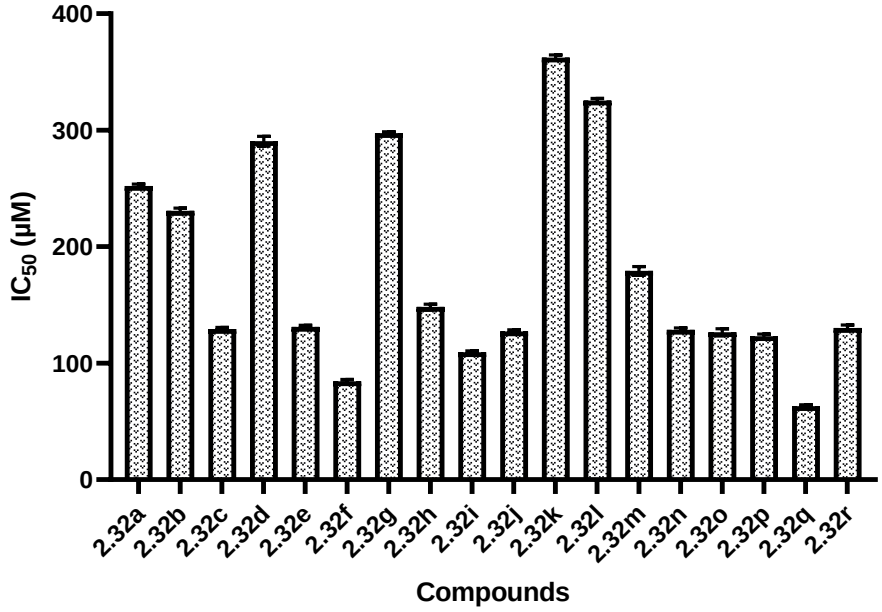

Figure 2.16. IC_{50} values of compounds **2.32a-2.32r** against HCT116 cancer cells. Data are presented as mean ± SEM (n=3).

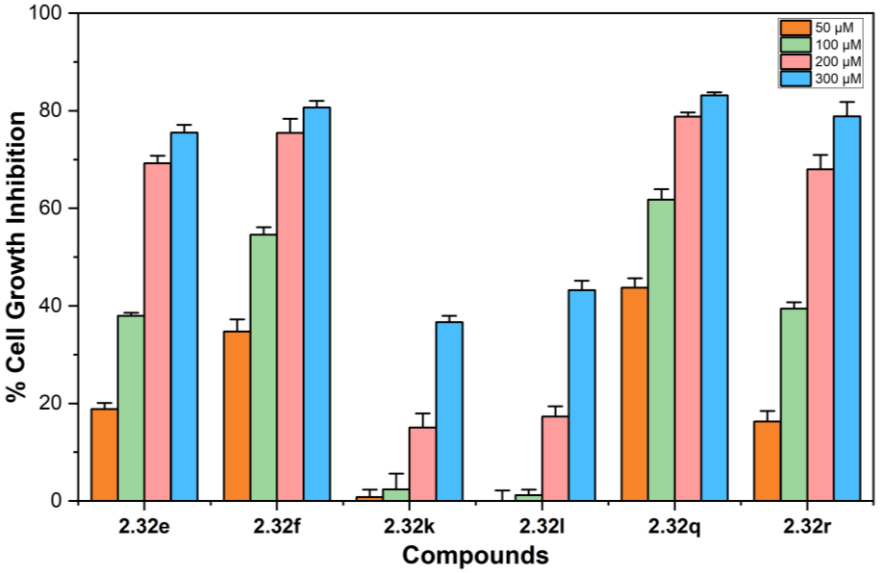

Figure 2.17. Graph showing percentage cell growth inhibition at different concentrations of phthalimide-containing compounds **2.32e**, **2.32f**, **2.32k**, **2.32l**, **2.32q** and **2.32r**. Data are presented as mean ± SEM (n=3).

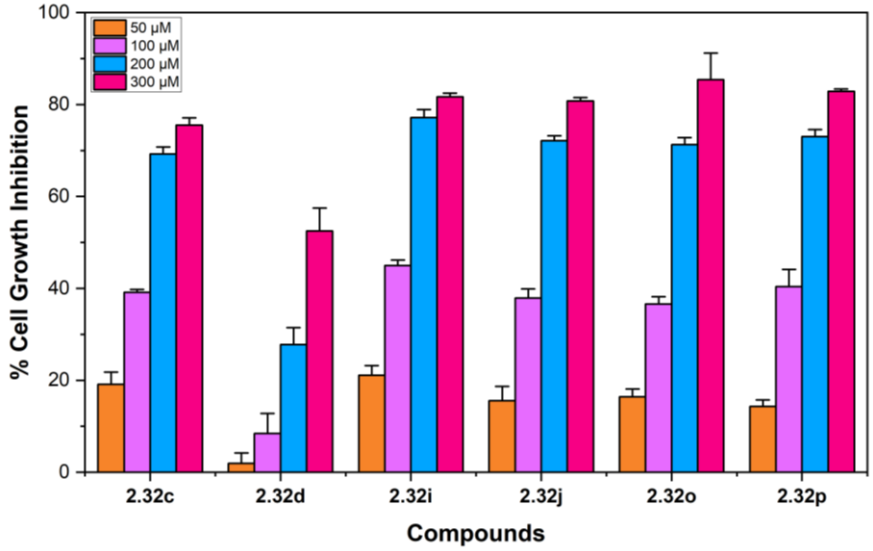

Figure 2.18. Graph showing percentage cell growth inhibition at different concentrations of morpholine-containing compounds **2.32c**, **2.32d**, **2.32i**, **2.32j**, **2.32o** and **2.32p**. Data are presented as mean ± SEM (n=3).

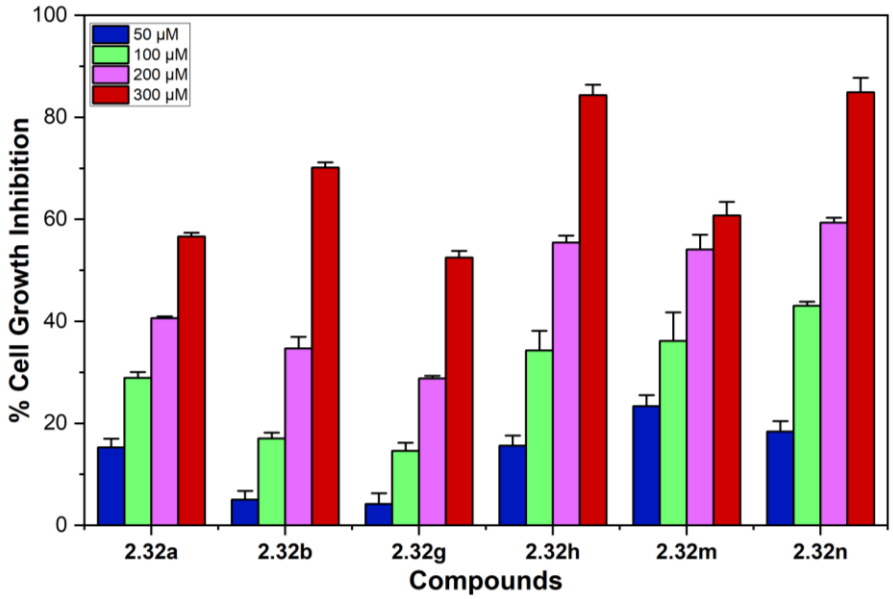

Figure 2.19. Graph showing percentage cell growth inhibition at different concentrations of imidazole-containing compounds **2.32a**, **2.32b**, **2.32g**, **2.32h**, **2.32m** and **2.32n**. Data are presented as mean ± SEM (n=3).

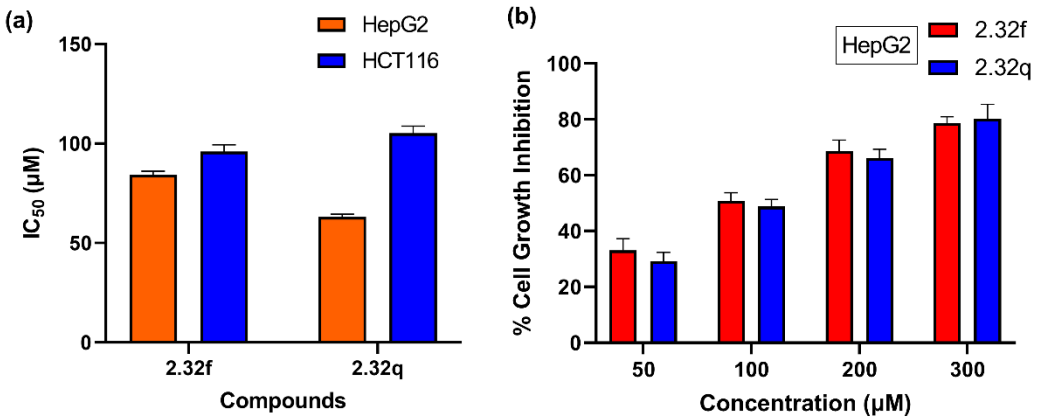

Figure 2.20. (a) IC_{50} values of compounds **2.32f** and **2.32q** against HepG2 and HCT116 cells. (b) Graph showing percentage cell growth inhibition **2.32f** and **2.32q** against HepG2 cells. Data are presented as mean ± SEM (n=3).

Analysis of the data presented in Table 2.6 and derivation of SAR highlights several key structural features influencing activity. Incorporation of a phthalimide moiety into the linker substantially enhanced cytotoxicity, whereas the inclusion of an imidazole group generally diminished activity, consistent with the observations in the **2.31a**-**2.31f** series (Figure 2.21). Electron-withdrawing chlorine substitution at the para position, along with an alkyl linker of n=1, resulted in improved activity in phthalimide-based compounds. In contrast, introducing electron-donating methoxy groups at the ortho position reduced cytotoxicity. For morpholine derivatives, ortho-methoxy substitution with n=1 favored higher activity, while para-methoxy substitution led to a noticeable decline, as seen in **2.32d**, whose cytotoxic potency was approximately 2.5 times lower than that of **2.32i**. Among imidazole-containing compounds, para-chlorine substitution with a linker length of n = 2 yielded the most active analogue, **2.32n**, which exhibited an IC_{50} of 128.6 ± 1.54 µM and inhibited cell growth by 23.02%, 38.87%, 49.77%, and 66.58% at 50, 100, 200, and 300 µM, respectively.

Overall, in the **2.32a**-**2.32r** series, cytotoxic activity depends on the nature of the linker, the type of secondary amine substituents, and both the position and electronic characteristics of the substituents on the phenyl ring. These observations

underscore the importance of structural modifications and electronic effects in optimizing the cytotoxic activity of these compounds.

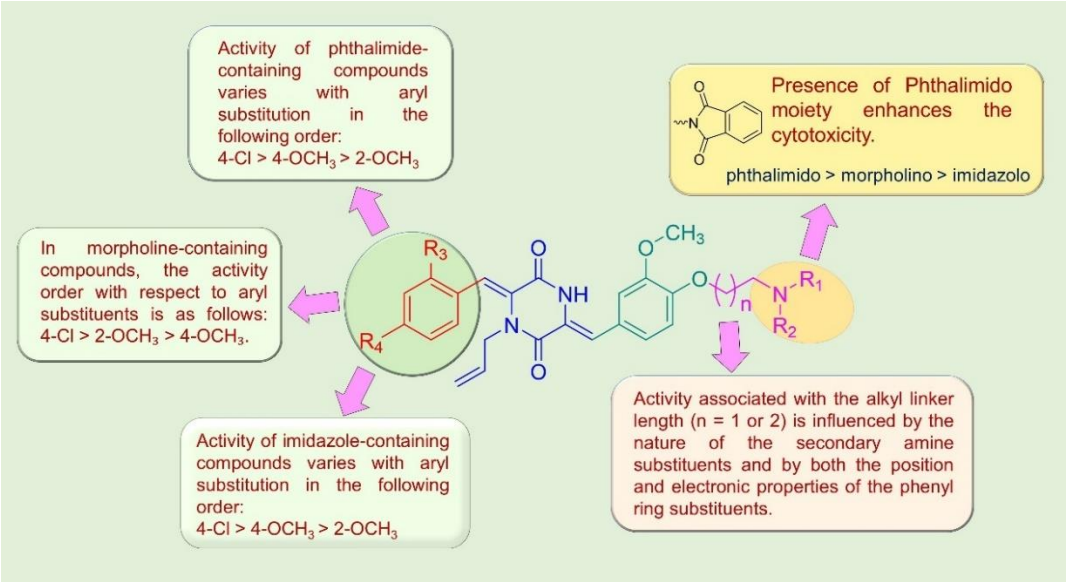

Figure 2.21. Structure activity relationship of compounds **2.32a-2.32r**.

2.4.6.3. Morphological Evidence of Apoptosis Induced by 2.32q

Apoptosis represents the most optimal form of programmed cell death, as it occurs without triggering an inflammatory response. This process is important and highly regulated, allowing cancer cells to undergo programmed cell death without damaging neighbouring healthy cells. Dysregulation of this process contributes to the development of various diseases, including cancer (Elmore, 2007). Moreover, a compound that induces apoptosis is a promising candidate for effective cancer chemotherapy (Tor et al., 2015). Therefore, to investigate apoptosis in HCT116 cells, a nuclear staining assay was performed using Acridine Orange (AO) and Ethidium Bromide (EtBr), followed by fluorescence microscopy. AO is a nucleic acid-selective fluorescent dye that permeates both viable and non-viable cells, staining their nuclei green. In contrast, EtBr penetrates only cells with compromised membrane integrity, staining their nuclei yellowish-orange. Consequently, viable cells exhibit green nuclei, while apoptotic cells display orange chromatin, typically condensed and fragmented due to EtBr uptake. This differential staining enables a clear distinction between viable, apoptotic, and necrotic cells under a fluorescence microscope.

Morphologically, apoptotic cells are characterized by nuclear shrinkage and chromatin condensation, and in the late stages of apoptosis, nuclear fragmentation gives rise to discrete apoptotic bodies.

In our study, treatment of HCT116 cells with varying concentrations of the compound **2.32q** for 24 hours resulted in notable morphological alterations compared to untreated control cells. The analysis of fluorescence microscopy image revealed that **2.32q** induced apoptosis distinct apoptotic features in HCT116 cells, including membrane blebbing, nuclear condensation, and nuclear fragmentation, all of which are classical hallmarks of apoptosis (Figure 2.23). Moreover, a quantitative analysis showed a dose-dependent increase in the apoptotic index, with the proportion of dead cells reaching 36.43%, 68.55%, and 84.65% at **2.32q** concentrations of 25 µM, 50 µM, and 80 µM, respectively, compared to only 1.5% in the control group (Figure 2.22). Furthermore, the apoptotic strength of compound **2.32q** at 80 µM was comparable to that of 5-FU at the same concentration. These findings indicate that **2.32q** effectively induces apoptosis in HCT116 cells in a concentration-dependent manner, supporting its potential as an anticancer agent.

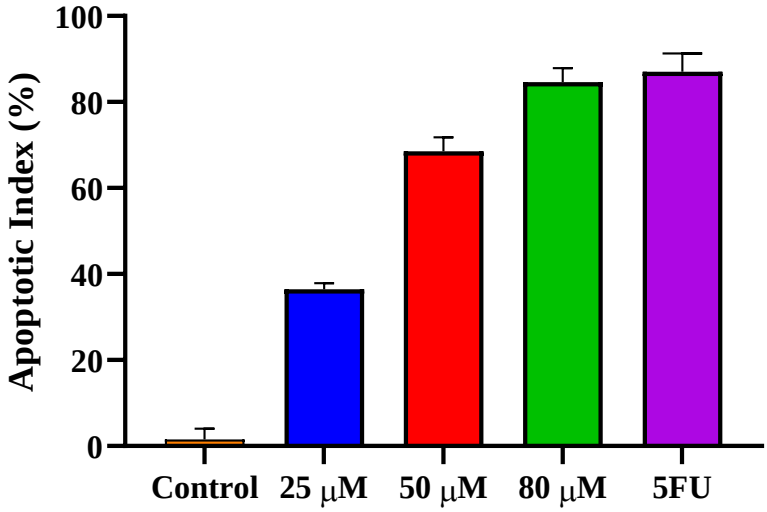

Figure 2.22. Percentage of apoptotic cells following treatment of HCT116 cells with 25 µM, 50 µM, and 80 µM concentrations of **2.32q** for 48 h. Concentration of 5FU is 80 µM. Data are presented as mean ± SEM.

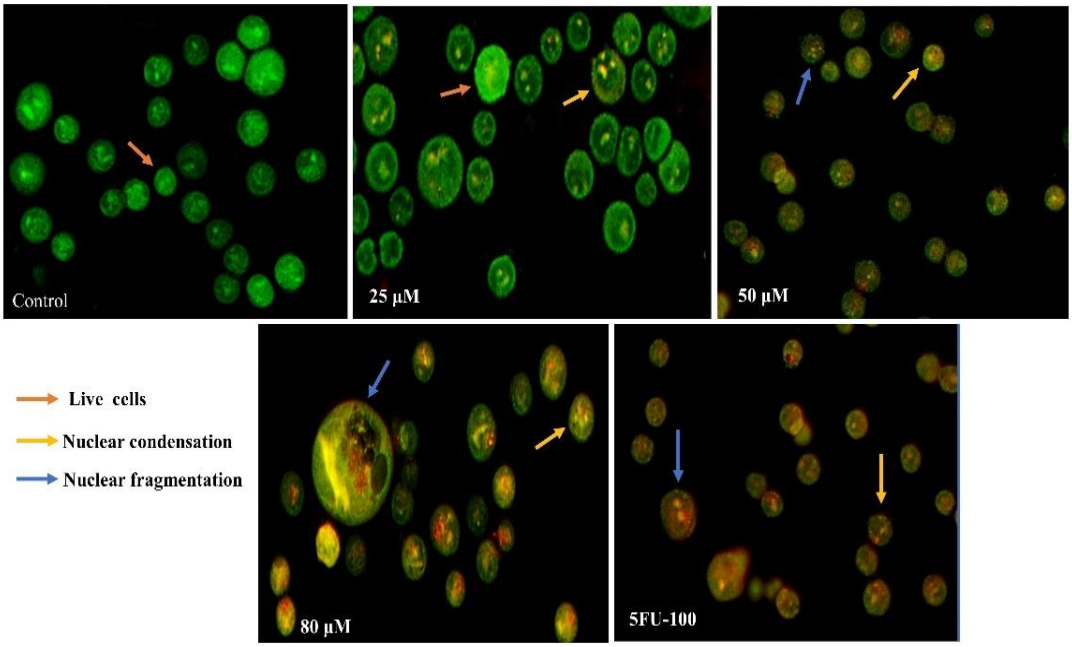

Figure 2.23. Morphological changes in HCT116 cells observed after dual staining with acridine orange and ethidium bromide following treatment with 25 µM, 50 µM, and 80 µM concentrations of **2.32q** for 24 h.

2.4.6.4. Activation of Caspase-6 by Compound 2.32q on HCT116 Cells

Effector caspase-6, a member of the cysteine-aspartic protease family, plays a pivotal role in the execution phase of apoptosis. To investigate the pro-apoptotic effect of **2.32q** in HCT116 cells, caspase-6 activity was measured by following treatment. Exposure of HCT116 cells to 50 µM **2.32q** led to a significant increase in caspase-6 activity, showing a 93.04% elevation, which is equivalent to approximately a 27-fold increase compared to the untreated control. Moreover, treatment with **2.32q** resulted in a 1.2-fold higher caspase-6 activity than that induced by the standard chemotherapeutic agent 5-FU (Figure 2.24).

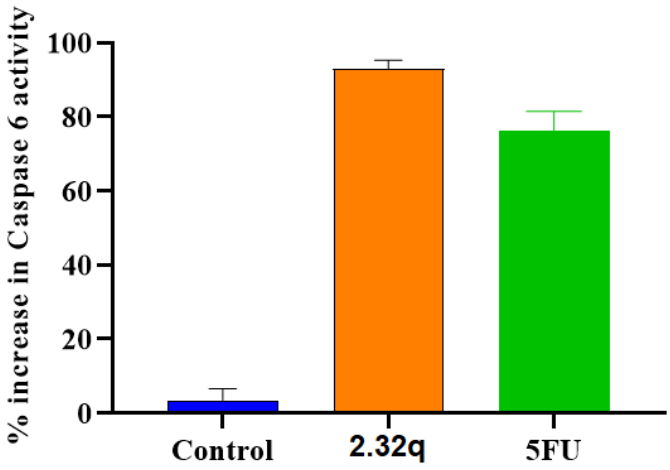

Figure 2.24. Effects of compound **2.32q** on activities of caspase-6 in HCT116 cells after 24 h treatment. Control indicates HCT116 cells without treatment while concentration of **2.32q** and **5FU** is 50 µM. Data are presented as mean ± SEM.

2.4.7. Molecular Modelling Studies

2.4.7.1. Molecular Docking Study with β-tubulin.

In silico molecular docking is a widely employed approach for predicting the binding modes and affinities of potential drug candidates. In the present study, we investigated the interactions of compounds **2.31a–2.31f** and **2.32a–2.32r** with β-tubulin at the colchicine binding site. Several clinically relevant anticancer agents, including plinabulin, colchicine, combretastatins, nocodazole, ABT-751, and indibulin, exert their cytotoxic effects by binding to this site and inhibiting microtubule polymerization. Considering the structural derivation of our compounds from plinabulin, β-tubulin (PDB ID: 5YL4) was selected as the docking target to elucidate their binding modes and the nature of non-covalent interactions responsible for stabilization.

The binding affinities of all compounds are summarized in Table 2.7. Molecular docking revealed that the ligands are generally stabilized within the colchicine binding site through a combination of hydrogen bonding and hydrophobic interactions, including π–π, π–σ, π–alkyl, and π–sulphur contacts.

Table 2.7. Binding affinities and residues involved in interactions of Plinabulin-based DKP derivatives in the colchicine binding site.

Comp	Binding affinity (kcal/mol)	Residues involved in H-bond	Residues involved in other interactions (π···cation, π···π, π···alkyl,)
2.31a	–8.0	Cys239	Met257, Ile368, Val236, Leu253, Ala314, Cys239, Lys350, Leu246
2.31b	–7.9	Cys239	Ile368, Met257, Val236, Leu246, Leu253, Ala314, Cys239, Lys350
2.31c	–6.4	Cys239	Tyr200, Met257, Ala314, Cys239, Leu250, Glu198, Val236, Ile368, Leu253, Lys350, Leu246
2.31d	–6.1	Cys239	Tyr200, Met257, Ala314, Cys239, Leu250, Glu198, Val236, Ile368, Leu253, Lys350, Leu246
2.31e	–5.0	Cys239	Met257, Ala314, Cys239, Tyr200, Leu250, Glu198, Val236, Ile368, Leu253, Lys350, Leu246
2.31f	–5.1	Cys239	Met257, Ile368, Val236, Leu253, Ala314, Cys239, Lys350, Leu246
2.32a	–8.0	Tyr200	Cys239, Leu246, Lys350, Val236, Phe167, Ile368, Met257, Leu253, Ala314
2.32b	–8.3	--	Cys239, Leu246, Lys350, Val236, Phe167, Ile368, Met257, Leu253, Ala314
2.32c	–8.0	Tyr200, Cys239	Ile368, Leu253, Ala314, Lys350, Leu246, Met257, Val236, Cys239
2.32d	–7.9	Tyr200	Met257, Ile368, Leu253, Ala314, Lys350, Leu246, Ala352, Val236, Cys239
2.32e	–8.7	Cys239	Leu246, Lys350, Leu250, Met233, Phe20, Val236, Ile368, Leu253, Met257, Ala314
2.32f	–9.7	Cys239	Leu246, Lys350, Leu250, Met233, Phe20, Val236, Ile368, Leu253, Met257, Ala314

2.32g	–8.3	--	Cys239, Leu246, Lys350, Val236, Phe167, Ile368, Met257, Leu253, Ala314
2.32h	–8.6	Tyr200	Cys239, Leu246, Lys350, Val236, Phe167, Ile368, Met257, Leu253, Ala314
2.32i	–8.3	Tyr200, Cys239	Glu198, Val236, Ala314, Met257, Ile368, Leu253, Lys350
2.32j	–8.0	Tyr200, Cys239	Ile368, Leu253, Ala314, Lys350, Leu246
2.32k	–9.5	--	Phe20, Phe167, Val236, Glu198, Ile368, Leu253, Lys350, Leu246, Met257, Ala314, Met233,
2.32l	–8.8	Cys239	Phe20, Met233, Val236, Leu250, Met257, Ile368, Lys350, Leu246, Ala314, Leu253, Cys239
2.32m	–8.3	Tyr200, Cys239	Lys350, Ala314, Leu253, Ile368, Val236, Cys239, Leu246
2.32n	–8.6	Tyr200, Cys239	Met257, Ile368, Leu253, Ala314, Lys350, Leu246, Ala352, Val236, Cys239
2.32o	–8.2	Tyr200, Cys239	Met257, Ile368, Leu253, Ala314, Lys350, Leu246, Ala352, Val236, Cys239
2.32p	–8.3	Tyr200, Cys239	Met257, Ile368, Leu253, Ala314, Lys350, Leu246, Ala352, Val236, Cys239
2.32q	–8.4	Cys239	Tyr200, Met233, Phe20, Leu250, Met257, Ala314, Lys350, Leu246, Cys239, Leu253, Ile368, Val236,
2.32r	–9.5	Cys239	Leu246, Lys350, Leu250, Met233, Phe20, Val236, Ile368, Leu253, Met257, Ala314

Phthalimide-containing derivatives were primarily stabilized by a hydrogen bond between the carbonyl oxygen of the DKP core and Cys239, in addition to extensive hydrophobic interactions with residues Leu246, Lys350, Leu250, Met233, Phe20, Val236, Ile368, Leu253, Met257, and Ala314. Figure 2.25 illustrates the binding orientation of **2.32q** and **2.32f**, which exhibited a binding affinity of −8.4 and

−9.7 kcal/mol and potent cytotoxicity against HCT116 cells. Similarly, morpholine- and imidazole-containing compounds displayed binding orientations comparable to phthalimide derivatives, indicating a conserved binding mode within the colchicine site. Despite this comparable binding orientation, the anticancer activities varied significantly. It is worth noting that phthalimide-containing compounds appear to achieve greater stabilization within the binding site through π–π stacking interactions involving the phthalimide rings. This enhanced stabilization likely contributes to the superior anticancer activities observed for **2.32f** (IC_{50} = 84.43 μM) and **2.32q** (IC_{50} = 63.15 μM).

All morpholine-containing derivatives, except **2.32d**, consistently formed hydrogen bonds with both Cys239 and Tyr200 residues, highlighting their ability to establish additional polar contacts compared to other analogues. This feature may likely explain their relatively improved cytotoxicity (IC_{50} = 109–129 μM), particularly for **2.32i**, the third-most-active compound in the series. In contrast, **2.32d**, lacking a hydrogen bond to Cys239, exhibited significantly reduced cytotoxicity against HCT116 cells (Figure 2.26). Similarly, imidazole-containing compounds generally did not form hydrogen bonds with the Cys239 residue, except for **2.32n** and **2.32m**. Among these, only **2.32n** showed improved activity, likely due to its ability to form hydrogen bonds with both Tyr200 and Cys239.

Furthermore, analysis of the co-crystal X-ray structure of the anticancer drug candidate plinabulin bound to β-tubulin (PDB: 5C8Y) revealed a critical hydrogen bond with Cys239, underscoring its role in ligand stabilization within the colchicine binding site. By analogy, our results suggest that effective stabilization of compounds through hydrogen bonding with Cys239 is a key determinant of anticancer activity, likely facilitating inhibition of β-tubulin polymerization. This finding highlights the importance of specific polar interactions in guiding structure–activity relationships, providing a rational framework for the design of novel derivatives with enhanced potency.

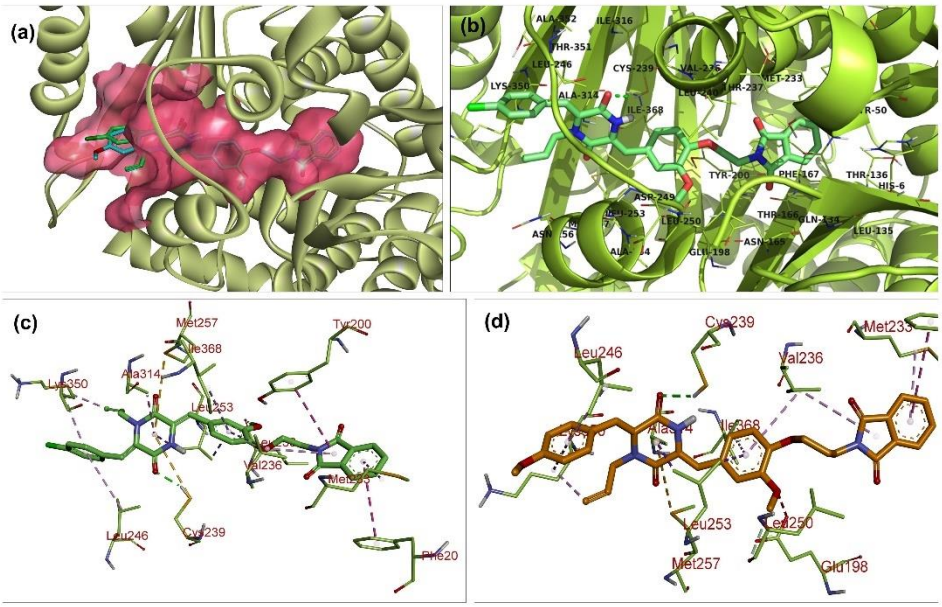

Figure 2.25. (a) Depiction of binding orientations of compound **2.32q** and **2.32f** in the binding pocket. Depiction of noncovalent interactions. (b), (c) **2.32q**. (d) **2.32f**.

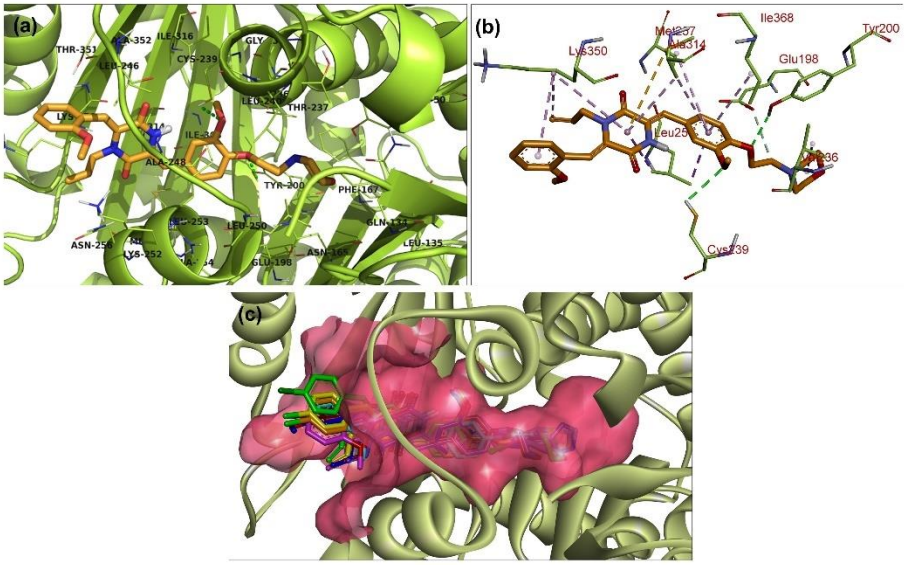

Figure 2.26. (a), (b) Depiction of binding orientations of compound **2.32i** in the binding pocket. (b). Overlay of some compounds in the binding pocket: **2.31c** (orange), **2.31f** (purple), **2.31b** (Dark red), **2.32g** (pink), **2.32b** (blue), **2.32m** (yellow), **2.32n** (orange), **2.32p** (green).

2.4.7.2. Molecular Docking Study with c-Met

Following the comprehensive docking analysis against β-tubulin, compounds (**2.31a–2.31f** and **2.32a–2.32r**) were subsequently evaluated for their binding potential toward c-Met, a receptor tyrosine kinase that plays a pivotal role in tumor growth, metastasis, and angiogenesis. Aberrant activation of c-Met signalling has been strongly implicated in cancer progression, making it an attractive therapeutic target. Several clinically investigated c-Met inhibitors bind to the ATP-binding pocket to suppress kinase activity. To gain additional mechanistic insights and assess possible multitarget interactions, molecular docking studies were performed using the c-Met crystal structure, focusing on identifying key hydrogen-bonding and hydrophobic interactions and defining potential structure–activity relationships within the kinase binding site. This dual docking approach enables a comparative analysis of the compounds' interaction profiles with both β-tubulin and c-Met, providing a broader understanding of their potential anticancer mechanisms.

Table 2.8. Binding affinities and residues involved in interactions of Plinabulin-based DKP hybrids in the binding pocket of c-Met.

Comp	Binding affinity (kcal/mol)	Residues involved in H-bond	Residues involved in other interactions (π···anion, π···sulphur, π···π, π···alkyl,)
2.31a	–8.3	Lys1110	Asp1222, Leu1157, Val1092, Ala1108, Phe1089, Met1211, Ile1084, Gly1085
2.31b	–8.6	Lys1110	Asp1222, Leu1157, Val1092, Ala1108, Phe1089, Met1211, Ile1084, Gly1085
2.31c	–9.4	--	Asp1222, Leu1157, Val1092, Ala1108, Phe1089, Met1211, Ile1084, Gly1085
2.31d	–9.6	Asp1222	Lys1110, Asp1222, Phe1089, Val1092, Met1211, Ile1084, Ala1108, Leu1157, Val1155, Met1131
2.31e	–10.1	Asp1222, Phe1223	Asp1222, Lys1110, Phe1089, Val1092, Met1211, Ala1108, Leu1157, Met1131, Leu1142, Val1155, Ile1130, Phe1200

2.31f	–10.4	Asp1222	Asp1222, Lys1110, Phe1089, Val1092, Met1211, Ala1108, Leu1157, Met1131, Leu1142, Val1155, Ile1130, Phe1200
2.32a	–9.0	Met1160	Phe1089, Glu1127, Lys1110, Asp1222, Ala1221, Ala1108, Ile1084, Met1211, Tyr1159, Leu1157, Val1155, Phe1124, Ile1115, Leu1112
2.32b	–9.0	Asp1222	Met1211, Leu1157, Met1211, Leu1142, Val1155, Phe1200, Ile1130, Lys1110, Asp1222, Ala1221, Phe1089, Ala1108, Ile1084, Met1160
2.32c	–9.1	Asp1222, Met1160	Glu1127, Lys1110, Asp1222, Phe1089, Ala1221, Ala1108, Ile1084, Met1211, Tyr1159, Leu1157, Val1155, Phe1124, Ile1115, Leu1112
2.32d	–9.4	Asp1222, Phe1223	Leu1157, Met1211, Leu1142, Val1155, Phe1200, Ile1130, Lys1110, Asp1222, Ala1221, Phe1089, Met1211, Ala1108, Ile1084, Met1160
2.32e	–10.2	Lys1110, Met1160	Leu1157, Ala1221, Asp1222, Val1155, Ala1108, Ile1084, Met1211
2.32f	–9.8	Asp1222	Met1131, Asp1222, Phe1089, Ala1108, Val1092, Met1211, Leu1157, Phe1223
2.32g	–8.7	Met1160	Phe1089, Glu1127, Lys1110, Asp1222, Ala1221, Ala1108, Ile1084, Met1211, Tyr1159, Leu1157, Val1155, Phe1124, Ile1115, Leu1112
2.32h	–8.7	Asp1222	Leu1157, Met1211, Leu1142, Val1155, Phe1200, Ile1130, Lys1110, Asp1222, Ala1221, Phe1089, Met1211, Ala1108, Ile1084, Met1160
2.32i	–7.8	Asp1222, Met1160	Glu1127, Lys1110, Asp1222, Phe1089, Ala1221, Ala1108, Ile1084, Met1211, Tyr1159, Leu1157, Val1155, Phe1124, Ile1115, Leu1112
2.32j	–8.4	Asp1222, Lys1110	Leu1112, Ile1115, Arg1114, Met1211, Phe1089, Val1092, Ala1108, Leu1157, Asp1222, Val1155, Phe1223, Leu1112,
2.32k	–10.2	Lys1110, Met1160	Met1131, Asp1222, Phe1089, Ala1108, Val1092, Met1211, Leu1157, Phe1223

2.32l	–10.2	Asp1222, Met1160	Leu1157, Ala1221, Asp1222, Val1155, Ala1108, Ile1084, Met1211,
2.32m	–9.5	Asp1222, Met1160	Glu1127, Lys1110, Asp1222, Phe1089, Ala1221, Ala1108, Ile1084, Met1211, Tyr1159, Leu1157, Val1155, Phe1124, Ile1115, Leu1112
2.32n	–9.1	Asp1222, Met1160	Glu1127, Lys1110, Asp1222, Phe1089, Ala1221, Ala1108, Ile1084, Met1211, Tyr1159, Leu1157, Val1155, Phe1124, Ile1115, Leu1112
2.32o	–9.5	Asp1222, Met1160	Glu1127, Lys1110, Asp1222, Phe1089, Ala1221, Ala1108, Ile1084, Met1211, Tyr1159, Leu1157, Val1155, Phe1124, Ile1115, Leu1112
2.32p	–9.4	Asp1222, Phe1223	Leu1157, Met1211, Leu1142, Val1155, Phe1200, Ile1130, Lys1110, Asp1222, Ala1221, Phe1089, Met1211, Ala1108, Ile1084, Met1160
2.32q	–10.6	Asp1222, Met1160	Phe1089, Lys1110, Ala1221, Leu1157, Ile1084, Leu1142, Val1155, Tyr1159, Ala1108, Met1211, Met1131, Ile1130, Phe1200
2.32r	–10.4	Asp1222, Met1160	Leu1157, Val1155, Phe1124, Ile1115, Leu1112, Glu1127, Lys1110, Asp1222, Phe1089, Ala1221, Ile1084, Ala1108, Met1211, Tyr1159

The compounds exhibited a linear binding mode, adopting an extended conformation that spanned from the kinase linker region to the DFG (Asp–Phe–Gly) motif or C-helix pocket. The binding affinities of all compounds are summarized in Table 2.8. Among **2.31a–2.31f**, compound **2.31b**, which exhibited the highest cytotoxicity, has the binding affinity of -10.1 kcal/mol. It exhibited two hydrogen-bond interactions, in which the carbonyl oxygen of the DKP core acted as a bifurcated hydrogen-bond acceptor, forming interactions with both Asp1222 and Phe1223 (Figure 2.27). Additionally, Asp1222 engaged in a π–π-anion interaction with the phenyl ring of the 4-phenylmorpholine moiety. Furthermore, the 4-methoxyphenyl ring occupied the hydrophobic region near the DFG pocket and formed π–π-sulphur interaction with Met1131. Additional hydrophobic stabilization was provided through

π–π, π alkyl, π–σ, and alkyl interactions with Lys1110, Phe1089, Val1092, Met1211, Ala1108, Leu1157, Leu1142, Val1155, Phe1200, Phe1223, and Ile1130.

The docking pose of **2.32f** revealed that the phthalimide ring occupied the DFG pocket and established a hydrogen bond with Asp1222, a π-sulfur and π-alkyl interaction with Met1131, a T-shaped π–π interaction with Phe1223, and π-alkyl interactions with Leu1157 (Figure 2.28). In addition to the hydrogen bond, Asp1222 also formed a π-anion interaction with the phthalimide ring. The 3-methoxyphenyl ring was positioned between the kinase linker and the DFG motif, forming π–π stacking interactions with Phe1089 and π-alkyl interactions with Ala1108, Val1092, and Met1211. The DKP core and 4-methoxyphenyl ring of **2.32f** were oriented toward the solvent-exposed region.

Interestingly, compound **2.32q** adopted a distinct orientation from **2.32f**. In this case, the DKP core occupied the DFG pocket, while the phthalimide ring was positioned near the kinase linker region (Figure 2.29). The carbonyl oxygen of the DKP core formed a hydrogen bond with Asp1222, whereas the phthalimide carbonyl interacted with Met1160 of the kinase linker. The 4-chlorophenyl ring was positioned in a hydrophobic pocket defined by Phe1200 and Ile1130, while the 3-methoxyphenyl group was located between the DFG pocket and the kinase linker. This group engaged in π–π stacking interactions with Phe1089, along with π-alkyl and π–σ interactions involving Lys1110, Ala1221, and Leu1157, as well as a π–anion interaction with Asp1222.

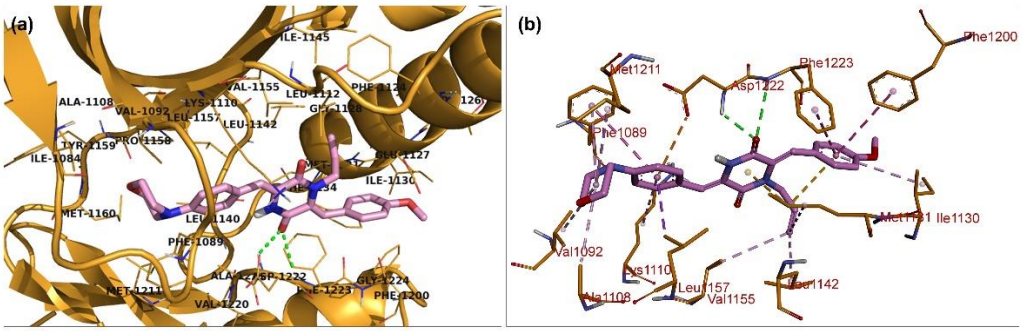

Figure 2.27. Illustration of binding orientations of compound **2.31b** in the c-Met binding pocket.

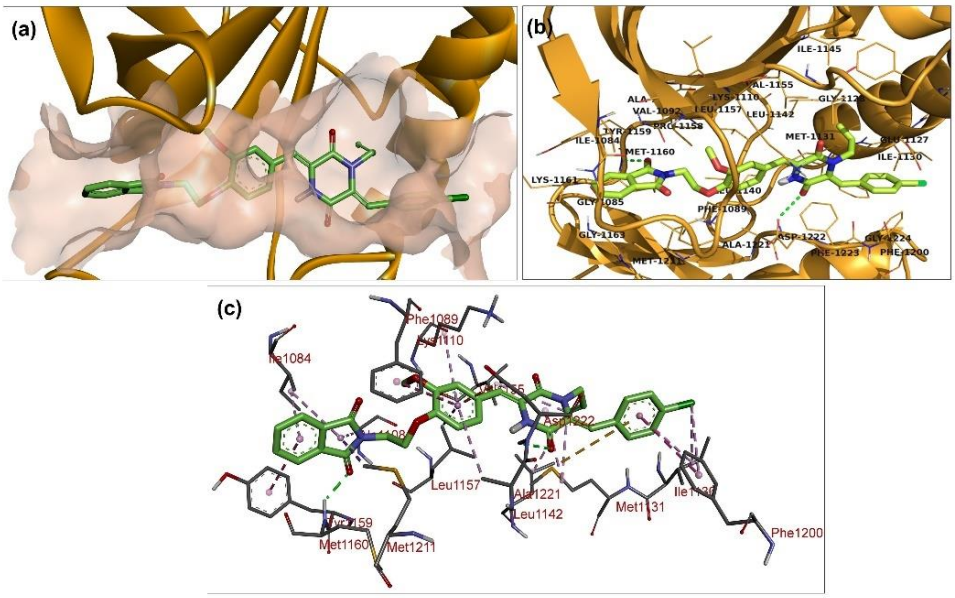

Figure 2.28. Illustration of binding orientations of compound **2.32q** in the c-Met binding pocket.

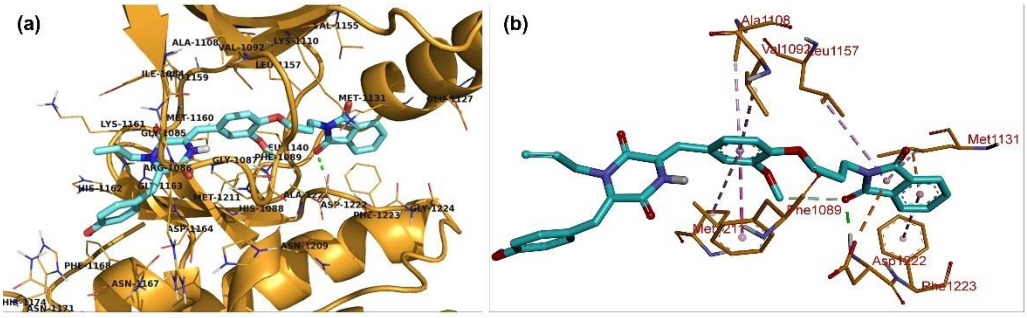

Figure 2.29. Illustration of binding orientations of compound **2.32f** in the c-Met binding pocket.

Altogether, the docking results against β-tubulin and c-Met provide valuable structural insights into the binding modes and structure–activity relationships of these plinabulin derivatives. The analysis revealed that hydrogen bonding with Cys239 within the colchicine binding site of β-tubulin is a critical determinant of cytotoxic activity, while additional hydrophobic and π–π stacking interactions further enhance ligand stabilization. Similarly, in the c-Met binding site, the most potent compounds adopted an extended conformation spanning the kinase linker and DFG pocket, establishing key hydrogen bonds with Asp1222 and Met1160, as well as π- anion, π-sulfur, and hydrophobic contacts that collectively stabilize the ligand. Compounds

such as **2.31b, 2.32f**, and **2.32q** exemplify how variations in ring orientation and functional groups can lead to distinct binding poses that maintain critical interactions while exploring secondary subpockets.

Overall, this dual-target docking analysis highlights the potential of DKP derivatives to act as multitarget inhibitors, capable of simultaneously disrupting microtubule polymerization and kinase signalling pathways. Such a dual mechanism could enhance anticancer efficacy and reduce the likelihood of resistance, thereby providing a rational framework for the further optimization and design of next-generation plinabulin-based DKP therapeutics.

2.5. Conclusion

In conclusion, a series of novel diketopiperazine analogues (**2.31a–2.31f** and **2.32a–2.32r**) was successfully synthesized using a molecular hybridization approach. All compounds were obtained in moderate yields and were fully characterized. Evaluation of their *in vitro* anticancer activity against HCT116 and HepG2 cancer cell lines revealed potent cytotoxic effects. Notably, compounds **2.31a, 2.32f, 2.32i**, and **2.32q** exhibited the most pronounced anticancer activity. Among these, compound **2.32q** was identified as a strong inducer of apoptosis. Fluorescence microscopy analysis of HCT116 cells treated with **2.32q** revealed characteristic apoptotic features, including membrane blebbing, nuclear condensation, and nuclear fragmentation, confirming its apoptotic mode of action. Moreover, treatment with **2.32q** resulted in a significant increase in caspase-6 activity, with a 93.04% rise, equivalent to approximately a 27-fold increase relative to the untreated control and a 1.2-fold increase relative to the standard chemotherapeutic agent 5-fluorouracil, further validating its pro-apoptotic potential. Molecular docking studies against β-tubulin and c-Met kinase provided valuable structural insights into protein-ligand interactions. Hydrogen bond interactions with Cys239 within the colchicine binding site of β-tubulin and with Asp1222 and Met1160 in the c-Met binding pocket were identified as key determinants of cytotoxic activity. Additionally, hydrophobic and π–π stacking interactions contributed to the stabilization of the ligand-protein complex.

Overall, this study highlights the strong potential of these diketopiperazine derivatives as promising lead candidates for the development of effective anticancer agents, warranting further pharmacological and mechanistic investigations.

2.6. ^{1}H NMR and ^{13}C NMR Spectra and HRMS Data of Selected Compounds

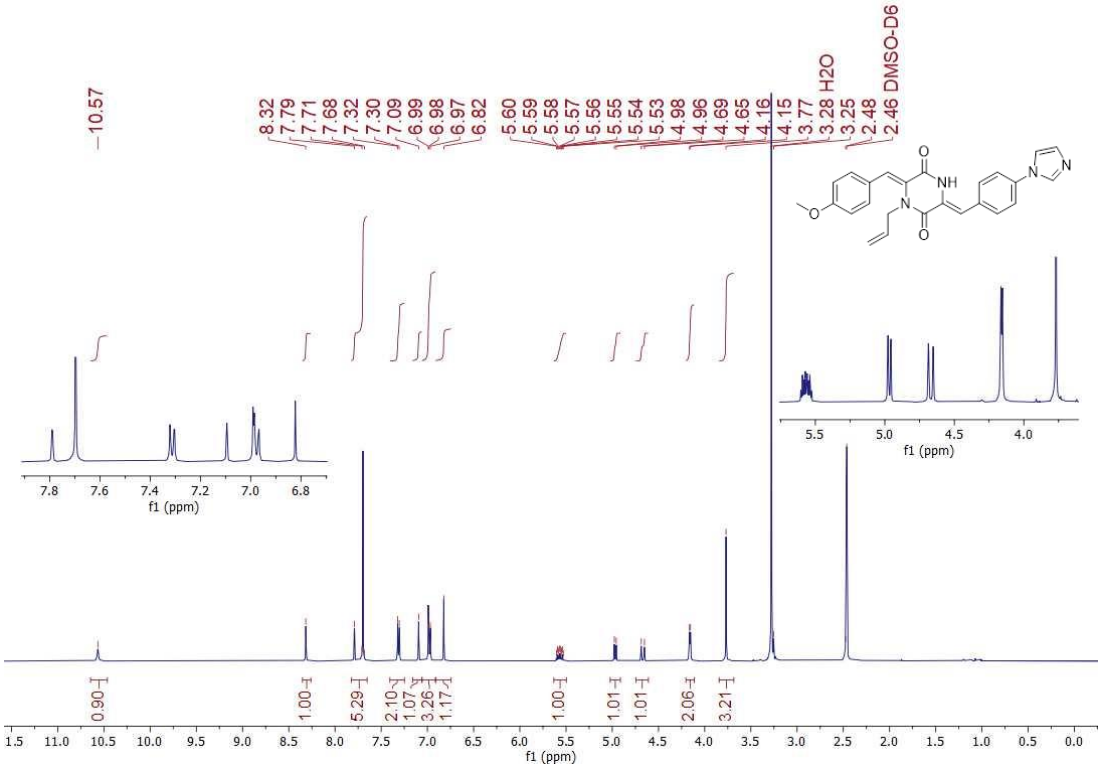

Figure 2.30. ^{1}H NMR of compound **2.31a**

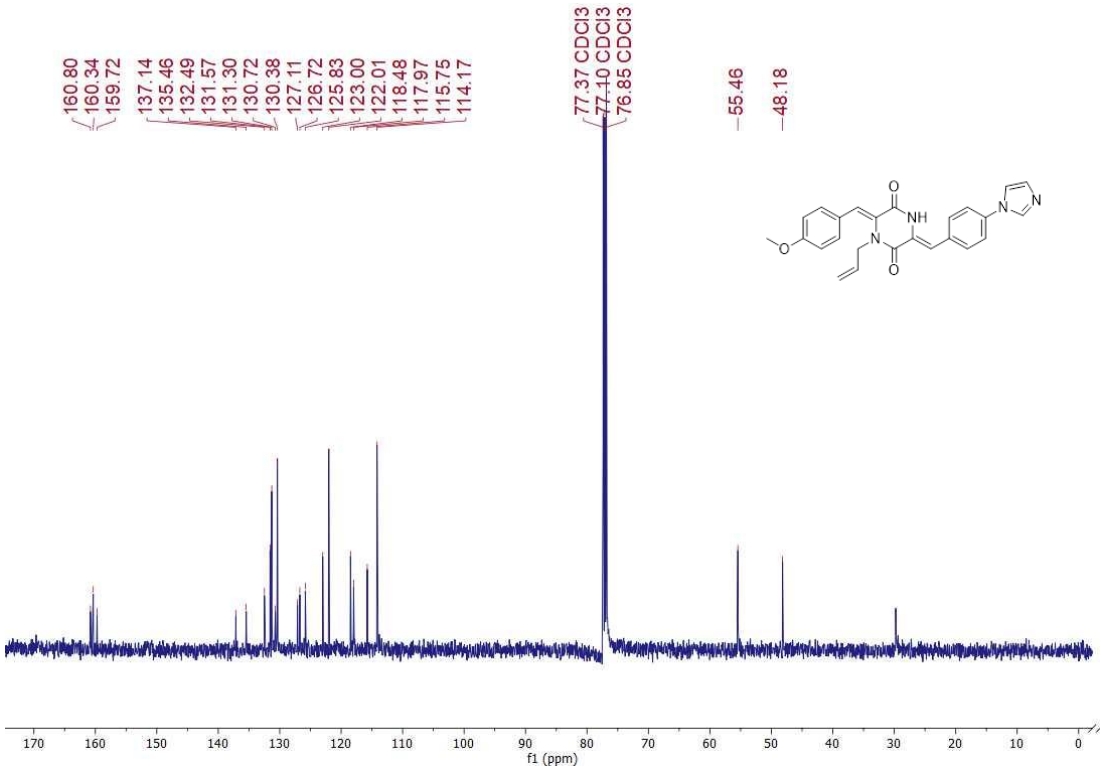

Figure 2.31. ^{13}C NMR of compound **2.31a**

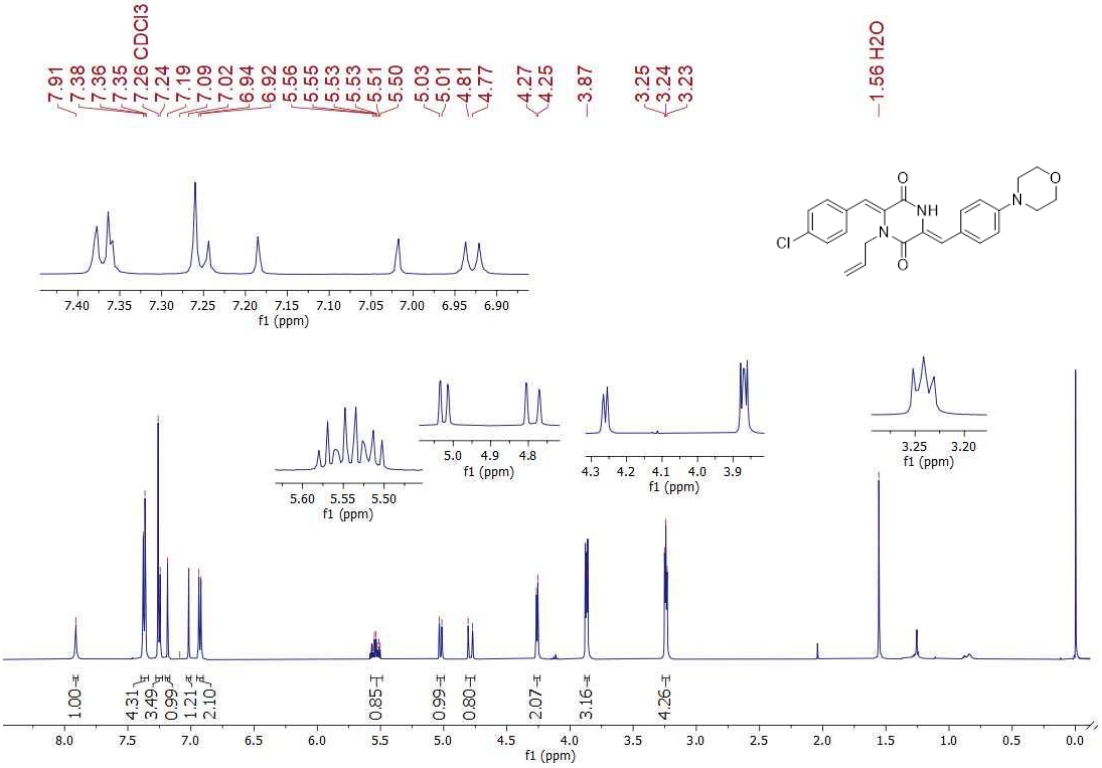

Figure 2.32. [1]H NMR of compound **2.31f**

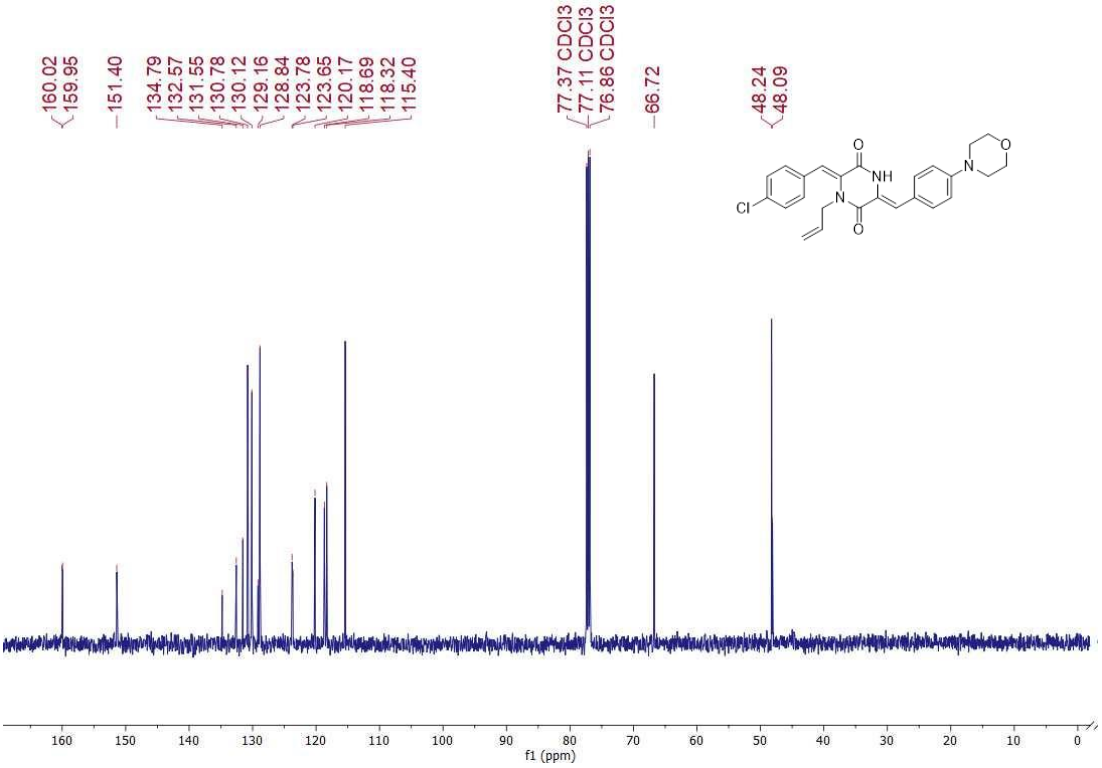

Figure 2.33. [13]C NMR of compound **2.31f**

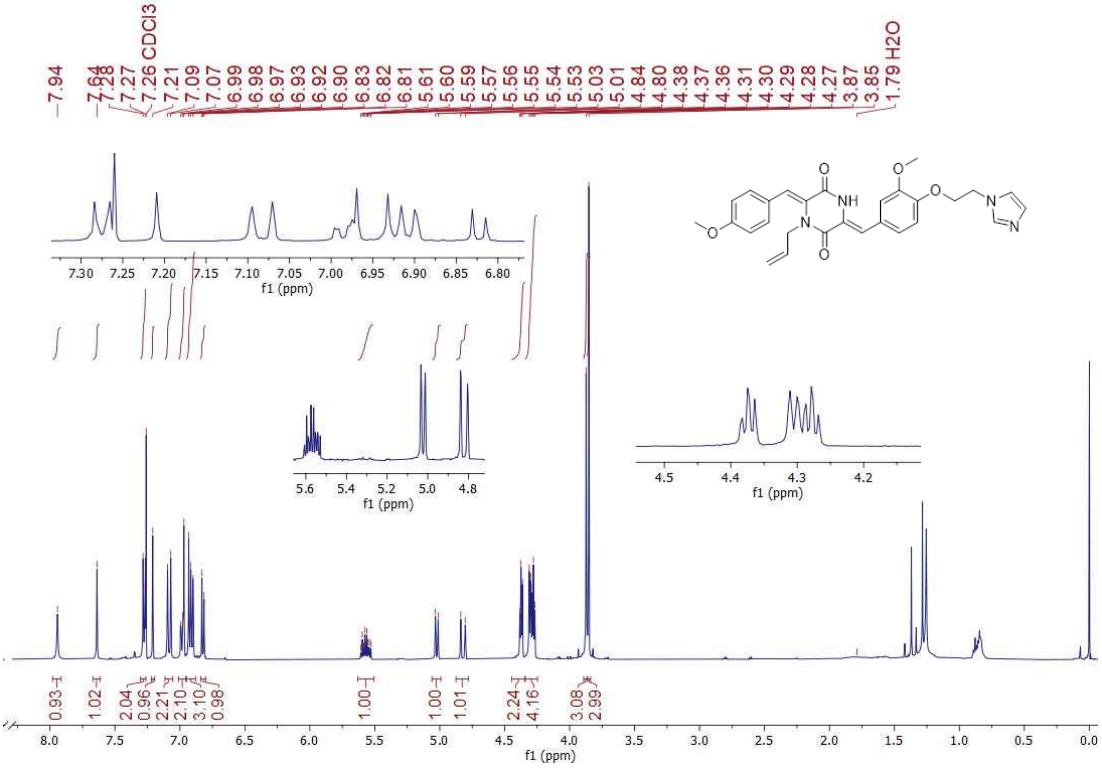

Figure 2.34. ^{1}H NMR of compound **2.32a**

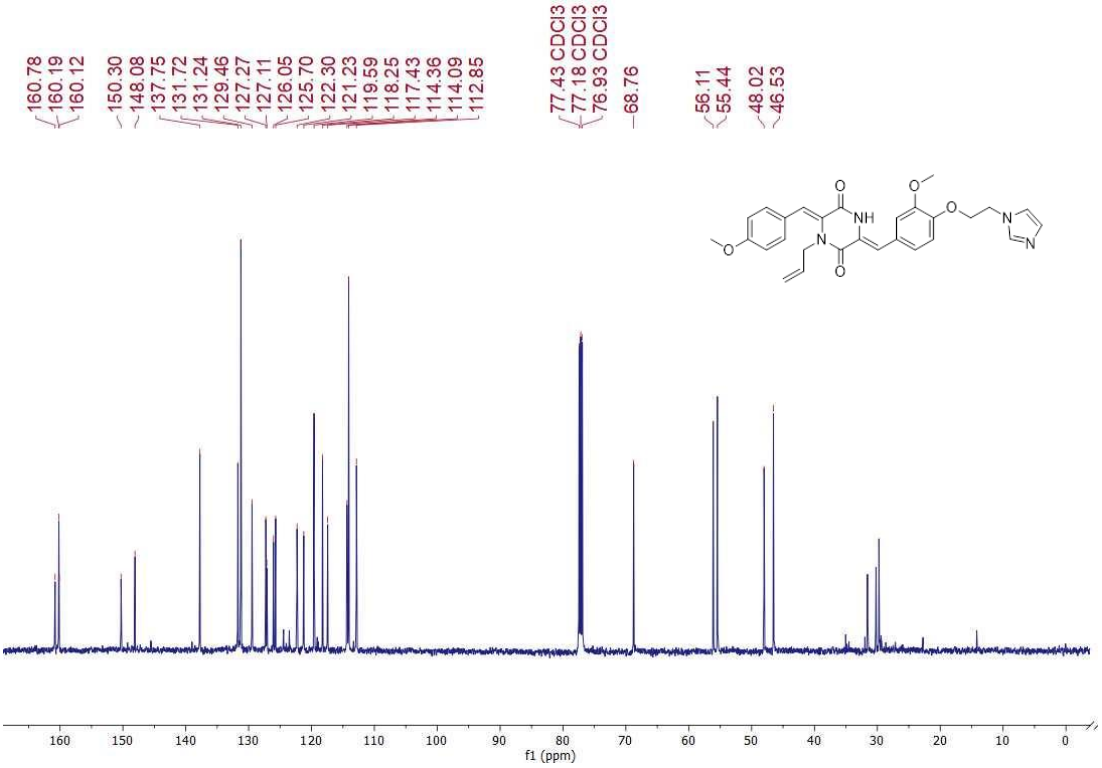

Figure 2.35. ^{13}C NMR of compound **2.32a**

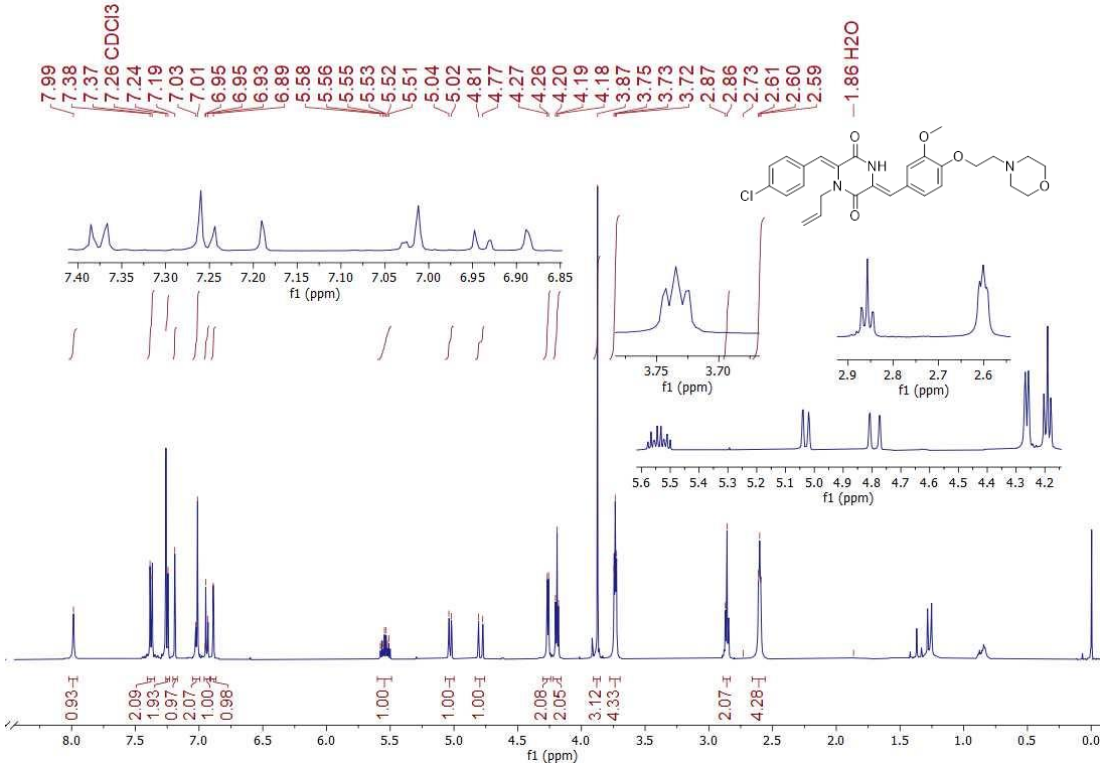

Figure 2.36. ^{1}H NMR of compound **2.32o**

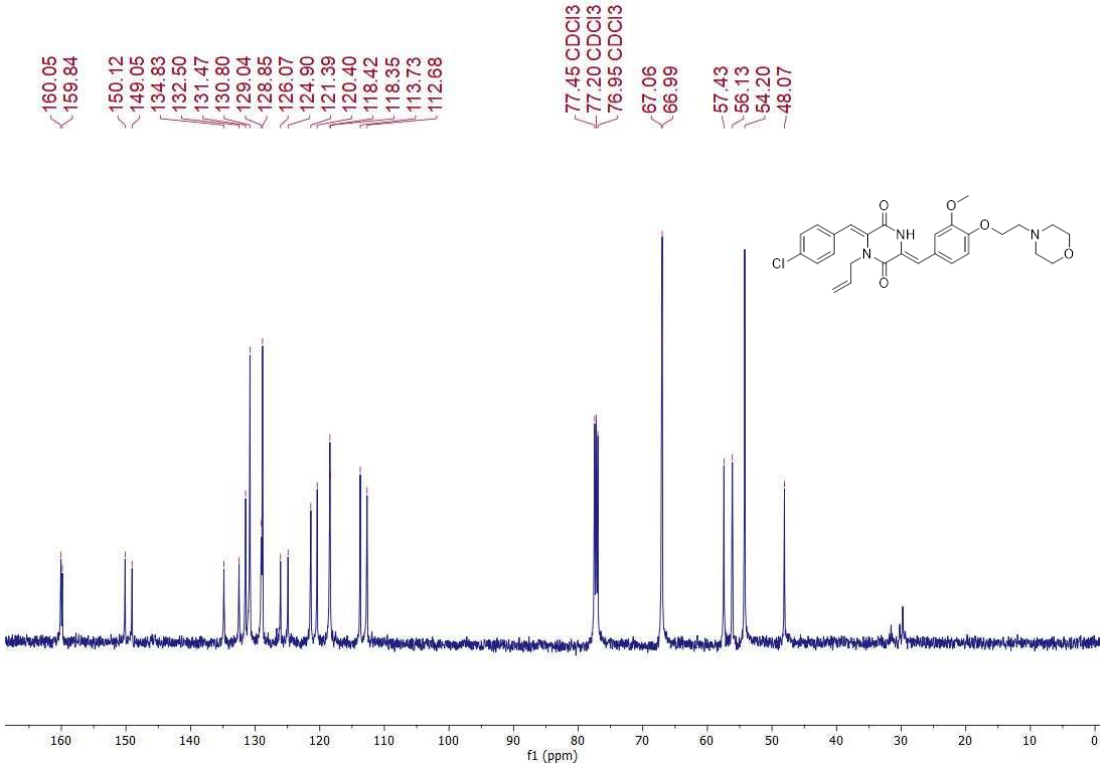

Figure 2.37. ^{13}C NMR of compound **2.32o**

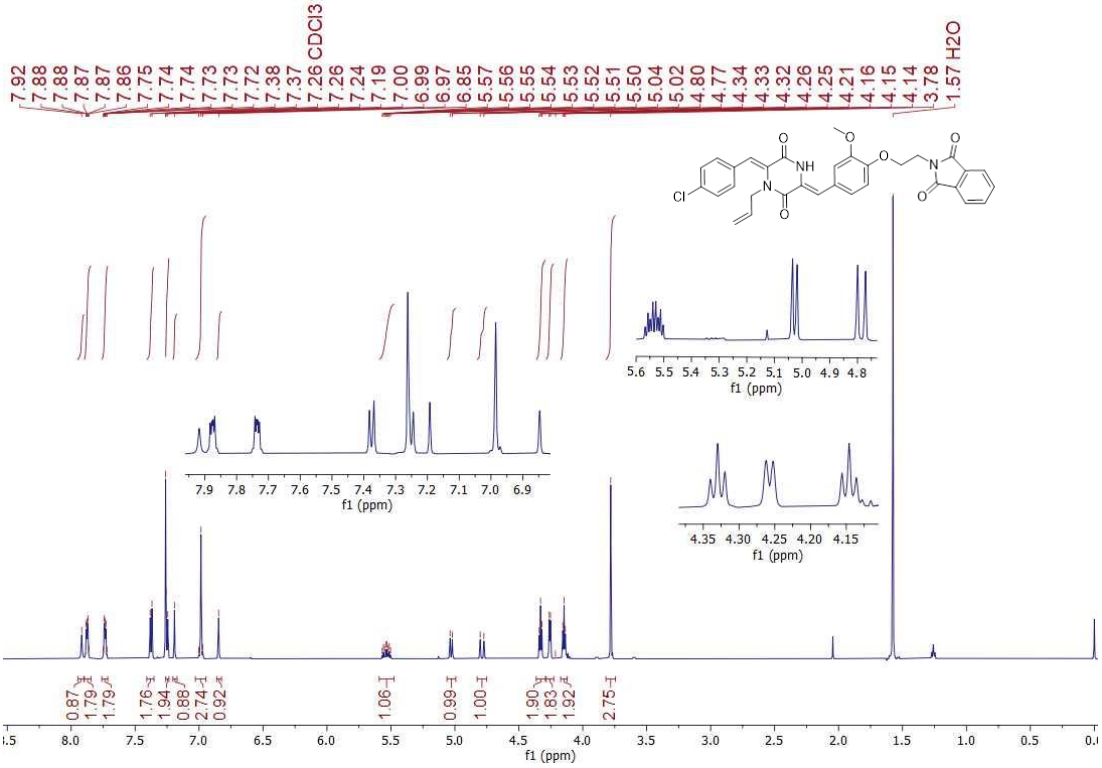

Figure 2.38. ^{1}H NMR of compound **2.32q**

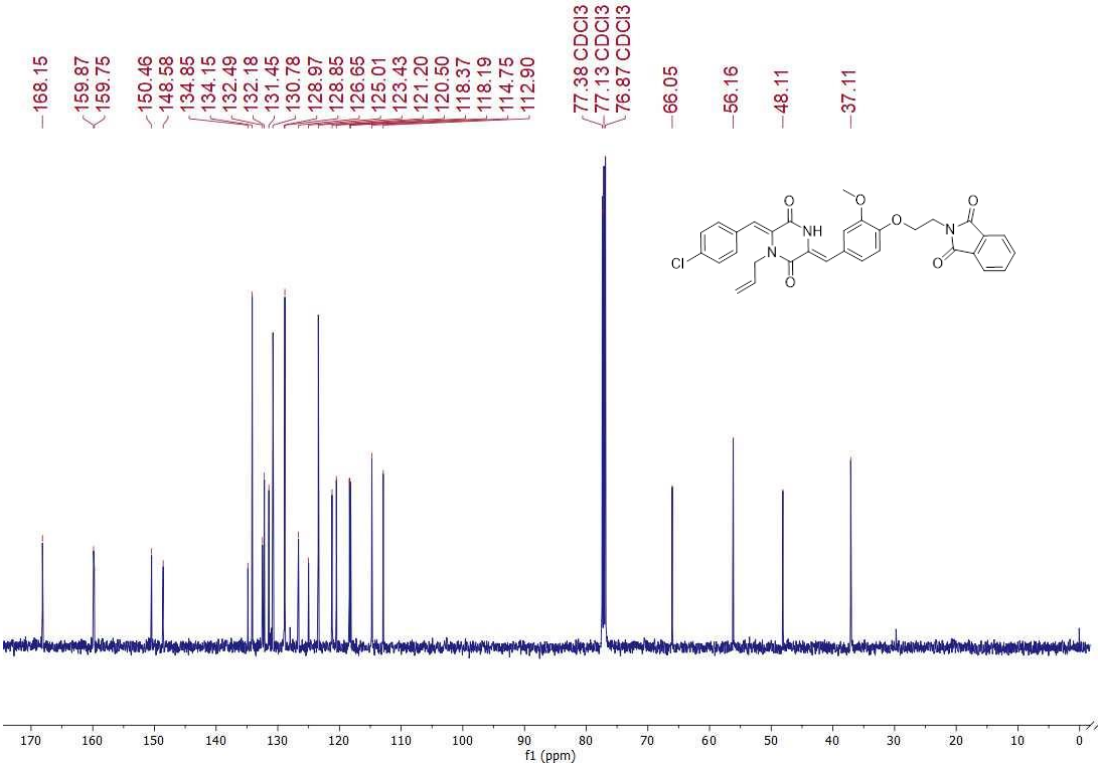

Figure 2.39. ^{13}C NMR of compound **2.32q**

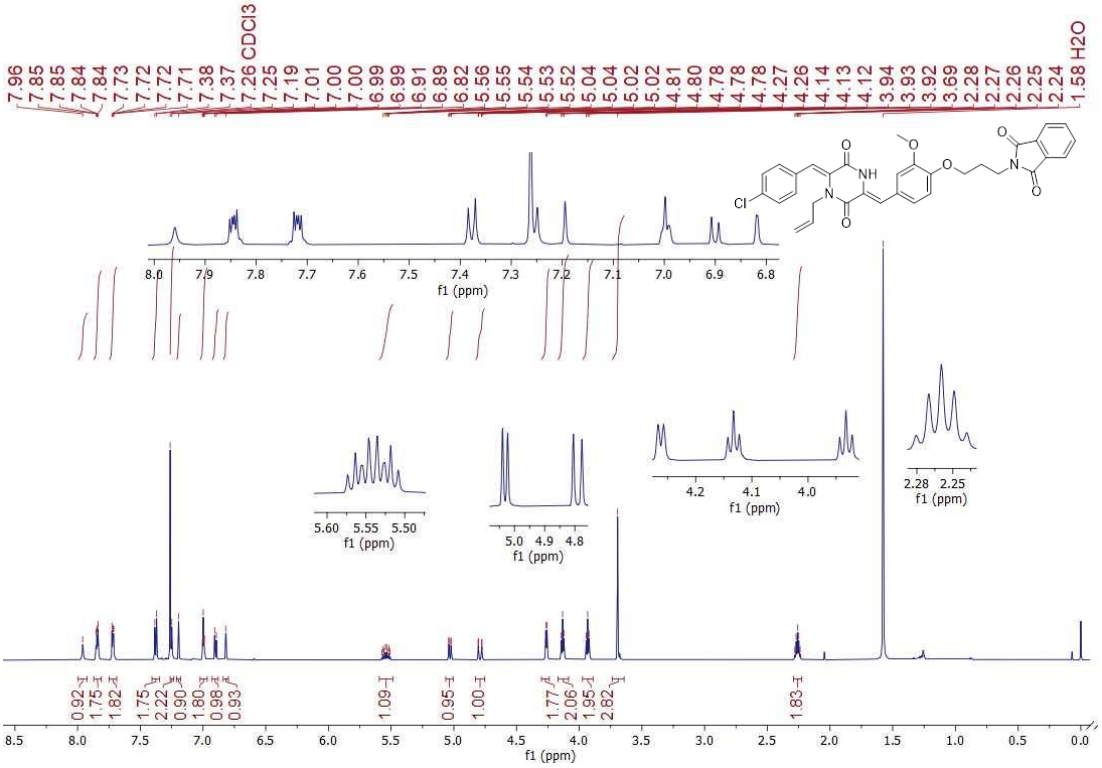

Figure 2.40. ^{1}H NMR of compound **2.32r**

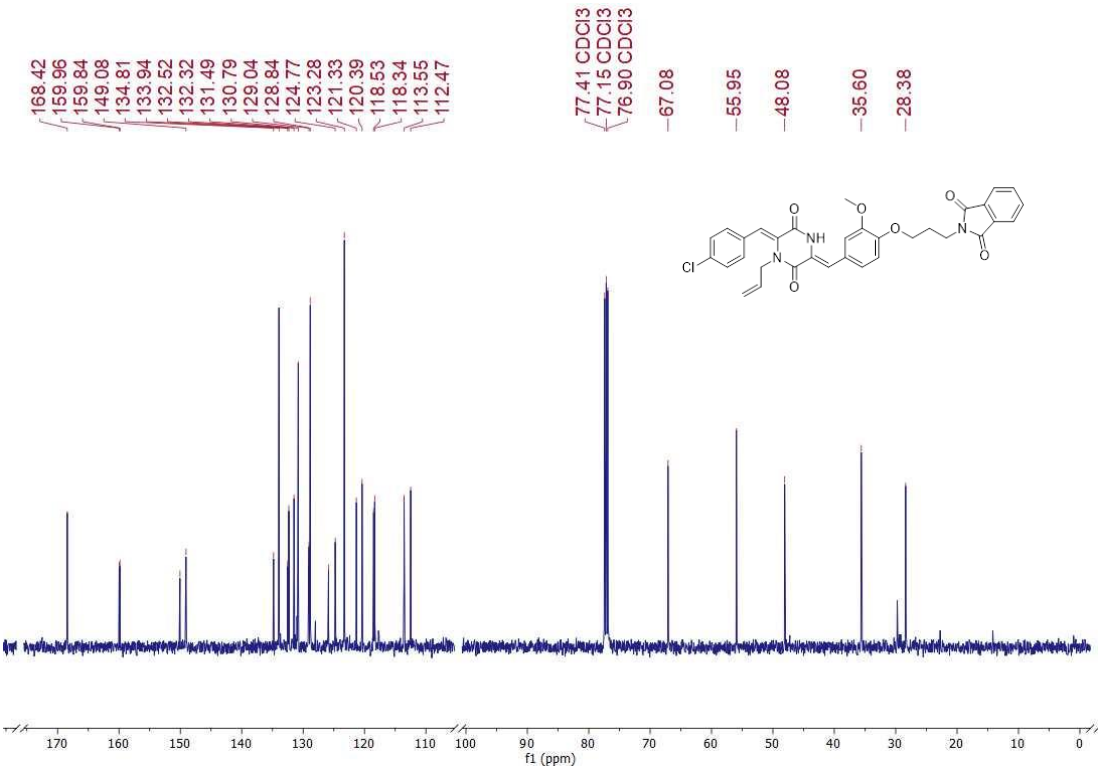

Figure 2.41. ^{13}C NMR of compound **2.32r**

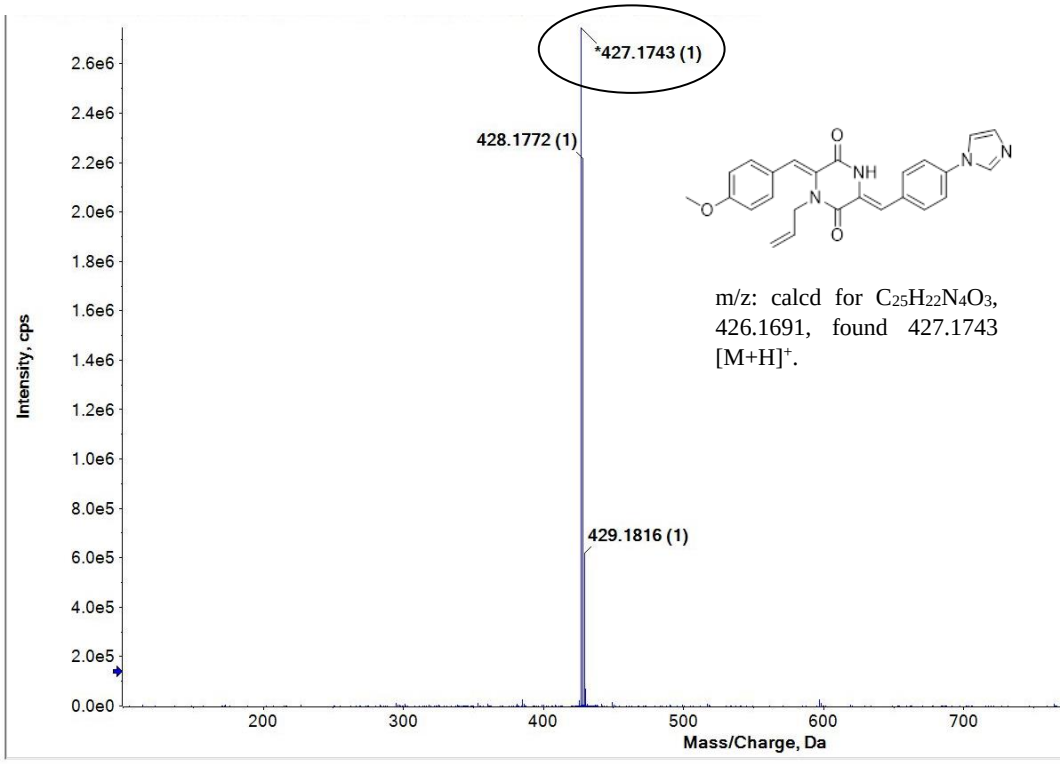

Figure 2.42. HRMS of compound **2.31a**

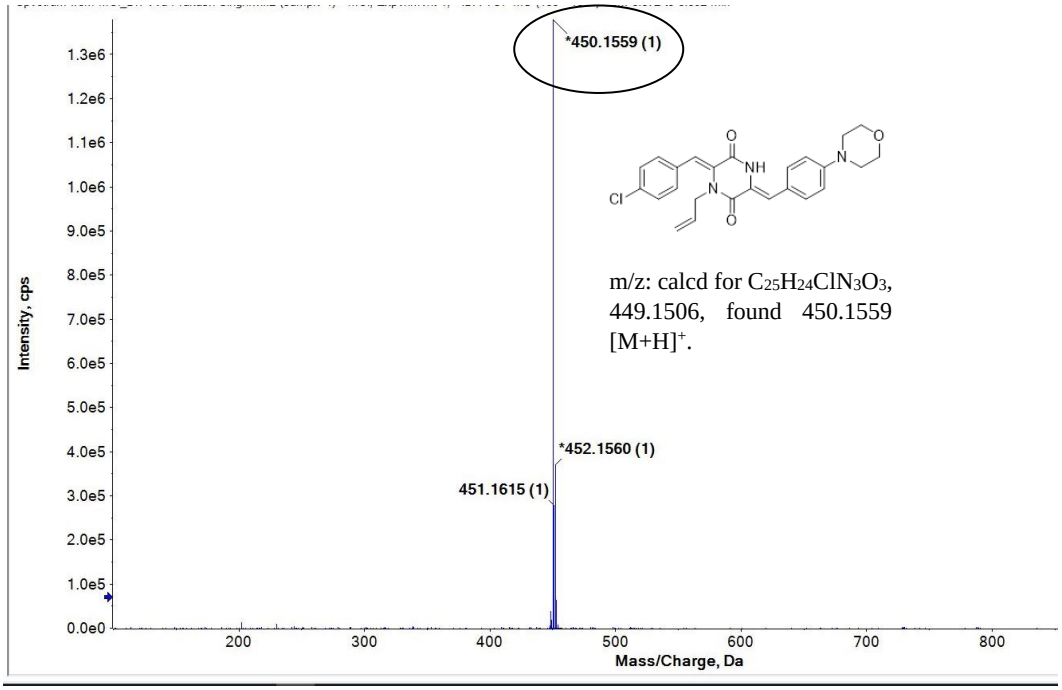

Figure 2.43. HRMS of compound **2.31f**

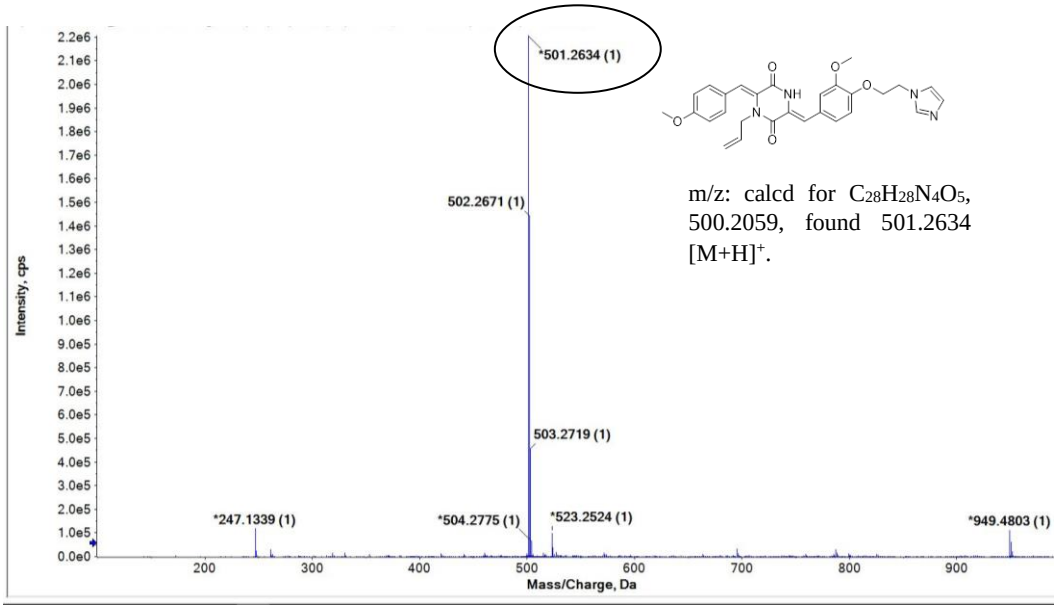

Figure 2.44. HRMS of compound **2.32a**

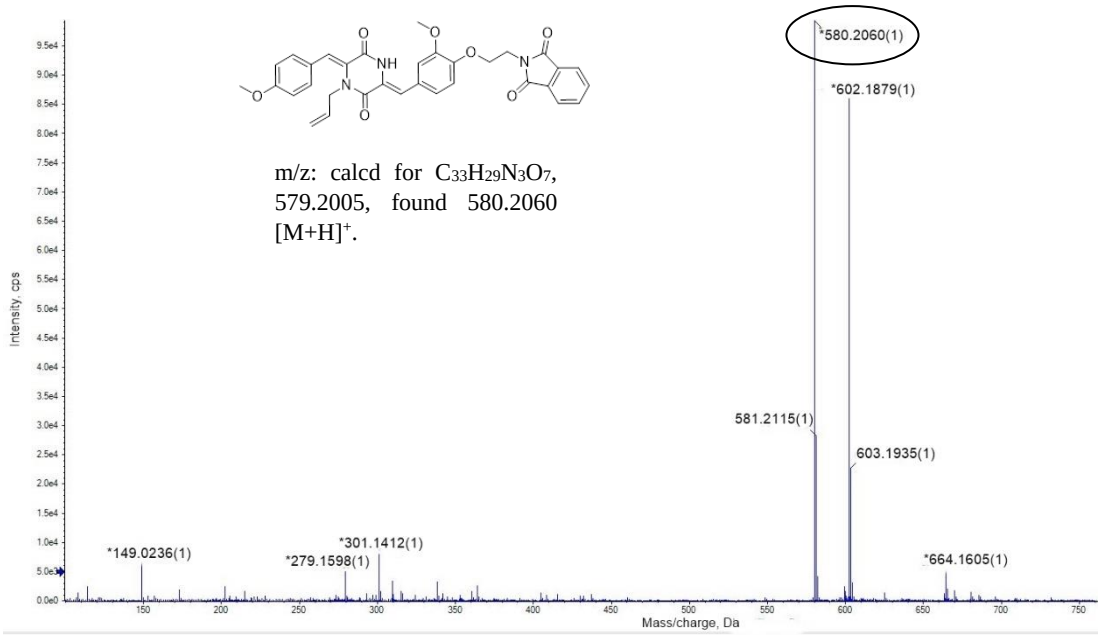

Figure 2.45. HRMS of compound **2.32e**

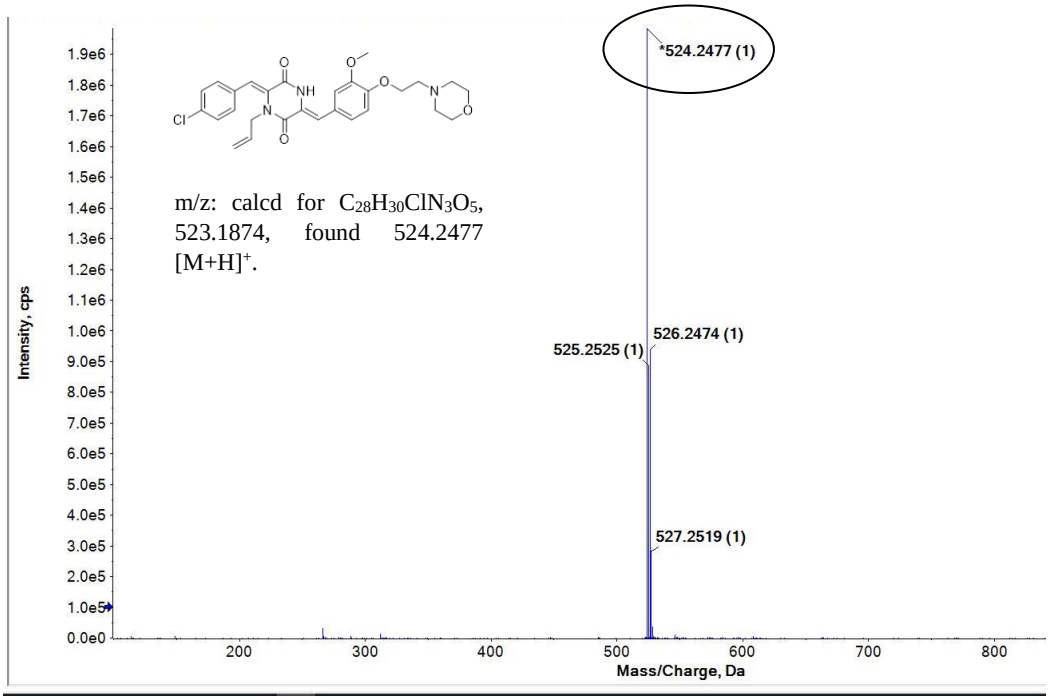

Figure 2.46. HRMS of compound **2.32o**

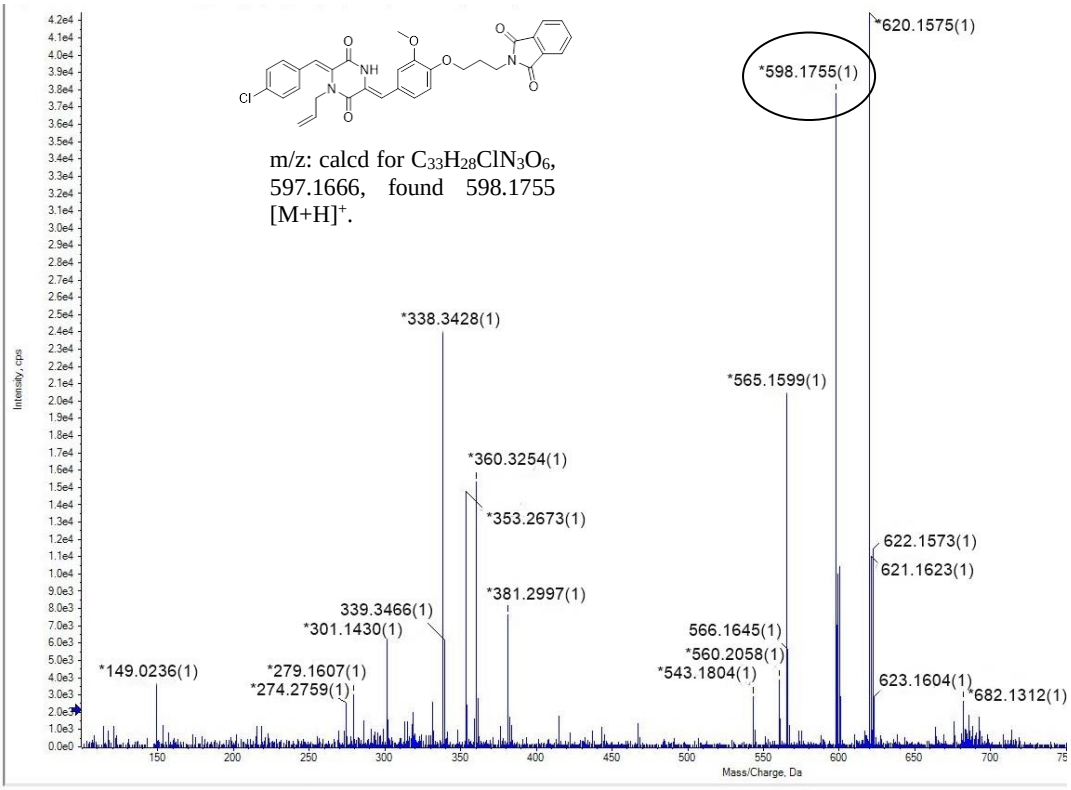

Figure 2.47. HRMS of compound **2.32r**

CHAPTER 3

SYNTHESIS AND ANTI-CANCER ACTIVITY OF NOVEL 2,5-DIKETOPIPERAZINE-BASED COUMARIN ANALOGUES

CHAPTER 3

SYNTHESIS AND ANTI-CANCER ACTIVITY OF NOVEL 2,5-DIKETOPIPERAZINE-BASED COUMARIN ANALOGUES

3.1. Background

Coumarins represent a prominent class of naturally occurring heterocyclic compounds. They have attracted considerable attention in medicinal chemistry due to their broad range of pharmacological properties. In Chapter 1, the pharmacological relevance and diverse biological activities of coumarin derivatives have been reviewed. Numerous studies have demonstrated their broad spectrum of activities, such as anticoagulant, antitumor, anti-inflammatory, antiviral, antioxidant, antimicrobial, and antibacterial properties. In oncology, coumarins and their derivatives have been extensively investigated for their potential to modulate key cellular processes in tumor development and progression. Several coumarins have been reported to induce cell cycle arrest at various checkpoints (G0, G1, S, and M phases). This ultimately leads to apoptosis (Govindaiah et al., 2019).

Similarly, 2,5-diketopiperazines (DKPs) represent another class of biologically active cyclic dipeptides known for their structural diversity and potent pharmacological activities, most notably anticancer properties.

Although numerous studies have explored the biological potential of DKP and coumarin scaffolds, no studies have reported the design or synthesis of hybrid molecules combining these two bioactive frameworks to explore their potential synergistic effects.

3.2. Present Work

In view of the structural diversity and pharmacological significance of both coumarin and DKP derivatives, the present study aims to develop novel hybrid molecules that integrate the coumarin core with the DKP scaffold, with the expectation that this molecular hybridization approach will enhance or produce positive synergistic properties, particularly anticancer activity.

In this context, this chapter presents the design, synthesis, and characterization of a new series of DKP-based coumarin analogues (Figure 3.1). In addition, *in vitro* anticancer evaluation assessed their cytotoxic activity against the human non-small cell lung cancer (A549) cell line. Molecular docking studies were also performed to gain insights into their possible mechanism of action by examining interactions with the β-tubulin binding site.

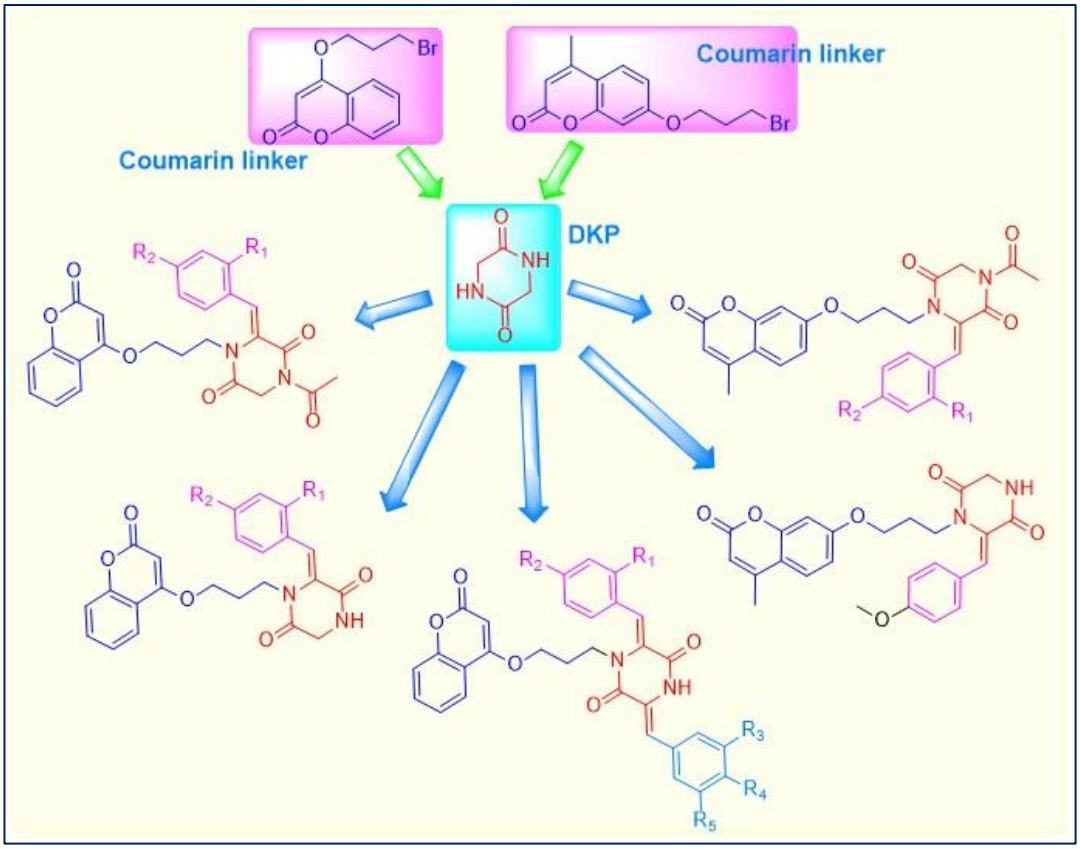

Figure 3.1. Schematic representation of the design strategy for DKP-based coumarin hybrids. Coumarin derivatives containing appropriate linkers were coupled with the central DKP scaffold to generate a series of novel hybrid molecules.

3.3. Materials and Methods

Unless otherwise specified, all chemicals and reagents were obtained from commercial suppliers and used as received, without further purification. Product characterization was performed using ^{1}H NMR, ^{13}C NMR, and High-Resolution Mass Spectrometry (HRMS). HRMS spectra were recorded on a SCIEX Model X500R

QTOF in positive-ion mode with internal calibration. NMR spectra were collected in DMSO-d_6 or $CDCl_3$ using a Bruker Avance spectrometer, operating at 500 or 600 MHz for ^1H NMR and 125 MHz for ^{13}C NMR, with tetramethylsilane (TMS) as the internal standard. Chemical shifts (δ) are reported in ppm relative to residual $CDCl_3$ (δ 7.26) and DMSO-d_6 (δ 2.50) for ^1H NMR, and $CDCl_3$ (δ 77.16) and DMSO-d_6 (δ 39.52) for ^{13}C NMR. Melting points were determined in open capillaries using a melting point apparatus and are uncorrected. Reaction progress was monitored by thin-layer chromatography (TLC) on Merck 60G F_{254} precoated aluminum plates, visualized under UV light or by staining with iodine vapors or with a potassium permanganate solution ($KMnO_4$, Na_2CO_3, deionized water). Flash chromatography separation was performed with silica gel (230–400 mesh). All solvents were of analytical grade. DMF was dried in CaH_2 and distilled.

3.3.1. Schemes for the Synthesis of Novel 2,5-Diketopiperazine-Based Coumarin Analogues

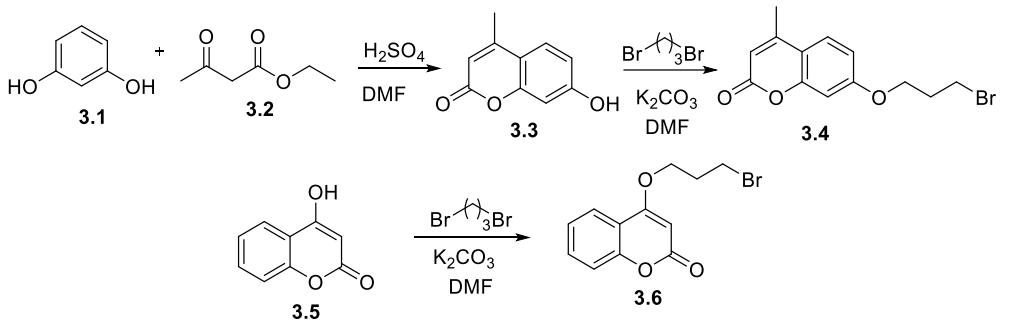

Scheme 3.1.

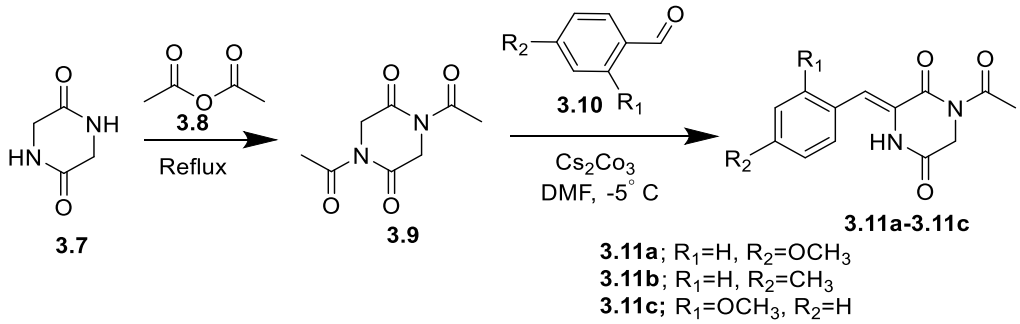

Scheme 3.2.

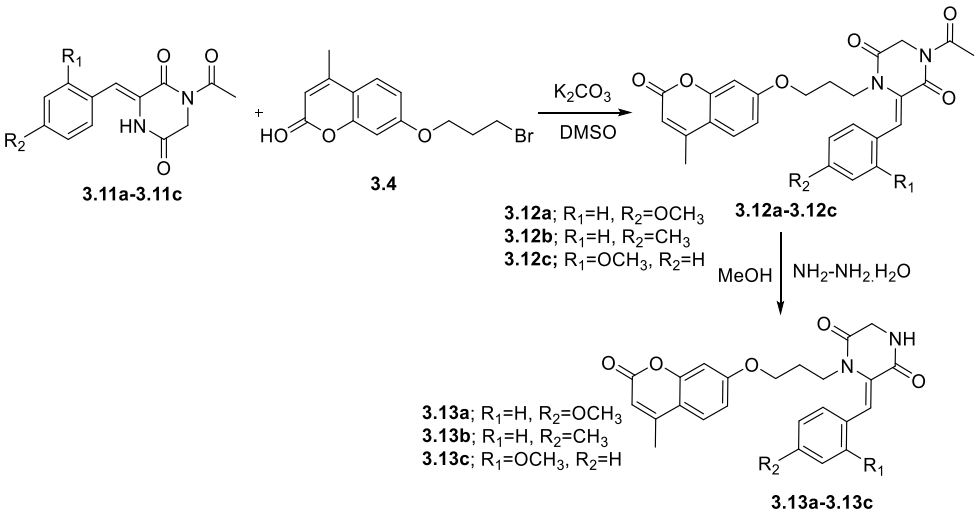

Scheme 3.3.

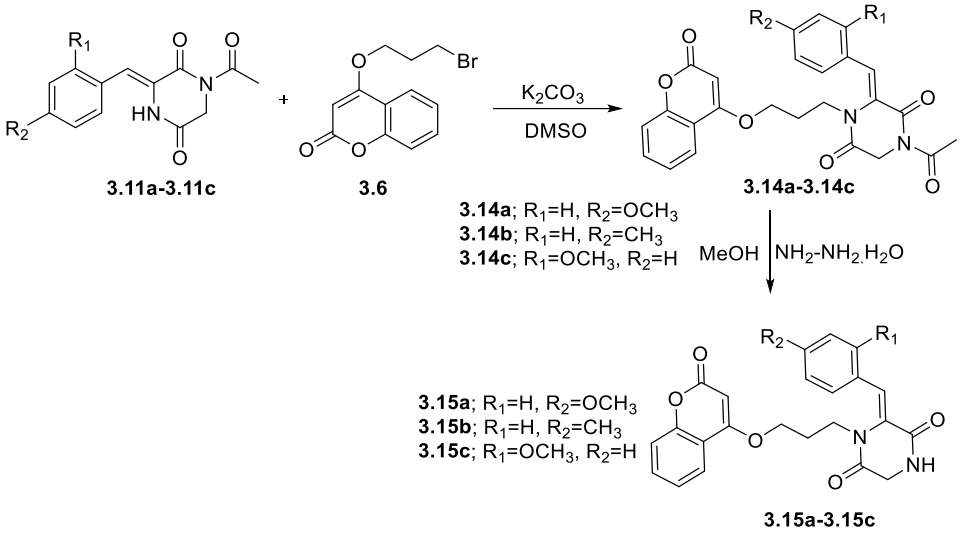

Scheme 3.4.

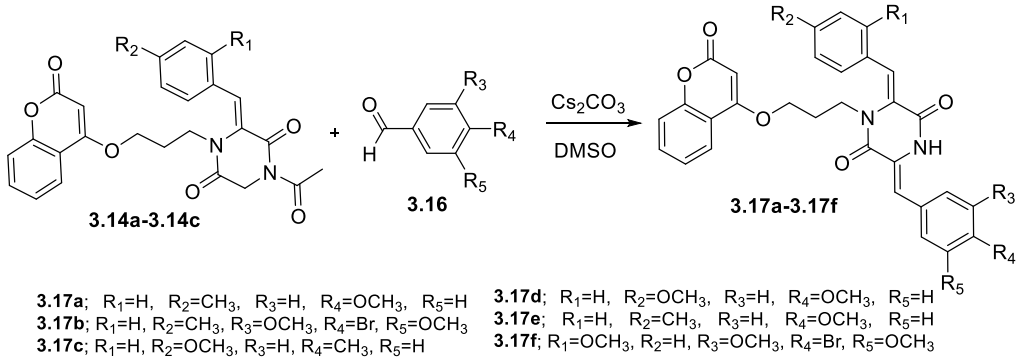

Scheme 3.5.

3.3.2. Procedure for the Synthesis of 7-Hydroxy-4-methyl-2H-chromen-2-one (3.3)

A 35 mL portion of concentrated H_2SO_4 was cooled to 0 °C in an ice bath. Resorcinol (**3.1**) (27.24 mmol) was pre-dissolved in ethyl acetoacetate (**2**) (32.69 mmol) by gentle heating. The resulting solution was slowly added to the cooled H_2SO_4 solution with stirring. The mixture was stirred at room temperature overnight. Upon completion, the mixture was carefully poured onto ice-cold water. The resulting precipitate was collected by filtration. The solid was washed thoroughly with water and recrystallized from ethanol to give the desired compound (**3.3**).

3.3.3. Procedure for the Synthesis of Compounds 3.4 and 3.6

To a stirred solution of 7-hydroxy-4-methyl-2H-chromen-2-one or 4-hydroxycoumarin (18.5 mmol) and anhydrous potassium carbonate (37 mmol) in 60 mL DMF was added aliphatic 1,3-dibromopropane (74 mmol). The reaction mixture was stirred at room temperature overnight. Upon completion of the reaction, as indicated by TLC, the mixture was poured into cold water and extracted with EtOAc (30 mL x 5). The organic layers were then combined, dried over anhydrous Na_2SO_4, and evaporated under reduced pressure using a rotary evaporator. The obtained crude product was purified by flash column chromatography over silica gel using hexane and EtOAc as the eluent to afford the desired compound.

3.3.4. Procedure for the Synthesis of 1,4-diacetylpiperazine-2,5-dione (3.9)

A mixture of glycine anhydride (**3.7**) (17.5 mmol) and acetic anhydride (**3.8**) (80 mL) was refluxed at 140°C for 18 hours. Upon completion, the excess acetic anhydride was removed under reduced pressure, and the crude solid was purified by flash column chromatography over silica gel using hexane and EtOAc as eluents to yield compound **3.9** as a light yellowish solid.

Light yellowish Solid; Yield: 96%; ^{1}H NMR (500 MHz, $CDCl_3$) δ 4.56 (s, 4H), 2.54 (s, 6H); 1^3C NMR (125 MHz, $CDCl_3$) δ 170.65, 165.83, 47.04, 26.58.

3.3.5. General procedure for the synthesis of compounds (3.11a-3.11c)

To a stirred solution of 1,4-diacetyl-2,5-diketopiperazine (**3.9**) (5 mmol) and aromatic aldehydes (12.6 mmol) in dry DMF (10 mL), Cs_2CO_3 (12.6 mmol) was added and stirred at room temperature overnight. The progress of the reaction was monitored

by TLC. After the reaction was complete, the mixture was poured into an iced-cold brine solution (30 mL), and the resulting precipitate was filtered. The solid was then recrystallised from ethanol to afford the desired compounds.

3.3.5.1. (Z)-1-acetyl-3-(4-methoxybenzylidene)piperazine-2,5-dione (3.11b)

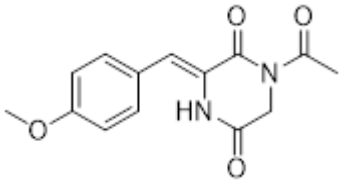

^{1}H NMR (500 MHz, $CDCl_3$) δ 7.84 (s, 1H), 7.36 (d, *J* = 8.1 Hz, 2H), 7.14 (s, 1H), 6.98 (d, *J* = 9.3 Hz, 2H), 4.52 (s, 2H), 3.86 (s, 3H), 2.65 (s, 3H); ^{13}C NMR (125 MHz, $CDCl_3$) δ 172.40, 163.05, 160.57, 130.48, 125.11, 124.44, 120.26, 115.07, 55.44, 46.06, 26.89; HRMS (ESI-TOF) m/z: calcd for $C_{14}H_{14}N_2O_4$, 274.0953, found 275.1010 $[M+H]^+$.

3.3.5.2. (Z)-1-acetyl-3-(4-methylbenzylidene)piperazine-2,5-dione (3.11b)

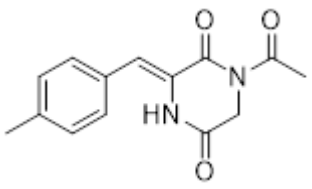

^{1}H NMR (500 MHz, $CDCl_3$) δ 7.88 (s, 1H), 7.33 – 7.26 (m, 4H), 7.16 (s, 1H), 4.52 (s, 2H), 2.65 (s, 3H), 2.40 (s, 3H); ^{13}C NMR (125 MHz, $CDCl_3$) δ 172.61, 162.90, 160.29, 139.94, 130.35, 129.73, 128.71, 125.17, 120.38, 46.18, 27.25, 21.50; HRMS (ES-TOF) m/z: calcd for $C_{14}H_{14}N_2O_3$, 258.1004 found 259.1067 $[M+H]^+$.

3.3.5.3. (Z)-1-acetyl-3-(2-methoxybenzylidene)piperazine-2,5-dione (3.11c)

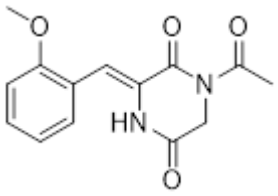

^{1}H NMR (500 MHz, $CDCl_3$) δ 8.44 (s, 1H), 7.39 (t, *J* = 8.0 Hz, 1H), 7.31 (d, *J* = 7.9 Hz, 1H), 7.17 (s, 1H), 7.07 – 7.00 (m, 2H), 4.48 (s, 2H), 3.95 (s, 3H), 2.66 (s, 3H); ^{13}C NMR (125 MHz, $CDCl_3$) δ 172.72, 162.59, 160.42, 156.42, 131.26, 131.21, 125.78, 121.74, 117.40, 112.17, 77.35, 77.10, 76.85, 56.12, 46.26, 27.27; HRMS (ESI-TOF) m/z: calcd for $C_{14}H_{14}N_2O_4$, 274.0953, found 275.1009 $[M+H]^+$.

3.3.6. General procedure for the synthesis of compounds (3.12a-3.12c)

To a stirred solution of compound **3.11** (1.82 mmol) and 7-(3-bromopropoxy)-4-methyl-2H-chromen-2-one (**3.4**) (2.7 mmol) in DMF (10 mL), anhydrous K_2CO_3 (3.7 mmol) was added. The reaction mixture was stirred overnight at room temperature. After the completion of the reaction, as indicated by TLC, the reaction mixture was poured into cold water, and the resulting precipitate was filtered. The solid

was then washed with a DMF-water mixture (4:1), followed by water and ethanol. The solid was then dried to obtain the pure product.

3.3.6.1. (Z)-1-acetyl-3-(4-methoxybenzylidene)-4-(3-((4-methyl-2-oxo-2H-chromen-7-yl)oxy)propyl)piperazine-2,5-dione (3.12a)

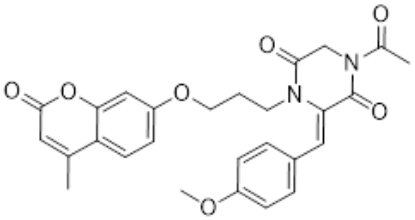

Yellowish Solid; Yield: 62%; White solid; Yield: 49%; M.p.: 70-71 ^{o}C; ^{1}H NMR (500 MHz, $CDCl_3$) δ 7.99 (d, *J* = 9.3 Hz, 2H), 7.48 (d, *J* = 9.2 Hz, 1H), 7.29 (s, 1H), 6.94 – 6.78 (m, 4H), 6.13 (s, 1H), 4.55 (t, *J* = 6.0 Hz, 2H), 4.45 (s, 2H), 4.19 (t, *J* = 6.0 Hz, 2H), 3.84 (s, 3H), 2.65 (s, 3H), 2.39 (s, 3H), 2.32 (p, *J* = 6.5, 2H). ^{13}C NMR (125 MHz, $CDCl_3$) δ 173.22, 162.51, 161.82, 161.24, 160.50, 158.78, 155.36, 152.51, 133.47, 129.56, 129.18, 127.78, 125.70, 114.02, 113.87, 112.49, 112.21, 101.63, 64.99, 63.59, 55.40, 43.68, 28.39, 27.43, 18.72. HRMS (ESI-TOF) m/z: calcd for $C_{27}H_{26}N_2O_7$, 490.1740, found 491.1785 $[M+H]^+$.

3.3.6.2. (Z)-1-acetyl-4-(3-((4-methyl-2-oxo-2H-chromen-7-yl)oxy)propyl)-3-(4-methylbenzylidene)piperazine-2,5-dione (3.12b)

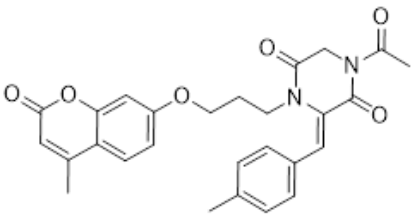

Light yellowish Solid; Yield: 69%; ^{1}H NMR (500 MHz, $CDCl_3$) δ 7.91 (d, *J* = 7.9 Hz, 2H), 7.48 (d, *J* = 8.1 Hz, 1H), 7.31 (s, 1H), 7.19 (d, *J* = 7.1 Hz, 2H), 6.87 – 6.80 (m, 2H), 6.13 (s, 1H), 4.55 (t, *J* = 6.0 Hz, 2H), 4.45 (s, 2H), 4.18 (t, *J* = 6.0 Hz, 2H), 2.66 (s, 3H), 2.39 (s, 3H), 2.37 (s, 3H), 2.31 (p, *J* = 6.4 Hz, 2H). ^{13}C NMR (125 MHz, $CDCl_3$) δ 173.31, 162.32, 161.89, 161.32, 160.59, 158.83, 155.42, 152.61, 133.53, 129.63, 129.26, 127.83, 125.78, 114.12, 113.93, 112.53, 111.89, 101.01, 64.40, 63.04, 43.05, 26.84, 20.98, 20.58, 18.11. HRMS (ESI-TOF) m/z: calcd for $C_{27}H_{26}N_2O_6$, 474.1790, found 475.1849 $[M+H]^+$.

3.3.6.3. (Z)-1-acetyl-3-(2-methoxybenzylidene)-4-(3-((4-methyl-2-oxo-2H-chromen-7-yl)oxy)propyl)piperazine-2,5-dione (3.12c)

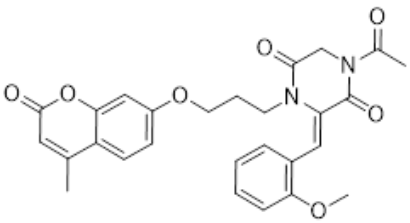

Light yellowish Solid; Yield: 67%; ^{1}H NMR (500 MHz, $CDCl_3$) δ 7.42 (d, *J* = 9.9 Hz, 2H), 7.38 (t, *J* = 7.9 Hz, 1H), 7.23 (d, *J* = 7.5 Hz, 1H), 7.01 – 6.92 (m, 2H), 6.70 – 6.60 (m, 2H), 6.12 (s, 1H), 4.49 (s, 2H), 3.85 (s, 3H), 3.80 (t, *J* = 5.4 Hz, 2H), 3.63 (t, *J* = 6.7 Hz, 2H), 2.58 (d, *J* = 7.7 Hz, 3H), 2.38 (s, 3H), 1.87 (p, *J* = 6.6, 6.0 Hz, 2H). ^{13}C NMR (125 MHz, $CDCl_3$) δ 171.43, 164.89, 164.28, 161.57, 161.20, 157.55, 155.15, 152.59, 131.49, 130.09, 129.92, 125.59, 122.15, 121.49, 120.61, 113.81, 112.25, 112.08, 110.99, 101.66, 65.76, 55.72, 45.37, 40.83, 26.77, 26.62, 18.68. HRMS (ESI-TOF) m/z: calcd for $C_{27}H_{26}N_2O_7$, 490.1740, found 491.1789 $[M+H]^+$.

3.3.7. General procedure for the synthesis of compounds (3.13a-3.13c)

Hydrazine hydrate (2 mmol) was added to a stirred solution of compound **3.12** (0.40 mmol) in methanol, and the reaction mixture was stirred at room temperature. Upon completion, as confirmed by TLC, cold water was added, and the resulting precipitate was filtered and washed successively with distilled water, a DMF-water mixture (4:1), water, and ethanol. The solid was dried to afford the pure product.

3.3.7.1. (Z)-6-(4-methoxybenzylidene)-1-(3-((4-methyl-2-oxo-2H-chromen-7-yl)oxy)propyl)piperazine-2,5-dione (3.13a)

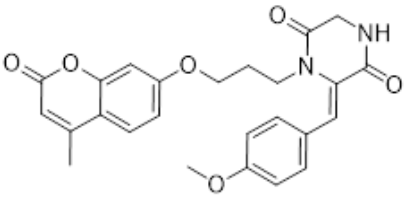

Yellowish Solid; Yield: 72%; ^{1}H NMR (500 MHz, $CDCl_3$) δ 7.95 (s, 2H), 7.47 (d, *J* = 9.3 Hz, 1H), 7.20 (s, 1H), 6.92 – 6.80 (m, 4H), 6.13 (s, 1H), 5.65 (s, 1H), 4.55 (t, *J* = 6.0 Hz, 2H), 4.21 (s, 2H), 4.19 (t, *J* = 6.0 Hz, 2H), 3.82 (s, 3H), 2.38 (s, 3H), 2.31 (p, *J* = 6.4 Hz, 2H). ^{13}C NMR (125 MHz, $CDCl_3$) δ 162.53, 161.85, 161.26, 160.53, 158.79, 155.39, 152.56, 133.50, 129.59, 129.20, 127.81, 125.74, 114.11, 113.89, 112.53, 112.26, 101.69, 64.83, 63.59, 55.41, 43.68, 28.43, 18.81. HRMS (ESI-TOF) m/z: calcd for $C_{25}H_{24}N_2O_6$, 448.1634, found 449.1693 $[M+H]^+$.

3.3.7.2. (Z)-1-(3-((4-methyl-2-oxo-2H-chromen-7-yl)oxy)propyl)-6-(4-methylbenzylidene)piperazine-2,5-dione (3.13b)

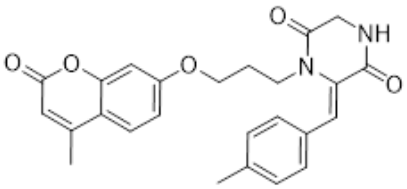

Yellowish Solid; Yield: 66%; ^{1}H NMR (500 MHz, $CDCl_3$) δ 7.90 (d, *J* = 8.0 Hz, 2H), 7.48 (d, *J* = 8.2 Hz, 1H), 7.23 – 7.13 (m, 3H), 6.90 – 6.78 (m, 2H), 6.14 (s, 1H), 5.80 (s, 1H), 4.54 (t, *J* = 6.0 Hz, 2H), 4.23 (s, 2H), 4.17 (t, *J* = 6.1 Hz, 2H), 2.39 (s, 3H), 2.36 (s, 3H), 2.31 (p, *J* = 6.1 Hz, 2H). ^{13}C NMR (125 MHz, $CDCl_3$) δ 162.33, 161.91, 161.33, 160.60, 158.84, 155.43, 152.62, 133.54, 129.65, 129.27, 127.84, 125.79, 114.13, 113.94, 112.55, 111.91, 101.07, 64.46, 63.11, 43.12, 26.89, 20.99, 20.61. HRMS (ESI-TOF) m/z: calcd for $C_{25}H_{24}N_2O_5$, 432.1685, found 433.1753 $[M+H]^+$.

3.3.7.3. (Z)-6-(2-methoxybenzylidene)-1-(3-((4-methyl-2-oxo-2H-chromen-7-yl) oxy)propyl)piperazine-2,5-dione (3.13c)

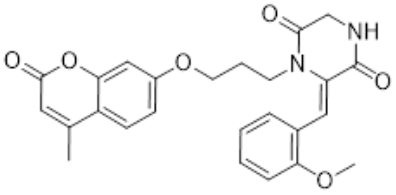

Yellowish Solid; Yield: 70%; ^{1}H NMR (500 MHz, $CDCl_3$) δ 7.94 (s, 2H), 7.46 (d, *J* = 9.3 Hz, 1H), 7.21 (s, 1H), 6.93 – 6.81 (m, 4H), 6.12 (s, 1H), 5.64 (s, 1H), 4.54 (t, *J* = 6.0 Hz, 2H), 4.20 (s, 2H), 4.18 (t, *J* = 6.0 Hz, 2H), 3.75 (s, 3H), 2.39 (s, 3H), 2.33 (p, *J* = 6.4 Hz, 2H). ^{13}C NMR (125 MHz, $CDCl_3$) δ 164.87, 164.26, 161.54, 161.17, 157.51, 155.12, 152.56, 131.45, 130.03, 129.90, 125.55, 122.11, 121.45, 120.58, 113.76, 112.21, 112.02, 110.93, 101.62, 65.72, 55.65, 45.33, 40.80, 26.72, 18.63. HRMS (ESI-TOF) m/z: calcd for $C_{25}H_{24}N_2O_6$, 448.1634, found 449.1922 $[M+H]^+$.

3.3.8. General procedure for the synthesis of compounds (3.14a-3.14c)

To a stirred solution of compound **3.11** (1.82 mmol) and 4-(3-bromopropoxy)-2H-chromen-2-one (**3.6**) (2.7 mmol) in DMF (10 mL), anhydrous K_2CO_3 (3.7 mmol) was added. The reaction mixture was stirred overnight at room temperature. After the completion of the reaction, as indicated by TLC, the reaction mixture was poured into cold water, and the resulting precipitate was filtered. The solid was then washed with a DMF-water mixture (4:1), followed by water and ethanol. The solid was then dried to obtain the pure product.

3.3.8.1. (Z)-1-acetyl-3-(4-methoxybenzylidene)-4-(3-((2-oxo-2H-chromen-4-yl)

oxy)propyl)piperazine-2,5-dione (3.14a)

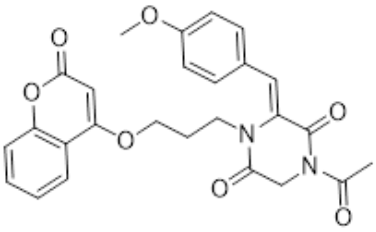

Light yellowish Solid; Yield: 61%; ^{1}H NMR (500 MHz, $CDCl_3$) δ 7.98 (d, *J* = 8.2 Hz, 2H), 7.80 (d, *J* = 8.0 Hz, 1H), 7.53 (t, *J* = 7.9 Hz, 1H), 7.35 – 7.29 (m, 2H), 7.24 – 7.20 (m, 1H), 6.89 (d, *J* = 9.3 Hz, 2H), 5.70 (s, 1H), 4.59 (t, *J* = 6.5 Hz, 2H), 4.46 (s, 2H), 4.31 (t, *J* = 6.2 Hz, 2H), 3.81 (s, 3H), 2.65 (s, 3H), 2.42 (p, *J* = 6.0 Hz, 2H). ^{13}C NMR (125 MHz, $CDCl_3$) δ 171.75, 164.42, 161.45, 159.35, 158.01, 152.29, 132.32, 131.61, 128.74, 127.54, 126.69, 123.09, 122.07, 115.64, 114.66, 113.04, 89.77, 65.22, 62.43, 54.36, 42.65, 26.88, 26.40. HRMS (ESI-TOF) m/z: calcd for $C_{26}H_{24}N_2O_7$, 476.1583, found 477.1637 $[M+H]^+$.

3.3.8.2. (Z)-1-acetyl-3-(4-methylbenzylidene)-4-(3-((2-oxo-2H-chromen-4-yl)oxy) propyl)piperazine-2,5-dione (3.14b)

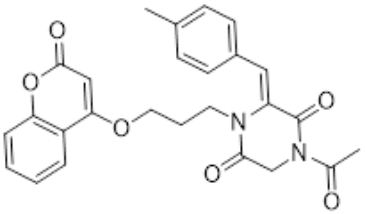

Yellowish Solid; Yield: 66%; ^{1}H NMR (500 MHz, $CDCl_3$) δ 7.90 (d, *J* = 7.9 Hz, 2H), 7.80 (d, *J* = 7.6 Hz, 1H), 7.56 – 7.51 (m, 1H), 7.32 (t, *J* = 4.0 Hz, 2H), 7.22 (t, *J* = 7.5 Hz, 1H), 7.17 (d, *J* = 8.0 Hz, 2H), 5.69 (s, 1H), 4.59 (t, *J* = 6.0 Hz, 2H), 4.46 (s, 2H), 4.30 (t, *J* = 6.0 Hz, 2H), 2.65 (s, 3H), 2.42 (p, *J* = 6.0, 5.5 Hz, 2H), 2.35 (s, 3H).^{13}C NMR (125 MHz, $CDCl_3$) δ 173.13, 165.39, 162.74, 162.33, 159.02, 153.45, 139.64, 132.58, 132.11, 131.67, 130.64, 129.49, 129.27, 124.01, 122.93, 116.93, 115.64, 90.87, 65.98, 63.45, 43.65, 27.96, 27.43, 21.57. HRMS (ESI-TOF) m/z: calcd for $C_{26}H_{24}N_2O_6$, 460.1634, found 461.1701 $[M+H]^+$.

3.3.8.3. (Z)-1-acetyl-3-(2-methoxybenzylidene)-4-(3-((2-oxo-2H-chromen-4-yl) oxy)propyl)piperazine-2,5-dione (3.14c)

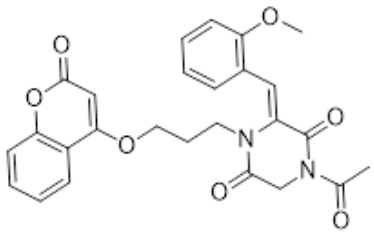

Yellowish Solid; Yield: 70%; ^{1}H NMR (500 MHz, $CDCl_3$) δ 8.41 (d, *J* = 7.9 Hz, 1H), 7.84 (s, 1H), 7.78 (d, *J* = 7.9 Hz, 1H), 7.53 (t, *J* = 8.0 Hz, 1H), 7.34 – 7.27 (m, 2H), 7.25 – 7.20 (m, 1H), 6.95 – 6.88 (m, 2H), 5.67 (s, 1H), 4.56 (t, *J* = 6.0 Hz, 2H), 4.45 (s,

2H), 4.29 (t, *J* = 6.4 Hz, 2H), 3.89 (d, *J* = 10.9 Hz, 3H), 2.67 (s, 3H), 2.39 (p, *J* = 6.5 Hz, 2H).^{13}C NMR (125 MHz, $CDCl_3$) δ 176.23, 165.29, 164.83, 163.36, 161.43, 157.09, 154.21, 137.21, 133.05, 132.53, 130.70, 126.12, 124.56, 124.29, 123.30, 122.58, 116.94, 116.08, 114.46, 91.50, 67.52, 55.40, 45.63, 42.19, 27.24, 26.59. HRMS (ESI-TOF) m/z: calcd for $C_{26}H_{24}N_2O_7$, 476.1583, found 476.1638 $[M+H]^+$.

3.3.9. General procedure for the synthesis of compounds (3.15a-3.15c)

Hydrazine hydrate (2 mmol) was added to a stirred solution of compound **3.14** (0.40 mmol) in methanol, and the reaction mixture was stirred at room temperature. Upon completion, as confirmed by TLC, cold water was added, and the resulting precipitate was filtered and washed successively with distilled water, a DMF-water mixture (4:1), water, and ethanol. The solid was dried to afford the pure product.

3.3.9.1. (Z)-6-(4-methoxybenzylidene)-1-(3-((2-oxo-2H-chromen-4-yl)oxy)propyl)piperazine-2,5-dione (3.15a)

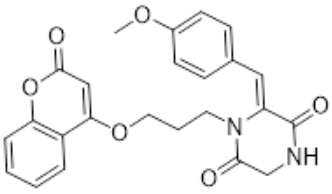

Yellowish Solid; Yield: 64%; ^{1}H NMR (500 MHz, $CDCl_3$) δ 7.70 (d, *J* = 8.0 Hz, 2H), 7.81 (d, *J* = 6.7 Hz, 1H), 7.58 – 7.51 (m, 1H), 7.33 (d, *J* = 8.0 Hz, 1H), 7.24 – 7.20 (m, 2H), 7.15 (d, *J* = 7.9 Hz, 2H), 5.77 (s, 1H), 5.70 (s, 1H), 4.58 (t, *J* = 6.1 Hz, 2H), 4.31 (t, *J* = 6.2 Hz, 2H), 4.24 (s, 2H), 3.85 (s, 3H), 2.42 (p, *J* = 6.7 Hz, 2H). ^{13}C NMR (125 MHz, $CDCl_3$) δ 163.41, 160.06, 157.70, 151.47, 146.77, 145.56, 130.85, 130.73, 128.11, 126.50, 122.29, 122.02, 121.30, 114.77, 112.18, 89.13, 64.85, 61.45, 53.50, 40.70, 26.09. HRMS (ESI-TOF) m/z: calcd for $C_{24}H_{22}N_2O_6$, 434.1477, found 435.1487 $[M+H]^+$.

3.3.9.2. (Z)-6-(4-methylbenzylidene)-1-(3-((2-oxo-2H-chromen-4-yl)oxy)propyl) piperazine-2,5-dione (3.15b)

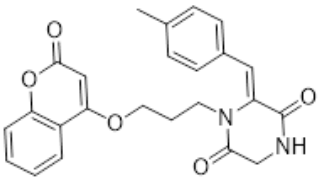

Yellowish Solid; Yield: 63%; ^{1}H NMR (500 MHz, $CDCl_3$) δ 7.89 (d, *J* = 8.0 Hz, 2H), 7.80 (d, *J* = 6.8 Hz, 1H), 7.57 – 7.50 (m, 1H), 7.32 (d, *J* = 8.1 Hz, 1H), 7.24 – 7.20 (m, 2H), 7.15 (d, *J* = 7.9 Hz, 2H), 5.77 (s, 1H), 5.70 (s, 1H), 4.58 (t, *J* = 6.1 Hz, 2H), 4.30 (t, *J* = 6.1 Hz, 2H), 4.23 (s, 2H), 2.41 (p, *J* = 6.7 Hz, 2H), 2.34 (s, 3H). ^{13}C NMR (125 MHz, $CDCl_3$) δ 165.46, 162.76, 162.17, 158.29, 153.36,

138.50, 132.54, 132.42, 131.18, 130.99, 129.71, 129.04, 128.85, 126.06, 124.02, 122.97, 116.80, 115.60, 90.72, 77.50, 77.25, 76.99, 66.01, 63.10, 42.77, 27.88, 21.42. HRMS (ESI-TOF) m/z: calcd for $C_{24}H_{22}N_2O_5$, 418.1528, found 419.1594 $[M+H]^+$.

3.3.9.3. (Z)-6-(2-methoxybenzylidene)-1-(3-((2-oxo-2H-chromen-4-yl)oxy)propyl)piperazine-2,5-dione (3.15c)

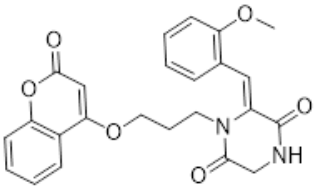

Light yellowish Solid; Yield: 59%; ^{1}H NMR (500 MHz, $CDCl_3$) δ 8.29 (d, *J* = 7.8 Hz, 1H), 7.69 (d, *J* = 8.0 Hz, 1H), 7.57 (s, 1H), 7.44 (t, *J* = 7.4 Hz, 1H), 7.23 – 7.10 (m, 3H), 6.80 (t, *J* = 8.0 Hz, 2H), 6.64 (s, 1H), 5.58 (s, 1H), 4.45 (t, *J* = 6.0 Hz, 2H), 4.19 (t, *J* = 6.0 Hz, 2H), 4.09 (s, 2H), 3.76 (s, 3H), 2.28 (p, *J* = 6.1, 5.6 Hz, 2H). ^{13}C NMR (125 MHz, CDCl3) δ 165.94, 164.83, 163.36, 158.39, 157.00, 154.21, 139.94, 133.05, 132.53, 130.64, 124.96, 124.56, 123.28, 122.58, 121.56, 116.94, 116.08, 114.46, 91.50, 67.52, 55.40, 43.45, 42.21, 27.24. HRMS (ESI-TOF) m/z: calcd for $C_{24}H_{22}N_2O_6$, 434.1477, found 435.1527 $[M+H]^+$.

3.3.10. General procedure for the synthesis of compounds (3.17a-3.17f)

Compound **3.14** (0.20 mmol) was dissolved in dry DMSO (5 mL), and substituted aldehyde (0.31 mmol) was added, followed by Cs_2CO_3 (0.31 mmol). The reaction mixture was stirred at 40 °C for approximately 5 h. Upon completion, as monitored by TLC, the mixture was poured into ice-cold brine, and the resulting solid was filtered, washed with water, and recrystallized from ethanol or EtOAc to afford the pure product.

3.3.10.1. 3-((Z)-4-methoxybenzylidene)-6-((Z)-4-methylbenzylidene)-1-(3-((2-oxo-2H-chromen-4-yl)oxy)propyl)piperazine-2,5-dione (3.17a)

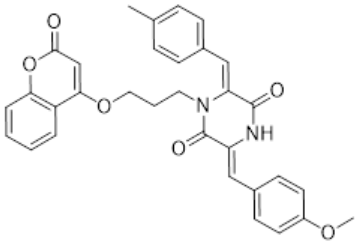

Yellowish Solid; Yield: 68%; ^{1}H NMR (500 MHz, $CDCl_3$) δ 8.26 (s, 1H), 7.98 (d, *J* = 8.2 Hz, 2H), 7.83 (d, *J* = 8.0 Hz, 1H), 7.52 (t, *J* = 8.0 Hz, 1H), 7.35 – 7.26 (m, 4H), 7.21 – 7.15 (m, 3H), 7.04 – 6.94 (m, 2H), 6.56 (s, 1H), 5.73 (s, 1H), 4.68 (t, *J* = 6.0 Hz, 2H), 4.38 (t, *J* = 6.0 Hz, 2H), 3.91 (s, 3H), 2.52 (p, *J* = 5.8 Hz, 2H), 2.36 (s, 3H). ^{13}C NMR (125 MHz, $CDCl_3$) δ 164.83, 163.36, 161.01, 160.31, 155.41, 154.21, 140.70, 138.32, 132.91,

132.53, 131.67, 129.77, 129.35, 127.24, 126.34, 124.56, 123.70, 122.58, 121.91, 116.94, 116.08, 113.94, 91.50, 67.51, 55.35, 42.21, 26.95, 21.41. HRMS (ESI-TOF) m/z: calcd for $C_{32}H_{28}N_2O_6$, 536.1947, found 537.2589 $[M+H]^+$.

3.3.10.2. 3-((Z)-4-bromo-3,5-dimethoxybenzylidene)-6-((Z)-4-methylbenzylidene)-1-(3-((2-oxo-2H-chromen-4-yl)oxy)propyl)piperazine-2,5-dione (3.17b)

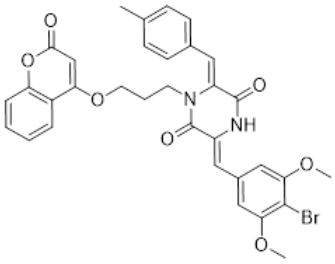

Yellowish Solid; Yield: 66%; ^{1}H NMR (500 MHz, $CDCl_3$) δ 7.98 (d, *J* = 7.9 Hz, 3H), 7.83 (d, *J* = 7.9 Hz, 1H), 7.54 (t, *J* = 7.9 Hz, 1H), 7.32 (t, *J* = 4.5 Hz, 2H), 7.23 – 7.17 (m, 3H), 6.52 (s, 2H), 6.47 (s, 1H), 5.75 (s, 1H), 4.69 (t, *J* = 6.1 Hz, 2H), 4.39 (t, *J* = 6.1 Hz, 2H), 3.92 (s, 6H), 2.53 (p, *J* = 6.3 Hz, 2H), 2.37 (s, 3H). ^{13}C NMR (125 MHz, $CDCl_3$) δ 165.50, 162.83, 160.07, 157.91, 153.46, 152.88, 139.79, 133.32, 132.62, 132.22, 131.86, 130.50, 129.71, 129.32, 125.02, 124.05, 122.99, 116.97, 115.64, 110.03, 104.68, 101.47, 90.90, 66.27, 63.68, 56.75, 28.03, 21.62. HRMS (ESI-TOF) m/z: calcd for $C_{33}H_{29}BrN_2O_7$, 644.1158, found 645.1937 $[M+H]^+$.

3.3.10.3. 6-((Z)-4-methoxybenzylidene)-3-((Z)-4-methylbenzylidene)-1-(3-((2-oxo-2H-chromen-4-yl)oxy)propyl)piperazine-2,5-dione (3.17c)

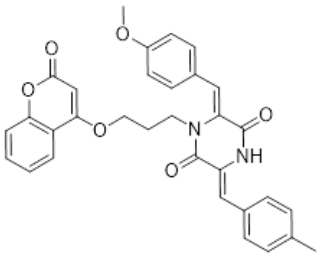

Yellowish Solid; Yield: 67%; ^{1}H NMR (500 MHz, $CDCl_3$) δ 8.09 (d, *J* = 8.2 Hz, 2H), 8.04 (s, 1H), 7.86 (d, *J* = 7.8 Hz, 1H), 7.56 (t, *J* = 7.9 Hz, 1H), 7.38 – 7.27 (m, 4H), 7.26 – 7.20 (m, 3H), 6.94 (d, *J* = 9.2 Hz, 2H), 6.53 (s, 1H), 5.78 (s, 1H), 4.71 (t, *J* = 6.0 Hz, 2H), 4.41 (t, *J* = 6.0 Hz, 2H), 3.85 (s, 3H), 2.55 (p, *J* = 6.4, 2H), 2.41 (s, 3H). ^{13}C NMR (125 MHz, $CDCl_3$) δ 165.56, 162.86, 160.00, 156.59, 153.45, 139.38, 132.54, 132.50, 131.70, 131.02, 130.33, 130.28, 129.25, 128.79, 124.30, 124.01, 123.05, 122.08, 121.47, 116.89, 115.70, 111.79, 107.59, 90.83, 66.38, 63.53, 55.91, 28.06, 21.59. HRMS (ESI-TOF) m/z: calcd for $C_{32}H_{28}N_2O_6$, 536.1947, found 537.2606 $[M+H]^+$.

3.3.10.4. 3,6-bis((Z)-4-methoxybenzylidene)-1-(3-((2-oxo-2H-chromen-4-yl)oxy)propyl)piperazine-2,5-dione (3.17d)

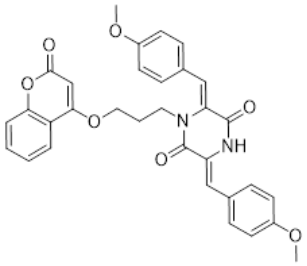

Yellowish Solid; Yield: 65%; ^{1}H NMR (500 MHz, $CDCl_3$) δ 8.25 (s, 1H), 8.07 (d, *J* = 8.1 Hz, 2H), 7.84 (d, *J* = 7.7 Hz, 1H), 7.52 (t, *J* = 7.9 Hz, 1H), 7.36 – 7.27 (m, 4H), 7.20 (t, *J* = 7.9 Hz, 1H), 7.06 – 6.88 (m, 4H), 6.55 (s, 1H), 5.74 (s, 1H), 4.69 (t, *J* = 6.4 Hz, 2H), 4.39 (t, *J* = 6.0 Hz, 2H), 3.91 (s, 3H), 3.83 (s, 3H), 2.53 (p, *J* = 6.0, 5.5 Hz, 2H). ^{13}C NMR (125 MHz, $CDCl_3$) δ 165.48, 160.05, 156.50, 153.07, 133.35, 132.47, 130.21, 130.12, 128.53, 124.31, 123.95, 122.96, 121.38, 116.83, 115.15, 113.93, 111.70, 107.12, 90.75, 66.30, 63.36, 55.83, 55.31, 27.99. HRMS (ESI-TOF) m/z: calcd for $C_{32}H_{28}N_2O_7$, 552.1896, found 553.2559 $[M+H]^+$.

3.3.10.5. 3-((Z)-4-bromo-3,5-dimethoxybenzylidene)-6-((Z)-2-methoxybenzylidene)-1-(3-((2-oxo-2H-chromen-4-yl)oxy)propyl)piperazine-2,5-dione (3.17e)

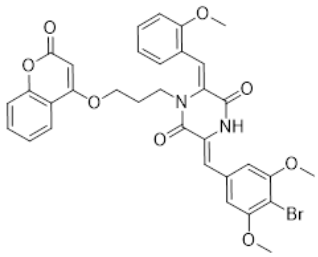

Light yellowish Solid; Yield: 59%; ^{1}H NMR (500 MHz, $CDCl_3$) δ 8.39 (s, 1H), 7.89 (d, *J* = 9.0 Hz, 2H), 7.67 (d, *J* = 8.0 Hz, 1H), 7.37 (t, *J* = 7.9 Hz, 1H), 7.13 (d, *J* = 8.6 Hz, 1H), 7.08 (s, 1H), 7.04 (t, *J* = 7.4 Hz, 1H), 6.75 (d, *J* = 8.1 Hz, 2H), 6.39 (s, 2H), 6.30 (s, 1H), 5.60 (s, 1H), 4.52 (t, *J* = 6.0 Hz, 2H), 4.25 (t, *J* = 6.2 Hz, 2H), 3.75 (s, 6H), 3.66 (s, 3H), 2.37 (p, *J* = 5.9 Hz, 2H). ^{13}C NMR (125 MHz, $CDCl_3$) δ 165.40, 162.56, 160.54, 160.09, 153.07, 138.67, 133.40, 132.46, 130.29, 130.20, 129.75, 128.72, 128.31, 128.11, 124.18, 123.93, 122.95, 116.89, 115.75, 114.06, 110.31, 90.91, 66.39, 63.54, 55.32, 28.17, 21.27. HRMS (ESI-TOF) m/z: calcd for $C_{33}H_{29}BrN_2O_8$, 660.1107, found 661.1918 $[M+H]^+$.

3.3.10.6. 3-((Z)-4-chlorobenzylidene)-6-((Z)-4-methoxybenzylidene)-1-(3-((2-oxo-2H-chromen-4-yl)oxy)propyl)piperazine-2,5-dione (3.17f)

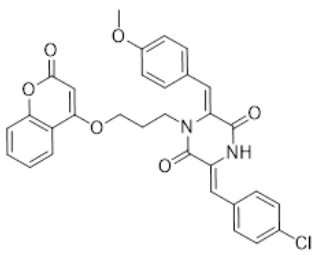

Yellowish Solid; Yield: 70%; ^{1}H NMR (500 MHz, $CDCl_3$) δ 8.11 (d, *J* = 8.2 Hz, 2H), 8.08 (s, 1H), 7.89 (d, *J* = 7.8 Hz, 1H), 7.58 (t, *J* = 7.9 Hz, 1H), 7.39 – 7.28 (m, 4H), 7.27 – 7.21 (m, 3H), 6.95 (d, *J* = 9.2 Hz, 2H), 6.53

(s, 1H), 5.78 (s, 1H), 4.75 (t, *J* = 6.0 Hz, 2H), 4.46 (t, *J* = 6.0 Hz, 2H), 3.86 (s, 3H), 2.56 (p, *J* = 6.4, 2H). ^{13}C NMR (125 MHz, $CDCl_3$) δ 165.42, 162.72, 160.02, 156.41, 153.32, 139.30, 132.43, 132.41, 131.63, 130.96, 130.20, 130.05, 129.16, 128.61, 124.21, 124.02, 123.03, 122.01, 121.34, 116.89, 115.70, 111.79, 107.59, 90.81, 66.27, 63.46, 55.85, 28.01. HRMS (ESI-TOF) m/z: calcd for $C_{31}H_{25}ClN_2O_6$, 556.1401, found 557.1468 $[M+H]^+$.

3.3.11. Materials and Methods for Biological Experiments

3.3.11.1. Reagents and chemicals for cell-based experiments

RPMI-1640 culture media, fetal bovine serum (FBS), 0.25% Trypsin-EDTA solution, MTT dye, and antibiotic-antimitotic reagents (100×) were bought from GIBCO (Grand Island, NY, USA). DMSO was bought from Merck (St. Louis, MO, USA).

3.3.11.2. Mammalian cell culture

The A549 cell line (human non-small cell lung cancer) was procured from ATCC (Manassas, VA, USA). All cells were cultured in RPMI-1640 medium containing 10% FBS and 1% antibiotics (penicillin and streptomycin, P/S). The cells were maintained in a humidified CO_2 incubator with 5% CO_2, and periodic observations and medium changes were performed. For providing the serum-starvation conditions, cells were cultured in RPMI-1640 containing 1% FBS and 1% P/S.

3.3.11.3. MTT assay

A549 cells (~8000 per well) were seeded into 96-well plates and allowed to attach. Further, cells were starved for 24 h, then treated with different concentrations (5, 10, 20, 40, and 80 μM) of the compounds, and incubated for 24 h in a CO_2 incubator. At the end of the incubation periods, the media in each well were aspirated and replaced with 50 μl of 5 mg/ml MTT solution prepared in 1 × PBS. The plates were returned to the CO_2 incubator and incubated for an additional 4 h. Purple formazan crystals, formed at the end of incubation, were dissolved by adding 100 μl

DMSO after removing MTT solution and subjected to spectrophotometric analysis at 570 nm using a Synergy 1 hybrid reader by BioTek (Winooski, VT, USA).

3.3.12. Molecular docking

The crystal structures of β-tubulin (PDB id: 5YL4) were retrieved from the Protein Data Bank (www.rcsb.org) in PDB format. Prior to docking, the protein structure was refined by removing co-crystallized ligands, cofactors, and water molecules. Missing residues were modelled, and polar hydrogens were added to complete the structures. The binding pocket coordinates for β-tubulin were defined based on the native ligand, centered at x = -15.868, y = -64.554, z = 35.133, with grid box dimensions of 20 Å × 20 Å × 30 Å. Docking simulation was carried out using AutoDock Vina with the exhaustiveness parameter set to 20. The docking results were visualized with PyMOL, UCSF Chimera, and Discovery Studio. The docking protocol was validated by redocking the native ligands and comparing the predicted binding orientations with the crystallographic conformations through structural superimposition.

3.3.13. ADMET Evaluation

The pkCSM server (https://biosig.lab.uq.edu.au/pkcsm) (Pires et. al., 2015) was employed to predict the ADMET (Absorption, Distribution, Metabolism, Excretion, and Toxicity) properties of the synthesized compounds. The following pharmacokinetic parameters were analyzed: absorption (Caco-2 permeability, human intestinal absorption, and P-glycoprotein substrate status), distribution (blood–brain barrier (BBB) and central nervous system (CNS) permeability), metabolism (CYP3A4 and CYP2D6 substrate potential; CYP2C19, CYP2C9, CYP2D6, and CYP3A4 inhibition), excretion (total clearance), and toxicity (AMES mutagenicity, maximum tolerated dose in humans, hERG I inhibition, and hepatotoxicity).

3.3.14. Statistical Analysis

Experimental results were expressed as mean ± standard error of the mean (SEM). Data were analyzed using one-way analysis of variance (ANOVA), followed

by Tukey's post hoc test. All statistical analyses were performed using SPSS (ver. 16.0) and OriginPro 25.

3.4. Results and Discussion

3.4.1. Synthesis and Characterization of the Compounds

A series of novel DKP-based coumarin derivatives was synthesized through multi-step procedures, as illustrated in Schemes 3.1–3.5. In Scheme 3.1, the synthesis began with the commercially available compound resorcinol (**3.1**) and ethyl acetoacetate (**3.2**), which undergoes a cyclization reaction to give compound **3.3**. Compounds **3.3** and **3.5** were then subjected to a nucleophilic substitution reaction with an excess of linear aliphatic dibromoalkanes in the presence of anhydrous K_2CO_3 in DMF at room temperature to give compounds **3.4** and **3.6**.

In Scheme 3.2, glycine anhydride (**3.7**) was acetyl-protected using excess acetic anhydride to obtain intermediate compound **3.9**. Compound **3.9** was then subjected to an aldol condensation with various aromatic aldehydes in dry DMF using Cs_2CO_3 at -5 °C, to afford intermediates **3.11a**-**3.11c**. These intermediates were then reacted with compounds **3.4** and **3.6** in the presence of anhydrous K_2CO_3 to afford compounds **3.12a**-**3.12c** and **3.14a**-**3.14c** (Schemes 3.3 & 3.4) (Figure 3.2). Thereafter, compounds **3.12a**-**3.12c** and **3.14a**-**3.14c** are deacetylated using hydrazine hydrate in methanol at room temperature to afford compounds **3.13a**-**3.13c** and **3.15a**-**3.15b** (Scheme 3.3 & 3.4). The aldol condensation of compounds **3.14a**-**3.14c** was again carried out with various aromatic aldehydes in dry DMSO using Cs_2CO_3 under inert conditions at 40 °C to obtain compound **3.17a**-**3.17f** series (Scheme 3.5) (Figure 3.2).

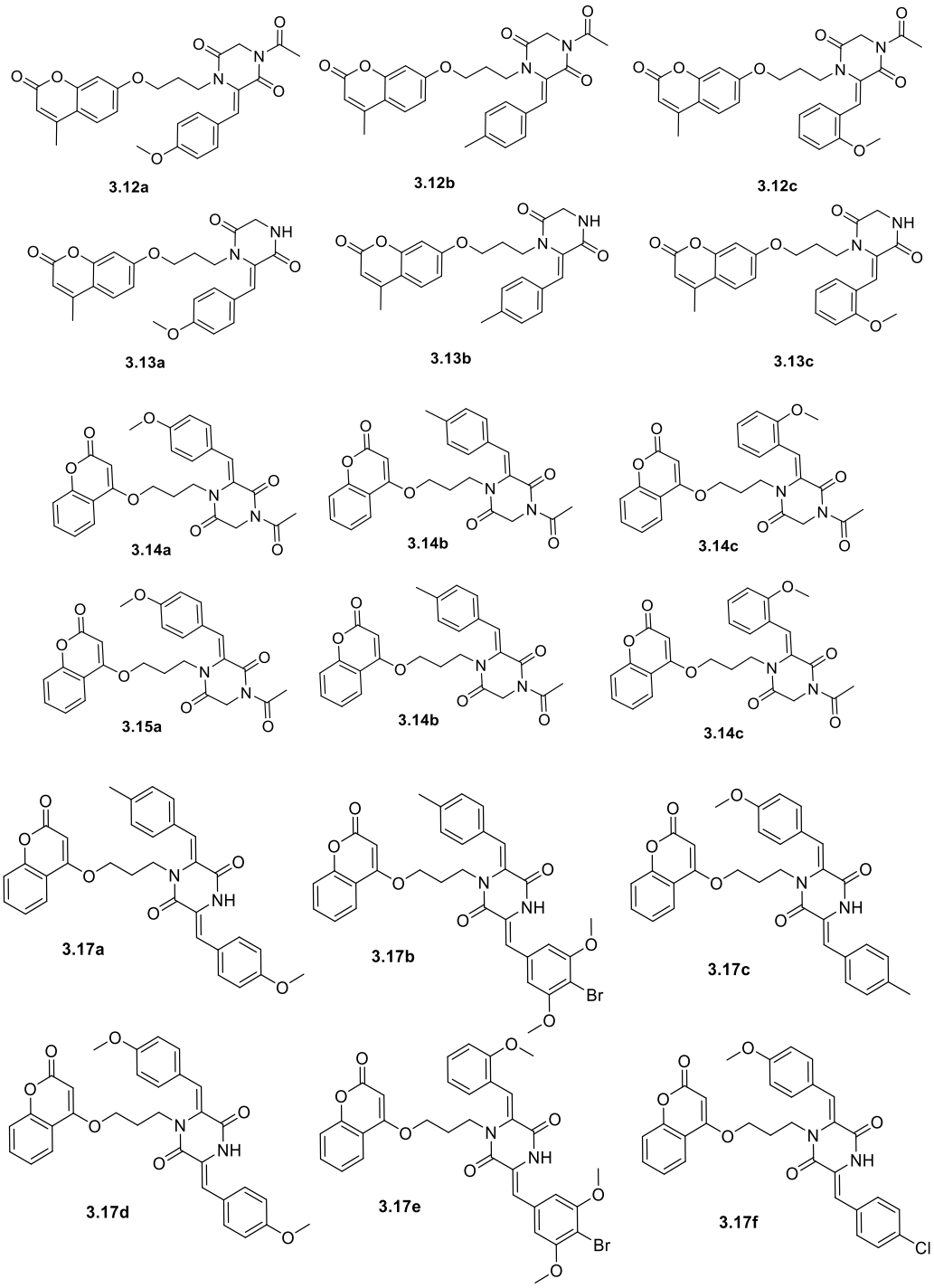

Figure 3.2. Chemical structures of novel DKP-based coumarin derivatives.

The NMR spectra (^{1}H NMR and ^{13}C NMR) of one of the final DKP-based coumarin derivatives, **3.12a**, recorded in $CDCl_3$, were selected to illustrate the characteristic chemical shifts and are shown in Figure 3.3. In the ^{1}H NMR spectrum, a pentet at δ 2.32 ppm of two protons and a triplet at δ 4.19 ppm and δ 4.55 ppm of

two protons each correspond to the propylene linker. The singlet peak at δ2.39 ppm of three protons corresponds to the methyl of the acetyl group. The singlet peaks at δ 2.65 ppm and δ 3.84 ppm, each corresponding to three protons, are assigned to the methyl and methoxy protons, respectively. Another singlet peak at δ 4.45 of two protons represents the methylene protons of the piperazine ring. The vinylic proton of the coumarin ring appears as a singlet at δ 6.13 ppm.

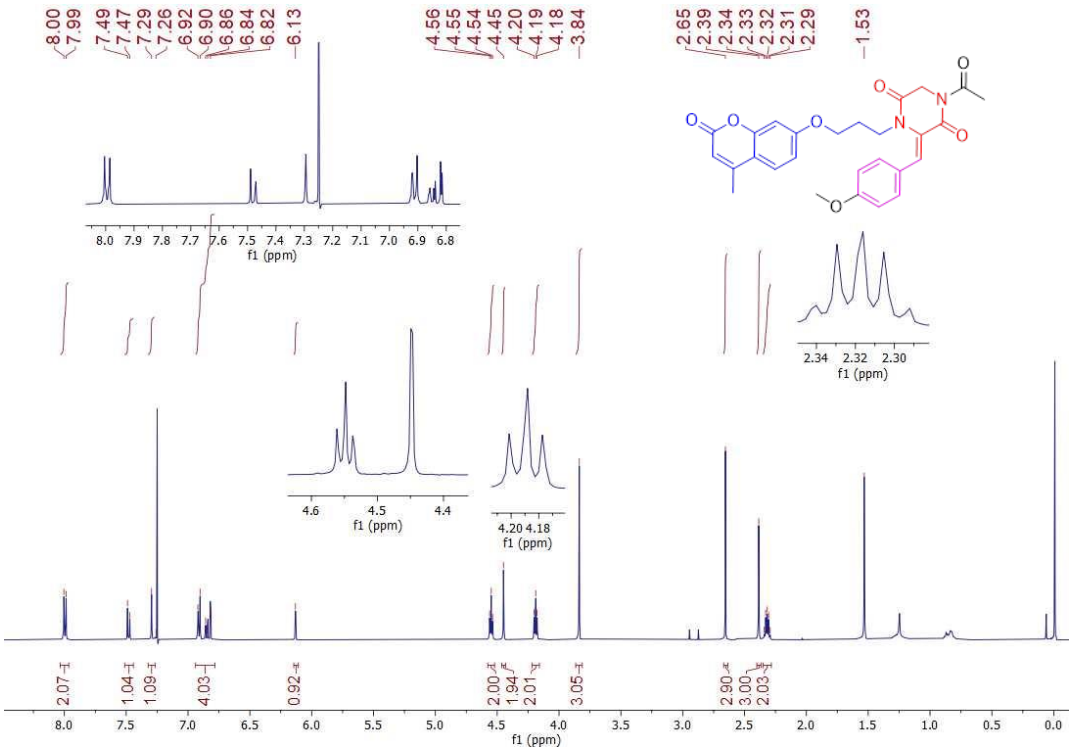

Figure 3.3. ^{1}H NMR spectrum of **3.12a.**

The ^{13}C NMR spectrum of compound **3.12a** exhibits twenty-five distinct carbon resonances (Figure 3.4). The signals at δ 28.39, 43.48, and 64.99 ppm correspond to the three carbon atoms of the propylene linker, while the signals at δ 18.72 and 63.59 ppm arise from the methyl and methoxy carbons, respectively. The acetyl carbon signal appears at δ 27.43 ppm, and the methylene carbon of the piperazine ring appears at δ 55.40 ppm. The lactone carbonyl carbon appears at δ 173.22 ppm, while the remaining sp2 carbons resonate at δ 162.51, 161.82, 161.24, 160.50, 158.78, 155.36, 152.51, 133.47, 129.56, 129.18, 127.78, 125.70, 114.02, 113.87, 112.49, 112.21, 101.63 ppm. High-resolution mass spectrometry (HRMS) of 3.12a (Figure 3.5) shows two significant peaks at m/z 491.1785 $[M+H]^{+}$, and 492.1836

$[M+2H]^{2+}$, consistent with the calculated value for $C_{27}H_{26}N_2O_7$ (m/z 490.5112 $[M]^+$), further confirming its molecular structure.

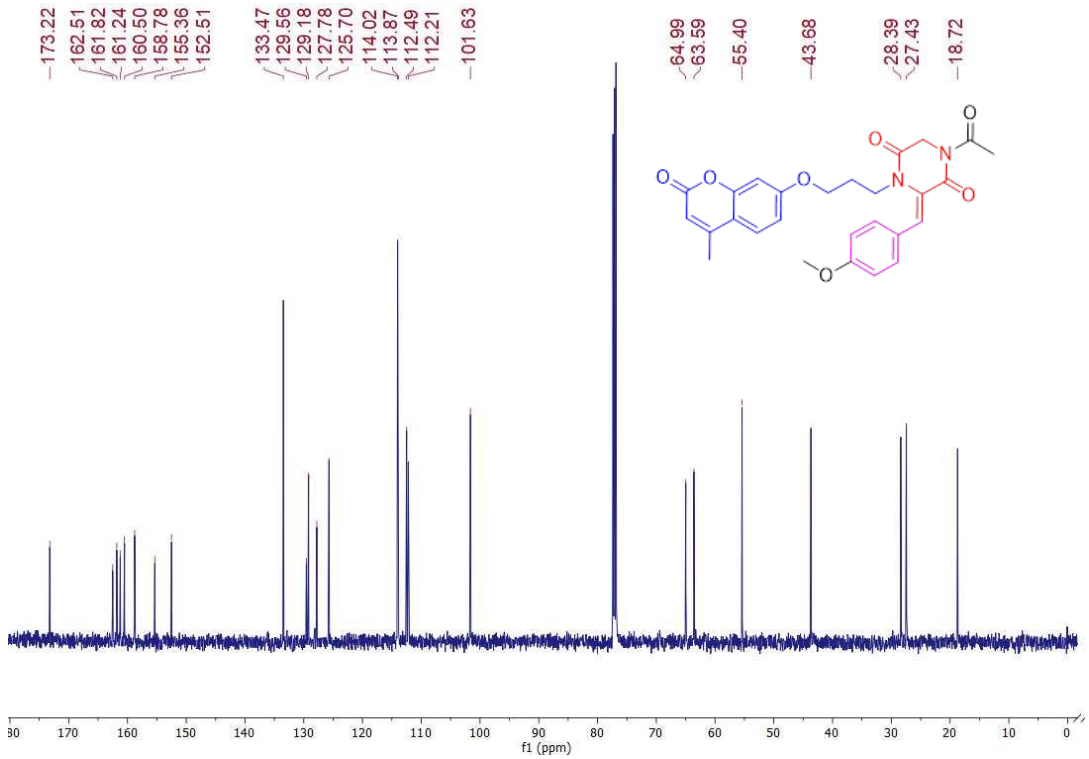

Figure 3.4. ^{13}C NMR spectrum of **3.12a.**

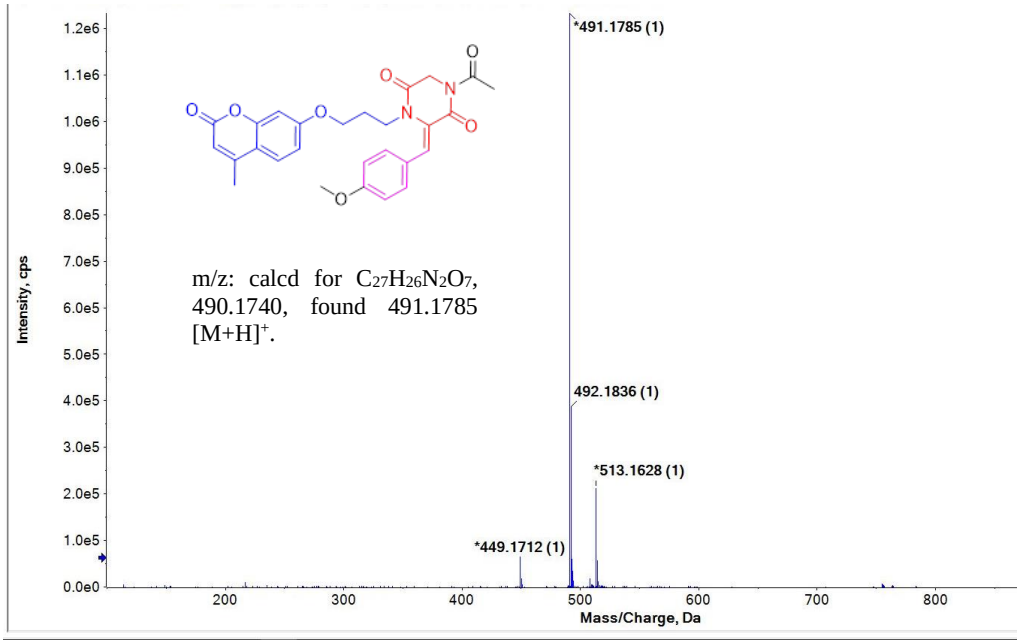

Figure 3.5. HRMS spectrum of **3.12a.**

3.4.2. *In Vitro* Anticancer Activity of 2,5-Diketopiperazine–Based Coumarin Analogues

The *in vitro* cytotoxicity of compounds **3.12a–3.12c, 3.13a–3.13c, 3.14a–3.14c, and 3.15a–3.15c** was evaluated against the human non-small cell lung cancer cell (A549) using the standard MTT assay after 24 and 48 hours of treatment.

Table 3.1. IC_{50} values of compounds against A549 cancer cell line. Data are presented as mean ± SEM (n=3).

	IC_{50} values (μM)	
Comp	**24 h**	**48 h**
3.12a	ND	ND
3.12b	52.21 ± 4.14	22.02 ± 3.98
3.12c	ND	ND
3.13a	NA	NA
3.13b	NA	NA
3.13c	NA	NA
3.14a	ND	ND
3.14b	ND	ND
3.14c	NA	NA
3.15a	ND	ND
3.15b	NA	NA
3.15c	NA	NA

[a]ND: Not determined. [b]NA: Not Active.

Overall, the synthesized compounds exhibited low to moderate cytotoxicity, with compound **3.12b** showing the most pronounced effect. Among the tested compounds, only the N-acetylated derivatives (**3.12a, 3.12b, 3.12c, 3.14a, 3.14b**) and one N-deacetylated compound (**15a**) exhibited measurable inhibitory activity. Notably, compound **3.12b** exhibited the highest activity, with an IC_{50} value of 42.21 ± 4.14 μM after 24 hours of treatment (Table 3.1). Its percentage inhibition values were

32.38%, 37.29%, 43.58%, 47.86%, and 56.21% at concentrations of 5, 10, 20, 40, and 80 μM, respectively (Figure 3.6).

Table 3.2. Maximum percentage of inhibition of compounds **3.12a-3.12c, 3.14a, 3.14b**, and **3.15a**. Data are presented as mean ± SEM (n=3).

	Maximum % cell growth inhibition	
Comp	**24 h**	**48 h**
3.12a	47.56 ± 4.23	48.57 ± 4.13
3.12b	56.21 ± 5.12	65.92 ± 5.36
3.12c	13.09 ± 2.65	20.78 ± 3.16
3.14a	48.77 ± 3.11	50.78 ± 3.25
3.14b	41.42 ± 4.34	46.74 ± 4.30
3.15a	32.83 ± 3.27	50.82 ± 2.95

For the remaining active compounds, the cytotoxicity profiles were inconsistent; with no clear dose-dependent response and therefore, their IC_{50} value have not been determined. For instance, compound **3.14a** displayed % inhibition values of 20.96%, 44.21%, 38.18%, 43.51%, and 48.78% at 5, 10, 20, 40, and 80 μM, respectively. These fluctuations are illustrated in Figures 3.6 and 3.7. The maximum cell growth inhibition percentages for compounds **3.12a–3.12c, 3.14a, 3.14b**, and **3.15a** after 24 h of treatment are summarized in Table 3.2. Due to the lack of a clear dose-dependent response, their activity is expressed only as the maximum percentage inhibition.

In contrast, compounds **3.13a-13c**, **3.14c**, **3.15b**, and **3.15c** exhibited very low or negligible cytotoxicity at all tested concentrations. The observed poor, inconsistent activity is likely due to the compounds' low solubility in the assay medium. The poor solubility likely arises from their hydrophobic aromatic rings and extensive intermolecular hydrogen bonding and π–π stacking within the DKP framework, which may promote the formation of linear or network-like supramolecular assemblies that

reduce solvation (Chapter 2, Figure 2.1) (Ando et al., 2011; Borthwick, 2012; Liao et al., 2014; Ressurreição et al., 2011).

To assess whether prolonged exposure could enhance activity, compounds **3.12a–3.12c, 3.14a, 3.14b**, and **3.15a** were re-evaluated after 48 h of treatment. A general increase in cytotoxicity was observed, with **3.12b** again emerging as the most active compound. It's IC_{50} decreased to 22.02 ± 3.98 µM, representing a ~2-fold improvement compared to the 24 h exposure (Figure 3.8). Compound **3.12b** exhibited % inhibition values of 41.45%, 43.46%, 46.92%, 51.52%, and 65.92% at 5, 10, 20, 40, and 80 µM, respectively. The maximum cell growth inhibition percentages for compounds **3.12a–3.12c, 3.14a, 3.14b**, and **3.15a** after 48 h of treatment are summarized in Table 3.2 and due to the absence of a clear dose-dependent response, their activity is also reported only as the maximum percentage inhibition.

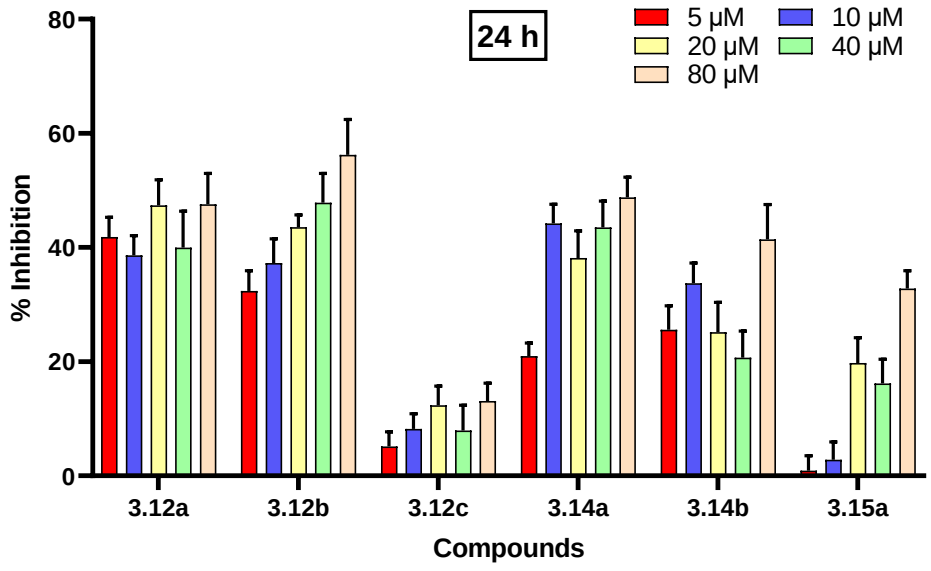

Figure 3.6. % Cell growth inhibition at different concentrations of compounds **3.12a–3.12c**, **3.14a**, **3.14b**, and **3.15a** after 24 h treatment. Data are presented as mean ± SEM (n=3).

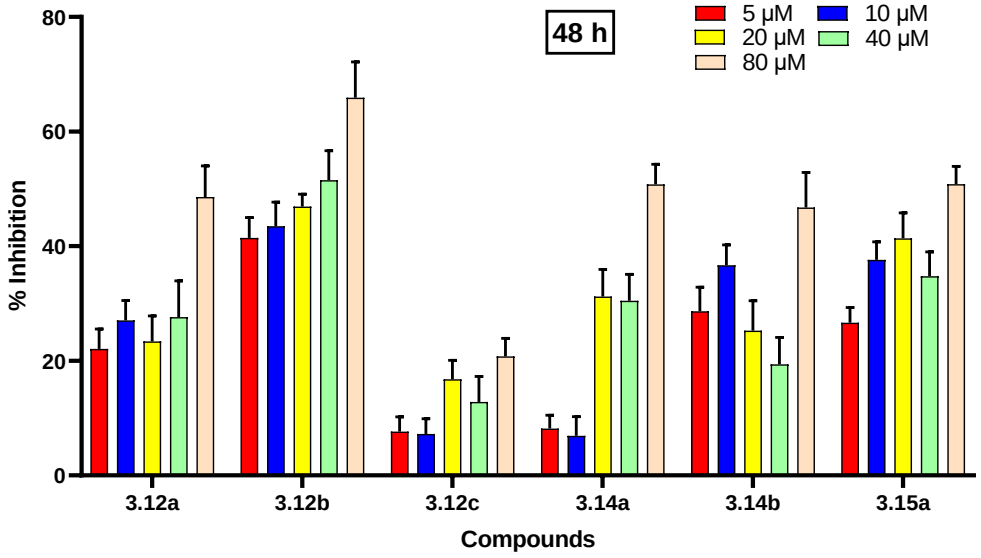

Figure 3.7. % Cell growth inhibition at different concentrations of compounds **3.12a**–**3.12c**, **3.14a**, **3.14b**, and **3.15a** after 48 h treatment. Data are presented as mean ± SEM (n=3).

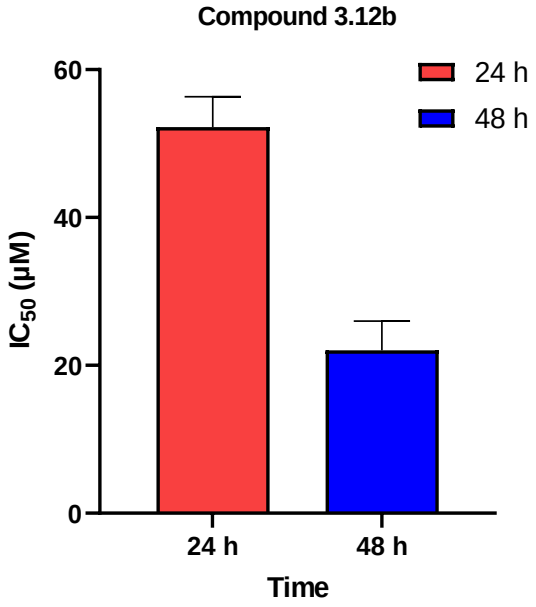

Figure 3.8. IC_{50} values of compound **3.12b** after 24 h and 48 h treatment. Data are presented as mean ± SEM (n=3).

3.4.3. Molecular Docking Study

3.4.3.1. Molecular Docking Study of Compounds 3.12a–3.12c, 3.13a–3.13c, 3.14a–3.14c, and 3.15a–3.15c.

Molecular docking simulations were performed to elucidate the binding modes of the synthesized compounds within the colchicine-binding site of β-tubulin. The results indicated that the poses of most compounds did not follow a uniform pattern and did not adopt a single conserved orientation within the colchicine-binding pocket; instead, their orientations were variable and compound-specific. The binding affinities and residues involved in interactions of these compounds within the colchicine binding site of β-tubulin are summarized in Table 3.3.

Table 3.3. Binding affinities and residues involved in interactions of DKP-based coumarin hybrids (**3.12a–3.12c, 3.13a–3.13c, 3.14a–3.14c, and 3.15a–3.15c**) within the colchicine binding site of β-tubulin.

Compound	Binding affinity (kcal/mol)	Residues involved in H-bond	Residues involved in other interactions (π···sulfur, π···σ, π···alkyl, alkyl)
3.12a	-8.0	Tyr200	Ala314, Ala352, and Cys239, Met257
3.12b	-8.1	Asn256	Ala314, Cys239, Ile368, Met257, Leu253
3.12c	-8.1	Tyr200	Ala314, Cys239, Ile316, Leu246, Ala352, Ile368, Met257, Leu253
3.13a	-8.1	Val236	Ala314, Cys239, Ala352, Asn256, Met257, Lys350
3.13b	-8.5	Val236	Ala314, Cys239, Ala352, Asn256, Met257, Lys350
3.13c	-7.9	Asn256	Ala314, Cys239, Ile316, Leu246, Ala352
3.14a	-8.2	Cys239	Ala314, Ile368, Met257, Leu253, Lys350
3.14b	-7.8	Tyr200	Ala314, Cys239, Leu246, Ala352, Leu253, Lys350, Lys252

3.14c	-8.0	Asn256	Leu253, Lys350, Lys252
3.15a	-8.1	Val236	Ala314, Cys239, Ala352, Asn256, Met257, Lys350
3.15b	-8.1	Val236	Ala314, Cys239, Ala352, Asn256, Met257, Lys350
3.15c	-8.2	Cys239	Ala314, Cys239, Ile316, Leu246, Ala352

Compounds **3.12a–3.12c, 3.14a, 3.14b**, and **3.15a** exhibited notable interactions within the binding site. Compound **3.12a** formed a hydrogen bond with Tyr200 residue, while its coumarin ring engaged in a π–sulfur interaction with Met257 residue, contributing to enhanced stabilization through hydrophobic and electronic complementarity (Figure 3.9a). Additional hydrophobic contacts were observed with Ala314, Ala352, and Cys239 residues. Compound **3.12b** adopted a slightly shifted orientation compared to **3.12a** and formed a hydrogen bond with the residue Asn256, accompanied by hydrophobic interactions involving Ala314, Cys239, Ile368, Met257, and Leu253 (Figure 3.9b). Compound **3.12c** also established a hydrogen bond with Tyr200 and engaged in multiple hydrophobic interactions with Ala314, Cys239, Ile316, Leu246, Ala352, Ile368, Met257, and Leu253 residues. Among the compound **3.14** series, compound **3.14a** formed a hydrogen bond with Cys239 and displayed hydrophobic contacts with Ala314, Ile368, Met257, Leu253, and Lys350, whereas compound **3.14b** interacted via a hydrogen bond with Tyr200 and additional hydrophobic contacts with Ala314, Cys239, Leu246, Ala352, Leu253, Lys350, and Lys252. The N-deacetylated compound **3.15a** exhibited a hydrogen bond with Val236, a critical residue for plinabulin-like anchoring within the pocket, and was further stabilized by hydrophobic interactions involving Ala314, Cys239, Ala352, Asn256, Met257, and Lys350 (Figure 3.9c).

The docking analysis of the N-deacetylated analogues (**3.13a, 3.13b, 3.15b**), whose cytotoxicity could not be determined due to poor solubility, revealed that the orientation of the central DKP ring closely resembled that of plinabulin, a known tubulin polymerization inhibitor (Figure 3.9a & Figure 3.10f). These analogues also formed a hydrogen bond with Val236, suggesting that despite their solubility

limitations, they may possess promising biological activity if their physicochemical properties are further optimized.

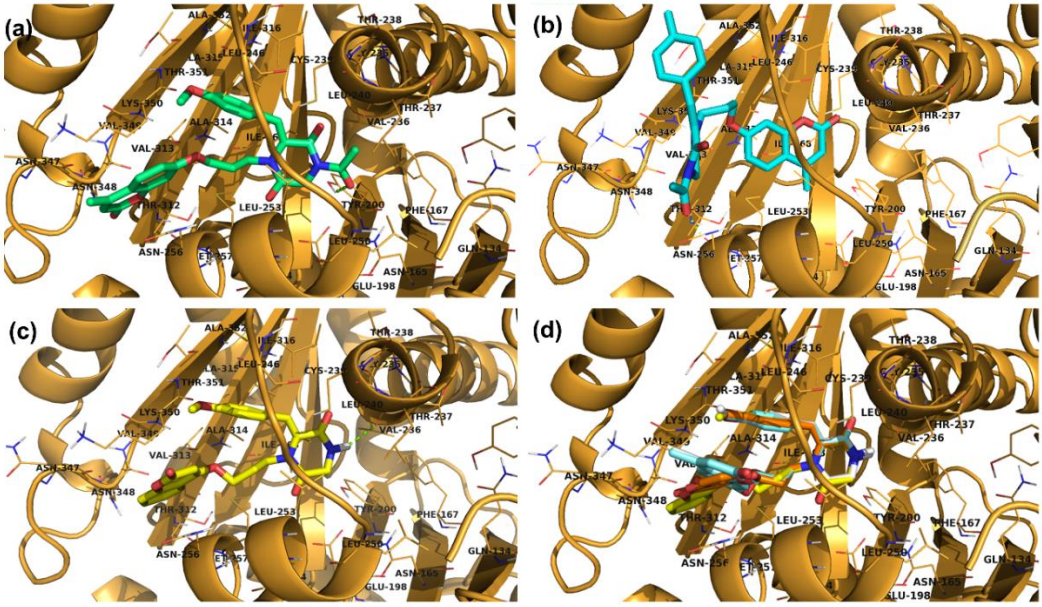

Figure 3.9. Binding poses of compounds **3.12a**, **3.12b**, **3.13a**, **3.13b**, **3.15a**, and **3.15b** within the colchicine-binding site of β-tubulin. (a) Compound **3.12a**; (b) **3.12b**; (c) **3.15a**; (d) Overlay of compounds **3.15a** (yellow), **3.13a** (gray), **3.13b** (cyan), and **3.15b** (orange).

3.4.3.2. Molecular Docking Studies of Compounds 3.17a-3.17f.

The binding conformation of compounds **3.17a, 3.17c, 3.17d**, and **3.17f** follows a uniform pattern, adopting a single conserved orientation within the colchicine binding pocket. The central DKP ring and the aryl rings occupy the same region of the pocket, while the positions of the coumarin moieties show only slight deviations from one another. Interestingly, these compounds exhibit a binding mode similar to that of plinabulin, in which the orientation of the central DKP ring and one of the aryl rings closely matches that of plinabulin. The binding affinities of compounds **3.17a, 3.17c, 3.17d**, and **3.17f** (–9.1 to –9.5 kcal/mol) were also comparable to that of plinabulin (–9.1 kcal/mol), indicating a similar binding strength within the colchicine pocket (Table 3.4). In accordance with this observation, compounds **3.17a, 3.17c, 3.17d**, and **3.17f** form a hydrogen bond between the amide NH group of the DKP ring and the Val236 residue, analogous to the key interaction

observed for plinabulin (Figure 3.10a–3.10f). Moreover, the coumarin and aryl rings, positioned on the same side of the DKP core, engage in π–sulfur interactions with Met257 and Cys239, respectively, further stabilizing the complex. These compounds are further stabilized through π–σ and π–alkyl interactions involving residues Ile368, Leu253, Ala314, Ala352, Asn256, and Lys350. Furthermore, in these compounds, the methoxy oxygen on the aryl ring, on the same side of the coumarin linker, forms additional hydrogen-bond interactions with the residue Thr351.

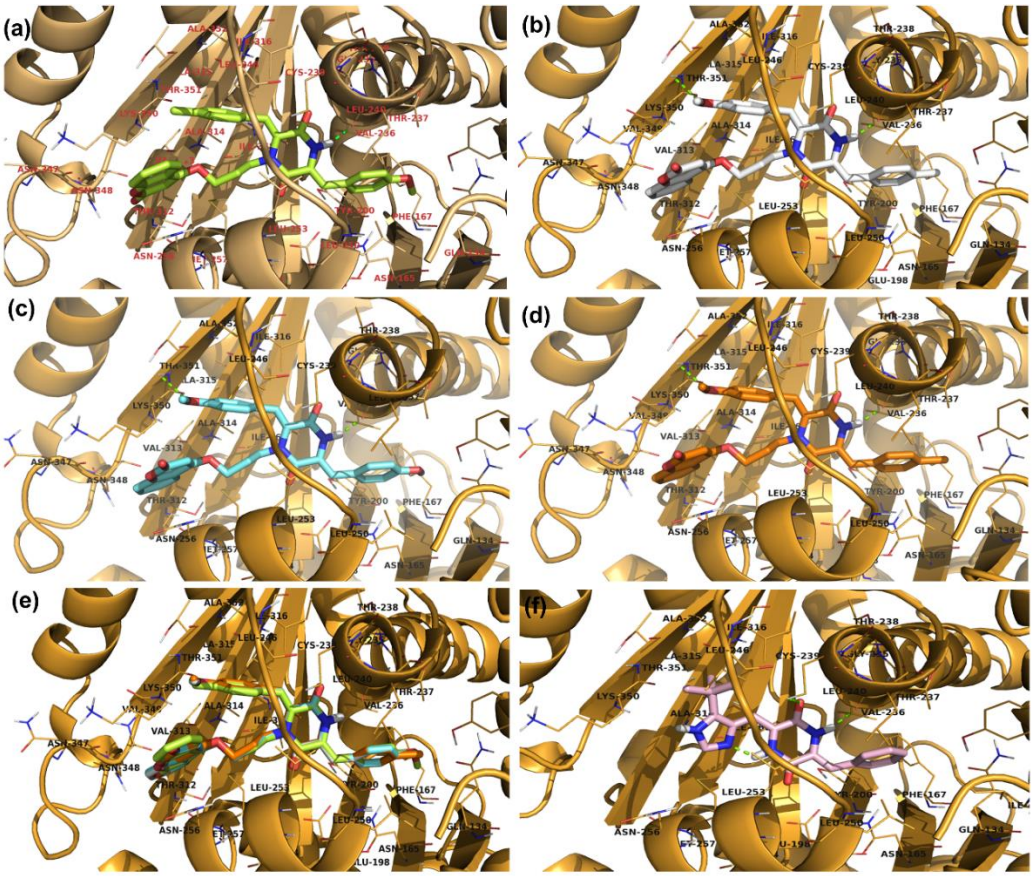

Figure 3.10. Binding poses of compounds **3.17a**-**3.17f** and Plinabulin within the colchicine-binding site of β-tubulin. (a) Compound **3.17a**; (b) **3.17c**; (c) **3.17d**; (d) **3.17f**; (e) Overlay of compounds **3.17a** (limon), **3.17c** (gray), **3.17d** (cyan), and **3.17f** (orange); (f) Plinabulin.

However, the binding conformations of compounds **3.17b** and **3.17e** differed notably from those of the other derivatives. Compound **3.17b** did not form any hydrogen bond interactions but was instead stabilized by π–alkyl, π–σ, and alkyl interactions with residues Cys239, Ile316, Ala314, Leu253, Leu246, and Lys350. In

contrast, compound **3.17e** established hydrogen bond interactions with Cys239 and Asn256, along with π–alkyl and π–σ interactions involving Ala314, Leu253, Lys350, and Met257. Moreover, the binding affinities of compounds **3.17b** and **3.17e** were lower than those of the other analogues, with docking scores of –7.5 kcal/mol and –7.6 kcal/mol, respectively, indicating comparatively weaker binding to the colchicine pocket.

Table 3.4. Binding affinities and residues involved in interactions of Plinabulin-based coumarin hybrids (**3.17a**–**3.17f**) in the colchicine binding site of β-tubulin.

Compound	Binding affinity (kcal/mol)	Residues involved in H-bond	Residues involved in other interactions (π···sulfur, π···σ, π···alkyl, alkyl)
3.17a	-9.1	Val236	Ile368, Leu253, Ala314, Ala352, Asn256, Lys350
3.17b	-7.5	--	Cys239, Ile316, Ala314, Leu253, Leu246, Lys350
3.17c	-9.5	Val236, Thr351	Ile368, Leu253, Ala314, Ala352, Asn256, Lys350
3.17d	-9.4	Val236, Thr351	Ile368, Leu253, Ala314, Ala352, Asn256, Lys350
3.17e	-7.6	Cys239, Asn256	Ala314, Leu253, Lys350, and Met257
3.17f	-9.2	Val236, Thr351	Ile368, Leu253, Ala314, Ala352, Asn256, Lys350
Plinabulin	-9.1	Cys239, Val236	Leu250, Val236, Cys239, Ile368, Leu253, Ala314, Met257

3.4.4. Absorption, Distribution, Metabolism, Excretion, and Toxicity (ADMET) of compounds 3.17a–3.17f

In silico ADMET (Absorption, Distribution, Metabolism, Excretion, and Toxicity) profiling of the synthesized analogs **3.17a–3.17f** was performed using the pkCSM web-based platform, which employs graph-based signatures to predict pharmacokinetic and toxicity parameters of small molecules (Pires et al., 2015). The

predicted parameters are summarized in Table 3.5. Overall, the results revealed that all six analogs exhibit favorable pharmacokinetic properties consistent with those of drug-like molecules.

Table 3.5. ADMET/pharmacokinetic properties of compounds **3.17a–3.17f.**

	Compounds					
	3.17a	**3.17b**	**3.17c**	**3.17d**	**3.17e**	**3.17f**
Absorption						
Caco2 permeability (log Papp in 10^{-6} cm/s)	0.739	0.671	0.658	0.711	0.593	0.545
Intestinal absorption (human) (% Absorbed)	94.081	97.165	97.017	95.075	92.958	97.725
P-glycoprotein substrate	Yes	Yes	Yes	Yes	Yes	Yes
Distribution						
BBB permeability (log BB)	-0.402	-0.743	-0.411	-0.614	-0.944	-0.586
CNS permeability (log PS)	-2.483	-3.056	-2.493	-3.172	-3.215	-2.453
Metabolism						
CYP2D6 substrate	No	No	No	No	No	No
CYP3A4 substrate	Yes	Yes	Yes	Yes	Yes	Yes
CYP2C19 inhibitior	Yes	Yes	Yes	Yes	Yes	Yes
CYP2C9 inhibitior	Yes	Yes	Yes	Yes	Yes	Yes
CYP2D6 inhibitior	No	No	No	No	No	No
CYP3A4 inhibitior	Yes	Yes	Yes	Yes	Yes	Yes
Excretion						
Total Clearance (log ml $min^{-1}kg^{-1}$)	0.795	-0.431	0.785	0.768	-0.221	-0.48
Toxicity						
AMES toxicity	No	No	No	No	No	No
Max. tolerated dose (human) (log mg $kg^{-1}day^{-1}$)	0.669	0.617	0.666	0.692	0.636	0.676
hERG I inhibitor	No	No	No	No	No	No
Hepatotoxicity	Yes	Yes	Yes	Yes	Yes	Yes

3.4.4.1. Absorption

The Caco-2 cell permeability values for compounds **3.17a–3.17f** ranged from 0.545 to 0.739 (log Papp in ×10-6 cm/s), indicating low-to-moderate passive permeability. Among them, **3.17a** (0.739) exhibited the highest predicted permeability, while **3.17f** (0.545) showed the lowest. Compounds are considered to have high Caco-2 permeability if their predicted log Papp is> 0.90.

The human intestinal absorption (HIA) was high for all compounds, ranging from 92.96% to 97.73%, with **3.17b, 3.17c**, and **3.17f** showing absorption rates above 97%. These values indicate that all compounds are expected to be well absorbed in the gastrointestinal tract, demonstrating excellent potential for oral bioavailability.

Moreover, all analogues were predicted to be P-glycoprotein (P-gp) substrates, suggesting possible efflux through intestinal and blood–brain barrier transporters. While P-gp efflux can reduce intracellular drug concentrations and lower effective permeability, it may also limit central nervous system (CNS) exposure, which is beneficial if the therapeutic target is peripheral and CNS-related side effects are undesirable (Lin et al., 2003).

3.4.4.2. Distribution

For blood–brain barrier (BBB) permeability, pkCSM classifies compounds with log BB > 0.3 as likely to cross the BBB and those with log BB < −1.0 as poorly distributed to the brain. The predicted log BB values (−0.402 to −0.944) indicate low BBB permeability across the series. None of the compounds exceeded 0.3, implying they are unlikely to penetrate the CNS, which is favorable when central effects are not desired. Moreover, compounds with log PS > −2 are considered capable of CNS penetration, whereas those with log PS < −3 are unable to do so. Accordingly, **3.17b**, **3.17d**, and **3.17e** (log PS < −3) are predicted to be non-penetrant, while 17a, 17c, and 17f (−3 < log PS < −2) exhibit borderline or limited CNS permeability (Table 3.5). These results corroborate the low log BB predictions, collectively confirming that the compounds have restricted CNS access, a desirable feature for non-CNS therapeutic targets.

3.4.4.3. Metabolism

Cytochrome P450 (CYP) inhibition was assessed to predict the likelihood of metabolic interactions. The data indicate that all compounds are CYP3A4 substrates and inhibitors of CYP3A4, CYP2C9, and CYP2C19, but are neither substrates nor inhibitors of CYP2D6. This consistent pattern suggests that metabolism will occur primarily via hepatic CYP3A4, a major phase I enzyme. Although inhibition of multiple CYP isoforms may increase the risk of drug–drug interactions (DDIs), the absence of CYP2D6 inhibition is advantageous because it reduces variability associated with CYP2D6 genetic polymorphism (Ingelman-Sundberg, 2015).

3.4.4.4. Excretion

The predicted total clearance (log ml/min/kg) varied among the compounds. **3.17a** (0.795), **3.17c** (0.785), and **3.17d** (0.768) exhibited relatively high clearance rates, suggesting rapid systemic elimination and a lower risk of bioaccumulation. Conversely, **3.17b** (−0.431), **3.17e** (−0.221), and **3.17f** (−0.480) displayed lower clearance and potentially longer systemic retention.

3.4.4.5. Toxicity

All compounds were predicted to be non-mutagenic (negative in the Ames test) and non-cardiotoxic (no hERG I inhibition), indicating favorable genotoxicity and cardiotoxicity profiles. The maximum tolerated dose (MTD) values ranged from 0.617 to 0.692 log (mg kg-1 day-1). Compounds with MRTD ≤ 0.477 log(mg/kg/day) are considered to have low tolerability, whereas those with MRTD > 0.477 log(mg/kg/day) are considered highly tolerated. As all compounds exceed this threshold, they are classified as high MRTD compounds, indicating low acute toxicity risk. However, all analogs were predicted as hepatotoxic.

3.5. Conclusion

In this chapter, a novel series of coumarin-based plinabulin derivatives was successfully designed and synthesized. The *in vitro* anticancer evaluation of compounds **3.12a**–**12c**, **3.13a**–**3.13c**, **3.14a**–**3.14c**, and **3.15a**–**3.15c** against the A549 human non-small cell lung cancer cell line revealed that compound **3.12b** exhibited

the highest cytotoxic activity, with IC_{50} values of 52.21 ± 4.14 μM and 22.02 ± 3.98 μM after 24 h and 48 h of exposure, respectively. This represents approximately a twofold increase in cytotoxic potency upon extended incubation. In contrast, compounds **3.12a**, **3.12c**, **3.14a**, **3.14b**, and **3.15a** showed low to moderate cytotoxicity, which was not dose-dependent, likely due to poor solubility under the experimental conditions. These findings suggest that **3.12b** serves as a promising lead molecule for further structural refinement and optimization.

Molecular docking studies performed against β-tubulin provided important structural insights into the binding interactions within the colchicine-binding pocket. The rational design and structural optimization efforts led to the synthesis of a new set of derivatives, **3.17a**–**17f**, of which **3.17a**, **3.17c**, **3.17d**, and **3.17f** displayed binding conformations and affinities (–9.1 to –9.5 kcal/mol) comparable to that of plinabulin (–9.1 kcal/mol). These results suggest that the new derivatives may possess similar tubulin polymerization inhibitory potential. Although compounds **3.17a**–**3.17f** have not yet been evaluated for their anticancer activity, the *in silico* ADMET profiles indicate favourable pharmacokinetic and safety characteristics, such as high human intestinal absorption, poor BBB and CNS permeability, acceptable genotoxicity and cardiotoxicity profiles, and low acute toxicity risk. These findings support their potential as viable candidates for subsequent biological evaluation.

Molecular docking studies performed against β-tubulin provided important structural insights into the binding interactions within the colchicine-binding pocket. The rational design and structural optimization efforts led to the synthesis of a new set of derivatives, **3.17a–17f**, of which **3.17a, 3.17c, 3.17d**, and **3.17f** displayed binding conformations and affinities (–9.1 to –9.5 kcal/mol) comparable to that of plinabulin (–9.1 kcal/mol). These results suggest that the new derivatives may possess similar tubulin polymerization inhibitory potential. Although compounds **3.17a–3.17f** have not yet been evaluated for their anticancer activity, the *in silico* ADMET profiles indicate favourable pharmacokinetic and safety characteristics, including high human intestinal absorption, low BBB and CNS permeability, acceptable genotoxicity and cardiotoxicity profiles, and low acute toxicity risk. These findings support their potential as viable candidates for subsequent biological evaluation.

In summary, this study provides a strong foundation for the continued development of coumarin–plinabulin hybrid scaffolds as potential anticancer agents. Future work will focus on the experimental validation of the anticancer and anti-tubulin polymerization activities of compounds **3.17a–3.17f**, along with structural modifications, solubility enhancement, and mechanistic investigations to further improve their potency, selectivity, and drug-like properties. The overall goal of these efforts is to advance this scaffold toward the discovery of more effective and safer anticancer therapeutics.

3.6. ^{1}H NMR and ^{13}C NMR Spectra and HRMS Data of Selected Compounds

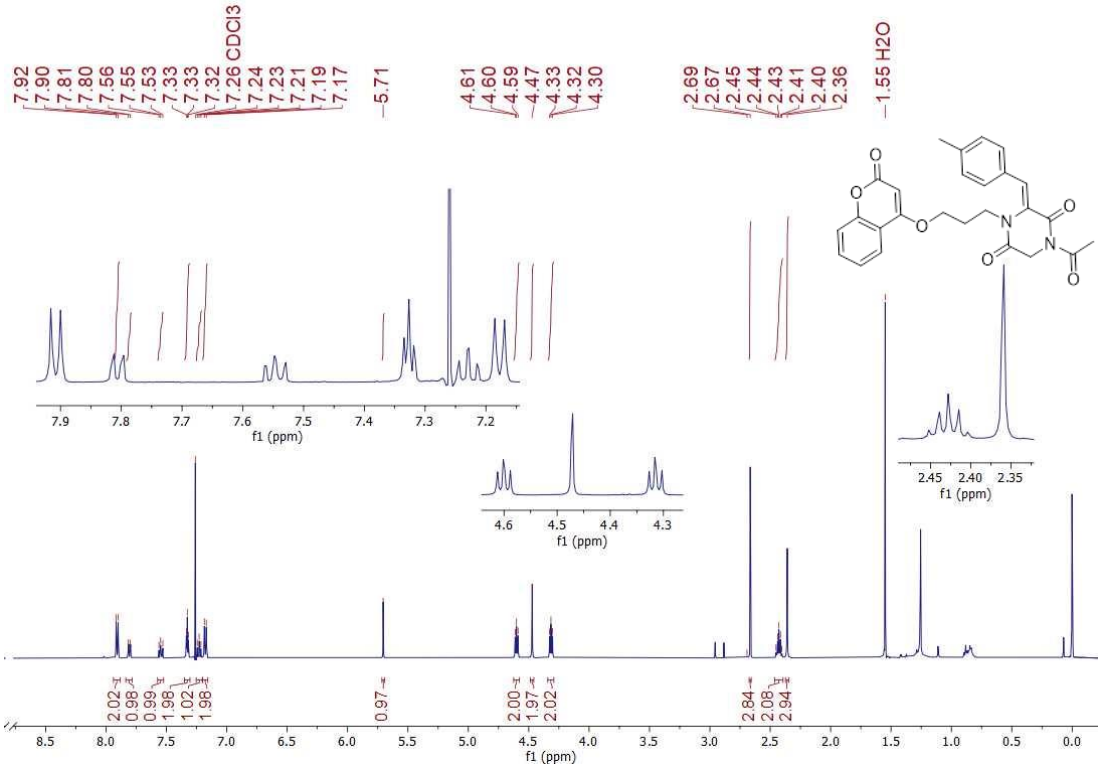

Figure 3.11. ^{1}H NMR of compound **3.14b.**

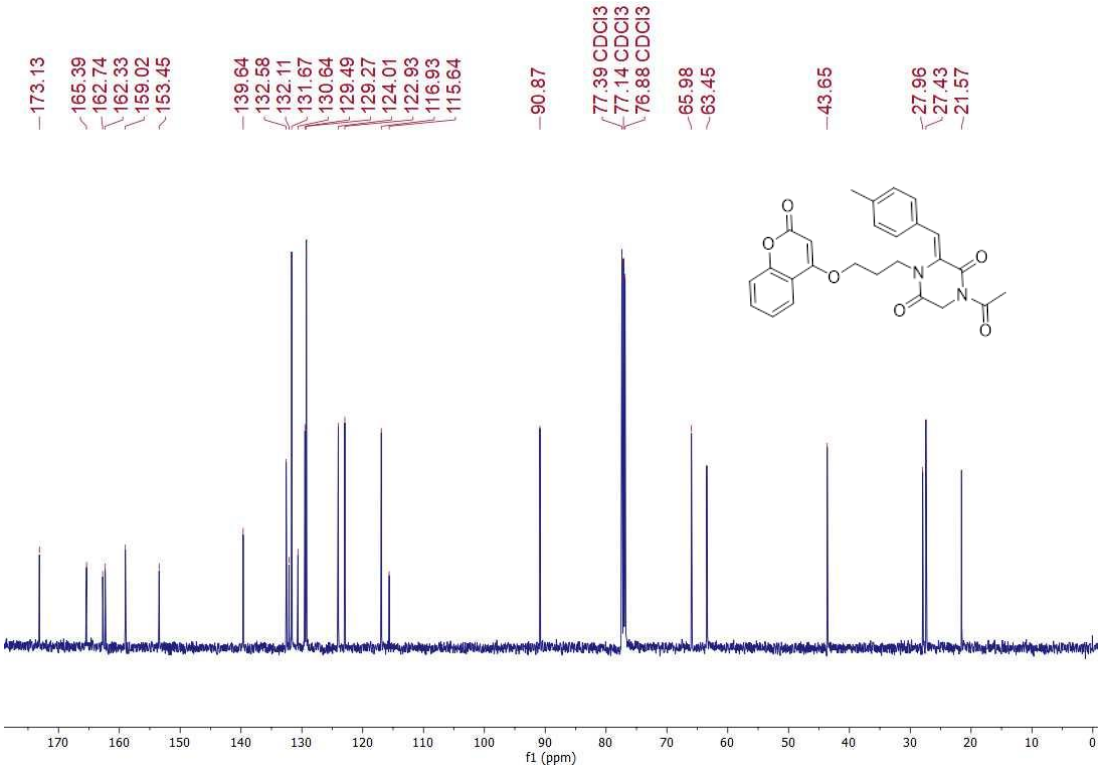

Figure 3.12. ^{13}C NMR of compound **3.14b.**

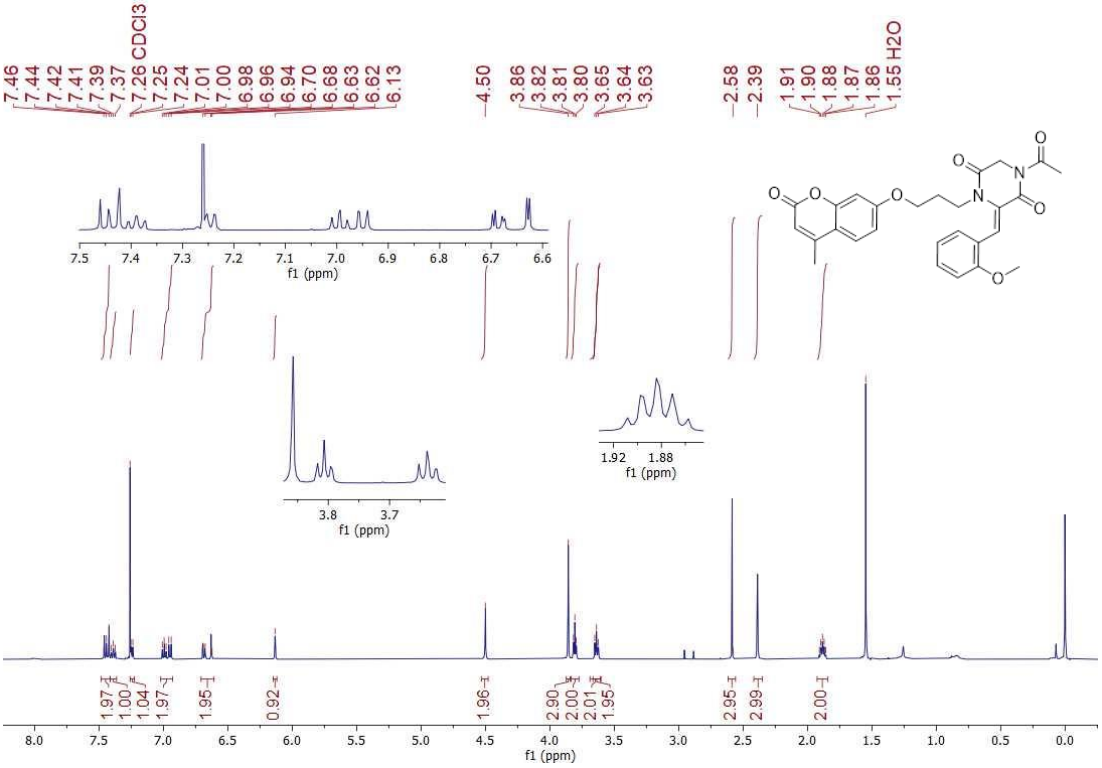

Figure 3.13. ^{1}H NMR of compound **3.12c.**

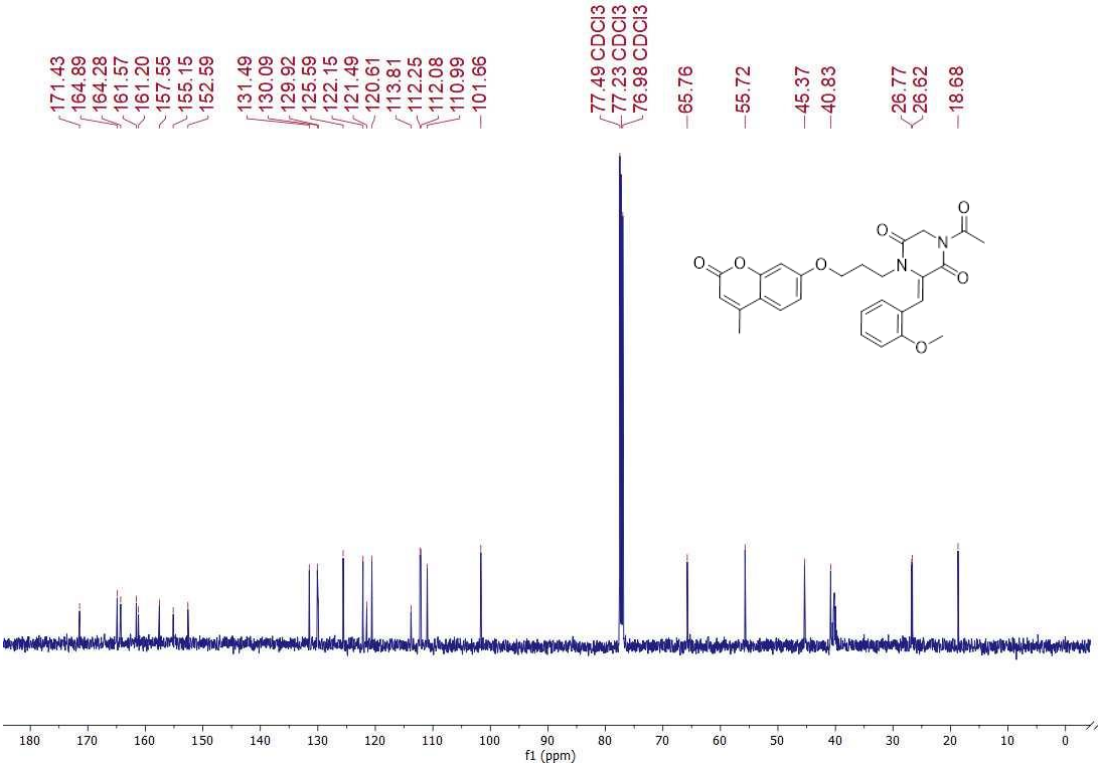

Figure 3.14. ^{13}C NMR of compound **3.12c.**

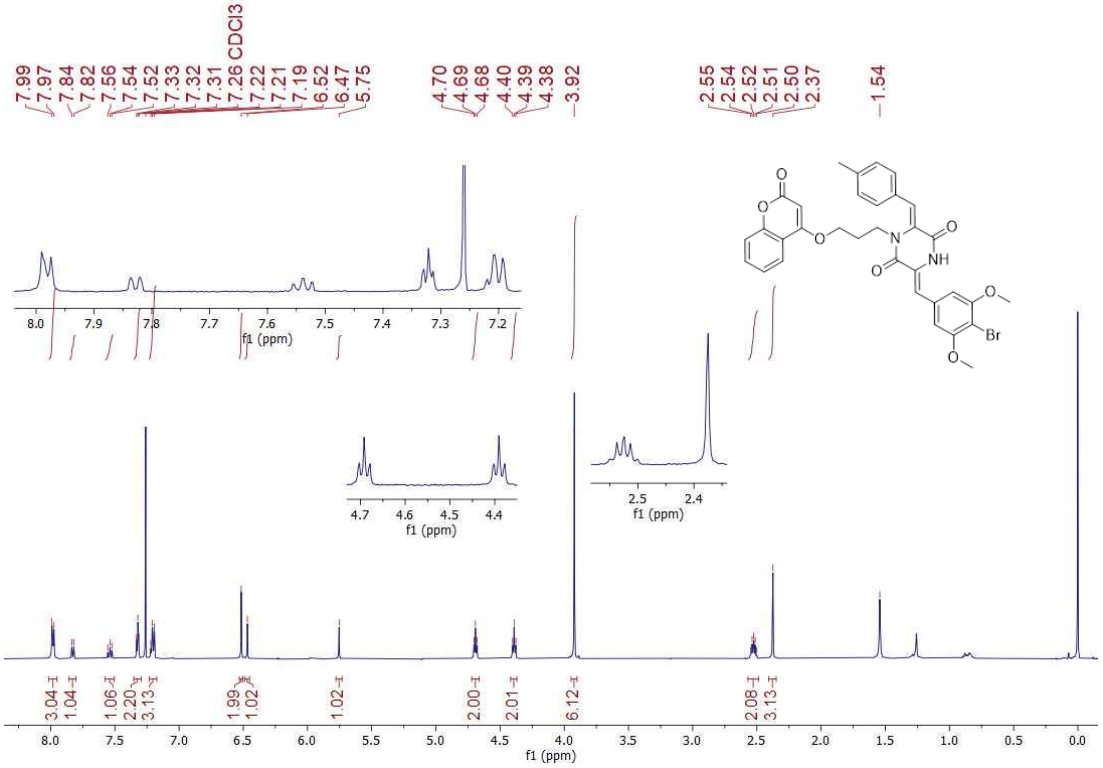

Figure 3.15. ^{1}H NMR of compound **3.17b.**

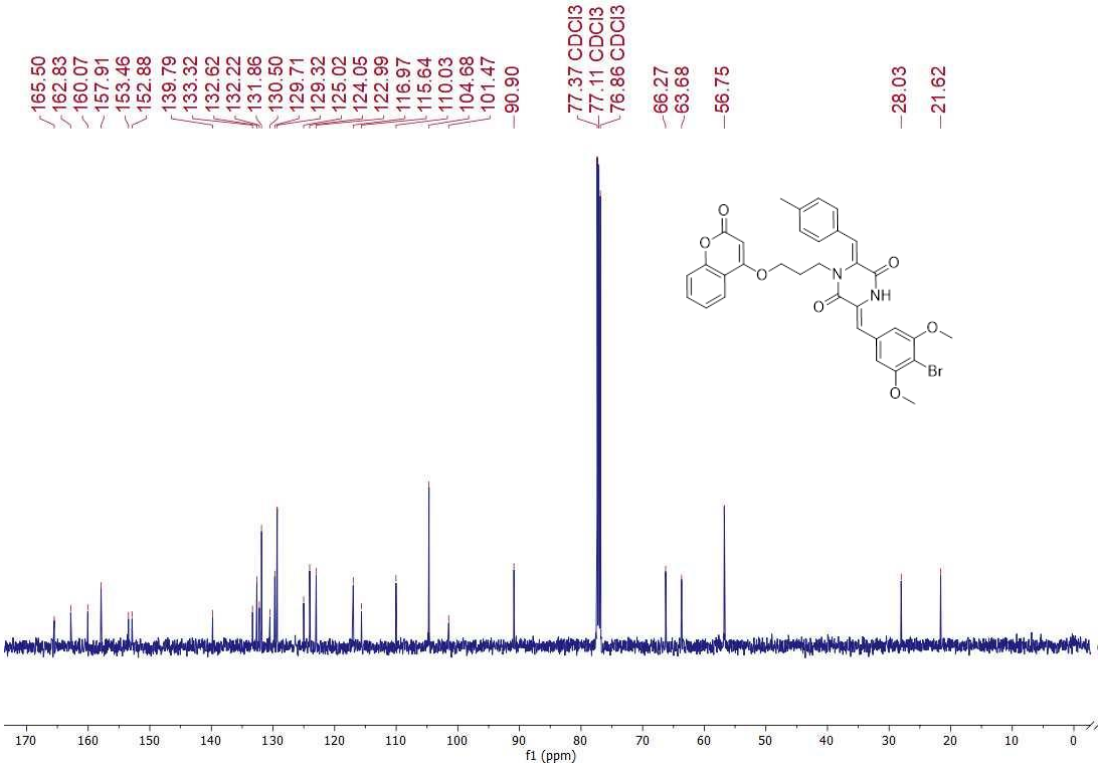

Figure 3.16. ^{13}C NMR of compound **3.17b.**

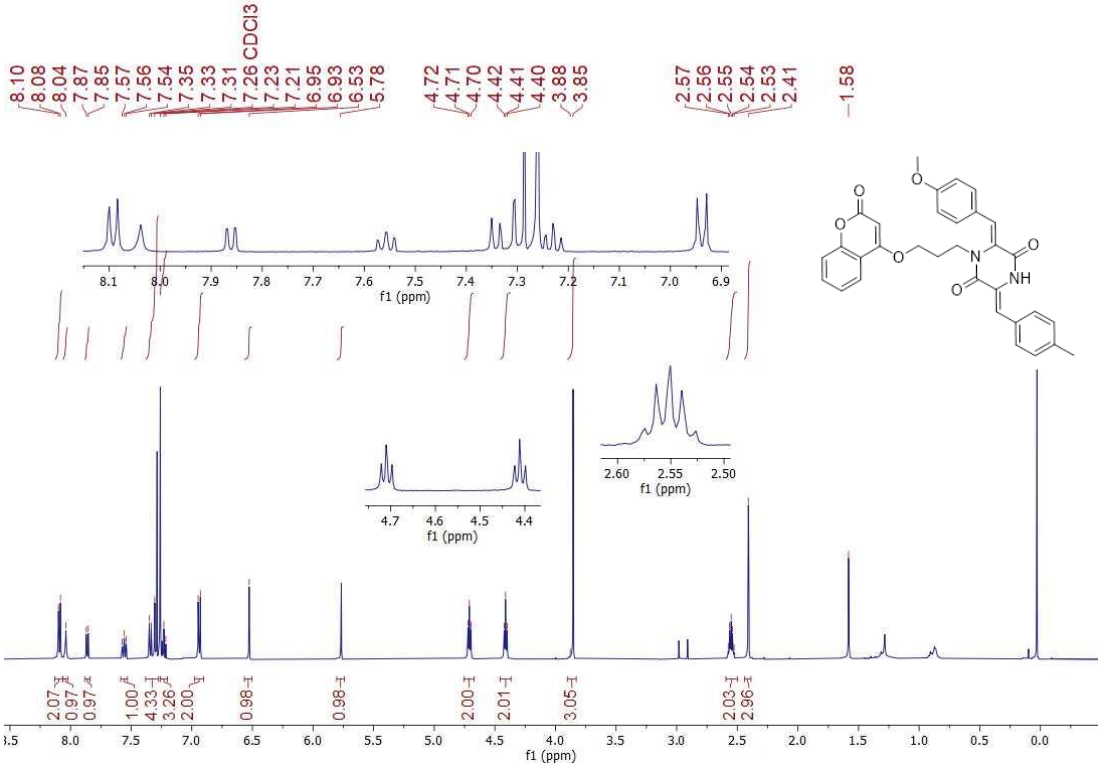

Figure 3.17. ^{1}H NMR of compound **3.17c.**

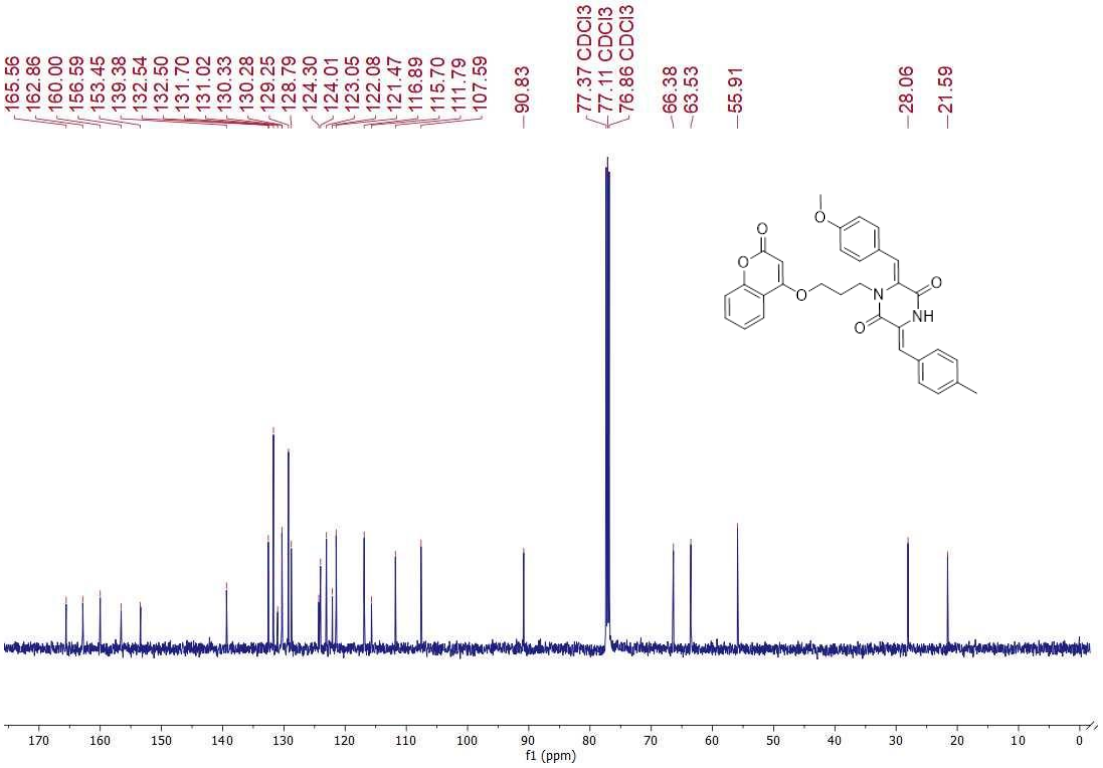

Figure 3.18. ^{13}C NMR of compound **3.17c.**

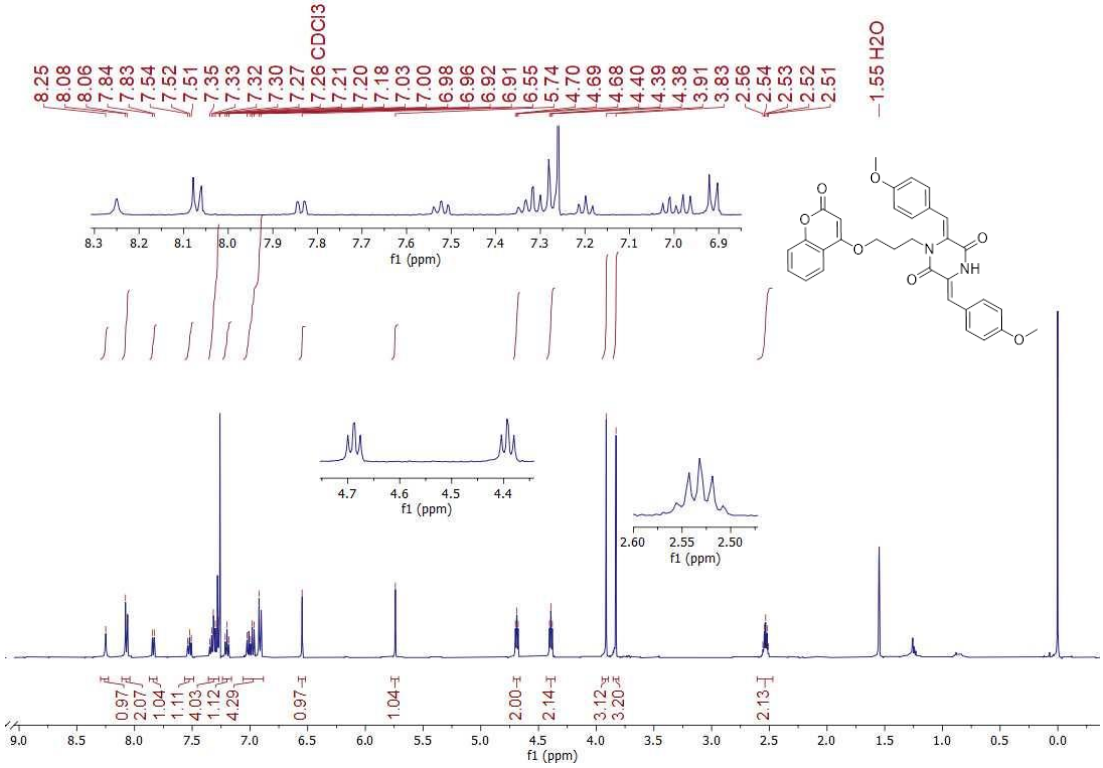

Figure 3.19. ^{1}H NMR of compound **3.17d.**

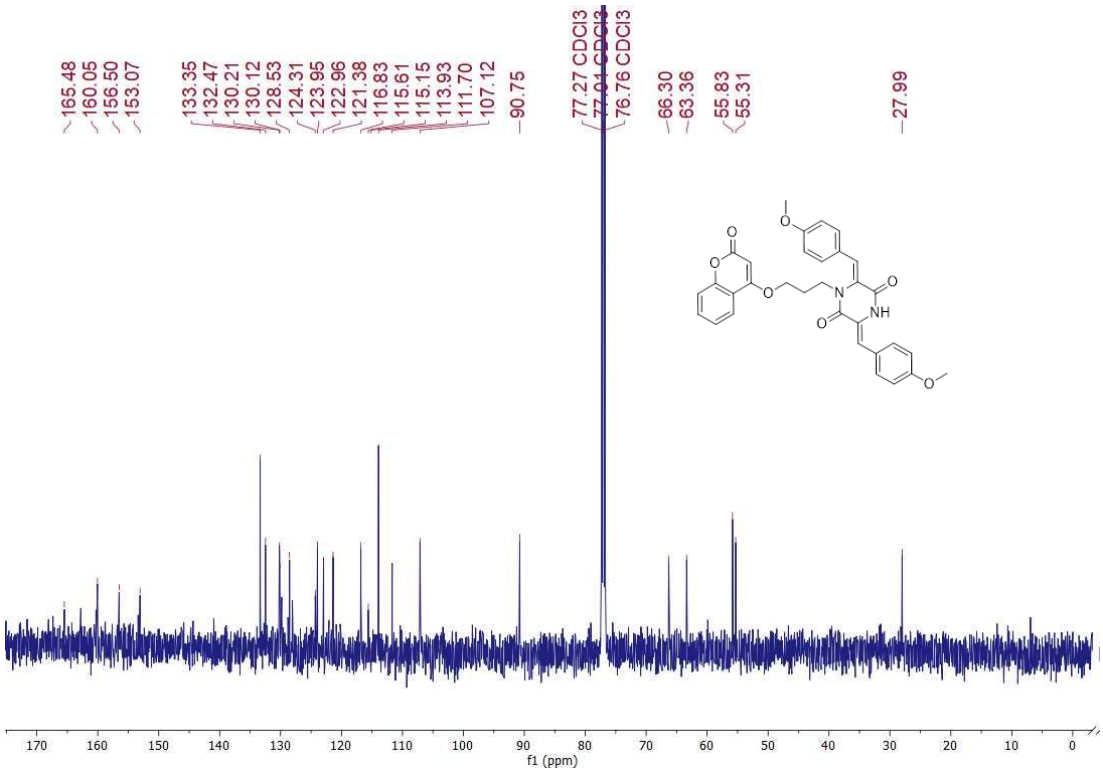

Figure 3.20. ^{13}C NMR of compound **3.17d.**

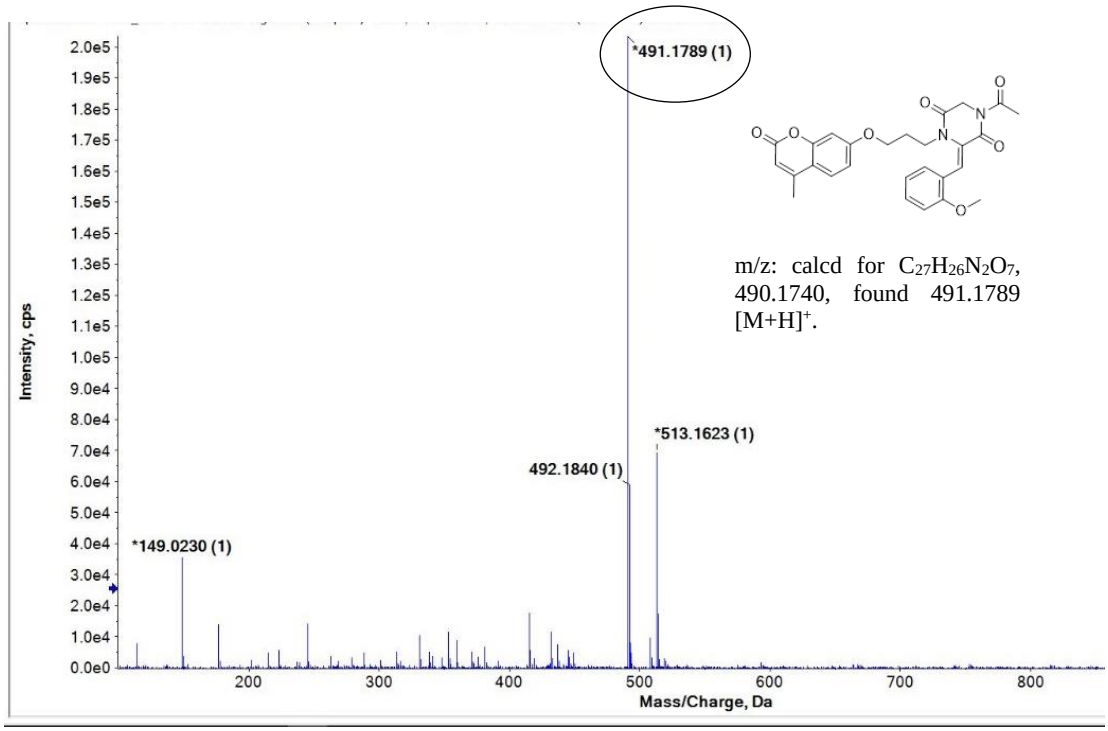

Figure 3.21. HRMS of compound **3.12c.**

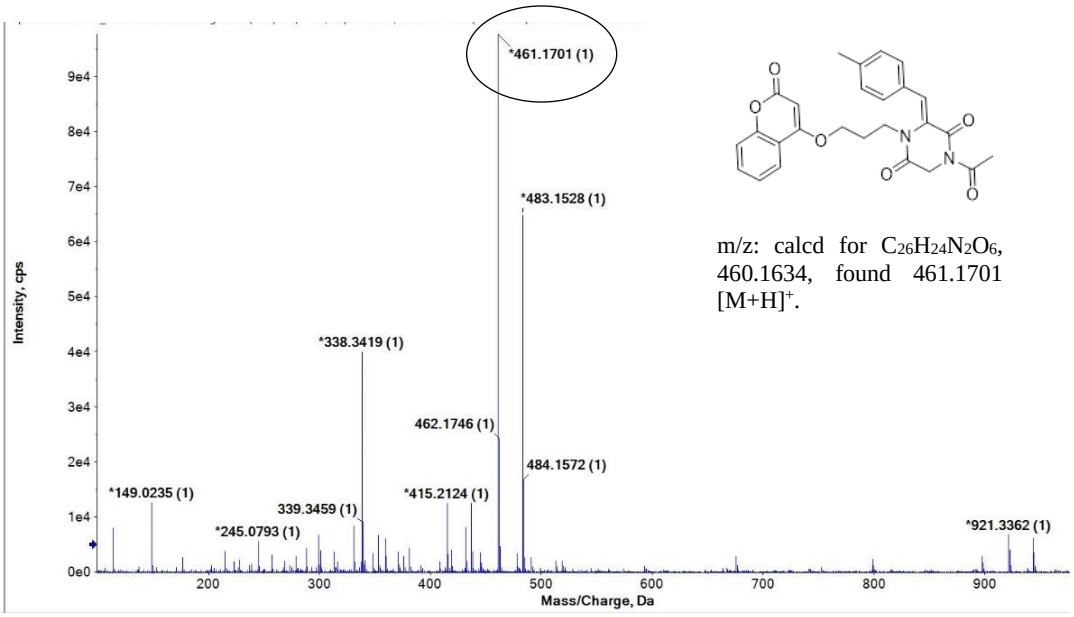

Figure 3.22. HRMS of compound **3.14b.**

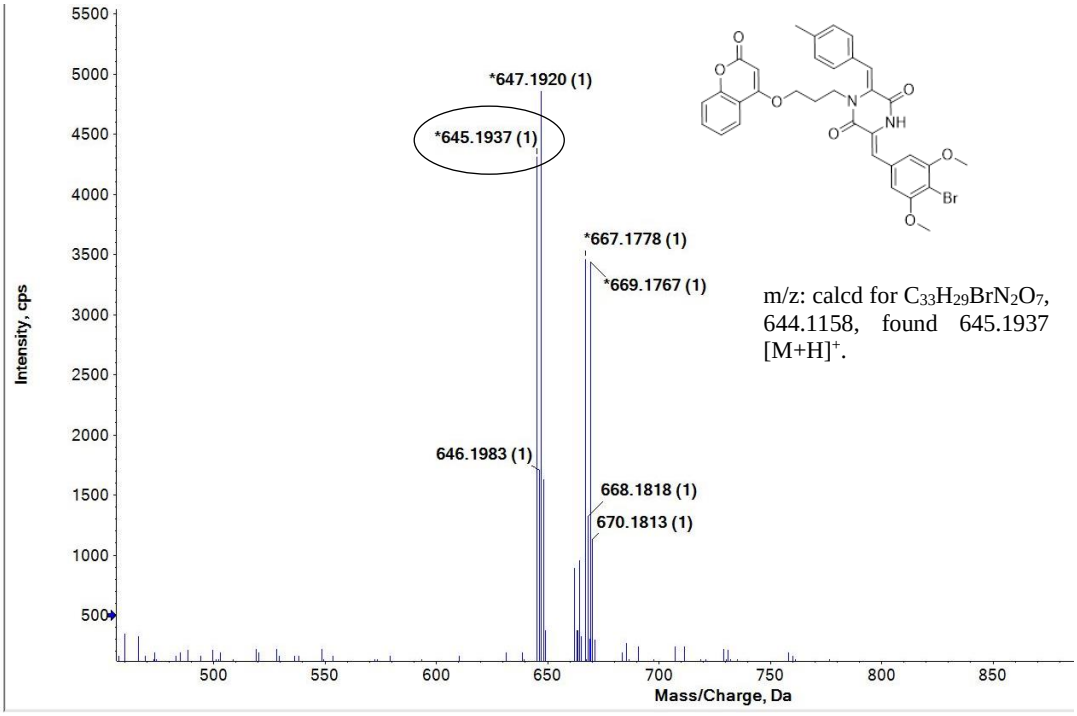

Figure 3.23. HRMS of compound **3.17b.**

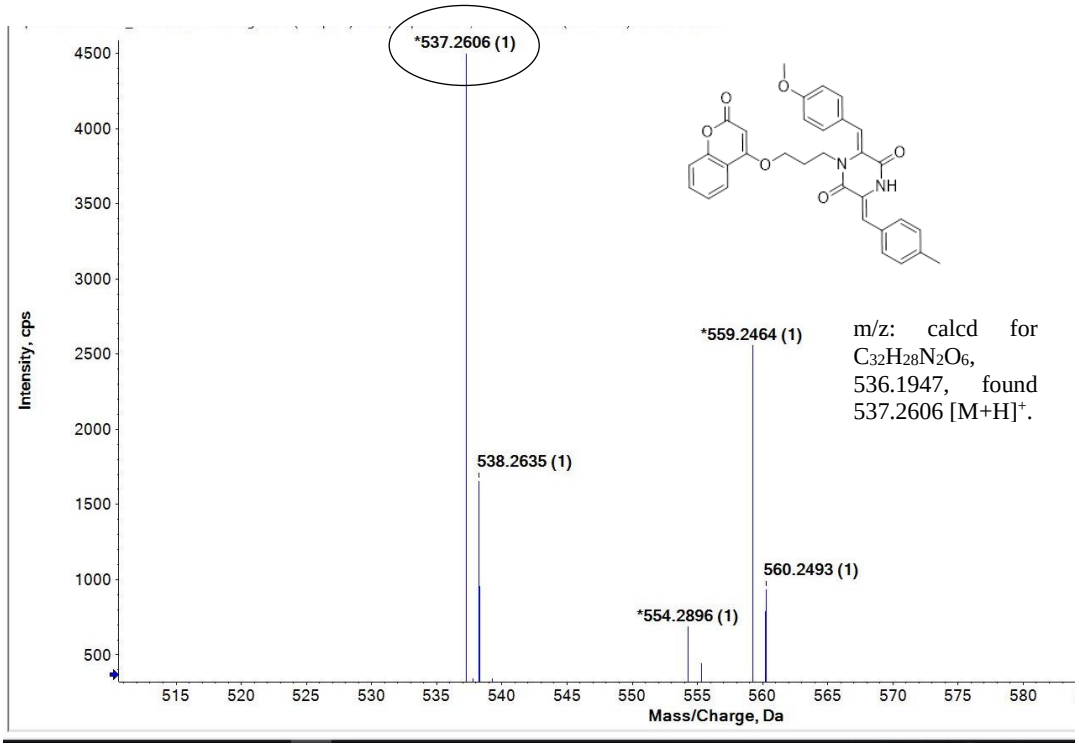

Figure 3.24. HRMS of compound **3.17c.**

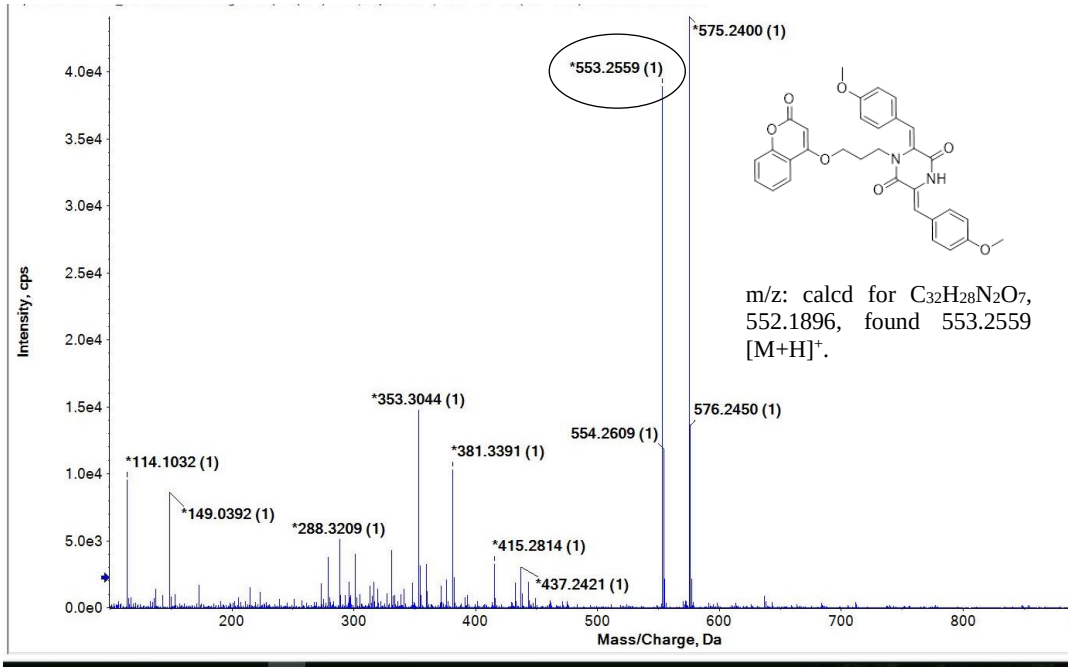

Figure 3.25. HRMS of compound **3.17d.**

CHAPTER 4

DESIGN AND DEVELOPMENT OF NOVEL HYBRIDS OF BIS-4-HYDROXYCOUMARIN DERIVATIVES AS ANTHELMINTIC AGENTS

CHAPTER 4

DESIGN AND DEVELOPMENT OF NOVEL HYBRIDS OF BIS-4-HYDROXYCOUMARIN DERIVATIVES AS ANTHELMINTIC AGENTS

4.1. Background

Helminthic infections pose a significant global health concern, particularly in impoverished regions where poor sanitation and limited access to healthcare services facilitate the spread of parasitic worms. These infections affect over billions of people worldwide and contribute to malnutrition, impaired cognitive development, and economic hardship. Helminths can infect both humans and animals via ingestion of eggs or larvae, as well as through skin penetration, leading to infestation of various tissues, organs, and organ systems (Laohapaisan et al., 2023). Soil-transmitted helminth infections are especially widespread, affecting approximately 1.5 billion people globally (Kumar et al., 2025).

Helminth infections are commonly treated with several classes of anthelmintic drugs such as such as benzimidazoles, macrocyclic lactones and nicotinic acetylcholine receptor agonists. Many of these agents exert their parasitic effects by inhibiting microtubule polymerization, thereby disrupting the growth of parasite and cellular processes. The polymerization and depolymerization of microtubules depend on the stability and solubility of the α/β-tubulin heterodimer, which serves as the fundamental unit of microtubules (Aguayo-Ortiz, Méndez-Lucio, Medina-Franco, et al., 2013). Preferably, a good anthelmintic should exhibit a broad spectrum of activity, achieve a high cure rate with a single therapeutic dose, and exhibit minimal toxicity to the host (Basumatary et al., 2020). However, currently available anthelmintics often show limited efficacy against certain helminth species and may cause significant adverse effects, including apoptosis and mitotic arrest. Additionally, the growing problem of drug resistance underscores the urgent need for the development of novel therapeutic agents with enhanced safety, efficacy, and resistance profiles (Geary et al., 2012; Paveley & Bickle, 2013).

As mentioned in section (Chapter 1, section 1.7), bis-coumarins have attracted attention in medicinal chemistry due to their wide-ranging biological activities, including antiparasitic, anticancer, antibacterial, antifungal, anti-HCV, anti-inflammatory, anti-HIV, antimalarial, antitubercular, anti-Alzheimer, and antipsychotic effects. Structural modifications, particularly the introduction of various functional groups, have been shown to enhance their potency and selectivity. Secondary amines, on the other hand, are important pharmacophores found in numerous bioactive molecules, valued for their hydrogen-bonding potential and favorable pharmacokinetic profiles. Therefore, functionalizing bis-coumarins with secondary amine groups via a linker offers a promising strategy for creating novel hybrid molecules with improved anthelmintic properties. To illustrate this approach, several coumarin and bis-coumarin derivatives, some of which are functionalised with secondary amines via linkers, are shown in Figure 4.1 (Basumatary et al., 2020; Kharrngi et al., 2021; Liu et al., 2016, 2021; Pan et al., 2016).

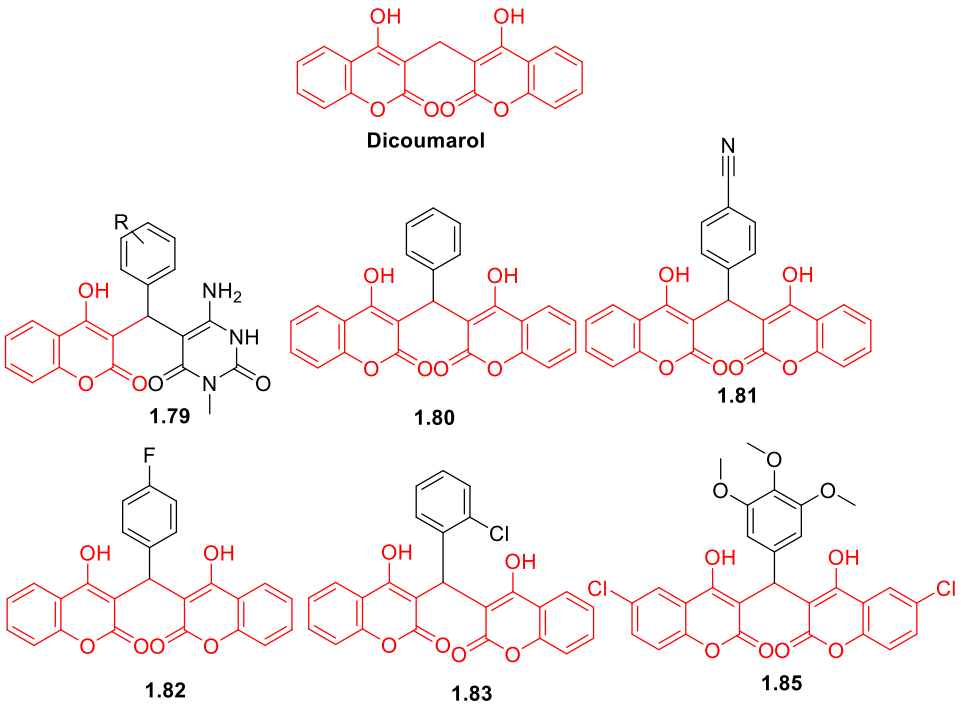

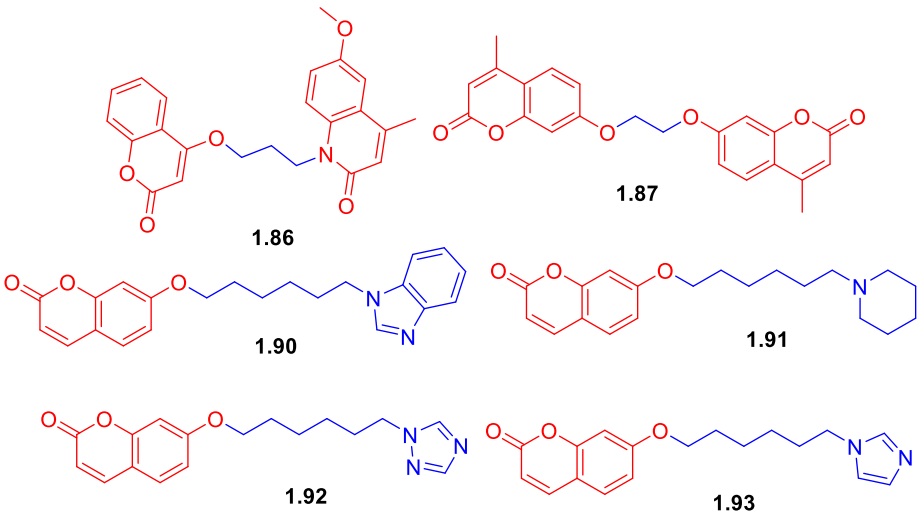

Figure 4.1. Chemical structures of some coumarin and bis-coumarin anthelmintic agents.

Microtubules have long been established as valuable therapeutic targets in cancer and other diseases, owing to their essential roles in cellular functions including mitosis, intracellular transport, and organelle organization (De Forges et al., 2012; Field et al., 2014; Jordan & Wilson, 2004). Microtubule-targeting agents (MTAs) bind to tubulin, disrupt its dynamic behavior, and are used clinically to treat both hematological malignancies and solid tumors. Several MTAs have also demonstrated efficacy as anti-helminthic agents. Under normal conditions, tubulin maintains a dynamic equilibrium in which subunit assembly and disassembly are balanced. Tubulin binding drugs disturbs this equilibrium and leads to depletion of the microtubule network, and accumulation of free tubulin. Since microtubules are critical for numerous cellular processes, their disruption ultimately causes the death of the parasite.

MTAs are broadly classified into two main categories: microtubule-stabilizing agents and microtubule-destabilizing agents. Microtubule-stabilizing agents (MSAs) promote the polymerization of tubulin and protect microtubules from depolymerization (Kanakkanthara et al., 2013). However, microtubule-destabilizing agents (MDAs) induce depolymerization of existing microtubules or inhibit tubulin heterodimers from assembling into polymers (Kanakkanthara et al., 2013). Furthermore, MSAs can be further subdivided according to their tubulin-binding sites.

One group, the taxane-site binding agents, includes compounds such as paclitaxel, docetaxel, discodermolide, epothilones, and zampanolide (Prota et al., 2013; Yang & Horwitz, 2017). Another group, the peloruside/laulimalide-site binding agents, includes peloruside A and laulimalide (Kanakkanthara et al., 2016) (Figure 4.1). Similarly, destabilizing agents are categorized based on their binding domains. The vinca domain-binding agents include vinblastine, vincristine, and halichondrin B (Cormier et al., 2010). The colchicine domain-binding agents, such as combretastatins and 2-methoxyestradiol, bind to a different binding site (Li et al., 2017). Other classes include maytansine site-binding agents, such as maytansine, rhizoxin, and PM60184 (Prota et al., 2014), and pironetin site-binding agents, such as pironetin (Prota et al., 2016) (Figure 4.2).

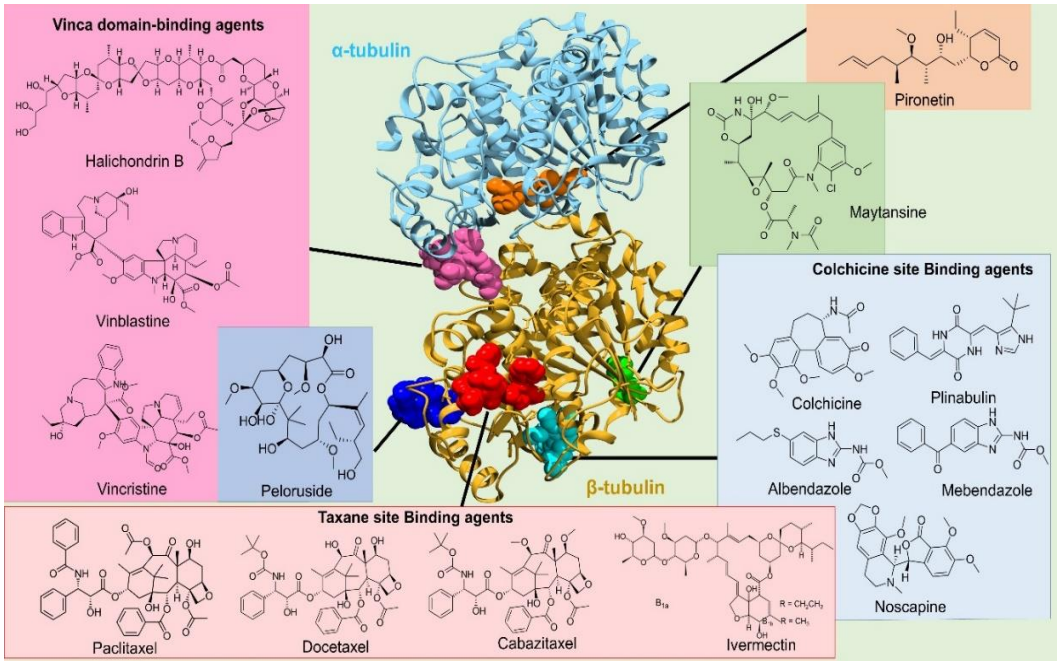

Figure 4.2. Known pharmacological binding sites of tubulin represented as a colored surface. α-Tubulin is shown in blue, and β-tubulin is shown in yellow. Representative pharmacological compounds corresponding to each binding site are also depicted. Taxane binding site (red), colchicine binding site (cyan), maytansine (green), peloruside (blue), vinca binding site (pink), pironetin (orange).

4.2. Present Work

Several anthelmintic drugs exert their activity by binding selectively to β-Tubulin of nematodes, cestodes and fluke, thereby disrupting microtubule structure and function. Anthelmintic agents from benzimidazole class like albendazole and mebendazole are microtubule stabilizing agents and bind in the colchicine binding pocket of the β-tubulin monomer of the parasite and thereby inhibit microtubule polymerization.

Ivermectin, a broad-spectrum anthelmintic, has been reported as a microtubule stabilizer (Ashraf et al., 2015; Ashraf & Prichard, 2016; J. Liu et al., 2020). Similarly, a naturally occurring dicoumarol (**1**) has also been reported to stabilize microtubules, thereby preventing their depolymerization (Madari et al., 2003). Furthermore, based on our preliminary molecular docking study, we hypothesized that the designed compounds would bind in the taxane pocket of β-tubulin. Therefore, in this study, we report the design and synthesis of a series of novel hybrids of bis-4-hydroxycoumarin derivatives linked to secondary amines and evaluate their anthelmintic activity (Figure 4.3). The rationale behind this approach lies in the synergistic potential of combining the bioactive bis-4-hydroxycoumarin core with secondary amine functionalities to yield compounds capable of targeting parasitic organisms effectively.

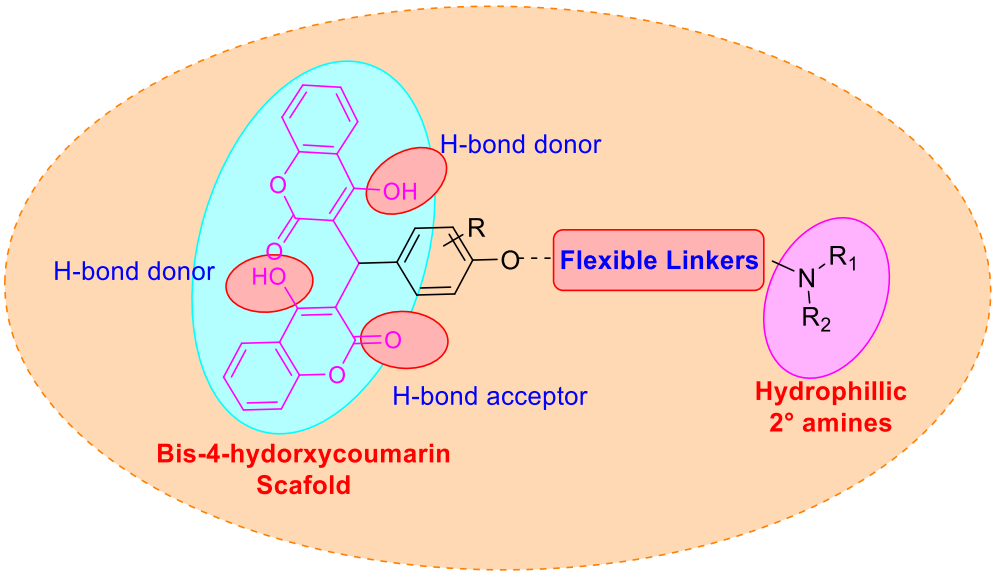

Figure 4.3. Molecular design of bis-4-hydroxycoumarin hybrids

4.3. Materials and Methods

Unless otherwise specified, all chemicals and reagents were obtained from commercial suppliers and used as received, without further purification. Product characterization was performed using High-Resolution Mass Spectrometry (HRMS), ^{1}H NMR, and ^{13}C NMR. High-resolution mass spectra were recorded on an SCIEX Model-X500R QTOF in positive ion mode with internal calibration. NMR spectra were collected in DMSO-d_6 or $CDCl_3$ using a Bruker Avance spectrometer, operating at 500 or 600 MHz for ^{1}H NMR and 125 MHz for ^{13}C NMR, with tetramethylsilane (TMS) as the internal standard. Chemical shifts (δ) are reported in ppm relative to residual $CDCl_3$ (δ 7.26) and DMSO-d_6 (δ 2.50) for ^{1}H NMR, and $CDCl_3$ (δ 77.16) and DMSO-d_6 (δ 39.52) for ^{13}C NMR. Melting points were determined in open capillaries using a melting point apparatus and are uncorrected. Reaction progress was monitored by thin-layer chromatography (TLC) on Merck 60G F_{254} pre-coated aluminum plates, visualized under UV light or by staining with iodine vapors or potassium permanganate solution ($KMnO_4$, Na_2CO_3, deionized water). Flash chromatography separation was performed with silica gel (230–400 mesh). All solvents were of analytical grade.

4.3.1. Schemes for the Synthesis of Novel Bis-4-hydroxycoumarin Hybrids

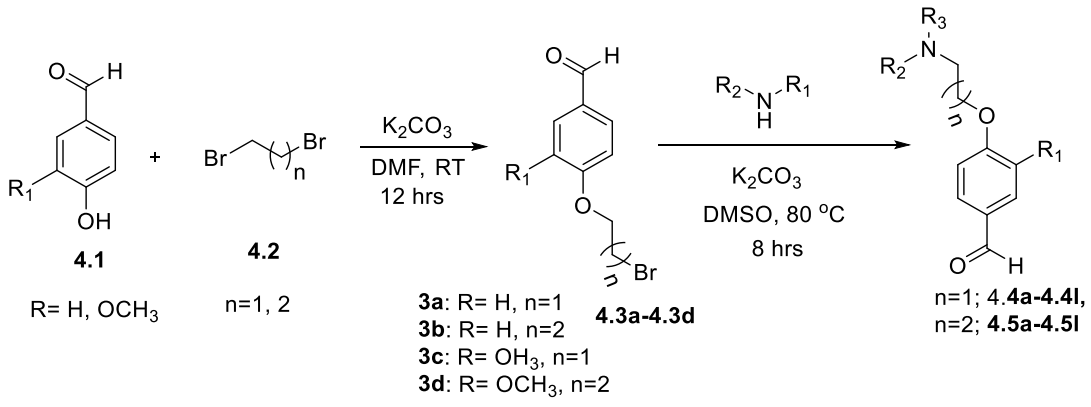

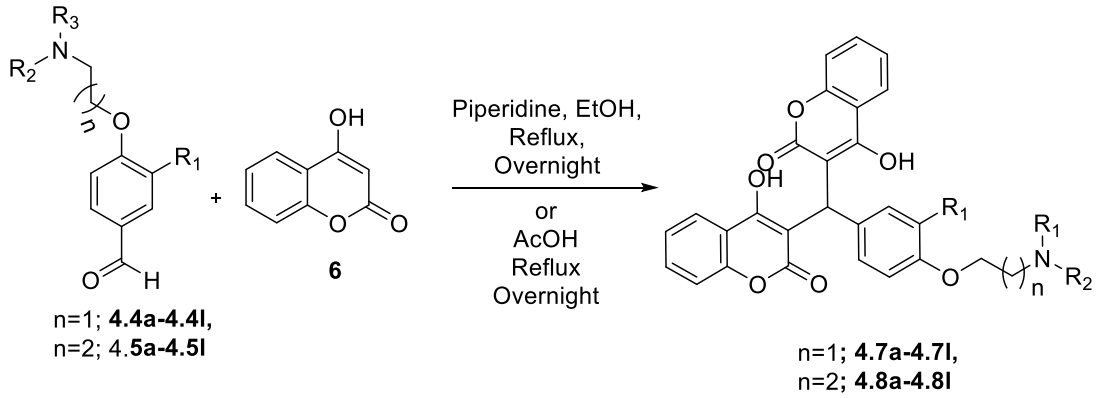

Scheme 4.1. Synthetic route for novel bis-4-hydroxycoumarin derivatives.

4.3.2. General Procedure for the Synthesis of Substituted Aldehydes 4.3a-4.3d

To a stirred solution of 4-hydroxy-3-methoxybenzaldehyde (26.29 mmol) or 4-hydroxybenzaldehyde and anhydrous potassium carbonate (52.57 mmol) in DMF (60 mL) was added the appropriate aliphatic dibromoalkane (105.16 mmol). The reaction mixture was stirred at room temperature overnight. Upon completion of the reaction, as indicated by TLC, the mixture was poured into cold water and extracted with EtOAc (4 × 40 mL). The combined organic layers were dried over anhydrous Na_2SO_4 and concentrated under reduced pressure using a rotary evaporator. The crude product was purified by flash column chromatography on silica gel, eluting with hexane/EtOAc, to afford the desired compound.

4.3.2.1. 4-(2-bromoethoxy)benzaldehyde (4.3a)

White solid; Yield: 55%; ^{1}H NMR (500 MHz, $CDCl_3$) δ 9.86 (s, 1H), 7.89 – 7.83 (m, 2H), 7.03 – 6.97 (m, 2H), 4.34 (t, *J* = 3.5 Hz, 2H), 3.75 (t, *J* = 3.5 Hz, 2H). ^{13}C NMR (125 MHz, $CDCl_3$) δ 190.89, 163.12, 132.01, 130.33, 115.38, 68.56, 29.20. HRMS (ESI-TOF) m/z: calcd for $C_9H_9BrO_2$ 227.9785, found 228.9871 $[M+H]^+$.

4.3.2.2. 4-(3-bromopropoxy)benzaldehyde (4.3b)

White solid; Yield: 56%; ^{1}H NMR (500 MHz, $CDCl_3$) δ 9.86 (s, 1H), 7.89 – 7.83 (m, 2H), 7.13 – 7.07 (m, 2H), 4.10 (t, *J* = 5.4 Hz, 2H), 3.60 (t, *J* = 5.0 Hz, 2H), 2.45 (q, *J* = 5.2 Hz, 2H). ^{13}C NMR (125 MHz, $CDCl_3$) δ 190.89, 163.63, 132.01, 130.32, 114.82, 66.81, 32.42, 29.97. HRMS (ESI-TOF) m/z: calcd for $C_{10}H_{11}BrO_2$ 241.9942, found 242.9967 $[M+H]^+$.

4.3.2.3. 4-(2-Bromoethoxy)-3-methoxybenzaldehyde (4.3c)

White solid; Yield: 49%; ^{1}H NMR (500 MHz, $CDCl_3$) δ 9.88 (s, 1H), 7.44 (dd, *J* = 5.9, 2.1 Hz, 2H), 7.01 (d, *J* = 8.6 Hz, 1H), 4.42 (t, *J* = 6.9 Hz, 2H), 3.95 (s, 3H), 3.70 (t, *J* = 7.1 Hz, 2H); ^{13}C·NMR (125 MHz, $CDCl_3$) δ 191.11, 153.05, 150.03, 130.84, 126.55, 112.35, 109.72, 68.77, 56.29, 29.65; HRMS (ESI-TOF) m/z: calcd for $C_{10}H_{11}BrO_3$, 259.9872, found 260.9875 $[M+H]^+$.

4.3.2.4. 4-(3-Bromopropoxy)-3-methoxybenzaldehyde (4.3d)

White solid; Yield: 56%; ^{1}H NMR (600 MHz, $CDCl_3$) δ 9.86 (s, 1H), 7.47 – 7.39 (m, 2H), 7.01 (d, *J* = 8.1 Hz, 1H), 4.25 (t, *J* = 5.9 Hz, 2H), 3.91 (s, 3H), 3.64 (t, *J* = 6.3 Hz, 2H), 2.42 (p, *J* = 6.1 Hz, 2H). ^{13}C·NMR (125 MHz, $CDCl_3$) δ 191.11, 153.63, 149.86, 130.25, 127.14, 111.79, 109.09, 66.79, 56.36, 32.38, 30.13. HRMS (ESI-TOF) m/z: calcd for $C_{11}H_{13}BrO_3$, 272.0048, found 273.0129 $[M+H]^+$.

4.3.3. General Procedure for the Synthesis of Amino Substituted Aldehydes (4.4a-4.4l, 4.5a-4.5l)

Compound **4.3** (3.66 mmol), anhydrous K_2CO_3 (21.96 mmol), and the desired secondary amine (10.98 mmol) were stirred in DMSO (10 mL) at 80 °C for 8 h. Upon completion of the reaction, as indicated by TLC, the mixture was poured into ice-cold water (60 mL) and extracted with EtOAc (5 × 20 mL). The combined organic layers were washed with brine (3 × 50 mL), dried over anhydrous Na_2SO_4, and concentrated under reduced pressure using a rotary evaporator to yield the secondary amine substituted aldehydes (**4.4a-4.4l, 4.5a-4.5l**) as an oily residue. The crude products were used directly in subsequent reactions without further purification.

4.3.4. General procedure for the synthesis of amino substituted aldehydes (4.4i-4.4j, 4.5i-4.5j)

Compound **3** (3.66 mmol), anhydrous K_2CO_3 (5.63 mmol), and phthalimide (2.81 mmol) were stirred in DMF (15 mL) at room temperature overnight. Upon completion of the reaction, as indicated by TLC, the mixture was poured into ice-cold water (50 mL), and the resulting precipitate was collected by filtration. The solids were recrystallized from EtOH to afford the pure compound as white solids.

4.3.5. General Procedure for the Synthesis of Bis-4-hydroxycoumarin Hybrids (4.7a-4.7l, 4.8a-4.8l)

A mixture of 4-hydroxycoumarin (4 mmol), amino-substituted aldehyde **4** or **5** (2 mmol), and a few drops of piperidine in EtOH was refluxed for 7 hours. Upon completion of the reaction, as indicated by TLC, the mixture was poured into ice-cold water (50 mL) and acidified with dilute HCl. The resulting precipitate was collected by filtration. The solids were recrystallised from methanol or ethanol to afford the pure products. For phthalimide-substituted aldehydes, the compounds were refluxed with 4-hydroxycoumarin for 7 hours in acetic acid. The resulting precipitate was filtered, washed with water followed by aqueous $NaHCO_3$, and recrystallised from methanol to yield the desired products.

4.3.5.1. 3,3'-((4-(2-morpholinoethoxy)phenyl)methylene)bis(4-hydroxy-2H-chromen-2-one) (4.7a)

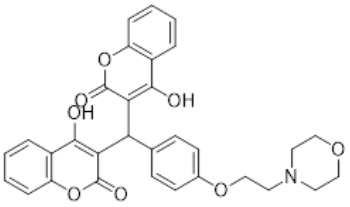

Light yellow solid; Yield: 78%; ^{1}H NMR (500 MHz, DMSO-d_6) δ 17.62 (s, 1H), 9.79 (s, 1H), 7.79 (d, J = 8.0 Hz, 2H), 7.49 (t, J = 7.8 Hz, 2H), 7.28 – 7.18 (m, 4H), 7.03 (d, J = 8.1 Hz, 2H), 6.82 (d, J = 9.3 Hz, 2H), 6.21 (s, 1H), 4.34 – 4.20 (m, 2H), 4.01 – 3.87 (m, 2H), 3.72 – 3.48 (m, 6H), 3.18 – 3.15 (m, 2H). ^{13}C NMR (125 MHz, DMSO-d_6) δ 168.17, 165.07, 155.67, 153.04, 135.77, 131.42, 128.29, 124.61, 123.40, 120.50, 116.00, 114.54, 104.12, 63.90, 62.40, 55.87, 52.34, 35.96. HRMS (ESI-TOF) m/z: calcd for $C_{31}H_{27}NO_8$ 541.1736, found 542.1829 $[M+H]^+$.

44.3.5.2. 3,3'-((3-methoxy-4-(2-morpholinoethoxy)phenyl)methylene)bis(4-hydroxy-2H-chromen-2-one) (4.7b)

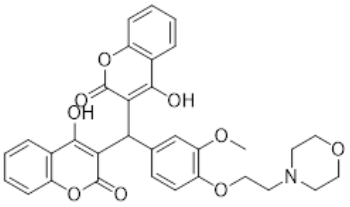

Light yellow solid; Yield: 66%; ^{1}H NMR (500 MHz, DMSO-d_6) δ 17.59 (s, 1H), 9.84 (s, 1H), 7.80 (d, J = 8.0 Hz, 2H), 7.49 (t, J = 6.9 Hz, 2H), 7.29 – 7.19 (m, 4H), 6.87 (d, J = 8.4 Hz, 1H), 6.73 (s, 1H), 6.66 (d, J = 8.4 Hz, 1H), 6.22 (s, 1H), 4.24 (t, J = 4.9 Hz, 2H), 4.02 – 3.94 (m, 2H), 3.68 (t, J = 12.4 Hz, 2H), 3.58 – 3.48 (m, 7H), 3.26 – 3.17 (m, 2H). ^{13}C NMR (125 MHz, DMSO-d_6) δ

168.33, 165.16, 153.07, 149.64, 145.11, 137.77, 131.46, 124.65, 123.46, 120.71, 120.50, 119.61, 116.04, 115.80, 112.05, 104.12, 64.64, 63.84, 56.04, 55.96, 52.50, 36.47. HRMS (ESI-TOF) m/z: calcd for $C_{32}H_{29}NO_9$, 571.1842, found 572.1922 $[M+H]^+$.

4.3.5.3. 3,3'-((4-(3-morpholinopropoxy)phenyl)methylene)bis(4-hydroxy-2H-chromen-2-one) (4.8a)

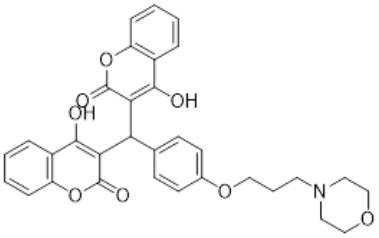

Light yellow solid; Yield: 54%; ^{1}H NMR (500 MHz, DMSO-d_6) δ 17.63 (s, 1H), 9.46 (s, 1H), 7.79 (d, *J* = 7.9 Hz, 2H), 7.49 (t, *J* = 7.5 Hz, 2H), 7.30 – 7.18 (m, 4H), 7.01 (d, *J* = 8.1 Hz, 2H), 6.75 (d, *J* = 8.1 Hz, 2H), 6.20 (s, 1H), 4.06 – 3.92 (m, 4H), 3.69 – 3.37 (m, 6H), 3.14 – 3.03 (m, 2H), 2.17 – 1.99 (m, 2H). ^{13}C NMR (125 MHz, DMSO-d_6) δ 168.16, 165.08, 156.22, 153.04, 135.15, 131.41, 128.23, 124.61, 123.39, 120.51, 116.00, 114.33, 104.16, 65.06, 64.08, 54.27, 51.89, 35.93, 23.89. HRMS (ESI-TOF) m/z: calcd for $C_{32}H_{29}NO_8$ 555.1893, found 556.1959 $[M+H]^+$.

4.3.5.4. 3,3'-((3-methoxy-4-(3-morpholinopropoxy)phenyl)methylene)bis(4-hydroxy-2H-chromen-2-one) (4.8b)

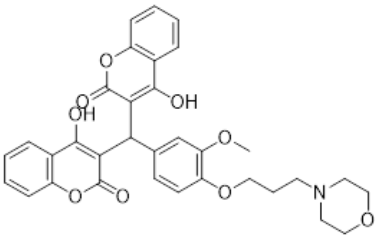

Light yellow solid; Yield: 69%; ^{1}H NMR (600 MHz, DMSO-d_6) δ 17.59 (s, 1H), 8.97 (s, 1H), 7.80 (d, *J* = 7.8 Hz, 2H), 7.48 (d, *J* = 7.7 Hz, 2H), 7.24 (d, *J* = 19.0 Hz, 4H), 6.64 (d, *J* = 8.9 Hz, 1H), 6.20 (s, 1H), 3.98 (t, *J* = 6.0 Hz, 2H), 3.54 (s, 3H), 3.47 – 3.32 (m, 4H), 3.31 – 2.99 (m, 6H), 2.07 (p, *J* = 6.7 Hz, 2H). ^{13}C NMR (125 MHz, DMSO-d_6) δ 168.25, 165.08, 153.03, 149.14, 145.74, 136.41, 131.41, 124.61, 123.41, 120.51, 119.48, 116.01, 113.91, 111.97, 104.15, 98.01, 66.58, 64.04, 56.00, 54.72, 51.92, 36.34, 23.91. HRMS (ESI-TOF) m/z: calcd for $C_{33}H_{31}NO_9$, 585.1998, found 586.2026 $[M+H]^+$.

4.3.5.5. 3,3'-((4-(2-(1H-imidazol-1-yl)ethoxy)phenyl)methylene)bis(4-hydroxy-2H-chromen-2-one) (4.7c)

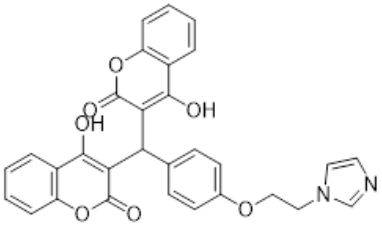

Whitish solid; Yield: 78%; ^{1}H NMR (600 MHz, DMSO-d_6) δ 17.62 (s, 1H), 9.16 (s, 1H), 7.84 – 7.77 (m, 3H), 7.67 (s, 1H), 7.50 (t, *J* = 7.7 Hz, 2H), 7.30 – 7.16 (m, 5H), 7.00 (d, *J* = 8.3 Hz, 2H), 6.74 (d, *J* = 8.3 Hz, 2H), 6.20 (s, 1H), 4.58 (t, *J* = 5.0 Hz, 2H), 4.30 (t, *J* = 5.0 Hz, 2H). ^{13}C NMR (125 MHz, DMSO-d_6) δ 168.23, 165.15, 155.83, 153.05, 136.43, 135.63, 131.42, 128.30, 124.64, 123.40, 122.86, 120.58, 120.51, 116.00, 114.43, 104.15, 66.32, 48.81, 35.98. HRMS (ESI-TOF) m/z: calcd for $C_{30}H_{22}N_2O_7$ 522.1427, found 523.1492 $[M+H]^+$.

4.3.5.6. 3,3'-((4-(2-(1H-imidazol-1-yl)ethoxy)-3-methoxyphenyl)methylene)bis(4-hydroxy-2H-chromen-2-one) (4.7d)

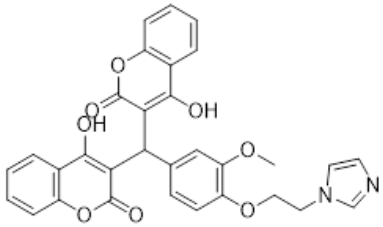

White solid; Yield: 79%; ^{1}H NMR (600 MHz, DMSO-d_6) δ 17.53 (s, 1H), 9.06 (s, 1H), 7.76 (d, *J* = 7.8 Hz, 3H), 7.62 (s, 1H), 7.45 (t, *J* = 7.5 Hz, 2H), 7.24 – 7.14 (m, 4H), 6.73 (d, *J* = 8.0 Hz, 1H), 6.65 (s, 1H), 6.59 (d, *J* = 8.1 Hz, 1H), 6.16 (s, 1H), 4.51 (t, *J* = 4.9 Hz, 2H), 4.24 (t, *J* = 5.2 Hz, 2H), 3.45 (s, 3H). ^{13}C NMR (125 MHz, DMSO-d_6) δ 168.29, 165.11, 153.03, 149.40, 145.38, 137.29, 136.46, 131.45, 124.63, 123.44, 122.89, 120.47, 120.35, 119.62, 116.02, 115.18, 112.29, 104.09, 68.06, 56.15, 48.97, 36.37. HRMS (ESI-TOF) m/z: calcd for $C_{31}H_{24}N_2O_8$ 552.1532, found 553.1590 $[M+H]^+$.

4.3.5.7. 3,3'-((4-(3-(1H-imidazol-1-yl)propoxy)phenyl)methylene)bis(4-hydroxy-2H-chromen-2-one) (4.8c)

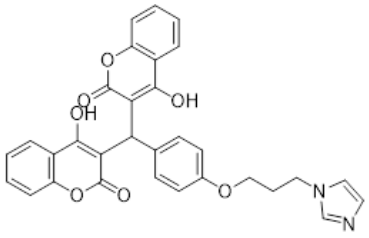

White solid; Yield: 71%; ^{1}H NMR (500 MHz, DMSO-d_6) δ 17.63 (s, 1H), 9.06 (s, 1H), 7.85 – 7.74 (m, 3H), 7.63 (s, 1H), 7.49 (t, *J* = 7.5 Hz, 2H), 7.33 – 7.13 (m, 5H), 6.98 (d, *J* = 8.1 Hz, 2H), 6.68 (d, *J* = 8.1 Hz, 2H), 6.19 (s, 1H), 4.34 (t, *J* = 6.7 Hz, 2H), 3.93 (t, *J* = 6.2 Hz, 2H), 2.25 (p, *J* = 6.5 Hz, 2H). ^{13}C NMR (125 MHz, DMSO-d_6) δ 168.14, 165.09, 156.30, 153.11, 136.05, 135.43, 131.27, 128.27, 124.64, 123.27, 122.68, 120.65,

120.55, 115.92, 115.73, 114.35, 104.20, 65.19, 46.92, 36.06, 29.72. HRMS (ESI-TOF) m/z: calcd for $C_{31}H_{24}N_2O_7$ 536.1583, found 537.1670 $[M+H]^+$.

4.3.5.8. 3,3'-((4-(3-(1H-imidazol-1-yl)propoxy)-3-methoxyphenyl)methylene)bis(4-hydroxy-2H-chromen-2-one) (8d)

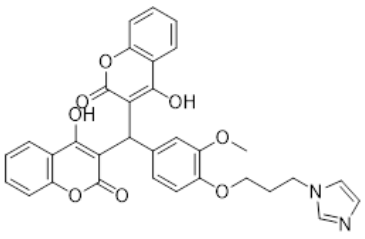

White solid; Yield: 80%; ^{1}H NMR (600 MHz, DMSO-d_6 δ 17.55 (s, 1H), 9.05 (s, 1H), 7.80 – 7.74 (m, 3H), 7.62 (s, 1H), 7.46 (t, *J* = 7.7 Hz, 2H), 7.24 – 7.15 (m, 4H), 6.71 (d, *J* = 9.1 Hz, 1H), 6.64 (s, 1H), 6.58 (d, *J* = 8.3 Hz, 1H), 6.16 (s, 1H), 4.31 (t, *J* = 6.7 Hz, 2H), 3.89 (t, *J* = 5.5 Hz, 2H), 3.49 (s, 3H), 2.22 (p, *J* = 6.0, 5.5 Hz, 2H). ^{13}C NMR (125 MHz, DMSO-d_6) δ 168.32, 165.19, 153.03, 149.18, 145.87, 136.32, 136.05, 131.45, 124.64, 123.46, 122.56, 120.54, 120.49, 119.49, 116.03, 114.07, 112.00, 104.16, 66.42, 55.97, 46.93, 36.34, 29.75. HRMS (ESI-TOF) m/z: calcd for $C_{32}H_{26}N_2O_8$ 566.1689, found 567.1724 $[M+H]^+$.

4.3.5.9. 3,3'-((4-(2-(piperidin-1-yl)ethoxy)phenyl)methylene)bis(4-hydroxy-2H-chromen-2-one) (4.7e)

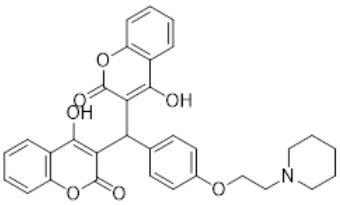

White solid; Yield: 69%; ^{1}H NMR (600 MHz, DMSO-d_6) δ 17.59 (s, 1H), 9.21 (s, 1H), 7.80 (d, *J* = 7.8 Hz, 2H), 7.49 (t, *J* = 7.8 Hz, 2H), 7.29 – 7.16 (m, 4H), 7.04 (d, *J* = 8.2 Hz, 2H), 6.81 (d, *J* = 6.6 Hz, 2H), 6.23 (s, 1H), 4.25 (t, *J* = 4.8 Hz, 2H), 3.59 – 3.35 (m, 4H), 3.10 – 2.84 (m, 2H), 1.89 – 1.24 (m, 6H). ^{13}C NMR (125 MHz, DMSO-d_6) δ 168.18, 165.09, 155.69, 153.05, 135.78, 131.45, 128.32, 124.63, 123.42, 120.51, 116.00, 114.55, 104.14, 64.94, 57.02, 55.06, 36.39, 24.36, 23.08. HRMS (ESI-TOF) m/z: calcd for $C_{32}H_{29}NO_7$ 539.1944, found 540.1987 $[M+H]^+$.

4.3.5.10. 3,3'-((3-methoxy-4-(2-(piperidin-1-yl)ethoxy)phenyl)methylene)bis(4-hydroxy-2H-chromen-2-one) (4.7f)

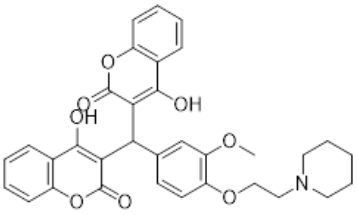

Yellowish solid; Yield: 82%; ^{1}H NMR (600 MHz, DMSO-d_6) δ 17.61 (s, 1H), 9.21 (s, 1H), 7.81 (d, J = 7.7 Hz, 2H), 7.49 (t, J = 7.8 Hz, 2H), 7.30 – 7.16 (m, 4H), 6.86 (d, J = 8.6 Hz, 1H), 6.74 (s, 1H), 6.67 (d, J = 8.4 Hz, 1H), 6.22 (s, 1H), 4.22 (t, J = 5.3 Hz, 2H), 3.60 – 3.50 (m, 5H), 3.48 – 3.40 (m, 2H), 3.05 – 2.94 (m, 2H), 1.85 – 1.33 (m, 6H). ^{13}C NMR (125 MHz, DMSO-d_6) δ 169.30, 166.45, 154.13, 149.94, 145.86, 138.69, 132.13, 125.07, 123.81, 121.18, 119.89, 116.77, 116.22, 113.16, 104.28, 68.24, 56.06, 54.71, 54.38, 35.51, 27.07, 23.02. HRMS (ESI-TOF) m/z: calcd for $C_{33}H_{31}NO_8$ 569.2049, found 570.2094 $[M+H]^+$.

4.3.5.11. 3,3'-((4-(3-(piperidin-1-yl)propoxy)phenyl)methylene)bis(4-hydroxy-2H-chromen-2-one) (4.8e)

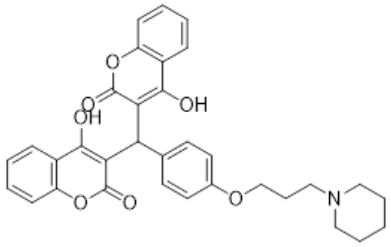

White solid; Yield: 65%; ^{1}H NMR (600 MHz, DMSO-d_6 δ 17.63 (s, 1H), 8.88 (s, 1H), 7.79 (d, J = 8.0 Hz, 2H), 7.49 (t, J = 7.4 Hz, 2H), 7.28 – 7.17 (m, 4H), 7.00 (d, J = 8.1 Hz, 2H), 6.74 (d, J = 9.2 Hz, 2H), 6.20 (s, 1H), 3.98 (t, J = 6.0 Hz, 2H), 3.53 – 3.38 (m, 2H), 3.24 – 3.10 (m, 2H), 2.94 – 2.77 (m, 2H), 2.13 – 2.01 (m, 2H), 1.87 – 1.27 (m, 6H). ^{13}C NMR (125 MHz, DMSO-d_6) δ 168.25, 165.19, 156.27, 153.07, 135.07, 131.45, 128.24, 124.65, 123.43, 120.54, 116.00, 114.32, 104.20, 65.13, 54.15, 52.83, 35.98, 24.15, 23.26, 21.81. HRMS (ESI-TOF) m/z: calcd for $C_{33}H_{31}NO_7$ 553.2100, found 554.2156 $[M+H]^+$.

4.3.5.12. 3,3'-((3-methoxy-4-(3-(piperidin-1-yl)propoxy)phenyl)methylene)bis(4-hydroxy-2H-chromen-2-one) (4.8f)

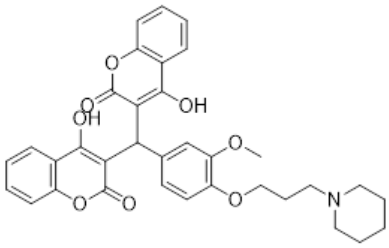

White solid; Yield: 74%; ^{1}H NMR (600 MHz, DMSO-d_6) δ 17.56 (s, 1H), 8.78 (s, 1H), 7.81 (dd, J = 7.8, 1.7 Hz, 2H), 7.50 (dd, J = 8.6, 7.2, Hz, 2H), 7.29 – 7.19 (m, 4H), 6.79 (d, J = 8.4 Hz, 1H), 6.70 (s, 1H), 6.65 (d, J = 8.4 Hz, 1H), 6.22 (s, 1H), 3.98 (t, J = 5.9 Hz, 2H), 3.59 – 3.43 (m, 5H), 3.18 (t, J = 7.8 Hz, 2H), 2.98 – 2.76 (m, 2H),

2.14 – 2.00 (m, 2H), 1.85 – 1.36 (m, 6H). ^{13}C NMR (125 MHz, DMSO-d_6) δ 169.27, 166.07, 154.01, 149.91, 145.85, 138.66, 132.05, 125.05, 123.76, 121.11, 119.85, 116.76, 116.24, 113.12, 104.35, 68.26, 56.09, 54.81, 54.41, 35.53, 27.21, 27.05, 23.03. HRMS (ESI-TOF) m/z: calcd for $C_{34}H_{33}NO_8$ 583.2206, found 584.2258 $[M+H]^+$.

4.3.5.13. 3,3'-((4-(2-(diethylamino)ethoxy)phenyl)methylene)bis(4-hydroxy-2H-chromen-2-one) (4.7g)

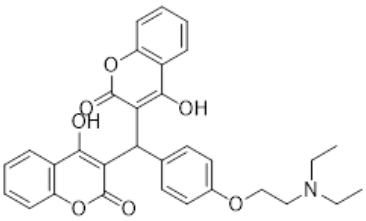

White solid; Yield: 75%; ^{1}H NMR (500 MHz, DMSO-d_6) δ 17.62 (s, 1H), 9.17 (s, 1H), 7.80 (d, *J* = 7.5 Hz, 2H), 7.50 (t, *J* = 7.4 Hz, 2H), 7.30 – 7.18 (m, 4H), 7.04 (d, *J* = 8.1 Hz, 2H), 6.81 (d, *J* = 8.6 Hz, 2H), 6.21 (s, 1H), 4.22 (t, *J* = 5.1 Hz, 2H), 3.55 – 3.41 (m, 2H), 3.28 – 3.12 (m, 4H), 1.20 (t, *J* = 7.2 Hz, 6H). ^{13}C NMR (125 MHz, DMSO-d_6) δ 168.19, 165.08, 155.65, 153.05, 135.80, 131.43, 128.31, 124.62, 123.40, 120.51, 116.00, 114.50, 104.13, 62.77, 51.01, 47.82, 35.99, 9.10. HRMS (ESI-TOF) m/z: calcd for $C_{31}H_{29}NO_7$ 527.1944, found 528.2014 $[M+H]^+$.

4.3.5.14. 3,3'-((4-(2-(diethylamino)ethoxy)-3-methoxyphenyl)methylene)bis(4-hydroxy-2H-chromen-2-one) (4.7h)

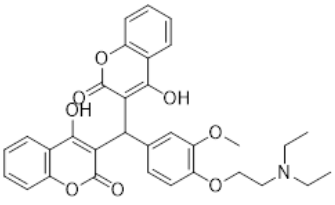

Yellowish solid; Yield: 79%; ^{1}H NMR (500 MHz, DMSO-d_6) δ 17.55 (s, 1H), 9.15 (s, 1H), 7.77 (d, *J* = 7.7 Hz, 2H), 7.46 (t, *J* = 7.8 Hz, 2H), 7.27 – 7.10 (m, 4H), 6.81 (d, *J* = 8.9 Hz, 1H), 6.70 (s, 1H), 6.63 (d, *J* = 8.3 Hz, 1H), 6.19 (s, 1H), 4.17 (t, *J* = 5.0 Hz, 2H), 3.52 (s, 3H), 3.47 – 3.38 (m, 2H), 3.26 – 3.13 (m, 4H), 1.18 (t, *J* = 7.1 Hz, 6H). ^{13}C NMR (125 MHz, DMSO-d_6) δ 168.30, 165.11, 153.05, 149.48, 145.16, 137.49, 131.46, 124.64, 123.45, 120.50, 119.55, 116.03, 115.15, 112.01, 104.11, 64.72, 56.08, 51.01, 48.01, 36.43, 9.14. HRMS (ESI-TOF) m/z: calcd for $C_{32}H_{31}NO_8$ 557.2049, found 558.2082 $[M+H]^+$.

4.3.5.15. 3,3'-((4-(3-(diethylamino)propoxy)phenyl)methylene)bis(4-hydroxy-2H-chromen-2-one) (4.8g)

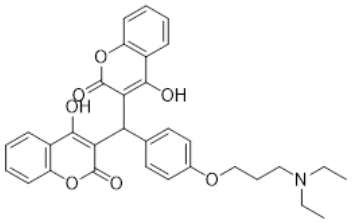

White solid; Yield: 68%; ^{1}H NMR (500 MHz, DMSO-d_6) δ 17.62 (s, 1H), 8.96 (s, 1H), 7.79 (d, *J* = 7.9 Hz, 2H), 7.49 (t, *J* = 7.9 Hz, 2H), 7.28 – 7.17 (m, 4H), 7.00 (d, *J* = 8.1 Hz, 2H), 6.75 (d, *J* = 9.2 Hz, 2H), 6.20 (s, 1H), 3.99 (t, *J* = 6.0 Hz, 2H), 3.24 – 3.10 (m, 6H), 2.12 – 1.99 (m, 2H), 1.18 (t, *J* = 7.3 Hz, 6H). ^{13}C NMR (125 MHz, DMSO-d_6) δ 168.14, 165.07, 156.23, 153.04, 135.15, 131.41, 128.23, 124.61, 123.39, 120.51, 116.00, 114.34, 104.16, 64.97, 48.86, 46.99, 35.92, 23.95, 9.13. HRMS (ESI-TOF) m/z: calcd for $C_{32}H_{31}NO_7$ 541.2100, found 542.2163 $[M+H]^+$.

4.3.5.16. 3,3'-((4-(3-(diethylamino)propoxy)-3-methoxyphenyl)methylene)bis(4-hydroxy-2H-chromen-2-one) (4.8h)

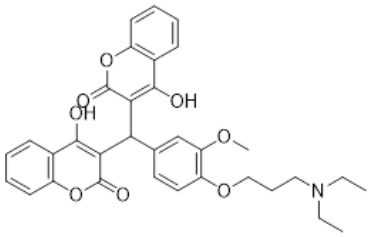

White solid; Yield: 58%; ^{1}H NMR (500 MHz, DMSO-d_6) δ 8.84 (s, 1H), 7.77 (d, *J* = 7.7 Hz, 2H), 7.46 (t, *J* = 7.4 Hz, 2H), 7.25 – 7.14 (m, 4H), 6.75 (d, *J* = 8.0 Hz, 1H), 6.66 (s, 1H), 6.61 (d, *J* = 8.1 Hz, 1H), 6.17 (s, 1H), 3.96 (t, *J* = 6.0 Hz, 2H), 3.50 (s, 3H), 3.19 – 3.08 (m, 6H), 2.05 – 1.95 (m, 2H), 1.14 (t, *J* = 7.2 Hz, 6H). ^{13}C NMR (125 MHz, DMSO-d_6) δ 168.22, 165.16, 153.03, 149.21, 145.82, 136.31, 131.49, 124.62, 123.48, 120.43, 119.57, 116.04, 114.13, 112.08, 104.19, 66.43, 56.08, 48.99, 47.06, 36.35, 23.97, 9.08. HRMS (ESI-TOF) m/z: calcd for $C_{33}H_{33}NO_8$ 571.2206, found 572.2278 $[M+H]^+$.

4.3.5.17. 2-(2-(4-(bis(4-hydroxy-2-oxo-2H-chromen-3-yl)methyl)phenoxy)ethyl) isoindoline-1,3-dione (4.7i)

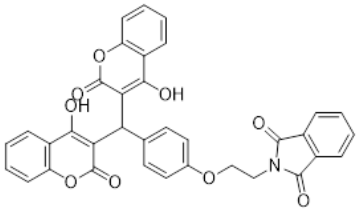

Whitish solid; Yield: 65%; ^{1}H NMR (600 MHz, DMSO-d_6) δ 7.92 – 7.80 (m, 6H), 7.55 (t, *J* = 7.8 Hz, 2H), 7.35 – 7.24 (m, 4H), 7.00 (d, *J* = 8.1 Hz, 2H), 6.73 (d, *J* = 8.0 Hz, 2H), 6.22 (s, 1H), 4.13 (t, *J* = 6.0 Hz, 2H), 3.94 (t, *J* = 5.9 Hz, 2H). ^{13}C NMR (125 MHz, DMSO-d_6) δ 168.22, 165.51, 164.87, 156.89, 152.60, 134.89, 132.72, 132.01, 131.55, 128.43, 124.56, 124.35, 123.57, 117.73, 116.63, 114.79, 105.11, 65.02, 37.54, 35.75. HRMS (ESI-TOF) m/z: calcd for $C_{35}H_{23}NO_9$ 601.1372, found 602.1447 $[M+H]^+$.

4.3.5.18. 2-(2-(4-(bis(4-hydroxy-2-oxo-2H-chromen-3-yl)methyl)-2-methoxyphenoxy)ethyl)isoindoline-1,3-dione (4.7j)

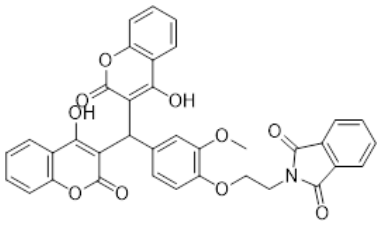

Whitish solid; Yield: 81%; ^{1}H NMR (500 MHz, $CDCl_3$) ^{1}H NMR (500 MHz, DMSO-D_6) δ 7.89 – 7.76 (m, 6H), 7.52 (t, J = 8.0 Hz, 2H), 7.31 – 7.20 (m, 4H), 6.77 (d, J = 9.2 Hz, 1H), 6.63 (s, 1H), 6.59 (d, J = 8.6 Hz, 1H), 6.19 (s, 1H), 4.08 (t, J = 6.0 Hz, 2H), 3.89 (t, J = 5.9 Hz, 2H), 3.36 (s, 3H). ^{13}C NMR (125 MHz, DMSO-d_6) δ 168.25, 165.37, 165.07, 152.64, 149.78, 146.63, 134.90, 133.38, 132.62, 132.10, 124.48, 124.35, 123.55, 119.65, 117.92, 116.60, 115.18, 112.77, 105.04, 66.39, 56.39, 37.63, 36.18. HRMS (ESI-TOF) m/z: calcd for $C_{36}H_{25}NO_{10}$ 631.1478, found 654.1365 $[M+Na]^+$.

4.3.5.19. 2-(3-(4-(bis(4-hydroxy-2-oxo-2H-chromen-3-yl)methyl)phenoxy)propyl)isoindoline-1,3-dione (4.8i)

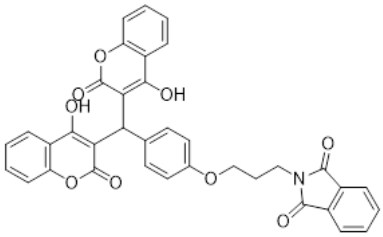

White solid; Yield: 63%; ^{1}H NMR (600 MHz, DMSO) δ 7.87 – 7.79 (m, 6H), 7.54 (t, J = 7.7 Hz, 2H), 7.32 – 7.23 (m, 4H), 6.96 (d, J = 8.3 Hz, 2H), 6.63 (d, J = 9.3 Hz, 2H), 6.21 (s, 1H), 3.94 (t, J = 6.0 Hz, 2H), 3.74 (t, J = 7.1 Hz, 2H), 2.02 (p, J = 6.1 Hz, 2H). ^{13}C NMR (125 MHz, DMSO-d_6) δ 168.46, 165.45, 165.03, 157.23, 152.64, 134.76, 132.66, 132.24, 131.33, 128.28, 124.50, 124.37, 123.47, 117.90, 116.60, 114.62, 105.08, 65.98, 35.75, 35.60, 28.23. HRMS (ESI-TOF) m/z: calcd for $C_{36}H_{25}NO_9$ 615.1529, found 616.1602 $[M+H]^+$.

4.3.5.20. 2-(3-(4-(bis(4-hydroxy-2-oxo-2H-chromen-3-yl)methyl)-2-methoxyphenoxy)propyl)isoindoline-1,3-dione (4.8j)

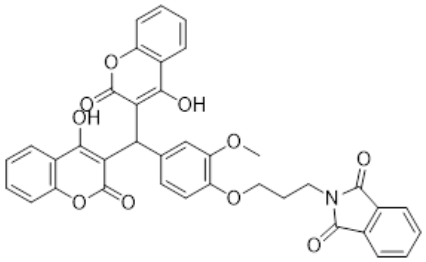

Whitish solid; Yield: 82%; ^{1}H NMR (500 MHz, $CDCl_3$) δ 11.28 (s, 2H), 8.06 – 7.99 (m, 2H), 7.84 – 7.80 (m, 2H), 7.70 – 7.67 (m, 2H), 7.61 (t, J = 7.9 Hz, 2H), 7.42 – 7.34 (m, 4H), 6.80 (d, J = 8.1 Hz, 1H), 6.71 (d, J = 8.3 Hz, 1H), 6.65 (s, 1H), 6.03 (s, 1H), 4.06 (t, J = 6.0 Hz, 2H), 3.90 (t, J = 6.7 Hz, 2H), 3.59 (s, 3H), 2.21 (p, J = 6.7 Hz, 2H). ^{13}C NMR (125 MHz, DMSO-d_6) δ 168.51, 165.83, 165.25, 152.75,

146.82, 134.71, 133.17, 132.37, 132.31, 129.19, 124.42, 124.21, 123.45, 119.42, 118.60, 116.45, 113.54, 112.09, 104.85, 67.08, 56.08, 36.18, 35.88, 28.40. HRMS (ESI-TOF) m/z: calcd for $C_{37}H_{27}NO_{10}$ 645.1634, found 646.1718 $[M+H]^+$.

4.3.5.21. 3,3'-((4-(2-(azepan-1-yl)ethoxy)phenyl)methylene)bis(4-hydroxy-2H-chromen-2-one) (4.7k)

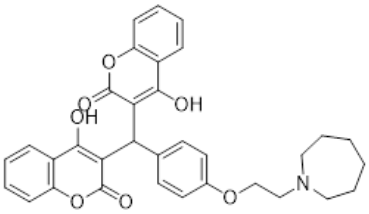

Whitish solid; Yield: 66%; ^{1}H NMR (500 MHz, DMSO-d_6) δ 17.63 (s, 1H), 9.37 (s, 1H), 7.80 (d, J = 7.8 Hz, 2H), 7.50 (t, J = 7.9 Hz, 2H), 7.31 – 7.17 (m, 4H), 7.04 (d, J = 8.3 Hz, 2H), 6.82 (d, J = 8.3 Hz, 2H), 6.21 (s, 1H), 4.24 (t, J = 4.9 Hz, 2H), 3.61 – 3.37 (m, 6H), 1.84 – 1.57 (m, 8H). ^{13}C NMR (125 MHz, DMSO-d_6) δ 168.21, 165.10, 155.70, 153.05, 135.78, 131.43, 128.31, 124.63, 123.40, 120.51, 116.00, 114.54, 104.13, 62.90, 55.62, 54.91, 35.99, 26.56, 23.29. HRMS (ESI-TOF) m/z: calcd for $C_{33}H_{31}NO_7$ 553.2100, found 554.2180 $[M+H]^+$.

4.3.5.22. 3,3'-((4-(2-(azepan-1-yl)ethoxy)-3-methoxyphenyl)methylene)bis(4-hydroxy-2H-chromen-2-one) (4.7l)

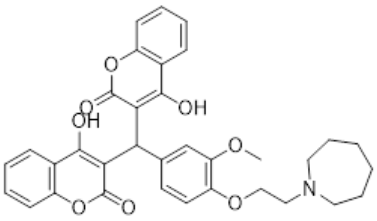

White solid; Yield: 68%; ^{1}H NMR (500 MHz, DMSO-d_6) δ 17.59 (s, 1H), 9.37 (s, 1H), 7.81 (d, J = 7.9 Hz, 2H), 7.50 (t, J = 7.3 Hz, 2H), 7.31 – 7.15 (m, 4H), 6.86 (d, J = 8.4 Hz, 1H), 6.73 (s, 1H), 6.66 (d, J = 8.3 Hz, 1H), 6.22 (s, 1H), 4.22 (t, J = 5.0 Hz, 2H), 3.56 (s, 3H), 3.54 – 3.39 (m, 6H), 1.90 – 1.53 (m, 8H). ^{13}C NMR (125 MHz, DMSO-d_6) δ 168.28, 165.08, 153.05, 149.60, 145.14, 137.67, 131.42, 124.64, 123.41, 120.51, 119.59, 116.01, 115.59, 112.08, 104.09, 65.06, 56.08, 55.89, 55.16, 36.44, 26.42, 23.47. HRMS (ESI-TOF) m/z: calcd for $C_{34}H_{33}NO_8$ 583.2206, found 584.2270 $[M+H]^+$.

4.3.5.23. 3,3'-((4-(3-(azepan-1-yl)propoxy)phenyl)methylene)bis(4-hydroxy-2H-chromen-2-one) (4.8k)

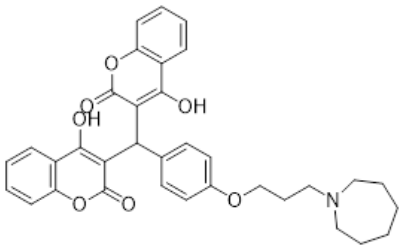

White solid; Yield: 76%; ^{1}H NMR (500 MHz, DMSO-d_6) δ 17.59 (s, 1H), 9.01 (s, 1H), 7.76 (d, J = 7.6 Hz, 2H), 7.46 (t, J = 7.4 Hz, 2H), 7.26 – 7.12 (m, 4H), 6.97 (d, J = 8.3 Hz, 2H), 6.71 (d, J = 8.3 Hz, 2H), 6.16 (s, 1H), 3.94 (t, J = 5.8 Hz, 2H), 3.40 – 3.31 (m, 2H), 3.21 – 3.06 (m, 4H), 2.09 – 1.98 (m, 2H), 1.87 – 1.63 (m, 4H), 1.61 – 1.49 (m, 4H). ^{13}C NMR (125 MHz, DMSO-d_6 δ 168.26, 165.19, 156.27, 153.06, 135.08, 131.44, 128.24, 124.65, 123.43, 120.54, 116.00, 114.34, 104.20, 65.10, 54.59, 54.46, 35.98, 26.23, 24.56, 23.64. HRMS (ESI-TOF) m/z: calcd for $C_{34}H_{33}NO_7$ 567.2257, found 568.2308 $[M+H]^+$.

4.3.5.24. 3,3'-((4-(3-(azepan-1-yl)propoxy)-3-methoxyphenyl)methylene)bis(4-hydroxy-2H-chromen-2-one) (4.8l)

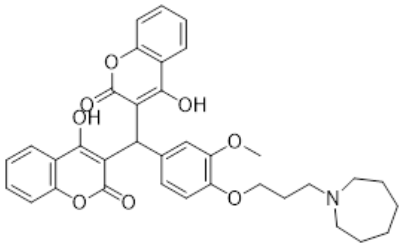

Whitish solid; Yield: 77%; ^{1}H NMR (600 MHz, DMSO-d_6) δ 17.59 (s, 1H), 9.33 (s, 1H), 7.80 (d, J = 7.9 Hz, 2H), 7.49 (t, J = 7.9 Hz, 2H), 7.28 – 7.17 (m, 4H), 6.78 (d, J = 8.1 Hz, 1H), 6.70 (s, 1H), 6.64 (d, J = 8.2 Hz, 1H), 6.21 (s, 1H), 4.04 – 3.92 (m, 4H), 3.61 (t, J = 12.8 Hz, 2H), 3.54 (s, 3H), 3.52 – 3.41 (m, 2H), 3.32 – 3.18 (m, 6H), 3.14 – 3.02 (m, 2H), 2.08 (p, J = 6.4 Hz, 2H). ^{13}C NMR (125 MHz, DMSO-d_6) δ 168.37, 165.21, 153.07, 149.22, 145.83, 136.39, 131.46, 124.65, 123.46, 120.54, 119.57, 116.02, 114.12, 112.09, 104.19, 66.60, 56.07, 54.83, 54.49, 36.41, 26.25, 24.65, 23.62. HRMS (ESI-TOF) m/z: calcd for $C_{35}H_{35}NO_8$ 597.2362, found 598.2382 $[M+H]^+$.

4.3.6. *In Vitro* Test for Anthelminthic Activity

Specimens of cestodes *Raillietina echinobothrida* were collected from the intestines of domestic fowls obtained at a local slaughterhouse. Freshly isolated worms were immediately transferred into lukewarm phosphate-buffered saline (PBS; pH 7.1–7.4) and rinsed thoroughly several times prior to use in *in vitro* experiments. Parasites were subsequently exposed to varying concentrations of synthesized bis-4-hydroxycoumarins (1 mg/mL, 0.5 mg/mL, and 0.25 mg/mL) prepared in 0.9% PBS supplemented with 1% DMSO. Each treatment was carried out in triplicate (n = 5).

Albendazole, prepared at equivalent concentrations, was used as the positive control, while parasites maintained in PBS containing 1% DMSO alone served as the negative control.

The treated parasites were incubated at 37 °C, and drug efficacy was evaluated at regular intervals by monitoring worm motility, survival, and histomorphological changes. Motility was evaluated based on both spontaneous movements and responses to physical stimulation. Death was confirmed by transferring worms into lukewarm PBS and verifying the complete absence of movement. The time of death for each individual worm was recorded.

4.3.7. Morphological Preparation for Scanning Electron Microscopy (SEM)

The bis-4-hydroxycoumarin derivatives with significant *in vitro* anthelmintic efficacy at the highest concentration were further investigated by Scanning Electron Microscopy. The treated cestodes were first washed with 0.8% normal saline and fixed in 10% neutral-buffered formalin for a minimum of 24 hours. Following fixation, worms were rinsed in PBS for 30 minutes with two buffer changes to remove surface debris. Subsequently, dehydration was performed through a graded acetone series (30%, 50%, 70%, 80%, 90%, 95%, and 100%). Samples were exposed to 30%, 50%, and 70% acetone for 15 minutes with two changes at each step, followed by 30 minutes with two changes at 80%, 90%, 95%, and 100% acetone. Worms were then immersed in tetramethylsilane (TMS) within open Eppendorf tubes and air-dried at room temperature until complete evaporation of TMS. Dried specimens were mounted on metal stubs and sputter-coated with gold using a fine-coat ion sputter (JFC-1100, JEOL) for 15–20 minutes. The samples were then examined under a scanning electron microscope (JSM-6360, JEOL) at magnifications of 300×, 500×, and 1000× to assess surface morphological alterations induced by albendazole and the synthesized bis-4-hydroxycoumarin.

4.3.8. Statistical Analysis

Experimental results were expressed as mean ± standard error of the mean (SEM). Data were analyzed using one-way analysis of variance (ANOVA), followed

by Tukey's post hoc test. All statistical analyses were performed using OriginPro 25 software.

4.3.9. Molecular Docking

The crystal structure of β-tubulin (PDB ID: 1JFF) was obtained from the Protein Data Bank (www.rcsb.org) in PDB format. Before docking, the protein structure was refined by removing co-crystallized ligands, cofactors, and water molecules. Missing residues were modelled, and polar hydrogens were added to complete the structure. For global docking, the entire protein was enclosed within a search grid centered at x = –1.143, y = –1.559, z = 3.928 with dimensions of 70 Å × 70 Å × 70 Å. For taxane-specific docking, the grid was restricted to the taxane binding pocket, defined based on the native ligand, with parameters centered at x = –0.082, y = –16.403, z = 14.621 and a grid size of 23 Å × 23 Å × 23 Å.

The coordinates of the colchicine binding pocket were obtained from the β-tubulin structure co-crystallized with colchicine (PDB ID: 1SA0). This structure was superimposed onto β-tubulin (PDB ID: 1JFF) to determine the colchicine site coordinates. Docking was performed using a grid centered at x = 16.152, y = –2.302, z = 2.168 with dimensions of 21 Å × 21 Å × 21 Å. Docking was carried out using AutoDock Vina with an exhaustiveness parameter set to 30. The docking results were visualized with PyMOL, UCSF Chimera, and Discovery Studio.

The docking protocol was validated by redocking the native ligands and comparing the predicted binding orientations with the crystallographic conformations through structural superimposition.

4.4. Results and Discussion

4.4.1 Synthesis of a Novel Hybrids of bis-4-hydroxycoumarin Derivatives

A series of novel hybrids of bis-4-hydroxycoumarin derivatives were synthesized through multi-step procedures, as illustrated in Scheme 4.1. The synthesis began with the commercially available compound 4-hydroxybenzaldehyde or 4-hydroxy-3-methoxybenzaldehyde (**4.1**), which underwent a nucleophilic substitution reaction with an excess of linear aliphatic dibromoalkanes (**4.2**) in the presence of

anhydrous K_2CO_3 in N,N-dimethylformamide (DMF) at room temperature. This reaction afforded aldehydes (**4.3a**–**4.3d**) bearing terminal bromo groups. These intermediates were subsequently subjected to nucleophilic substitution with various secondary amines to yield the corresponding amino-substituted aldehydes (**4.4a-4.4h, 4.4k–4.4l, 4.5a–4.5h, 4.5k–4.5l**). The condensation of two equivalent of 4-hydroxycoumarin and amino-substituted aldehydes in the presence of piperidine gave the desired bis-4-hydroxycoumarin hybrids. However, in the case of phthalimide substituted aldehydes the desired yield was not obtained in the presence of piperidine in ethanol as solvent. Therefore, phthalimide substituted bis-4-hydroxycoumarins (**4.7i–4.7j**, **4.8i–4.8j**) were synthesized by refluxing phthalimide substituted aldehydes with two equivalents of 4-hydroxycoumarin in acetic acid. Structures of all the synthesized compounds were confirmed from the spectroscopic analysis using High Resolution Mass Spectrometry (HRMS), ^{1}H NMR, and ^{13}C NMR.

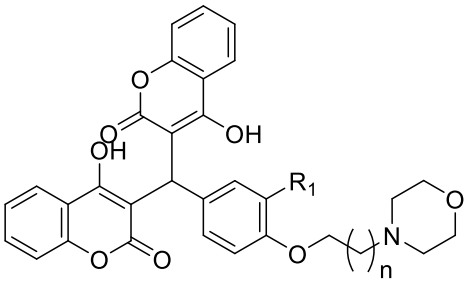

4.7a; R_1 = H; n=1
4.8a; R_1 = H; n=2
4.7b; R_1= OCH_3; n=1
4.8b; R_1= OCH_3; n=2

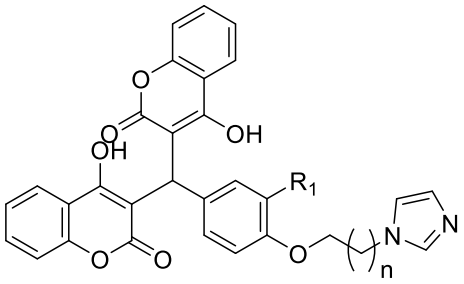

4.7c; R_1 = H; n=1
4.8c; R_1 = H; n=2
4.7d; R_1= OCH_3; n=1
4.8d; R_1= OCH_3; n=2

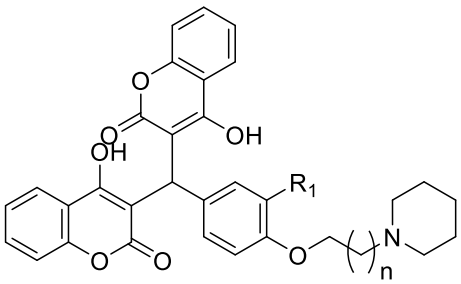

4.7e; R1 = H; n=1
4.8e; R1 = H; n=2
4.7f; R1= OCH_3; n=1
4.8f; R1= OCH_3; n=2

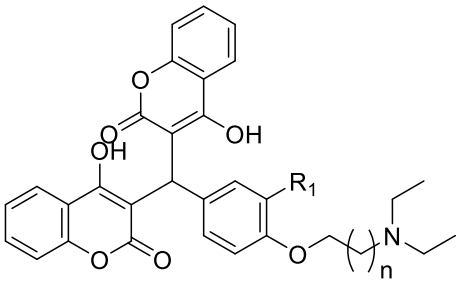

4.7g; R_1 = H; n=1
4.8g; R_1 = H; n=2
4.7h; R_1= OCH_3; n=1
4.8h; R_1= OCH_3; n=2

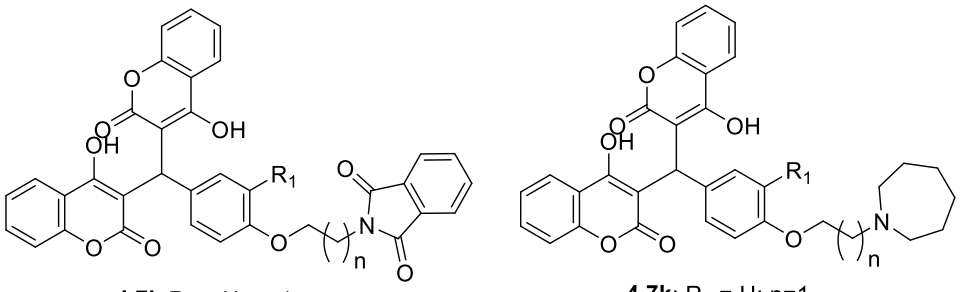

Figure 4.4. Chemical structures of novel bis-4-hydroxycoumarin conjugates linked to various amino functionalities.

The NMR spectra (^{1}H NMR and ^{13}C NMR) of one of the final bis-4-hydroxycoumarin derivative, **4.8c**, recorded in DMSO-*d*$_6$, were selected to illustrate its chemical shifts and are shown in the Figure 4.5 & 4.6. In the ^{1}H NMR spectrum, a pentet at δ 2.25 ppm of two protons and a triplet at δ 3.93 ppm and δ 4.34 ppm of two proton each correspond to the propylene linker. A singlet peak at δ 6.19 ppm corresponds to the methine (CH) proton. Doublet peaks at δ 6.68, δ 6.98 of two protons each, a multiplet at δ 7.23 ppm of five protons, a triplet at 7.49 ppm of two protons, a singlet peak at δ 7.63 ppm of one proton, and multiplet peak at δ 7.79 ppm of three protons are assigned to the aromatic protons of the bis-4-hydroxycoumarin and imidazole rings. Two deshielded singlets at δ 9.06 and δ 17.63 ppm of one proton each correspond to the hydroxyl protons of the bis-4-hydroxycoumarin rings. The unusually downfield shift of one hydroxyl proton (δ 17.63 ppm) is likely due to strong intramolecular hydrogen bonding between the hydroxyl group of one coumarin core and the lactone carbonyl group of another coumarin core. The ^{13}C NMR spectrum of compound **4.8c** exhibits twenty-one distinct signals (Figure 4.6). Peaks at δ 29.72 ppm, δ 46.92 ppm and δ 65.19 ppm represents the three carbon atoms of propylene alkyl chain linker, while the signal at δ 36.06 ppm arises from the methine carbon. The signals of aromatic sp^2 carbons appear at δ 165.09, 156.30, 153.11, 136.05, 135.43, 131.27, 128.27, 124.64, 123.27, 122.68, 120.65, 120.55, 115.92, 115.73, 114.35, 104.20 ppm. The lactone carbonyl carbons (C=O) appear at a peak δ 168.14 ppm. HRMS of compound **4.8c** (Figure 4.7) shows three significant peaks at m/z 537.1670

$[M+H]^+$, 538.1714 $[M+2H]^{2+}$, and 559.1510 $[M+H+Na]^+$ (calculated m/z $C_{31}H_{24}N_2O_7$ 536.1583 $[M]^+$), further confirming its molecular structure.

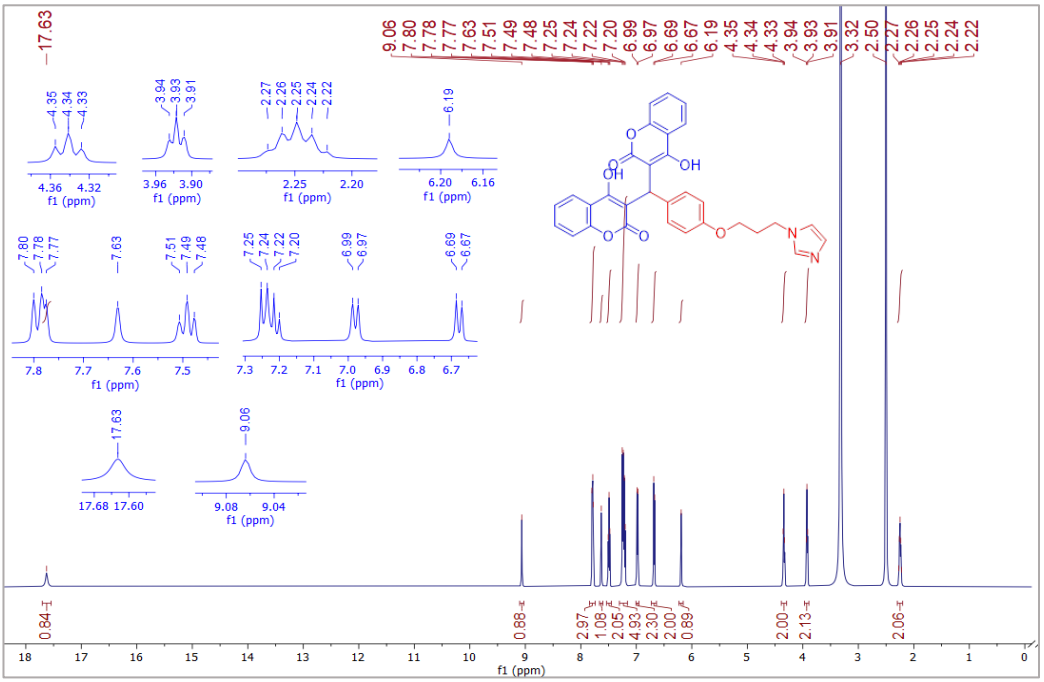

Figure 4.5. ^{1}H NMR spectrum of **4.8c**.

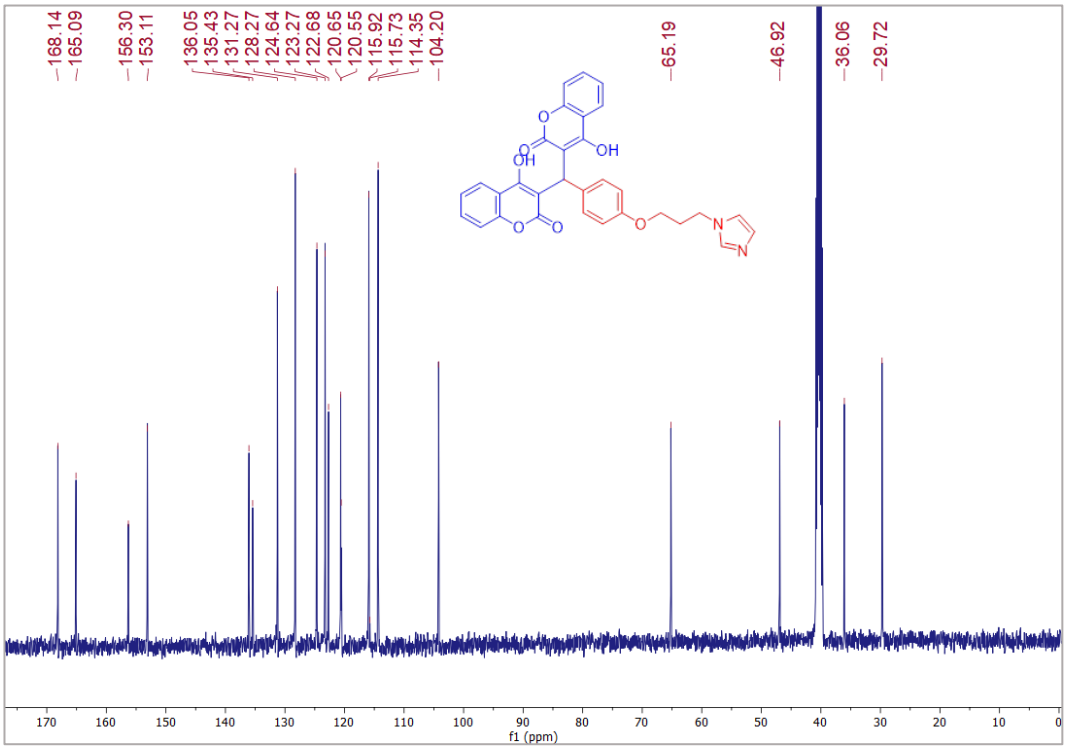

Figure 4.6. ^{13}C NMR spectrum of **4.8c**.

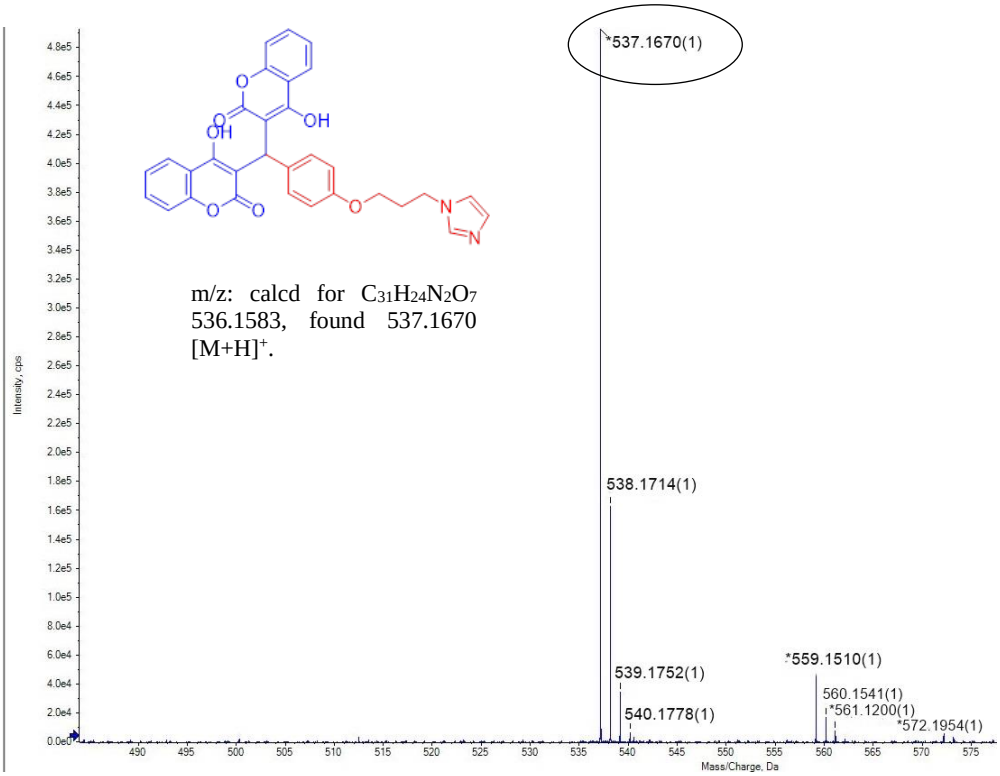

Figure 4.7. HRMS spectrum of **4.8c**.

4.4.2. *In vitro* Anthelmintic Activity

Table 4.1. *In vitro* efficacy of novel secondary amines functionalised bis-4-hydroxycoumarins against cestode, *R. echinobothrida*.

	Mortality time (h)		
Control	71.815 ± 0.47		
Compounds	**1 mg/mL**	**0.5 mg/mL**	**0.25 mg/mL**
4.7a	2.85 ± 0.26[a]	11.32 ± 0.61[a]	26.57 ± 1.26[a]
4.7b	3.43± 0.43[a]	15.29 ± 0.58[a]	31.08 ± 1.59[a]
4.8a	4.96 ± 0.38[a]	18.77 ± 1.22[a]	36.0 ± 2.15[a]
4.8b	4.20 ± 0.14[a]	18.42 ± 0.66[a]	34.61 ± 1.80[a]
4.7c	2.79 ± 0.22[a]	10.45 ± 0.65[a]	26.98 ± 1.77[a]

4.7d	3.05 ± 0.17[a]	12.06 ± 0.96[a]	28.36 ± 1.47[a]
4.8c	3.49 ± 0.19	16.48 ± 0.84	33.06 ± 1.34
4.8d	3.17 ± 0.17[a]	14.37 ± 1.04[a]	29.87 ± 1.78[a]
4.7e	8.93 ± 0.69[a]	26.55 ± 0.78[a]	51.65 ± 1.56[a]
4.7f	5.52 ± 0.46[a]	22.78 ± 0.71[a]	49.98 ± 2.11[a]
4.8e	9.52 ± 0.80[a]	30.2 ± 1.60[a]	53.65 ± 2.30[a]
4.8f	17.16 ± 0.54[a]	36.38 ± 0.65[a]	56.46 ± 2.08[a]
4.7g	9.95 ± 0.49[a]	25.08 ± 1.4[a]	51.3 ± 2.46[a]
4.7h	15.8 ± 0.41[a]	43.88 ± 1.24[a]	52.42 ± 1.89[a]
4.8g	10.92 ± 0.87[a]	34.17 ± 1.6[a]	51.59 ± 2.57[a]
4.8h	18.41 ± 1.55[a]	36.24 ± 0.93[a]	56.75 ± 1.03[a]
4.7i	11.33 ± 0.55[a]	35.24 ± 0.48[a]	55.37 ± 1.08[a]
4.7j	15.38 ± 0.26[a]	44.59 ± 0.68[a]	59.25 ± 1.14[a]
4.8i	19.08 ± 0.88[a]	47.59 ± 1.12[a]	64.43 ± 1.23[b]
4.8j	27.53 ± 1.21[a]	57.37 ± 0.87[a]	66.53 ± 1.27[c]
4.7k	24.25 ± 0.82[a]	42.65 ± 1.99[a]	67.57 ± 1.42[ns]
4.7l	33.0 ± 1.47[a]	49.78 ± 1.38[a]	68.98 ± 1.15[ns]
4.8k	29.14 ± 1.47[a]	46.65 ± 1.23[a]	68.65 ± 1.26[ns]
4.8l	37.54 ± 0.67[a]	61.02 ± 1.44[a]	68.16 ± 1.12[ns]
Abendazole (Abz)	23.81 ± 0.39[a]	37.34 ± 0.35[a]	51.08 ± 0.98[a]

Data is expressed as mean ± S.E.M.; [a]$p \leq 0.001$, [b]$p \leq 0.01$, [c]$p \leq 0.05$, [n.s.] not significant, as compared to control value; one way ANOVA, followed by Tukey's test.

The *in vitro* anthelmintic evaluation of the novel bis-4-hydroxycoumarin hybrids against *Raillietina echinobothrida* at concentrations of 1 mg/mL, 0.5 mg/mL and 0.25 mg/mL demonstrated their potent anthelmintic efficacy (Table 4.1, Figure 4.8-4.11). In the untreated control group, parasites survived for 71.52 ± 0.25 h, confirming

natural viability in the absence of treatment. Albendazole, used as the reference drug, induced parasite death within 23.81 ± 0.39 h (1 mg/mL) to 51.08 ± 0.98 h (0.25 mg/mL), thereby establishing a baseline for comparative efficacy.

Overall, the bis-4-hydroxycoumarin hybrids exhibited significant anthelmintic activity in a concentration-dependent manner. At the highest concentration (1 mg/mL), all compounds caused rapid and pronounced parasite mortality. Notably, imidazolo- and morpholino-functionalized bis-4-hydroxycoumarins (**4.7c**, **4.7d**, **4.8c**, **4.8d**, **4.7a**, **4.7b**, **4.8a** and **4.8b**) exhibited the most pronounced activity across all tested concentrations (Figure 4.8 & 4.9). These compounds consistently induced potent mortality at 1 mg/mL and retained efficacy even at lower concentrations. Among them, imidazolo-based bis-4-hydroxycoumarin derivatives **4.7c** (2.79 ± 0.22 h), **4.7d** (3.05 ± 0.17 h), **4.8c** (3.49 ± 0.19 h), and **4.8d** (3.17 ± 0.17 h) induced parasite death within ~3 h at 1 mg/mL, which is more than a 7-fold increase in potency over albendazole. Similarly, morpholino-based bis-4-hydroxycoumarin derivatives **4.7a** (2.85 ± 0.26 h), **4.7b** (3.43± 0.43 h), **4.8a** (4.96 ± 0.38 h), and **4.8b** (4.20 ± 0.14 h) also caused parasite death within ~4 h, corresponding to a 6-fold greater potency than albendazole.

The length of the alkyl linker (n=1 or n=2) did not significantly alter activity, particularly among the imidazolo and morpholino derivatives (**4.7c**, **4.7d**, **4.8c**, **4.8d**, **4.7a**, **4.7b**, **4.8a** and **4.8b**), although compounds with n=1 induced slightly faster mortality than their n=2 analogues. Furthermore, substitution patterns on the phenyl ring influenced potency slightly, where at n=1, 3-methoxy derivatives (**7b**, **7d**) showed slightly reduced activity compared to unsubstituted counterparts (**7a**, **7c**), whereas at n=2, 3-methoxy substitution (**4.8b**, **4.8d**) conferred a modest increase in activity over their unsubstituted analogues (**4.8a**, **4.8c**). This observation aligns with molecular docking analysis, which suggest comparable orientation of both linker and substitution types within the taxane-binding site of β-tubulin (section 4.4.4.).

At 0.5 mg/mL, the activity was reduced but remained substantial for many compounds. For instance, **4.7a** (11.32 ± 0.61 h), **4.7b** (15.29 ± 0.58), **4.8a** (18.77 ± 1.22 h), **4.8b** (18.42 ± 0.66 h), **4.7c** (10.45 ± 0.65), **4.7d** (12.06 ± 0.96), **4.8c** (16.48 ± 0.84), **4.8d** (14.37 ± 1.04) maintained higher potency relative to albendazole (23.81 ±

0.39 h). Interestingly, even at a concentration of 0.5 mg/mL, imidazolo- and morpholino-linked compounds were more effective than albendazole at 1 mg/mL, indicating a favorable dose-response behavior. However, at the lowest concentration (0.25 mg/mL), the activity declined further, with mortality time extending beyond 40–60 h for most compounds. Nevertheless, most derivatives still exhibited significantly greater potency than albendazole, indicating sustained potency even at lower doses.

Piperidino-, diethylamino-, and phthalimido-based bis-4-hydroxycoumarins (**4.7e–4.7j**, **4.8e–4.8j**) exhibited potent anthelmintic activity at a concentration of 1 mg/mL, with the exception of compound **4.8j**, which showed a longer mortality time than albendazole. In contrast, incorporation of an azepino group (**4.7k**, **4.7l**, **4.8k**, **4.8l**) markedly reduced activity across all tested concentrations, with activity at 0.25 mg/mL being either insignificant or only marginally significant ($p \leq 0.05$) compared to the control.

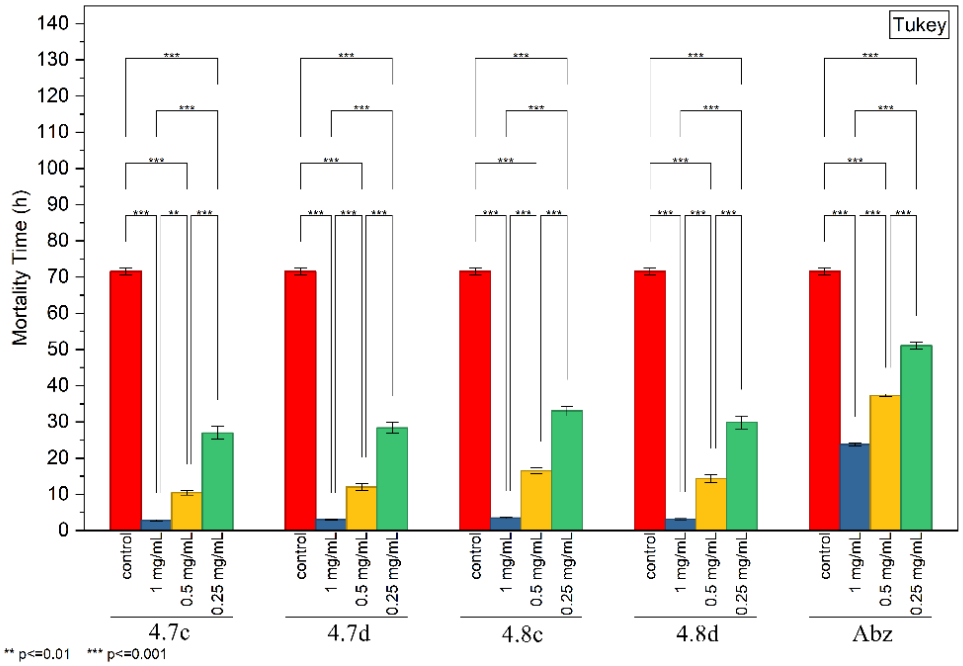

Figure 4.9. Anthelmintic efficacy of imidazole containing bis-4-hydroxycoumarin derivatives (**4.7c–4.7d**, **4.8c–4.8d**) and albendazole (**Abz**).

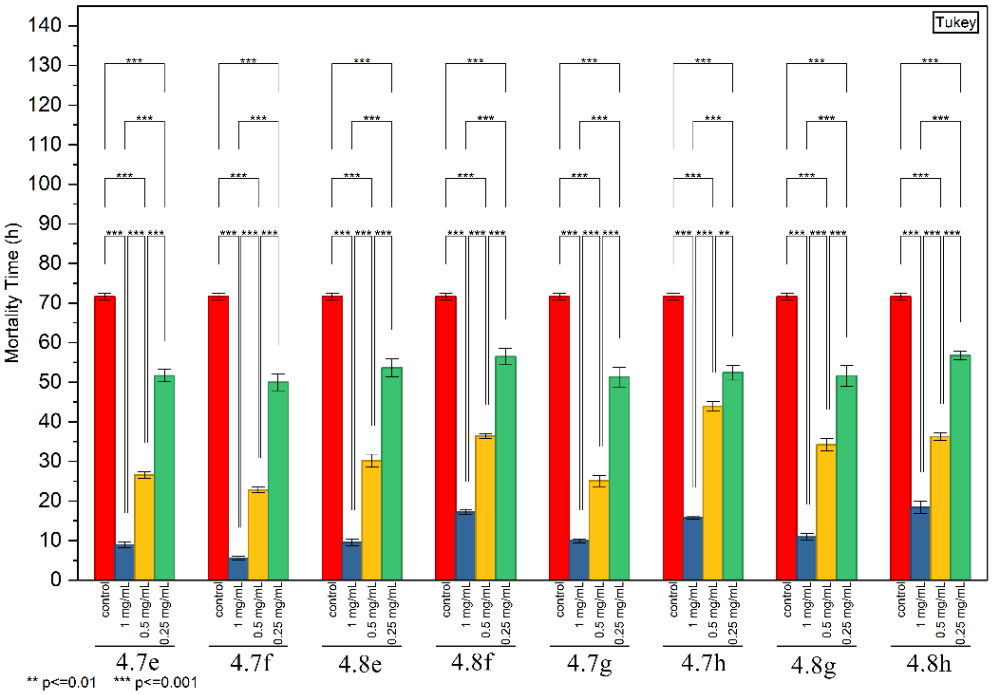

Figure 4.10. Anthelmintic efficacy of compounds (**4.7e–4.7h**, **4.8e–4.8h**)

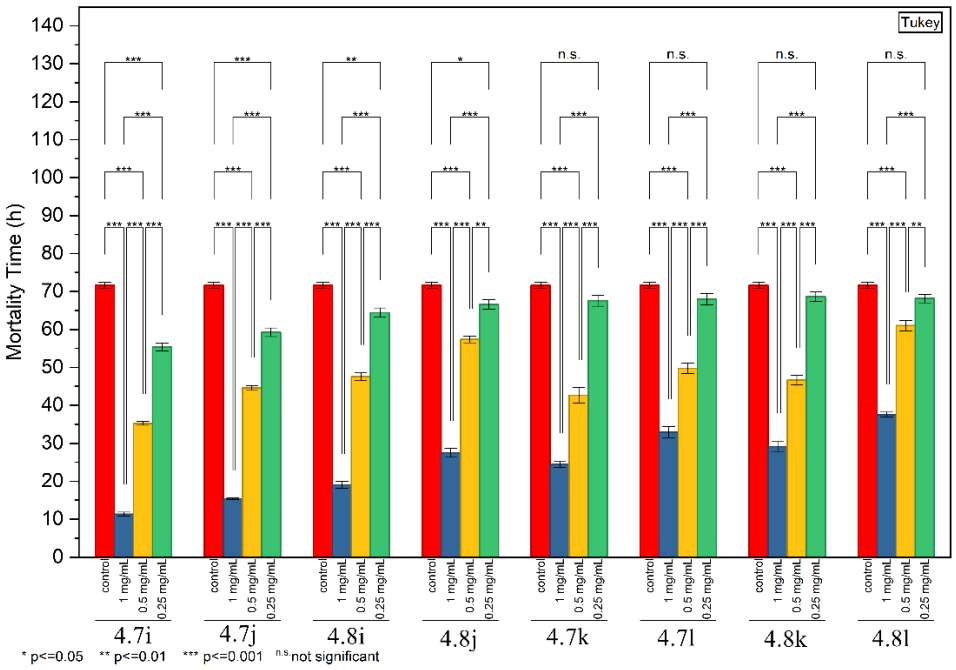

Figure 4.11. Anthelmintic efficacy of compounds (**4.7i–4.7l**, **4.8i–4.8l**)

4.4.3. Morphological Alterations in Cestode *R. echinobothrida* After Treatment with Novel bis-4-hydroxycoumarin Hybrids.

Compounds demonstrating significant *in vitro* anthelmintic activity were selected for morphological investigation using scanning electron microscopy (SEM). Cestodes treated with 1 mg/mL concentrations of **4.7c**, **4.8c**, **4.7d**, **4.8d**, and **4.7a** were examined, as this dosage produced the most pronounced anthelmintic efficacy.

In untreated controls, the cestode exhibited the typical morphology of a tapeworm: a knob-like scolex at the anterior end, followed by a flattened neck and an elongated strobila. The scolex bore four oval suckers surrounding the apical rostellum. Each sucker, functioning as an attachment organ, possessed several rows of sharply pointed spines. The strobila consisted of a ribbon-like chain of proglottides, and the entire body surface was covered by a tegument densely ornamented with microtriches, imparting a velvety appearance (Figure 4.12).

In contrast, worms treated with the bis-4-hydroxycoumarin derivatives exhibited extensive and irreversible damage across the body surface (Figure 4.13–4.18). Treatment with **4.7c**, **4.8c**, **4.7d**, **4.8d**, and **4.7a** caused severe deformation of the scolex, manifested as folding, shrinkage, and invagination of the suckers and rostellum. The spines of the suckers were either completely dislodged or left bent and irregular. The strobila showed massive tegumental damage, including abnormal folds, deep erosions, cracks, pits, and a pronounced loss of microtriches.

Furthermore, compound-specific effects were also observed. Treatment with **4.7c** induced irregular folding of the scolex, resulting in a broad, deep trough posterior to the suckers (Figure 4.13). In worms treated with **4.8c**, the proglottides appeared severely constricted and wrinkled, with pronounced narrowing at the interproglottidal junctions and irregular curling of the segmental edges (Figure 4.15).

Comparable structural damage was observed in albendazole-treated worms. The entire body of the cestode appeared severely deformed, showing extensively irregular tegumental folds and a constricted scolex. The suckers and rostellum were markedly shrunken and invaginated, while the proglottids exhibited cracks, pits, blebbing, and an obvious loss of microtriches (Figure 4.18).

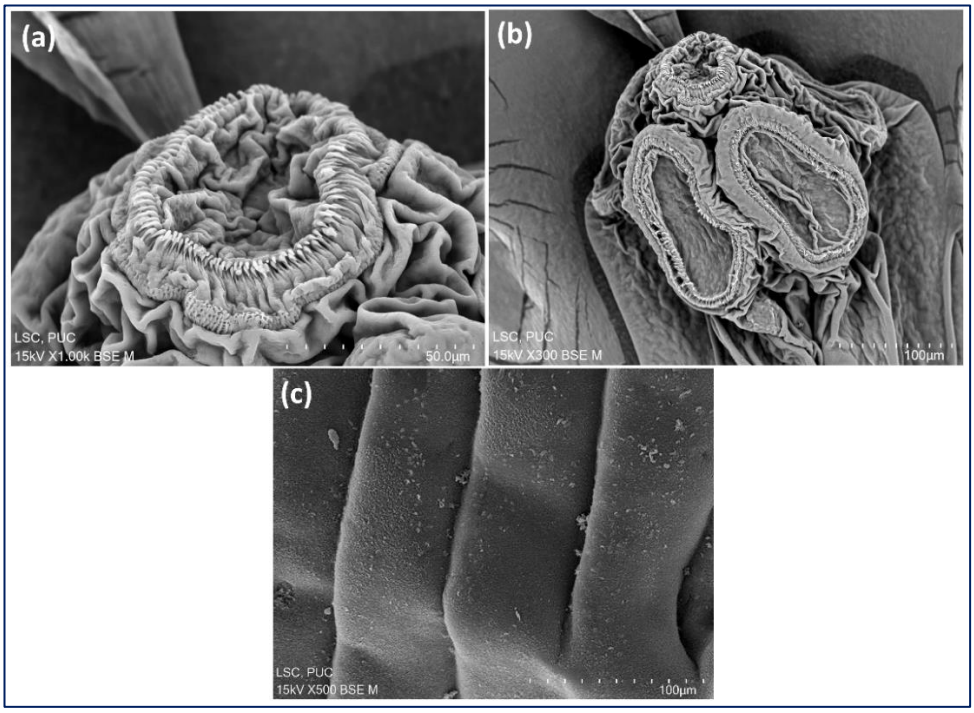

Figure 4.12. Scanning electron micrographs of untreated control cestode *R. echinobothrida*. (a) Magnified view of the scolex showing the rostellum. (b) Magnified view of the scolex showing suckers with intact spines. (c) Magnified view of the strobila showing proglottids.

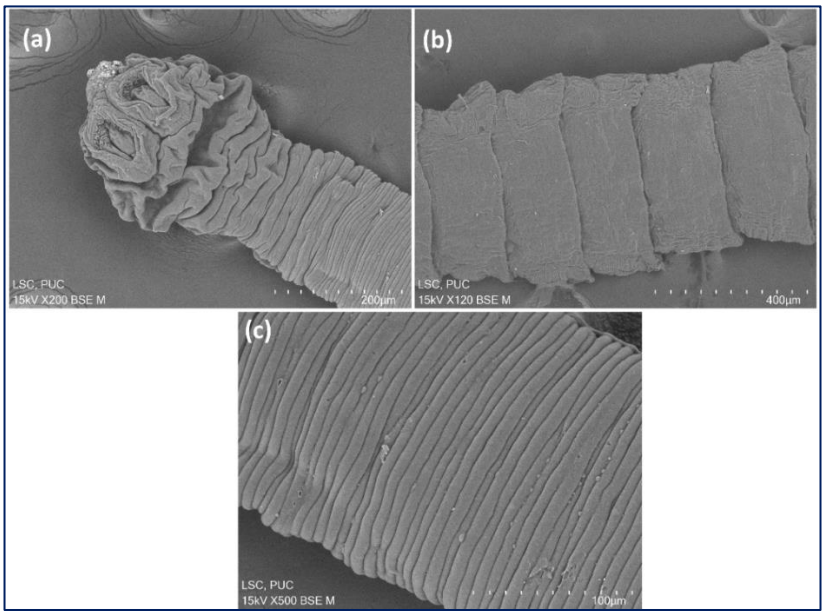

Figure 4.13. Scanning electron micrograph of the cestode *R. echinobothrida* treated with 1 mg/mL of **4.7c**. (a) Deformed scolex showing severe constriction and folding, with a broad deep trough posterior to the suckers, protuberances of the rostellum and suckers, and

distortion or detachment some spines. (b, c) Proglottids exhibiting tegumental disfiguration, wrinkles, and the formation of cracks, pits, and eroded surfaces.

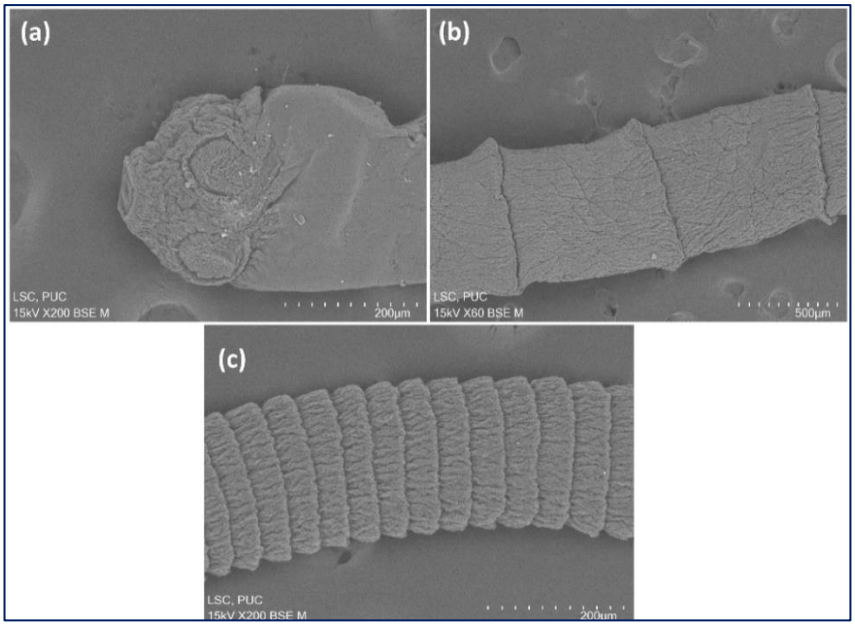

Figure 4.14. Scanning electron micrograph of the cestode *R. echinobothrida* treated with 1 mg/mL of **4.7d**. (a) Deformed scolex with protuberant suckers and complete detachment of spines. (b, c) Magnified views of proglottids showing severe tegumental folding and shrinkage.

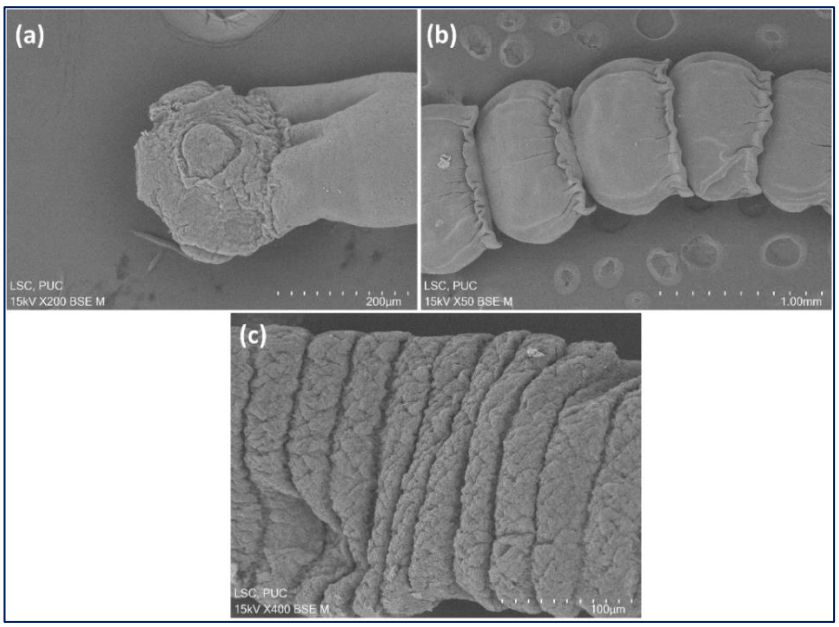

Figure 4.15. Scanning electron micrograph of the cestode Raillietina echinobothrida treated with 1 mg/mL of **4.8c**. (a) Deformed scolex with protuberant suckers and complete detachment of spines. (b) Severe constriction and narrowing at the interproglottidal

junctions, with irregular curling of the segmental edges. (c) Magnified view of proglottids showing severe tegumental folding and shrinkage.

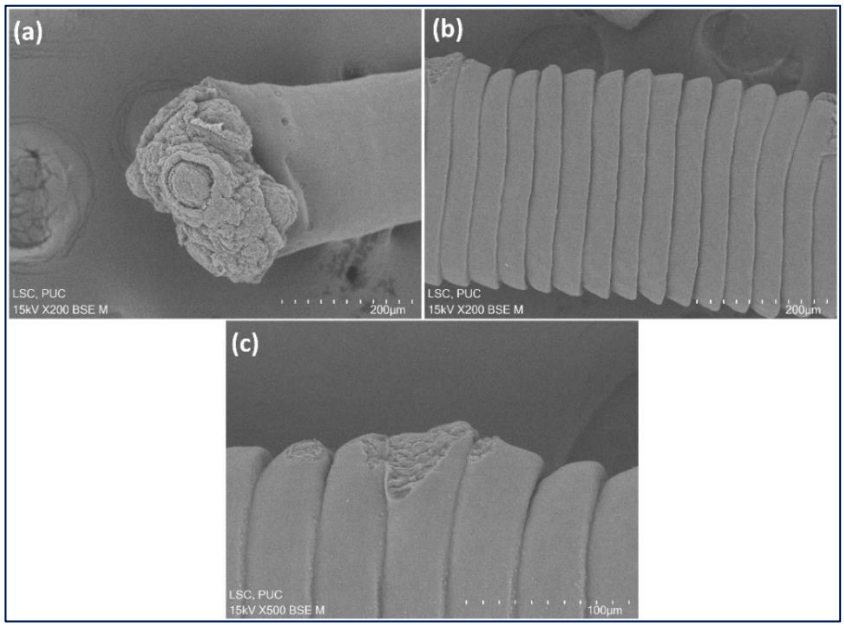

Figure 4.16. Scanning electron micrograph of the cestode *R. echinobothrida* treated with 1 mg/mL of **4.8d**. (a) Deformed scolex with protuberant suckers and distortion or detachment of some spines. (b, c) Proglottids showing tegumental damage and severe erosion.

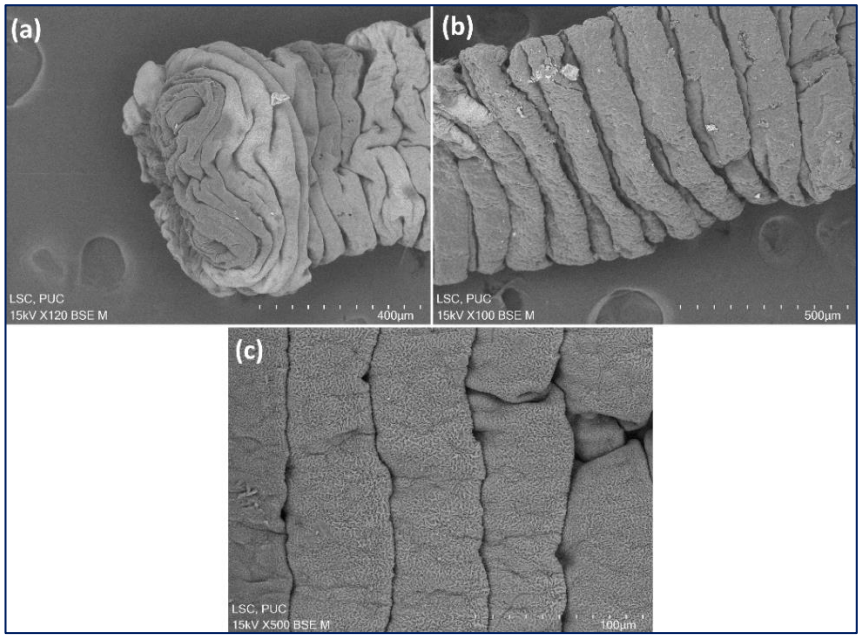

Figure 4.17. Scanning electron micrograph of the cestode *R. echinobothrida* treated with 1 mg/mL of **4.7a**. (a) Severe constriction and deformation of the scolex resulting in scolex infolding. (b, c) Proglottids showing severe shrinkage, cracks, erosion, and loss of microtriches.

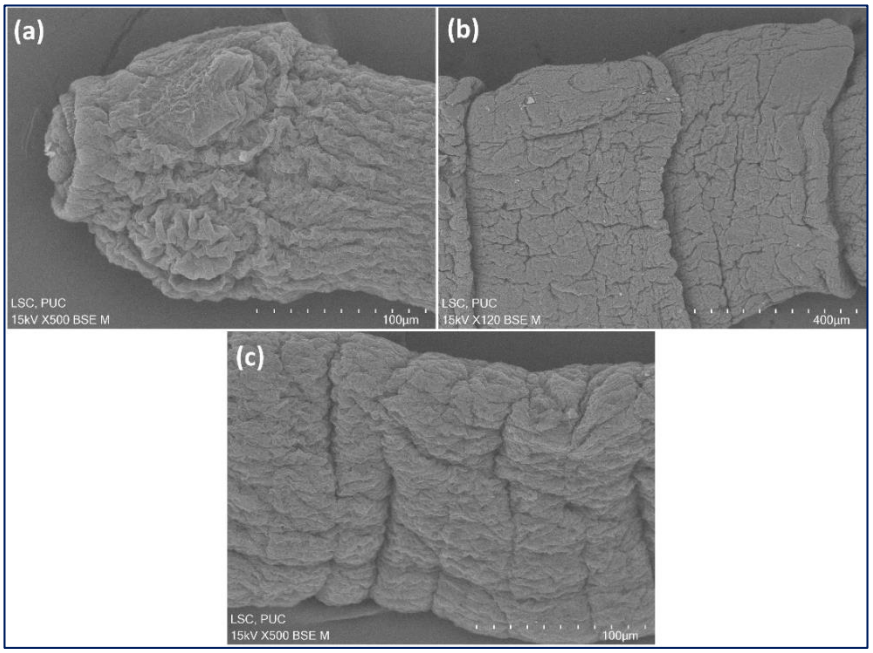

Figure 4.18. Scanning electron micrograph of the cestode *R. echinobothrida* treated with 1 mg/mL of albendazole. (a) Deformed scolex with complete loss of spines from the suckers. (b, c) Proglottids showing severe shrinkage, cracks, and loss of microtriches.

4.4.4. Molecular Docking Study

Molecular modelling and docking approaches have emerged as indispensable tools in modern drug discovery, enabling the prediction of the binding orientation, affinity, and stability of ligands within the active or allosteric sites of their protein targets. To elucidate the binding mode of the test compounds, we performed computational modelling studies to investigate their possible orientations and interactions within the binding pockets of β-tubulin. Since β-tubulin possesses six distinct binding sites, it is challenging to predict with certainty which site the compounds will preferentially occupy to exert their anthelminthic activity. Previous studies, however, have shown that many anthelmintic drugs, such as benzimidazoles, act by binding in the colchicine binding pocket and thereby disrupting β-tubulin polymerization, while others, such as ivermectin and dicoumarol, function as tubulin-stabilizing agents. Given that our compounds are dicoumarol derivatives, we hypothesized that they may bind at the taxane-binding pocket and stabilize microtubules.

To test this hypothesis, we first conducted globular docking by covering the entire β-tubulin protein with a search grid. As expected, the majority of stable conformations with the highest binding affinities were localized within the taxane-binding pocket across all compounds. To further refine these results, localized molecular docking was performed by restricting the grid to the taxane pocket. Additionally, to compare binding preferences, we conducted localized docking with the colchicine-binding pocket. Our results demonstrated that all compounds exhibited stronger binding affinity for the taxane-binding pocket compared to the colchicine-binding site. The binding affinities from globular and localized docking experiments are summarized in Table 4.2.

Table 4.2. Binding affinities and residues involved in interactions of bis-4-hydroxycoumarin hybrids with β-tubulin.

	Binding affinity (kcal/mol)			**Taxane Binding Pocket**	
Comp	**GD-TBP[b]**	**TBP[a]**	**CBP[c]**	**Residues involved in H-bond**	**Residues involved in other interactions (π···cation, π···π, π···alkyl,)**
4.7a	-9.3	-9.3	-6.1	Gly370	His229, Leu371, Leu275, Ala233, Pro360, Val23
4.7b	-9.2	-9.4	-5.8	Gly370	His229, Leu371, Leu275, Ala233, Pro360, Val23
4.8a	-9.0	-9.0	-5.2	Gly370	His229, Leu275, Leu230, Ala233, Pro360, Val23, Leu371
4.8b	-9.1	-9.2	-5.1	Ser236, Gly370	His229, Val23, Ala233, Leu275, Pro360, Leu371, Pro274, Leu286
4.7c	-9.3	-9.3	-4.7	Ser236, Pro274, Gly370	His229, Leu371, Leu275, Ala233, Pro360, Val23.

4.7d	-9.1	-9.1	-6.3	Ser236, Pro274, Gly370	His229, Leu230, Leu275, Ala233, Pro360, Val23, Leu371
4.8c	-9.2	-9.2	-6.1	Pro274, Gly370	His229, Leu371, Leu275, Ala233, Val23
4.8d	-8.7	-8.9	-6.0	Ser236, Pro274, Gly370	His229, Leu275, Leu230, Ala233, Pro360, Leu371, Val23
4.7e	-9.5	-9.5	-5.1	Pro274, Gly370	His229, Leu371, Leu275, Pro360, Ala233, Val23
4.7f	-9.1	-9.1	-5.3	Pro274, Pro274	His229, Leu371, Leu275, Pro360, Ala233, Val23, Leu230
4.8e	-9.4	-9.4	-6.0	Pro274, Gly370	His229, Leu371, Leu275, Pro360, Ala233, Val23
4.8f	-8.9	-8.9	-5.7	Pro274, Pro274	His229, Leu371, Leu275, Pro360, Ala233, Val23
4.7g	-8.4	-8.4	-5.3	Pro274, Gly370	His229, Leu371, Leu275, Ala233
4.7h	-7.9	-8.3	-5.0	Pro274, Gly370	His229, Leu371, Leu275, Ala233
4.8g	-8.5	-8.5	-5.3	Pro274, Gly370	His229, Leu371, Leu275, Ala233
4.8h	-7.9	-8.1	-4.9	Pro274, Gly370	His229, Leu371, Leu275, Ala233
4.7i	-9.8	-9.9	-4.2	Arg369, Gly370	Leu289, Pro274, Leu371, Val23, Pro360, Ala233, Leu275
4.7j	-9.4	-9.4	-5.5	His229	Val23, Pro360, Ala233, Leu275
4.8i	-8.9	-8.9	-5.9	Thr276	His229, Arg278, Leu371, Leu217, Pro360, Val23, Ala233
4.8j	-8.7	-9.1	4.1	Arg369	His229, Leu275, Ala233, Val23, Pro360,
4.7k	-8.9	-8.9	-6.2	Pro274, Gly370	His229, Leu371, Leu275, Ala233, Val23
4.7l	-8.7	-8.7	-5.8	Pro274, Gly370	His229, Leu371, Leu275, Ala233, Val23

4.8k	-8.8	-8.9	-5.5	Pro274, Gly370	His229, Leu371, Leu275, Ala233, Val23
4.8l	-8.3	-8.3	-5.3	Thr276, Gly370	Arg278, Phe272, Ala233, and Leu371.

[a]TBP-Taxane Binding Pocket, [b]GD-TBP- Globular Docking with lowest energy in TBP, [c]CBP- Colchicine Binding Pocket

The molecular docking results revealed that all compounds, except **4.8i**, occupied the binding pocket in a similar orientation (Figure 4.19), primarily via hydrogen bond interactions with the amino acid residues Ser236, Pro274, Gly370, Thr276, Arg369, and His229. The bis-4-hydroxycoumarin cores were predominantly positioned within domains A and B (Figure 4.19a & 4.19b), while the secondary amine moieties, linked via a flexible spacer, were oriented toward domain C.

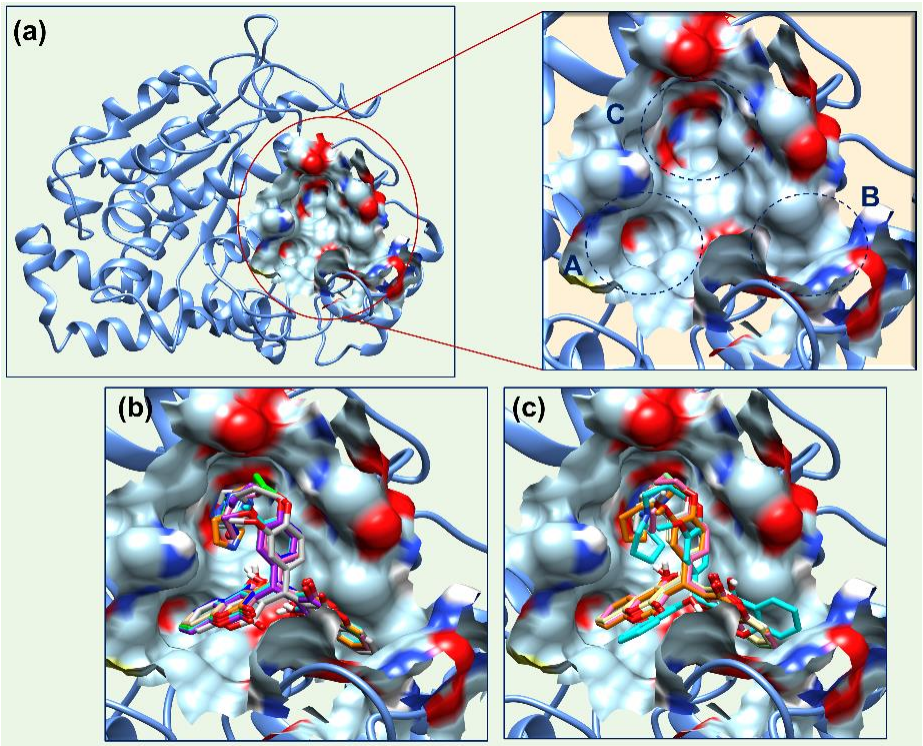

Figure 4.19. (a) Depiction of taxane binding pocket. (b) Overlay of compounds in the binding pocket: **4.7c** (khaki), **4.8c** (orange), **4.7d** (cyan), **4.8d** (purple), **4.7a** (blue), **4.8a** (blue), **4.7b** (Pink), **4.8b** (gray). (c) Overlay of compounds in the binding

pocket: **4.8g** (khaki), **4.7h** (gray), **4.7l** (orange), **4.8l** (cyan), **4.7e** (light green), **4.8e** (Pink).

Further analysis of docking within the taxane-binding pocket showed that imidazole series exhibited a consistent pattern of hydrogen bond interactions. Specifically, the 4-hydroxy group of coumarin core formed hydrogen bond interaction with the residue Pro274, while the propoxy oxygen atom served as an acceptor to form hydrogen bond with the residue Gly370. In addition, the hydrogen bond interactions between the N atom of imidazole and the residue Ser236 further enhanced the stability of compounds **4.7c–4.8d** (Figure 4.20 & 4.21). However, in compound **4.8c**, this hydrogen bond interaction was absent due to a deviation in the orientation of the imidazole ring, caused by intramolecular hydrogen bonding between the 4-hydroxy group and the imidazole nitrogen, as well as π–π stacking between the imidazole and phenyl rings. Moreover, compounds **4.7c–4.8d** are further stabilized by the electrostatic pi-cation and multiple hydrophobic interactions such as pi-pi stacking, pi-sigma and pi-alkyl, with the amino acid residues His229, Leu275, Leu230, Ala233, Pro360, Leu371, Val23. The enhance activity of the imidazole series **4.7c–4.8d** can be attributed to the presence of hydrogen bonding between the imidazole nitrogen and Ser236, a feature not observed in the other derivatives.

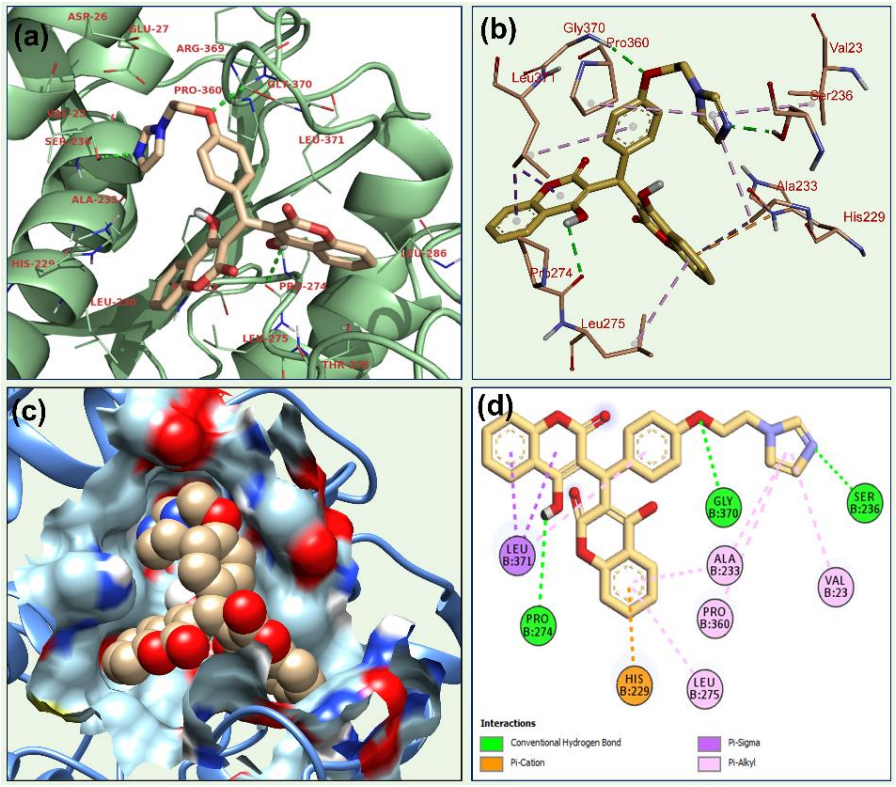

Figure 4.20. (a), (b), (d) Depiction of noncovalent interactions of compound **4.7c** in the binding pocket. (c) Depiction of compound **4.7c** as spheres in the binding pocket.

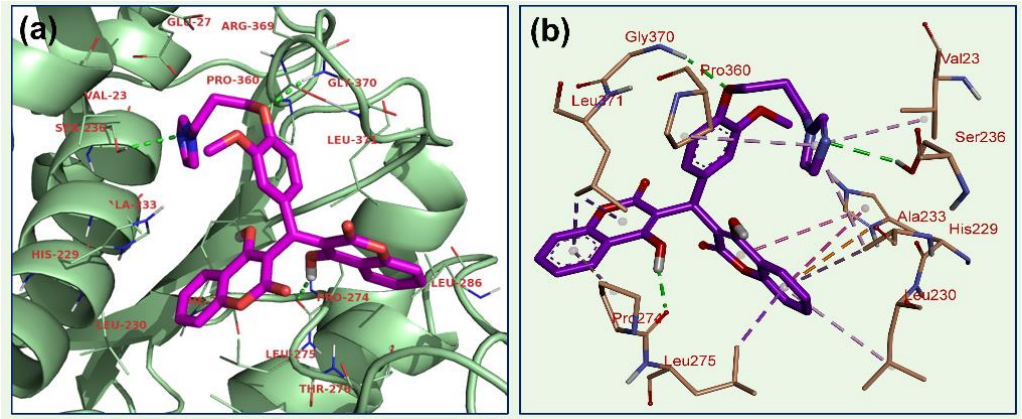

Figure 4.21. (a), (b) Depiction of noncovalent interactions of compound **4.8d** in the binding pocket.

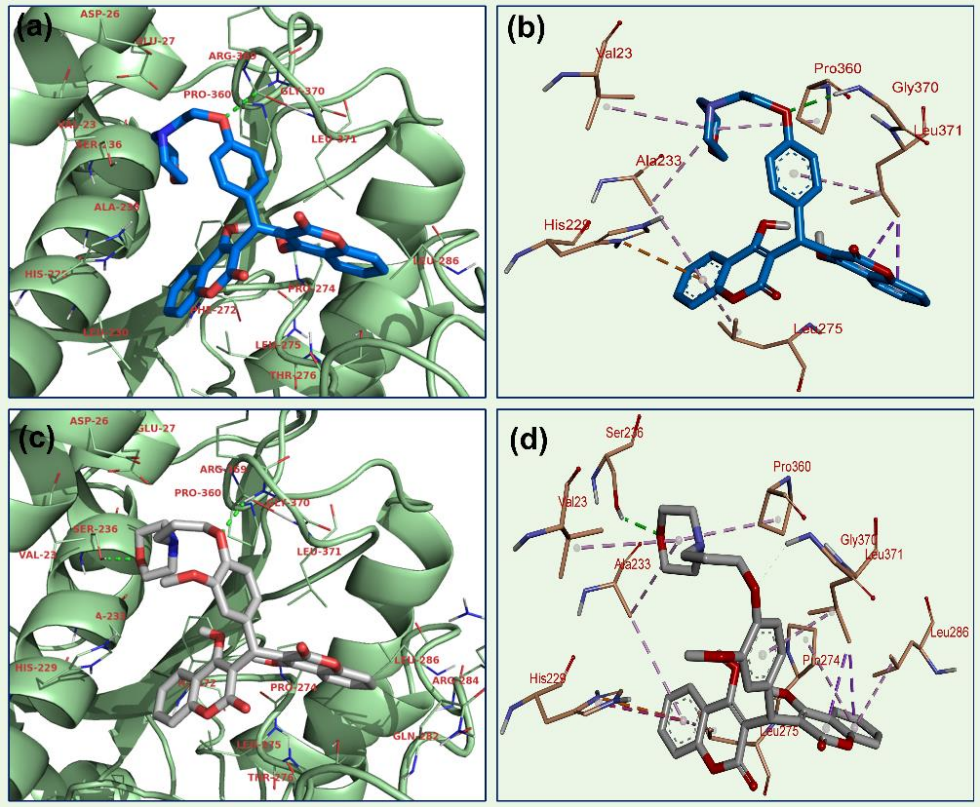

Figure 4.22. Depiction of noncovalent interactions of compounds in the binding pocket. (a), (b) **4.7a**; (c), (d) **4.8b**

The morpholine derivatives adopted a similar orientation within the binding pocket but generally formed only a single hydrogen bond between the propoxy oxygen atom and the residue Gly370 (Figure 4.22). Notably, in the case of **4.8b**, the flexible propoxy chain was aligned in such a way that the oxygen atom of the morpholine group formed an additional hydrogen bond with the residue Ser236 (Figure 4.22c & 4.22d). Furthermore, the morpholine derivatives were stabilized by electrostatic pi-cation and hydrophobic interactions with the residues His229, Val23, Ala233, Leu275, Pro360, Leu371, Pro274, Leu286.

The piperidine, diethylamine and azepane series exhibited a conserved binding mode, by consistently forming two hydrogen bonds with the residues Pro274 and Gly370 (Figure 4.25). However, the incorporation of azepino group (**4.7k**, **4.7l**, **4.8k**, & **4.8l**) significantly diminished the anthelmintic activity, although their binding mode was similar to other series of the compounds. In the lowest-energy conformation of

4.8l, the coumarin carbonyl oxygen formed a hydrogen bond with Thr276, in addition to the interaction with the residue Gly370. This altered orientation may explain the reduced anthelmintic activity of **4.8l** compared to the rest of the series. Moreover, these derivatives were further stabilized within the binding pocket by hydrophobic interactions, such as π–π stacking, π–alkyl, and π–σ interactions.

In contrast, the binding orientation of the phthalimide series was less consistent, although most compounds aligned within domains A, B, and C in a manner similar to the other derivatives. An exception was **4.8i**, which displayed a completely distinct orientation (Figure 4.24). Within the binding pocket, **4.7i** established two hydrogen bonds with Arg369 and Gly370 (Figure 4.23), while **4.7j** and **4.8j** each formed a single hydrogen bond with His229 and Arg369, respectively. Compound **4.8i**, however, primarily formed two hydrogen bonds with Thr276. This different binding orientation and interaction profile may be the reason for the reduced anthelmintic activity of **4.8i** relative to other phthalimide derivatives.

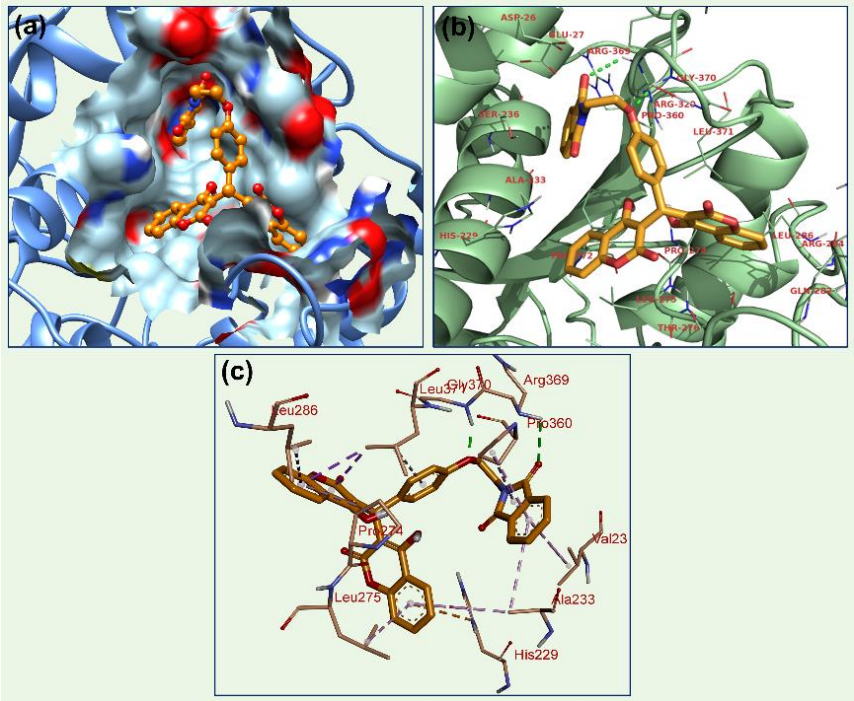

Figure 4.23. (a) Depiction of orientation of compound **4.7i** in the binding pocket. (b), (c) Depiction of noncovalent interactions of compound **4.7i** in the binding pocket.

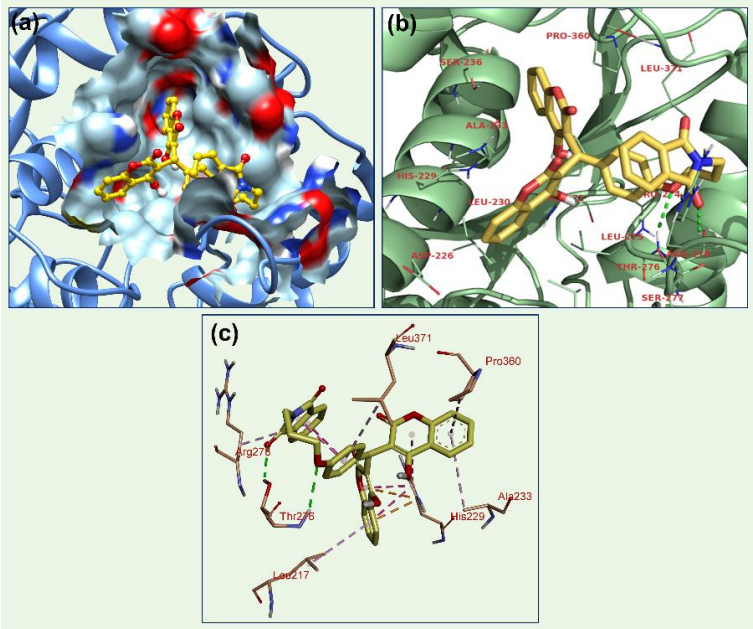

Figure 4.24. (a) Depiction of orientation of compound **4.8i** in the binding pocket. (b), (c) Depiction of noncovalent interactions of compound **4.8i** in the binding pocket.

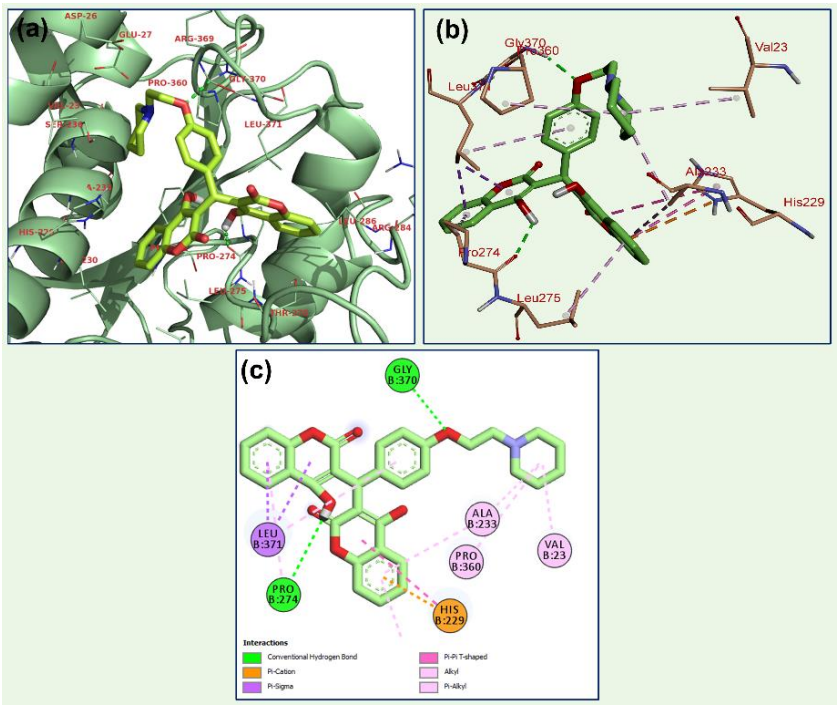

Figure 4.25. (a), (b) Depiction of noncovalent interactions of compound **4.7e** in the binding pocket.

Overall, the docking results and *in vitro* anthelmintic activity assays clearly indicated that Ser236, Pro274, and Gly370 are the key residues required for optimal interaction and stability. The incorporation of imidazole and morpholine groups into the bis-4-hydroxycoumarin core was found to be particularly important for imparting anthelmintic properties. Interestingly, despite differences in linker length (n = 1 or n = 2), the orientation of the secondary amine group and the overall binding conformation within the pocket remained largely similar. This similarity in binding orientation may explain why compounds within the same derivative series, even with different linker sizes, exhibited only minor differences in activity, especially in the imidazole and morpholine series.

4.5. Novel bis-4-hydroxycoumarin Hybrids: A Scaffold for Dual Anthelmintic and Anticancer Therapy

Microtubules are valuable therapeutic targets in both cancer treatment and anthelmintic therapy. Consequently, several anthelmintic drugs have attracted attention for their potential repurposing as anticancer agents. For instance, albendazole has been reported to effectively suppress the proliferation of various cancer cell types, including colorectal cancer, hepatocellular carcinoma, and several other human cancer cell lines (Pourgholami et al., 2001, 2005). Similarly, mebendazole, another benzimidazole-based anthelmintic, exhibits strong antitumor activity against lung cancer cells (Mukhopadhyay et al., 2002; Sasaki et al., 2002). MN-029, a benzimidazole carbamate structurally related to nocodazole, acts as a reversible inhibitor of microtubule assembly, leading to cytoskeletal disruption in tumor-associated vascular endothelial cells (Kelland, 2005). These drugs primarily target tubulin, and their binding sites overlap with that of colchicine (Aguayo-Ortiz, Méndez-Lucio, Medina-Franco, et al., 2013; Aguayo-Ortiz, Méndez-Lucio, Romo-Mancillas, et al., 2013).

In addition to benzimidazole derivatives, several well-established anticancer agents, including paclitaxel (taxol), docetaxel, discodermolide, epothilones, and zampanolide, are known microtubule-stabilizing drugs (Prota et al., 2013; Yang & Horwitz, 2017). Interestingly, ivermectin, a broad-spectrum anthelmintic, has also

been reported to bind to the taxol-binding pocket on tubulin, thereby stabilizing microtubules. Beyond its antimitotic effects, ivermectin inhibits angiogenesis, modulates multidrug resistance proteins, and targets cancer stem-like cells. Its mechanism of action closely resembles that of taxol, and preclinical studies suggest that ivermectin exerts potent antitumor effects, highlighting its potential clinical benefits in cancer therapy (Ashraf et al., 2015; Ashraf & Prichard, 2016; J. Liu et al., 2020).

Moreover, dicoumarol, a naturally occurring compound and the parent scaffold of synthesized bis-4-hydroxycoumarin hybrids, has also been reported to stabilize microtubules (Madari et al., 2003). Since our *in-silico* studies demonstrates strong affinity of bis-4-hydroxycoumarin hybrids to the taxane-binding pocket, and *in vitro* studies confirm their potent anthelmintic activity, it is reasonable to hypothesize that these compounds may also exhibit anticancer properties. This possibility warrants further investigation, and the evaluation of bis-4-hydroxycoumarin hybrids as potential anticancer agents will be the focus of our future studies.

4.6. Conclusion

In summary, conjugates of bis-4-hydroxycoumarin linked to secondary amine via alkyl chains (**4.7a–4.7l**, **4.8a–4.8l**) were synthesized based on molecular hybridisation approach. All compounds were obtained in good yields and were fully characterized. The *in vitro* anthelmintic evaluation against *R. echinobothrida* revealed that bis-4-hydroxycoumarin conjugates bearing imidazole and morpholine moieties exhibited the highest potency, demonstrating approximately ~6–7-fold greater activity than the standard drug albendazole. Morphological studies of treated parasites further showed that mortality was associated with irreversible structural alterations, including severe scolex deformation, protuberances on suckers and the rostellum, detachment of spines from suckers, crack and pit formation, abnormal folding and wrinkling of proglottids, tegumental erosion, and disfiguration or loss of microtriches.

In silico molecular docking studies suggested that the synthesized bis-4-hydroxycoumarin hybrids have a higher binding affinity for the taxane-binding pocket compared to other known sites. The results also indicated that varying the alkyl chain

length (n = 1–2) did not produce significant conformational deviations within the binding pocket. Moreover, residues Ser236, Pro274, and Gly370 were identified as key contributors to optimal binding interactions and stability.

Overall, this study demonstrates that hybrids of bis-4-hydroxycoumarin derivatives have strong potential as lead candidates for the development of potent anthelmintic drugs and warrant further pharmacological evaluation.

4.7. ^{1}H NMR and ^{13}C NMR Spectra and HRMS Data of Selected Compounds

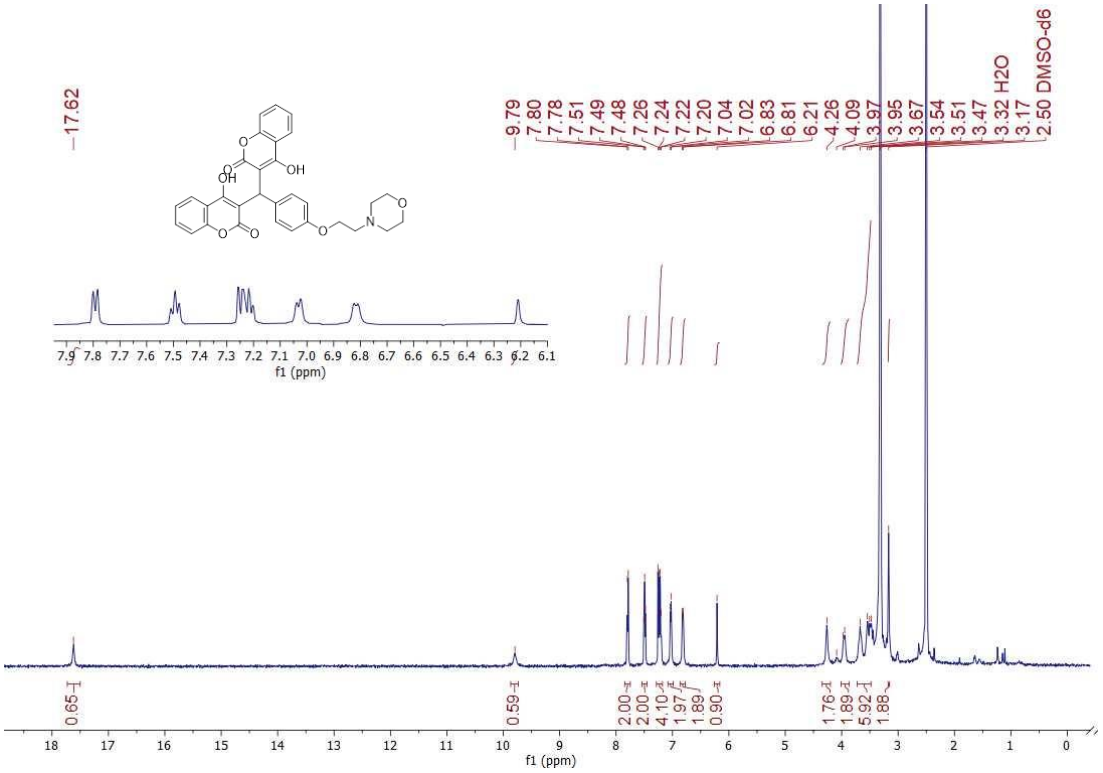

Figure 4.26. ^{1}H NMR of compound **4.7a.**

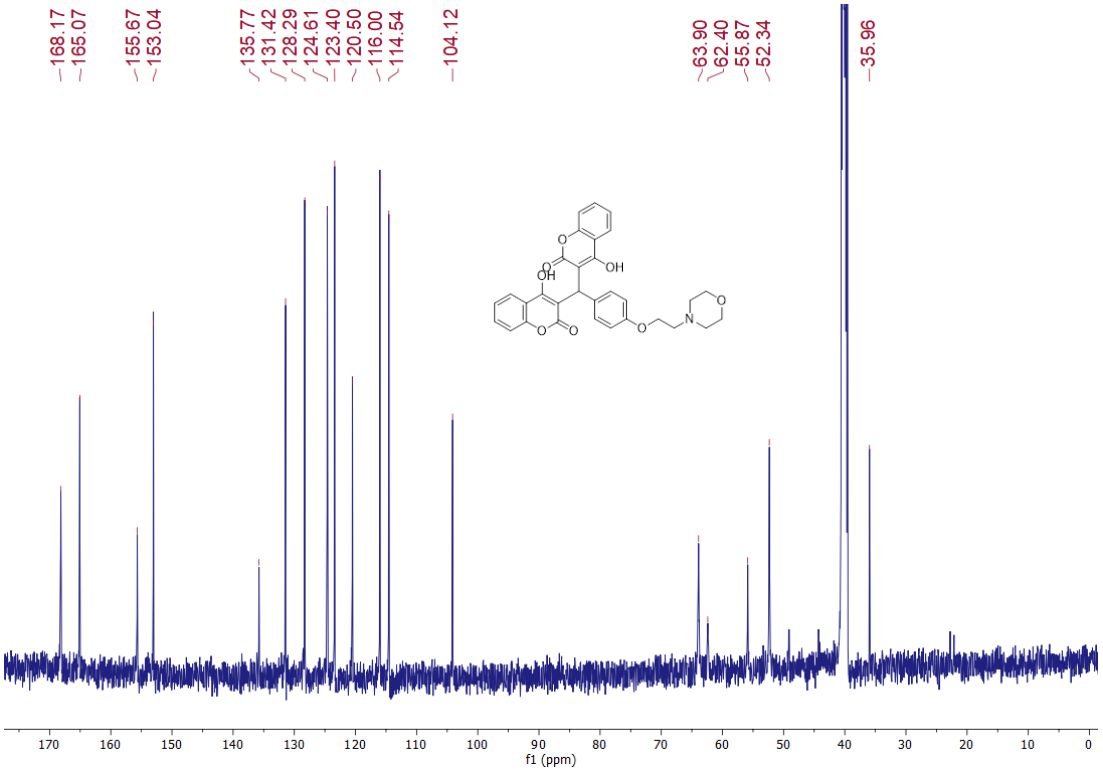

Figure 4.27. ^{13}C NMR of compound **4.7a.**

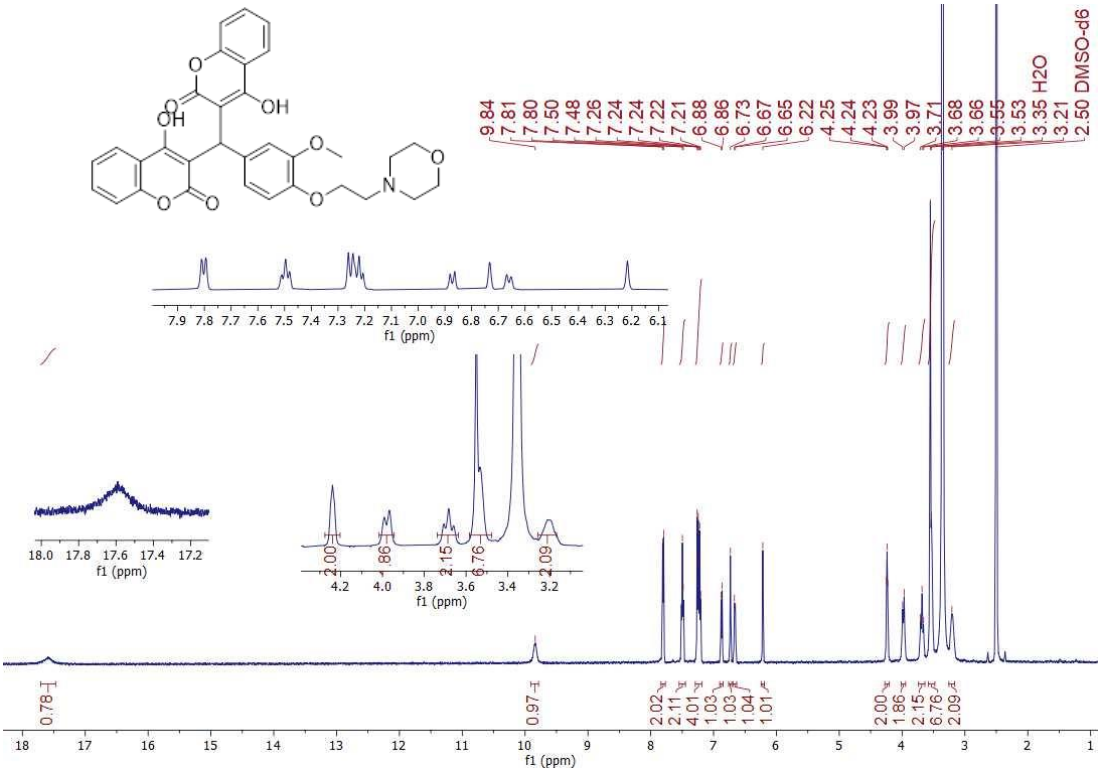

Figure 4.28. ^{1}H NMR of compound **4.7b.**

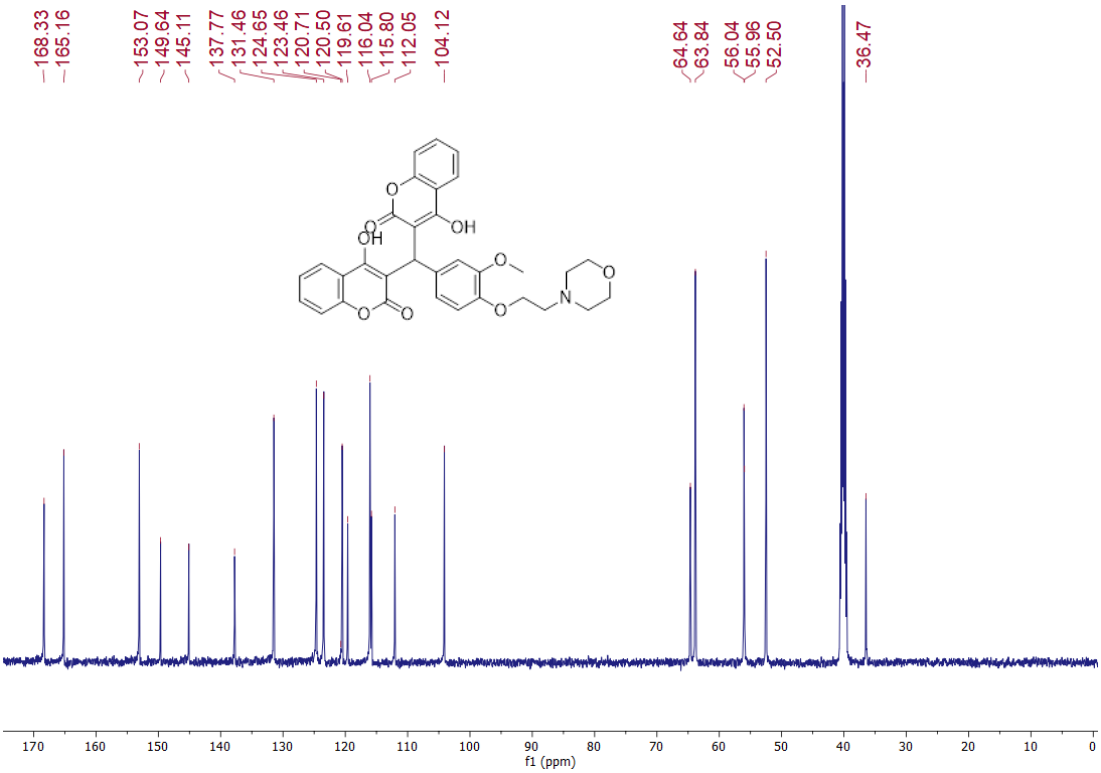

Figure 4.29. ^{13}C NMR of compound **4.7b.**

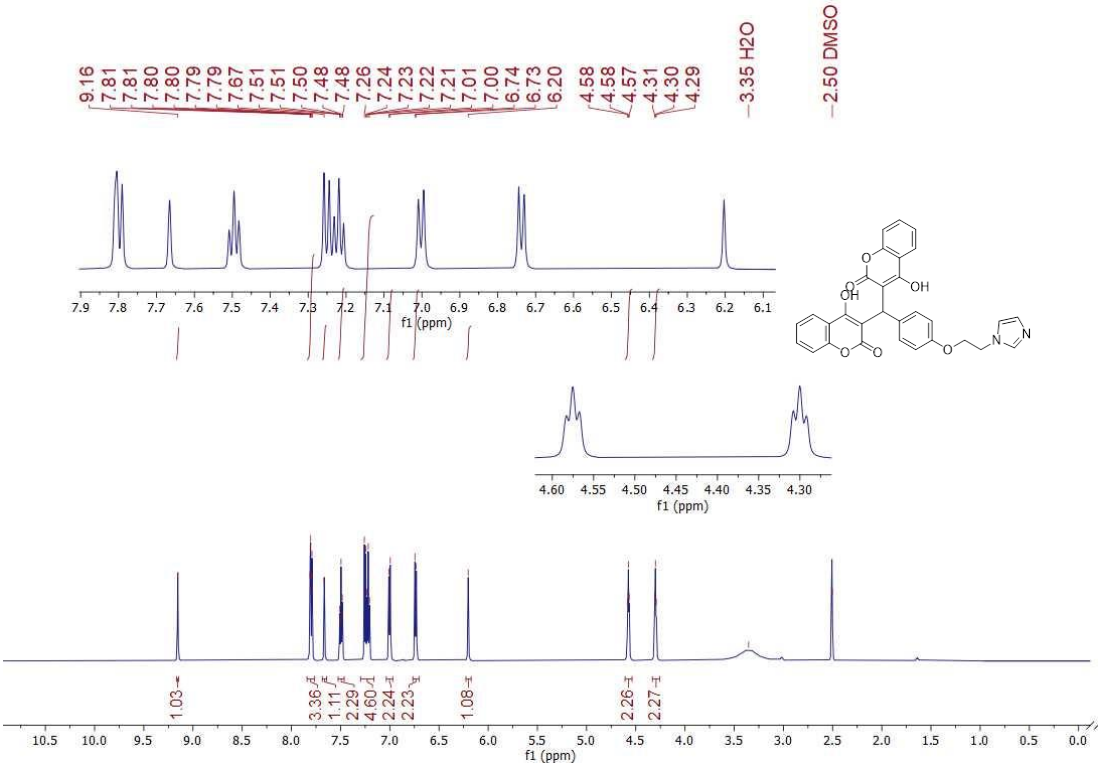

Figure 4.30. ^{1}H NMR of compound **4.7c.**

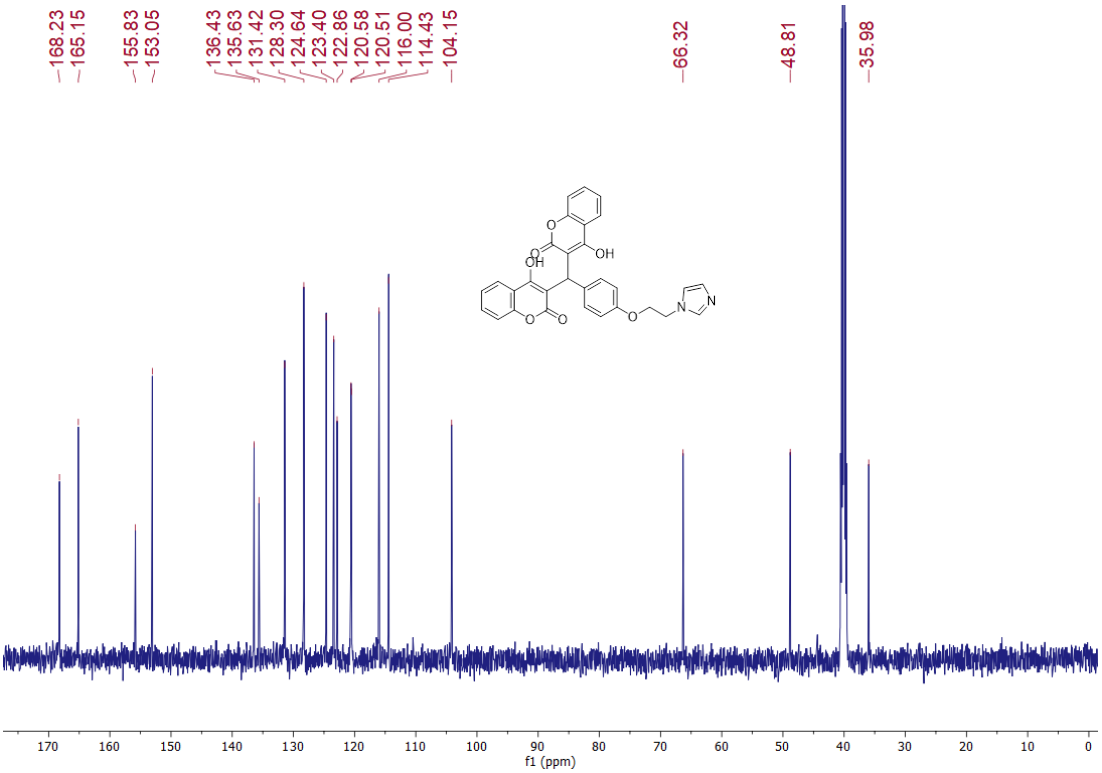

Figure 4.31. ^{13}C NMR of compound **4.7c.**

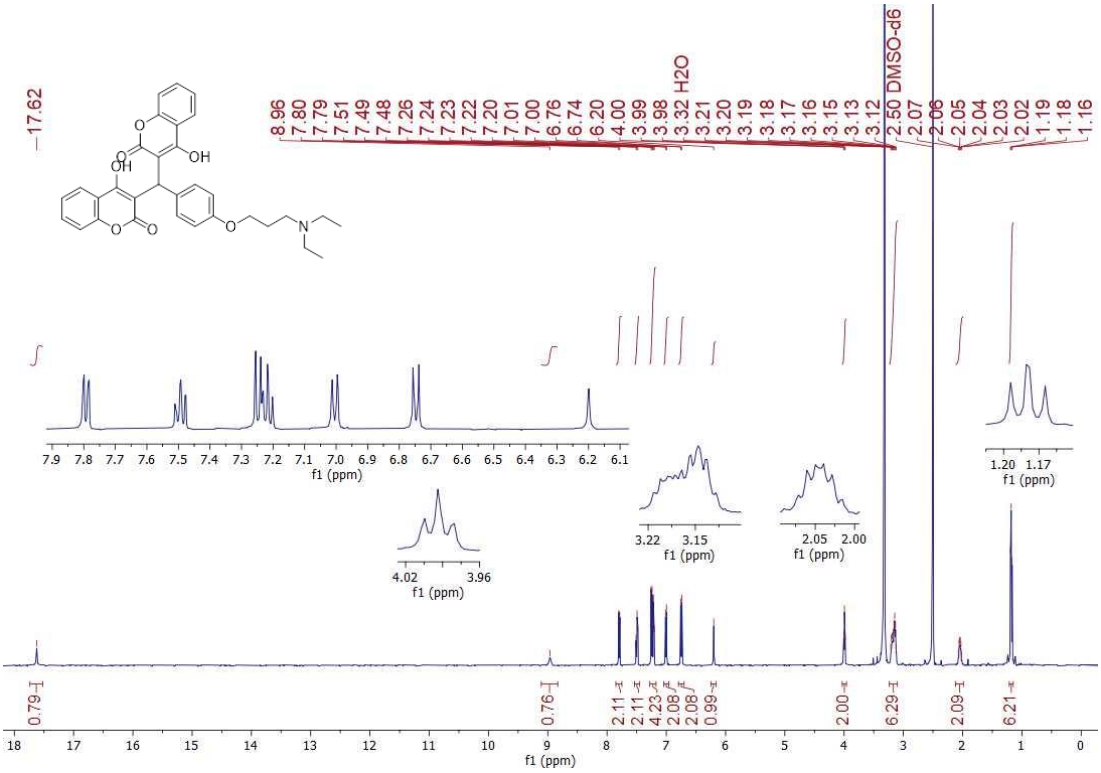

Figure 4.32. ^{1}H NMR of compound **4.8g.**

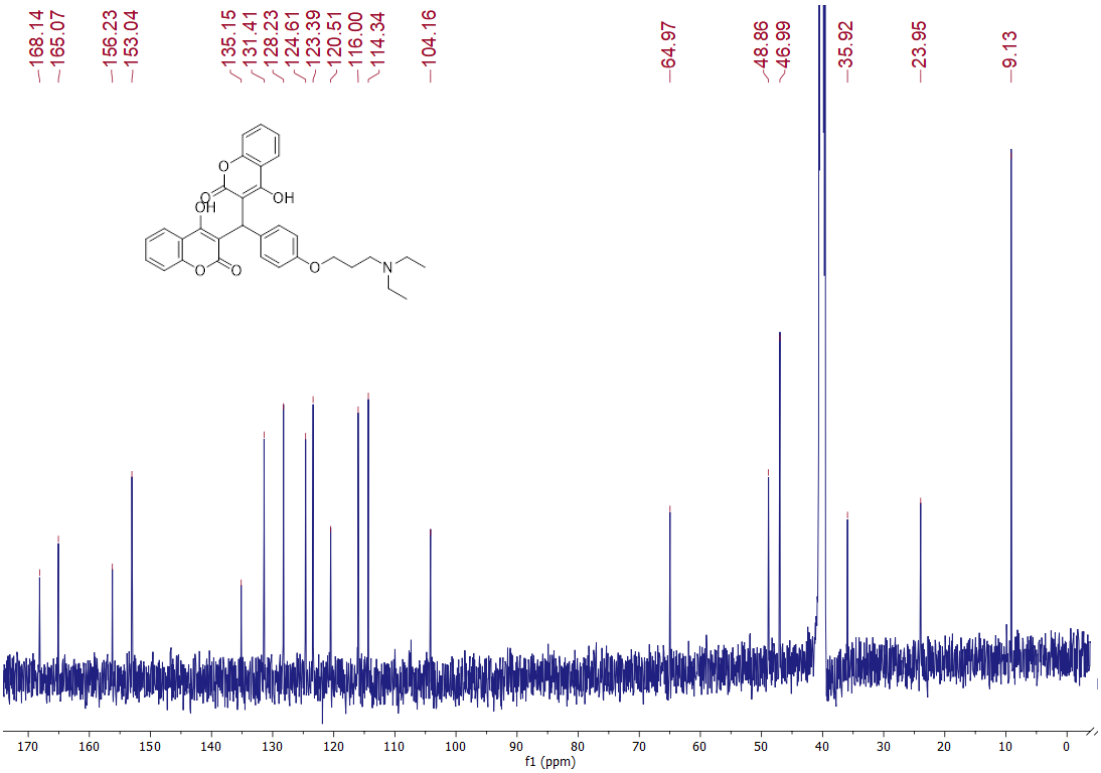

Figure 4.33. ^{13}C NMR of compound **4.8g.**

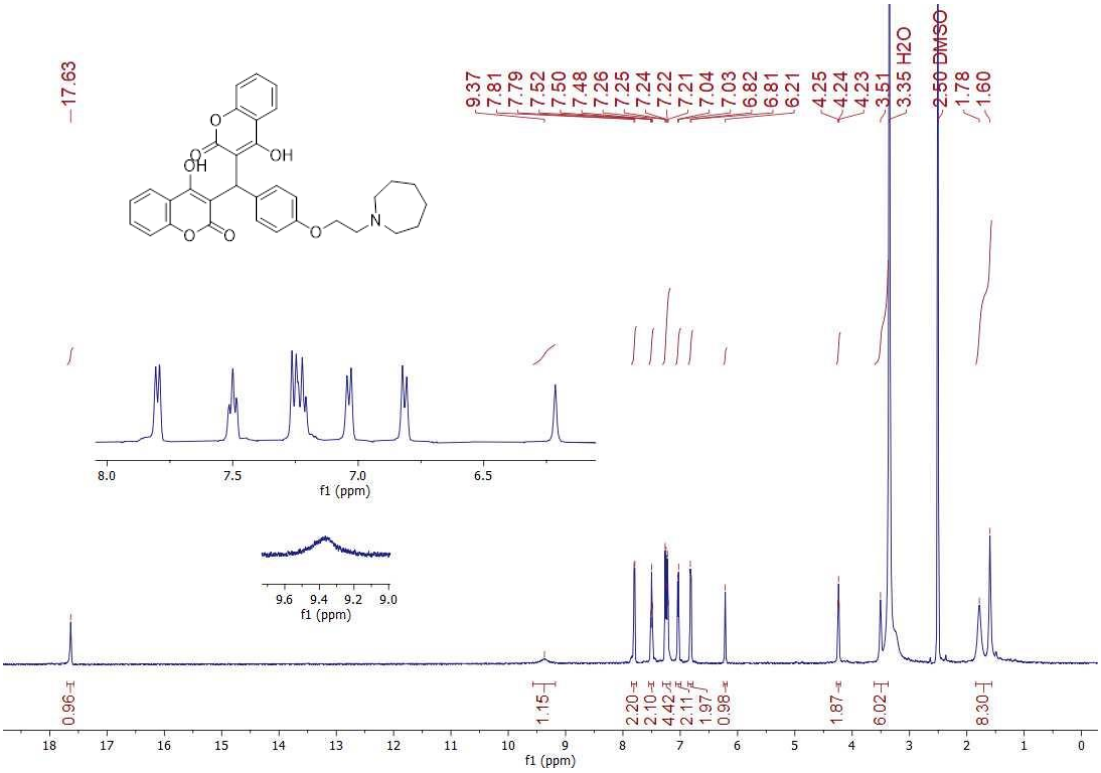

Figure 4.34. ^{1}H NMR of compound **4.7k.**

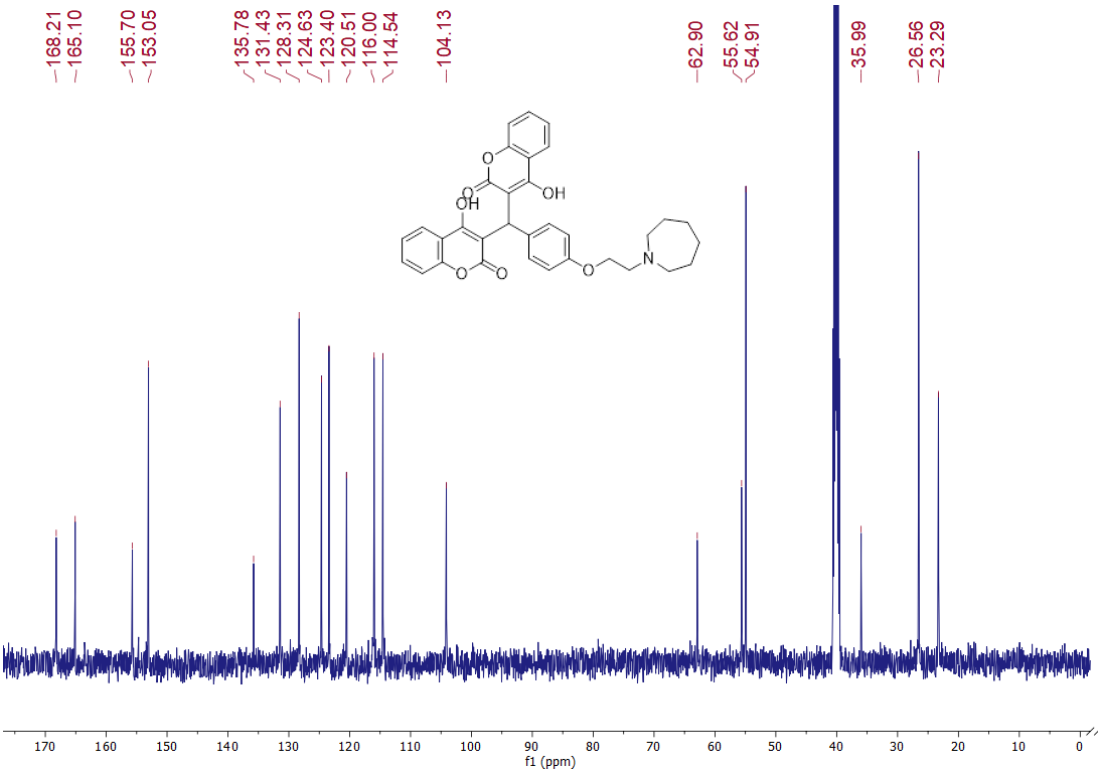

Figure 4.35. ^{13}C NMR of compound **4.7k.**

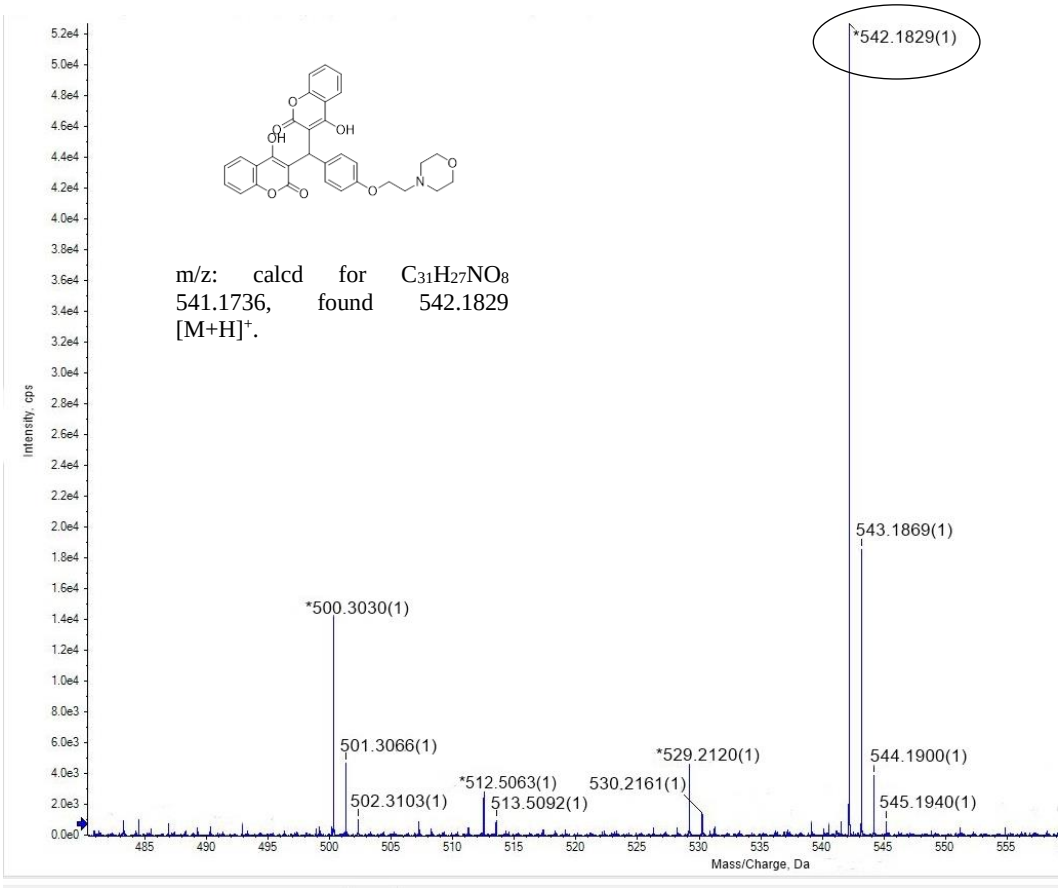

m/z: calcd for $C_{31}H_{27}NO_8$ 541.1736, found 542.1829 $[M+H]^+$.

Figure 4.36. HRMS of compound **4.7a.**

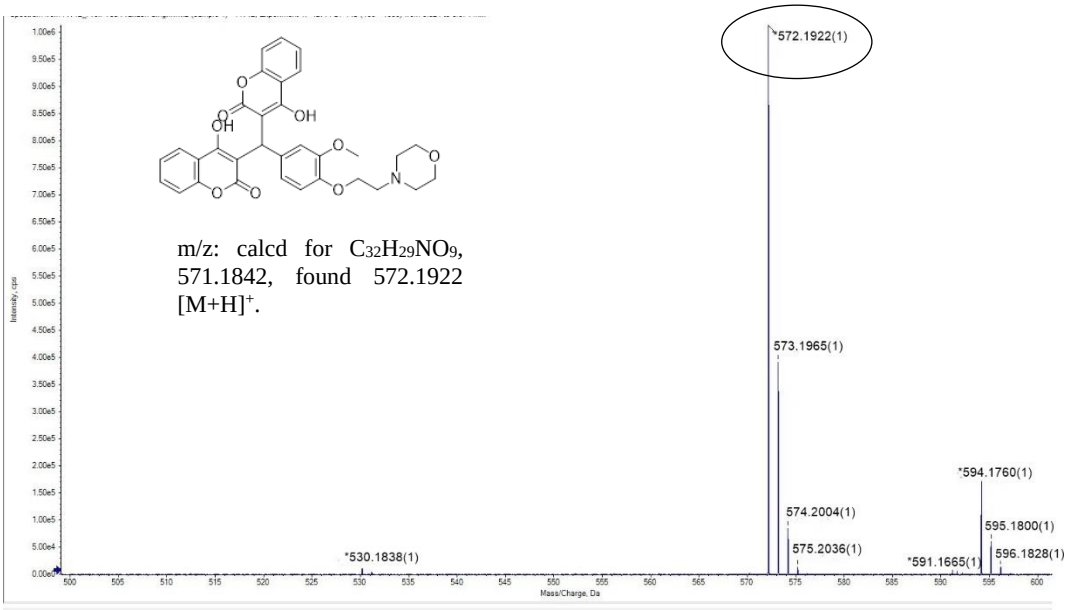

m/z: calcd for $C_{32}H_{29}NO_9$, 571.1842, found 572.1922 $[M+H]^+$.

Figure 4.37. HRMS of compound **4.7b.**

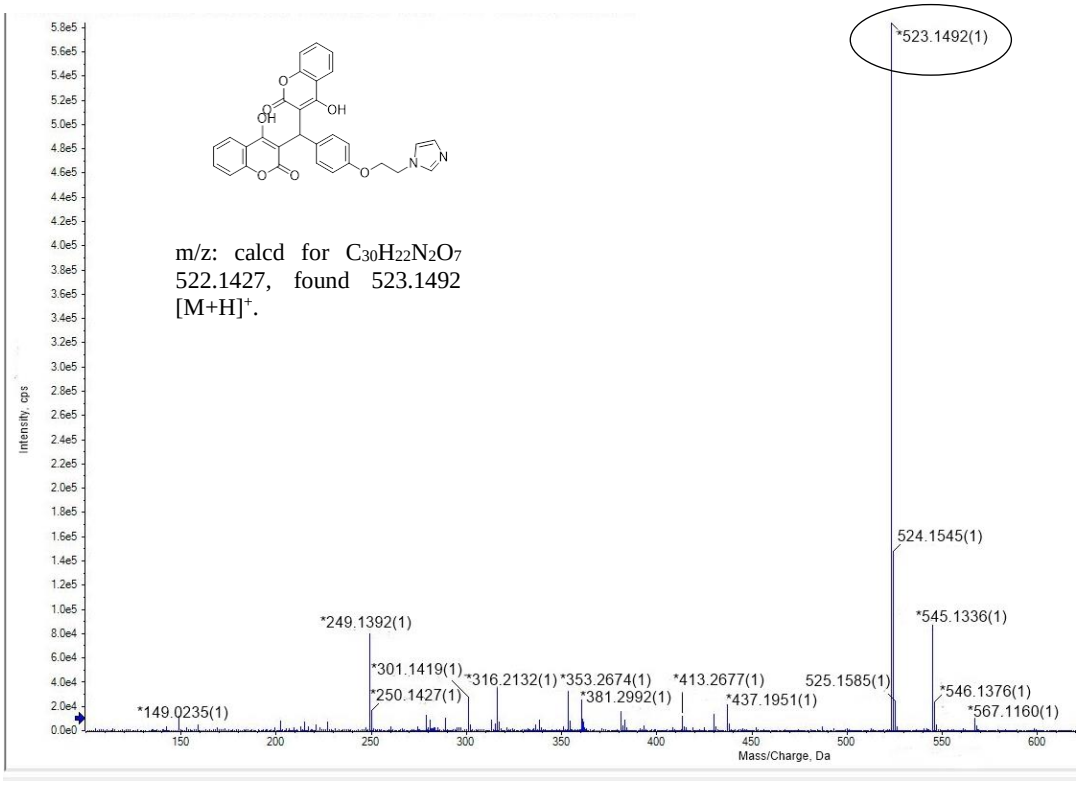

Figure 4.38. HRMS of compound **4.7c.**

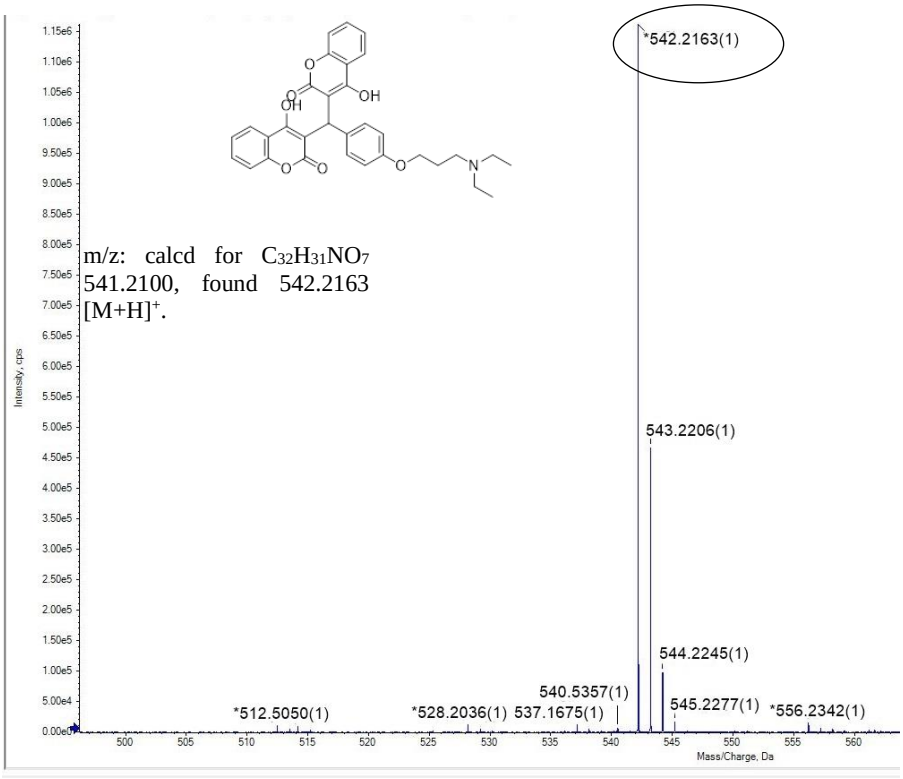

Figure 4.39. HRMS of compound **4.8g.**

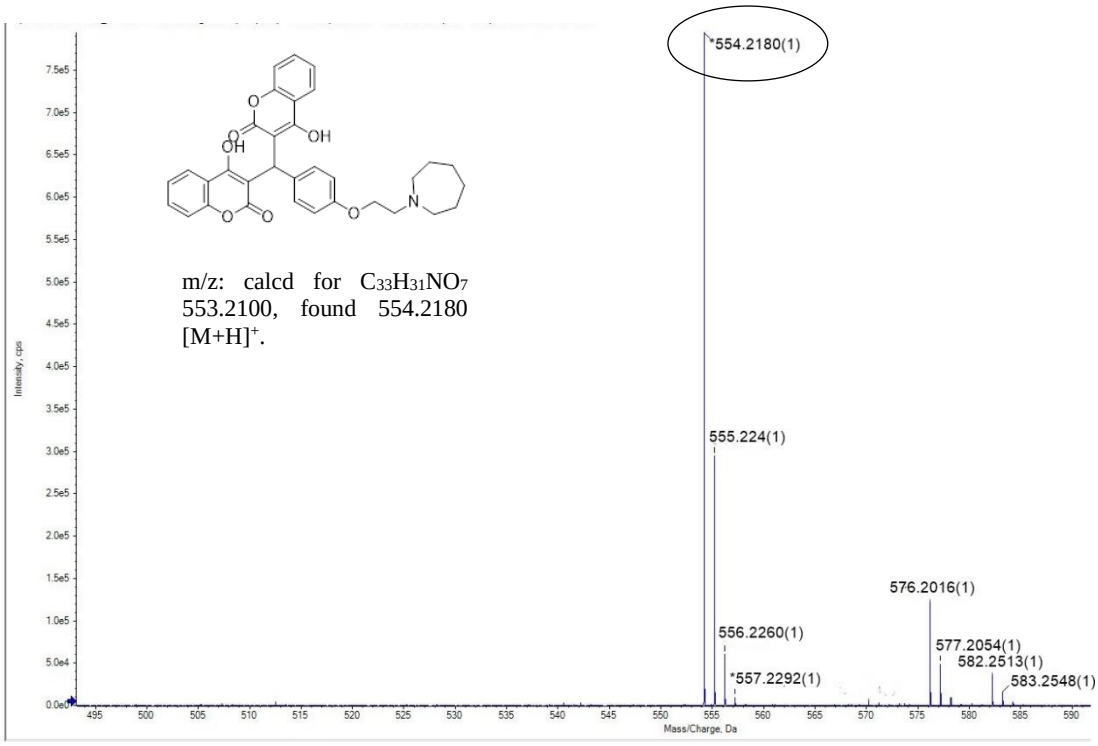

Figure 4.40. HRMS of compound **4.7k.**

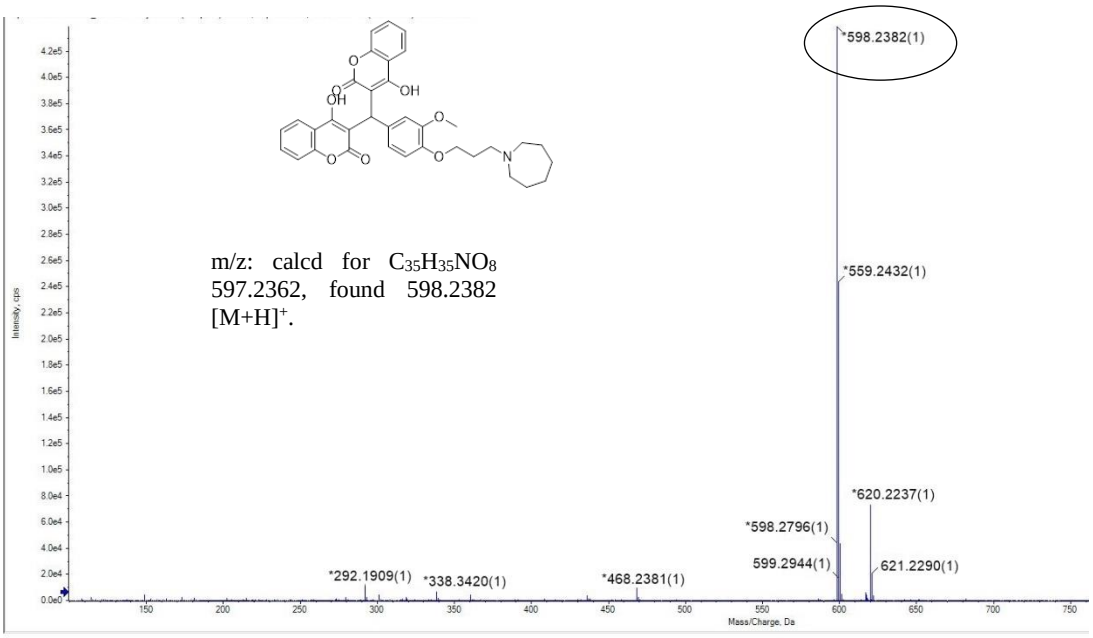

Figure 4.41. HRMS of compound **4.7l.**

CHAPTER 5

SUMMARY AND CONCLUSION

CHAPTER 5

SUMMARY AND CONCLUSION

Natural products have long served as a cornerstone of drug discovery and development. Their structural diversity and biological activity have inspired the design of many therapeutic agents, many of which remain in use today. A large proportion of modern pharmaceuticals are derived from secondary metabolites produced by natural sources such as plants, microorganisms, and marine organisms. These compounds often provide unique motifs that serve as templates for new chemical entities with enhanced efficacy and pharmacological profiles. **Chapter 1** presents a comprehensive review of the existing literature relevant to the design and development of bioactive molecules derived from natural products.

Building upon this foundation, the present thesis, entitled "Design, Synthesis, and Study of Bioactive Natural Product Congeners," investigates the rational design, synthesis, and biological evaluation of structurally novel analogues inspired by naturally occurring molecules. To this end, three main classes of compounds were developed and studied:

- Plinabulin-based 2,5-diketopiperazine (DKP) analogues,
- DKP–based coumarin hybrids, and
- Bis-4-hydroxycoumarin hybrids.

In the first part of this work (**Chapter 2**), Plinabulin-based DKP analogues were designed using phenylahistin and its potent anticancer derivative, Plinabulin, as inspiration. Since DKPs are valued for their structural motifs and diverse biological activities, a series of novel derivatives was developed by introducing amino functionalities onto the aromatic ring or through flexible alkyl linkers. Furthermore, a lipophilic allyl group was incorporated to improve pharmacokinetic and solubility properties.

Based on these designs, 24 novel Plinabulin-based DKP analogues were synthesized and fully characterized (Figure 5.1). Single-crystal X-ray diffraction (SCXRD) of compound **2.31f** revealed critical details about its molecular

conformation and packing. Further analyses using Hirshfeld surface and energy frameworks elucidated key aspects of the compound's self-assembly in the solid state.

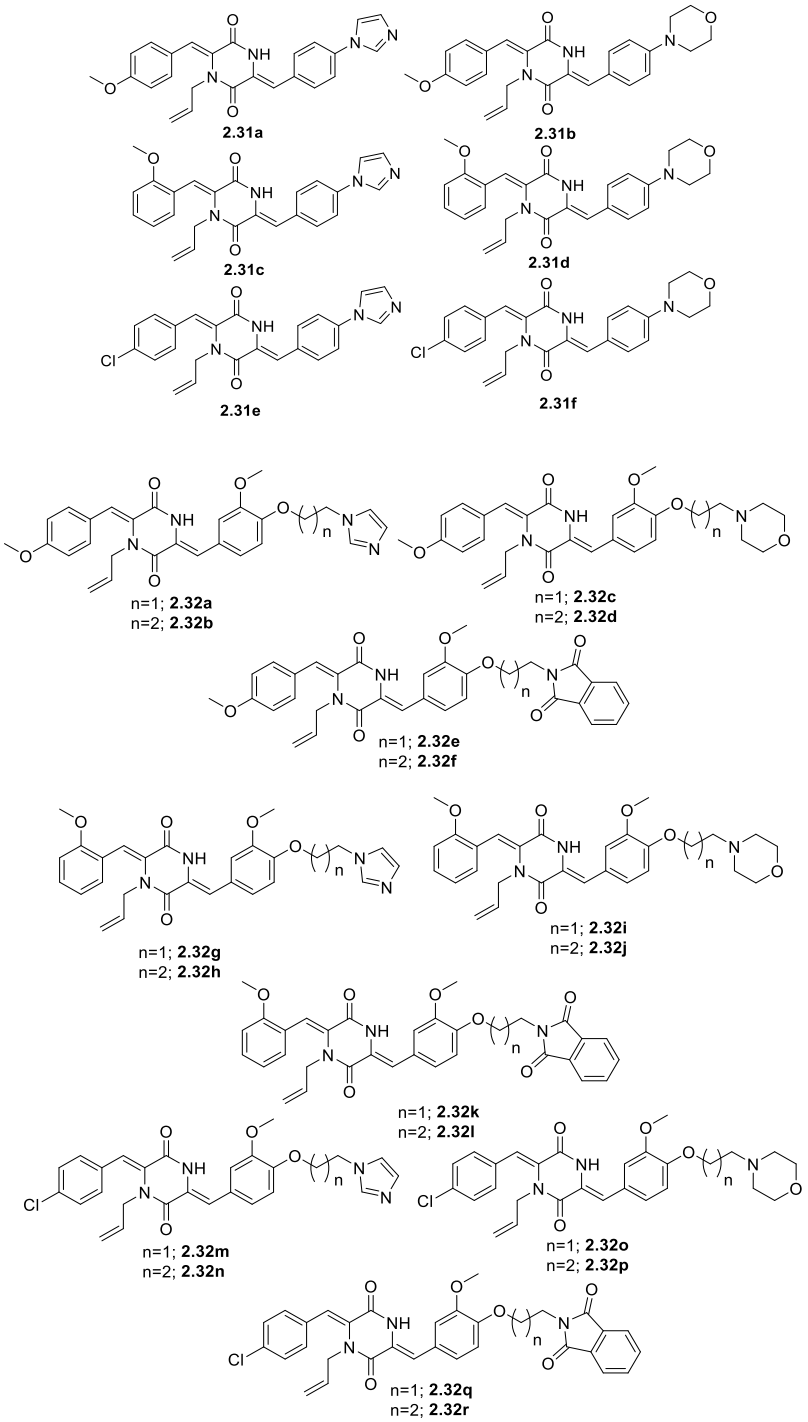

Figure 5.1. Chemical structures of novel Plinabulin-based DKP derivatives (**2.31a–2.31f** and **2.32a–2.32f**) designed and synthesized as potential anticancer agents.

The *in vitro* anticancer activity of the synthesized compounds was evaluated using the MTT assay on HepG2 (human hepatocellular carcinoma) and HCT116 (human colon carcinoma) cell lines. In the series **2.31a**–**2.31f**, where amino functionalities were directly attached to the aryl ring of the DKP scaffold, compounds **2.31b** and **2.31d** exhibited the strongest cytotoxic effects, with IC_{50} values of 91.81 ± 3.90 μM and 105.1 ± 4.75 μM, respectively, against HepG2 cells after 24 hours of treatment. These results indicate promising cytotoxic potency relative to the standard chemotherapeutic drug 5-Fluorouracil (5-FU) (IC_{50} = 77.64 ± 0.25 μM). In the series **2.32a**–**2.32r**, where amino functionalities were introduced through flexible alkyl linkers, compounds **2.32q** and **2.32f** were most active against both HCT116 and HepG2 cell lines. Their IC_{50} values were 63.15 ± 1.22 μM and 84.43 ± 1.58 μM, respectively, against HCT116 cells, and 96.03 ± 2.33 μM and 105.2 ± 2.50 μM, respectively, against HepG2 cells after 24 hours of treatment. These results were also comparable with a standard drug 5-FU (IC_{50} = 61.13 ± 0.29 μM for HCT116 and 77.64 ± 0.25 μM for HepG2).

Mechanistic studies involving apoptosis revealed that compound **2.32q** induced apoptosis in HCT116 cells in a dose-dependent manner, with an apoptotic index ranging from 36.43% to 84.65% at concentrations of 25–80 μM. Distinct apoptotic features such as membrane blebbing, nuclear condensation, and fragmentation were observed. At 50 μM, the apoptotic potency of compound **2.32q** was comparable to that of 5-fluorouracil (5-FU) at the same concentration. Furthermore, compound **2.32q** significantly increased caspase-6 activity by 93.04%, which was approximately 1.2-fold higher than that induced by 5-FU.

Molecular docking analyses revealed that DKP analogues displayed strong binding affinities for β-tubulin and c-Met proteins, primarily via hydrogen bonding and hydrophobic contacts, including π–π, π–σ, π–alkyl, π–sulphur, and π–cation interactions. Notably, phthalimide-containing derivatives showed enhanced stabilization within the binding site through π–π stacking involving their phthalimide rings. This enhanced stabilization is likely linked to the superior anticancer activity observed for compounds **2.32f** and **2.32q**.

Overall, the studies presented in **Chapter 2** demonstrate that Plinabulin-based DKP analogues represent promising lead candidates for the development of effective anticancer agents and warrant further pharmacological and mechanistic investigations.

Coumarins are well known for their pharmacological properties, which include anticoagulant, antitumor, anti-inflammatory, antiviral, and antimicrobial activities. In **Chapter 3**, given the promising anticancer potential of the DKP analogues from **Chapter 2**, the design and synthesis of DKP–based coumarin hybrids were explored. Coumarin moieties were linked to the DKP core via flexible linkers. This generated hybrid scaffolds that combined pharmacophores from both systems.

A total of 18 novel DKP–based coumarin hybrids were synthesized (Figure 5.2). Of the 12 derivatives evaluated against the A549 human non-small cell lung cancer cell line, compound **3.12b** exhibited the highest potency, with IC_{50} values of 52.21 ± 4.14 μM at 24 hours and 22.02 ± 3.98 μM at 48 hours. The remaining compounds displayed only moderate to low anticancer activity, which may be attributed to their limited solubility.

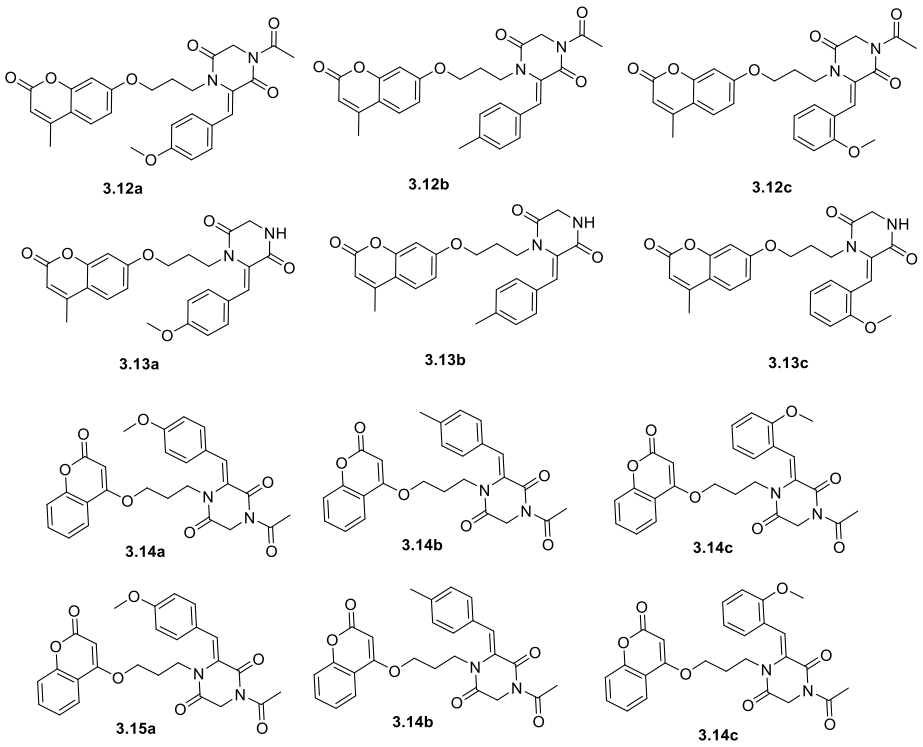

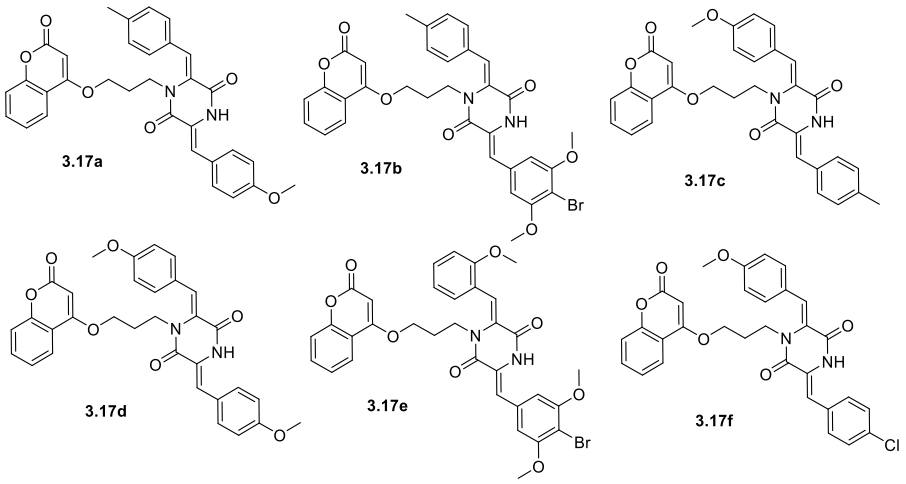

Figure 5.2. Chemical structures of novel DKP-based coumarin derivatives.

Rational design and subsequent structural optimization led to the synthesis of a new set of derivatives, **3.17a**–**3.17f**. These compounds showed predicted binding conformations and affinities (–9.1 to –9.5 kcal/mol) comparable to plinabulin (–9.1 kcal/mol). These findings suggest that the new derivatives may possess similar tubulin polymerization inhibitory potential. Compounds **3.17a–3.17f** has not yet been evaluated experimentally for anticancer activity. *In silico* ADMET profiles indicate favorable pharmacokinetic and safety characteristics, including high intestinal absorption, poor BBB and CNS permeability, acceptable genotoxicity and cardiotoxicity profiles, and low acute toxicity. These findings support further biological evaluation of these candidates.

Bis-coumarins have attracted considerable attention in medicinal chemistry due to their wide range of biological activities, including antiparasitic, anticancer, antibacterial, antifungal, anti-HCV, anti-inflammatory, anti-HIV, antimalarial, antitubercular, anti-alzheimer, and antipsychotic effects. **Chapter 4** describes the design of bis-4-hydroxycoumarin hybrids functionalized by amino functionalities via a flexible alkyl linker as potential anthelmintic agents. A library of 24 bis-4-hydroxycoumarin hybrids were synthesized (Figure 5.3) and tested for *in vitro* anthelmintic activity against the cestode *R. echinobothrida*. The results revealed that imidazolo- and morpholino-substituted derivatives (**4.7a**–**4.7d**, **4.8a**–**4.8d**) displayed excellent anthelmintic activity, exhibiting approximately 6- to 7-fold higher potency

than the standard drug albendazole. Morphological examination of treated parasites done through scanning electron microscopy (SEM) confirmed extensive and irreversible structural alterations, such as severe scolex deformation, protuberances on suckers and the rostellum, detachment of spines from suckers, crack and pit formation, abnormal folding and wrinkling of proglottids, tegumental erosion, and disfiguration or loss of microtriches. *In silico* molecular docking studies further suggested that these bis-4-hydroxycoumarin hybrids possess strong binding affinities for the taxane-binding pocket compared to other known sites, with residues Ser236, Pro274, and Gly370 identified as key contributors to optimal binding interactions and stability.

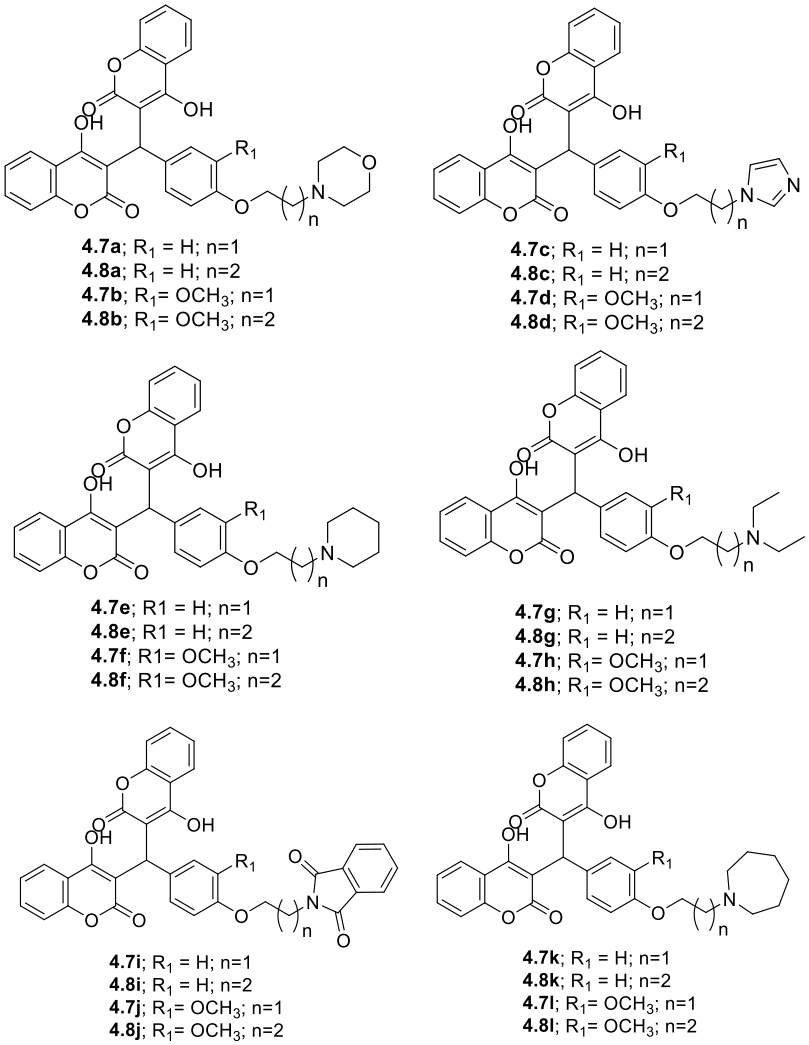

Figure 5.3. Chemical structures of novel bis-4-hydroxycoumarin conjugates linked to various amino functionalities.

5.1. General Conclusion

Overall, this thesis highlights the versatility of natural product frameworks as templates for drug discovery and design. The findings not only identify new lead compounds with promising anticancer and anthelmintic activities but also establish a foundation for future optimization, mechanistic elucidation, and *in vivo* evaluation. Continued investigation into these scaffolds, particularly through pharmacokinetic and toxicity profiling, could contribute significantly to the discovery of novel, effective, and safer therapeutic agents derived from natural product congeners.

REFERENCES

Aguayo-Ortiz, R., Méndez-Lucio, O., Medina-Franco, J. L., Castillo, R., Yépez-Mulia, L., Hernández-Luis, F., & Hernández-Campos, A. (2013). Towards the identification of the binding site of benzimidazoles to β-tubulin of Trichinella spiralis: Insights from computational and experimental data. *Journal of Molecular Graphics and Modelling*, *41*, 12–19. https://doi.org/10.1016/j.jmgm.2013.01.007

Aguayo-Ortiz, R., Méndez-Lucio, O., Romo-Mancillas, A., Castillo, R., Yépez-Mulia, L., Medina-Franco, J. L., & Hernández-Campos, A. (2013). Molecular basis for benzimidazole resistance from a novel β-tubulin binding site model. *Journal of Molecular Graphics and Modelling*, *45*, 26–37. https://doi.org/10.1016/j.jmgm.2013.07.008

Ahmad Bhat, A., Kaur, G., Tandon, N., Tandon, R., & Singh, I. (2024). Current advancements in synthesis, anticancer activity, and structure–activity relationship (SAR) of coumarin derivatives. *Inorganic Chemistry Communications*, *167*, 112605. https://doi.org/10.1016/j.inoche.2024.112605

Ahmed, E. Y., Abdel Latif, N. A., El-Mansy, M. F., Elserwy, W. S., & Abdelhafez, O. M. (2020). VEGFR-2 inhibiting effect and molecular modeling of newly synthesized coumarin derivatives as anti-breast cancer agents. *Bioorganic & Medicinal Chemistry*, *28*(5), 115328. https://doi.org/10.1016/j.bmc.2020.115328

Ali, I., Lone, M. N., & Aboul-Enein, H. Y. (2017). Imidazoles as potential anticancer agents. *Med. Chem. Commun.*, *8*(9), 1742–1773. https://doi.org/10.1039/c7md00067g

Alvarez, M. E., Houck, D. R., White, C. B., Brownell, J. E., Bobko, M. A., Rodger, C. A., Stawicki, M. B., Sun, H. H., Gillum, A. M., & Cooper, R. (1994). Isolation and structure elucidation of two new calpain inhibitors from Streptomyces griseus. *The Journal of Antibiotics*, *47*(11), 1195–1201. https://doi.org/10.7164/antibiotics.47.1195

Ando, S., Grote, A. L., & Koide, K. (2011). Diastereoselective Synthesis of Diketopiperazine Bis-α,β-epoxides. *The Journal of Organic Chemistry*, *76*(4), 1155–1158. https://doi.org/10.1021/jo102096d

Arora, N., Dhiman, P., Kumar, S., Singh, G., & Monga, V. (2020). Recent advances in synthesis and medicinal chemistry of benzodiazepines. *Bioorganic Chemistry*, *97*, 103668. https://doi.org/10.1016/j.bioorg.2020.103668

Ashraf, S., & Prichard, R. (2016). Ivermectin exhibits potent anti-mitotic activity. *Veterinary Parasitology*, *226*, 1–4. https://doi.org/10.1016/j.vetpar.2016.06.015

Ashraf, S., Beech, R. N., Hancock, M. A., & Prichard, R. K. (2015). Ivermectin binds to Haemonchus contortus tubulins and promotes stability of microtubules. *International Journal for Parasitology*, *45*(9–10), 647–654. https://doi.org/10.1016/j.ijpara.2015.03.010

Baruah, P., Basumatary, G., Yesylevskyy, S. O., Aguan, K., Bez, G., & Mitra, S. (2019). Novel coumarin derivatives as potent acetylcholinesterase inhibitors: Insight into efficacy, mode and site of inhibition. *Journal of Biomolecular Structure and Dynamics*, *37*(7), 1750–1765. https://doi.org/10.1080/07391102.2018.1465853

Basumatary, G., Dhar, E. D., Das, D., Deka, R. Ch., Yadav, A. K., & Bez, G. (2020). Coumarin-based Trisubstituted Methanes as Potent Anthelmintic: Synthesis, Molecular Docking and *in vitro* Efficacy. *Journal of Chemical Sciences*, *132*(1), 40. https://doi.org/10.1007/s12039-020-1737-z

Bertelsen, L. B., Shen, Y. Y., Nielsen, T., Stødkilde-Jørgensen, H., Kenneth Lloyd, G., Siemann, D. W., & Horsman, M. R. (2011). Vascular effects of plinabulin (NPI-2358) and the influence on tumour response when given alone or combined with radiation. *International Journal of Radiation Biology*, *87*(11), 1126–1134. https://doi.org/10.3109/09553002.2011.605418

Borthwick, A. D. (2012). 2,5-Diketopiperazines: Synthesis, Reactions, Medicinal Chemistry, and Bioactive Natural Products. *Chemical Reviews*, *112*(7), 3641–3716. https://doi.org/10.1021/cr200398y

Borthwick, A. D., & Da Costa, N. C. (2017). 2,5-diketopiperazines in food and beverages: Taste and bioactivity. *Critical Reviews in Food Science and Nutrition*, *57*(4), 718–742. https://doi.org/10.1080/10408398.2014.911142

Bradford M. M. (1976). A rapid and sensitive method for the quantitation of microgram quantities of protein utilizing the principle of protein-dye binding. *Analytical biochemistry*, *72*(1-2), 248-254. https://doi.org/10.1016/0003-2697(76)90527-3.

Bray, F., Laversanne, M., Sung, H., Ferlay, J., Siegel, R. L., Soerjomataram, I., & Jemal, A. (2024). Global cancer statistics 2022: GLOBOCAN estimates of incidence and mortality worldwide for 36 cancers in 185 countries. *CA: A Cancer Journal for Clinicians*, *74*(3), 229–263. https://doi.org/10.3322/caac.21834

Chen, L. Z., Sun, W. W., Bo, L., Wang, J. Q., Xiu, C., Tang, W. J., Shi, J. B., Zhou, H. P., & Liu, X. H. (2017). New arylpyrazoline-coumarins: Synthesis and anti-inflammatory activity. *European Journal of Medicinal Chemistry*, *138*, 170–181. https://doi.org/10.1016/j.ejmech.2017.06.044

Chen, X., Chen, X., Steimbach, R. R., Wu, T., Li, H., Dan, W., Shi, P., Cao, C., Li, D., Miller, A. K., Qiu, Z., Gao, J., & Zhu, Y. (2020). Novel 2, 5-diketopiperazine derivatives as potent selective histone deacetylase 6 inhibitors: Rational design, synthesis and antiproliferative activity. *European Journal of Medicinal Chemistry*, *187*, 111950. https://doi.org/10.1016/j.ejmech.2019.111950

Chen, Y., Wang, S., Xu, X., Liu, X., Yu, M., Zhao, S., Liu, S., Qiu, Y., Zhang, T., Liu, B.-F., & Zhang, G. (2013). Synthesis and Biological Investigation of Coumarin Piperazine (Piperidine) Derivatives as Potential Multireceptor Atypical Antipsychotics. *Journal of Medicinal Chemistry*, *56*(11), 4671–4690. https://doi.org/10.1021/jm400408r

Cheng, W., Yuan, Y., Qiu, N., Peng, P., Sheng, R., & Hu, Y. (2014). Identification of novel 4-anilinoquinazoline derivatives as potent EGFR inhibitors both under normoxia and hypoxia. *Bioorganic & Medicinal Chemistry*, *22*(24), 6796–6805. https://doi.org/10.1016/j.bmc.2014.10.038

Chi, C.-L., Xu, L., Li, J.-J., Liu, Y., & Chen, B.-Q. (2022). Synthesis, antiproliferative, and antimicrobial properties of novel phthalimide derivatives. *Medicinal Chemistry Research*, *31*(1), 120–131. https://doi.org/10.1007/s00044-021-02823-5

Chiang, C., Cheng, M., Peng, C., Huang, H., & Chen, I. (2010). A Novel Dimeric Coumarin Analog and Antimycobacterial Constituents from *Fatoua pilosa*. *Chemistry & Biodiversity*, *7*(7), 1728–1736. https://doi.org/10.1002/cbdv.200900326

Chinh, P. T., Tham, P. T., Quynh, D. H., Tuyen, N. V., Van, D. T., Phuong, P. T., Thu Hang, T. T., & Van Kiem, P. (2021). Synthesis and Cytotoxic Activity of Several Novel *N* -Alkyl-Plinabulin Derivatives With Aryl Group Moieties. *Natural Product Communications*, *16*(4), 1934578X211010040. https://doi.org/10.1177/1934578X211010040

Ciaffaglione, V., Intagliata, S., Pittalà, V., Marrazzo, A., Sorrenti, V., Vanella, L., Rescifina, A., Floresta, G., Sultan, A., Greish, K., & Salerno, L. (2020). New Arylethanolimidazole Derivatives as HO-1 Inhibitors with Cytotoxicity against MCF-7 Breast Cancer Cells. *International Journal of Molecular Sciences*, *21*(6), 1923. https://doi.org/10.3390/ijms21061923

Cohen, M. H., Williams, G. A., Sridhara, R., Chen, G., McGuinn, W. D., Morse, D., Abraham, S., Rahman, A., Liang, C., Lostritto, R., Baird, A., & Pazdur, R. (2004). United States Food and Drug Administration Drug Approval Summary. *Clinical Cancer Research*, *10*(4), 1212–1218. https://doi.org/10.1158/1078-0432.ccr-03-0564

Cormier, A., Knossow, M., Wang, C., & Gigant, B. (2010). The Binding of Vinca Domain Agents to Tubulin. In *Methods in Cell Biology* (Vol. 95, pp. 373–390). Elsevier. https://doi.org/10.1016/S0091-679X(10)95020-6

Crichton, E. G., & Waterman, P. G. (1978). Dihydromammea C/OB: A new coumarin from the seed of Mammea africana. *Phytochemistry*, *17*(10), 1783–1786. https://doi.org/10.1016/S0031-9422(00)88695-1

Cui, H., Jin, H., Liu, Q., Yan, Z., Ding, L., & Qin, B. (2014). Nematicidal metabolites from roots of *Stellera chamaejasme* against *Bursaphelenchus xylophilus* and

Bursaphelenchus mucronatus. *Pest Management Science*, *70*(5), 827–835. https://doi.org/10.1002/ps.3625

Cunha, S., Iunes, C. E. M., Oliveira, C. C., & Santana, L. L. B. D. (2015). SYNTHESIS OF 3-COUMARIN-CARBOXYLIC ACIDS AND THEIR APPLICATION IN THE TOTAL SYNTHESIS OF AIAPIN, COUMARIN, AND UMBELIFERONE. *Química Nova*. https://doi.org/10.5935/0100-4042.20150096

Dadák, V., & Hoďák, K. (1966). Some relations between the structure and the antibacterial activity of natural coumarins. *Experientia*, *22*(1), 38–39. https://doi.org/10.1007/BF01897757

Dai, H., Huang, M., Qian, J., Liu, J., Meng, C., Li, Y., Ming, G., Zhang, T., Wang, S., Shi, Y., Yao, Y., Ge, S., Zhang, Y., & Ling, Y. (2019). Excellent antitumor and antimetastatic activities based on novel coumarin/pyrazole oxime hybrids. *European Journal of Medicinal Chemistry*, *166*, 470–479. https://doi.org/10.1016/j.ejmech.2019.01.070

Dandriyal, J., Singla, R., Kumar, M., & Jaitak, V. (2016). Recent developments of C-4 substituted coumarin derivatives as anticancer agents. *European Journal of Medicinal Chemistry*, *119*, 141–168. https://doi.org/10.1016/j.ejmech.2016.03.087

De Forges, H., Bouissou, A., & Perez, F. (2012). Interplay between microtubule dynamics and intracellular organization. *The International Journal of Biochemistry & Cell Biology*, *44*(2), 266–274. https://doi.org/10.1016/j.biocel.2011.11.009

Deng, D., Pei, H., Lan, T., Zhu, J., Tang, M., Xue, L., Yang, Z., Zheng, S., Ye, H., & Chen, L. (2020). Synthesis and discovery of new compounds bearing coumarin scaffold for the treatment of pulmonary fibrosis. *European Journal of Medicinal Chemistry*, *185*, 111790. https://doi.org/10.1016/j.ejmech.2019.111790

Deng, M., Li, L., Zhao, J., Yuan, S., & Li, W. (2018). Antitumor activity of the microtubule inhibitor MBRI-001 against human hepatocellular carcinoma as monotherapy or in combination with sorafenib. *Cancer Chemotherapy and Pharmacology*, *81*(5), 853–862. https://doi.org/10.1007/s00280-018-3547-2

Ding, Z., Cheng, H., Wang, S., Hou, Y., Zhao, J., Guan, H., & Li, W. (2017). Development of MBRI-001, a deuterium-substituted plinabulin derivative as a potent anti-cancer agent. *Bioorganic & Medicinal Chemistry Letters*, *27*(6), 1416–1419. https://doi.org/10.1016/j.bmcl.2017.01.096

Ding, Z., Li, F., Zhong, C., Li, F., Liu, Y., Wang, S., Zhao, J., & Li, W. (2020). Structure-based design and synthesis of novel furan-diketopiperazine-type derivatives as potent microtubule inhibitors for treating cancer. *Bioorganic & Medicinal Chemistry*, *28*(10), 115435. https://doi.org/10.1016/j.bmc.2020.115435

Donarska, B., Świtalska, M., Płaziński, W., Wietrzyk, J., & Łączkowski, K. Z. (2021). Effect of the dichloro-substitution on antiproliferative activity of phthalimide-thiazole derivatives. Rational design, synthesis, elastase, caspase 3/7, and EGFR tyrosine kinase activity and molecular modeling study. *Bioorganic Chemistry*, *110*, 104819. https://doi.org/10.1016/j.bioorg.2021.104819

Duarte, J., Vallejo, I., Pérez-Vizcaino, F., Jiménez, R., Zarzuelo, A., & Tamargo, J. (1997). Effects of Visnadine on Rat Isolated Vascular Smooth Muscles. *Planta Medica*, *63*(03), 233–236. https://doi.org/10.1055/s-2006-957660

El-Damasy, A. K., Cho, N.-C., Pae, A. N., Kim, E. E., & Keum, G. (2016). Novel 5-substituted-2-anilinoquinolines with 3-(morpholino or 4-methylpiperazin-1-yl)propoxy moiety as broad spectrum antiproliferative agents: Synthesis, cell based assays and kinase screening. *Bioorganic & Medicinal Chemistry Letters*, *26*(14), 3307–3312. https://doi.org/10.1016/j.bmcl.2016.05.047

Elmore, S. (2007). Apoptosis: A Review of Programmed Cell Death. *Toxicologic Pathology*, *35*(4), 495–516. https://doi.org/10.1080/01926230701320337

Field, J. J., Kanakkanthara, A., & Miller, J. H. (2014). Microtubule-targeting agents are clinically successful due to both mitotic and interphase impairment of microtubule function. *Bioorganic & Medicinal Chemistry*, *22*(18), 5050–5059. https://doi.org/10.1016/j.bmc.2014.02.035

Fonseca, A., Reis, J., Silva, T., Matos, M. J., Bagetta, D., Ortuso, F., Alcaro, S., Uriarte, E., & Borges, F. (2017). Coumarin versus Chromone Monoamine Oxidase B Inhibitors: Quo Vadis? *Journal of Medicinal Chemistry*, *60*(16), 7206–7212. https://doi.org/10.1021/acs.jmedchem.7b00918

Fu, Z., Hou, Y., Ji, C., Ma, M., Tian, Z., Deng, M., Zhong, L., Chu, Y., & Li, W. (2018). Design, synthesis and biological evaluation of anti-pancreatic cancer activity of plinabulin derivatives based on the co-crystal structure. *Bioorganic & Medicinal Chemistry*, *26*(8), 2061–2072. https://doi.org/10.1016/j.bmc.2018.03.005

Geary, T. G., Chibale, K., Abegaz, B., Andrae-Marobela, K., & Ubalijoro, E. (2012). A new approach for anthelmintic discovery for humans. *Trends in Parasitology*, *28*(5), 176–181. https://doi.org/10.1016/j.pt.2012.02.006

Geisler, J., Sasano, H., Chen, S., & Purohit, A. (2011). Steroid sulfatase inhibitors: Promising new tools for breast cancer therapy? *The Journal of Steroid Biochemistry and Molecular Biology*, *125*(1–2), 39–45. https://doi.org/10.1016/j.jsbmb.2011.02.002

Govindaiah, P., Dumala, N., Grover, P., & Jaya Prakash, M. (2019). Synthesis and biological evaluation of novel 4,7-dihydroxycoumarin derivatives as anticancer agents. *Bioorganic & Medicinal Chemistry Letters*, *29*(14), 1819–1824. https://doi.org/10.1016/j.bmcl.2019.05.008

Govindaiah, P., Dumala, N., Grover, P., & Jaya Prakash, M. (2019). Synthesis and biological evaluation of novel 4,7-dihydroxycoumarin derivatives as anticancer agents. *Bioorganic & Medicinal Chemistry Letters*, *29*(14), 1819–1824. https://doi.org/10.1016/j.bmcl.2019.05.008

Gupton, J. T., Yeudall, S., Telang, N., Hoerrner, M., Huff, E., Crawford, E., Lounsbury, K., Kimmel, M., Curry, W., Harrison, A., Juekun, W., Shimozono, A., Ortolani, J., Lescalleet, K., Patteson, J., Moore-Stoll, V., Rohena, C. C., Mooberry, S. L., Obaidullah, A. J., … Sikorski, J. A. (2017). Ortho group activation of a bromopyrrole ester in Suzuki-Miyaura cross-coupling reactions: Application to the synthesis of new microtubule depolymerizing agents with potent cytotoxic activities. *Bioorganic & Medicinal Chemistry*, *25*(12), 3206–3214. https://doi.org/10.1016/j.bmc.2017.04.012

Gurrapu, S., Jonnalagadda, S. K., Alam, M. A., Ronayne, C. T., Nelson, G. L., Solano, L. N., Lueth, E. A., Drewes, L. R., & Mereddy, V. R. (2016). Coumarin carboxylic acids as monocarboxylate transporter 1 inhibitors: *In vitro* and *in*

vivo studies as potential anticancer agents. *Bioorganic & Medicinal Chemistry Letters*, *26*(14), 3282–3286. https://doi.org/10.1016/j.bmcl.2016.05.054

Hamulakova, S., Janovec, L., Hrabinova, M., Spilovska, K., Korabecny, J., Kristian, P., Kuca, K., & Imrich, J. (2014). Synthesis and Biological Evaluation of Novel Tacrine Derivatives and Tacrine–Coumarin Hybrids as Cholinesterase Inhibitors. *Journal of Medicinal Chemistry*, *57*(16), 7073–7084. https://doi.org/10.1021/jm5008648

Han, B., Feinstein, T., Shi, Y., Chen, G., Yao, Y., Hu, C., Shi, J., Feng, J., Wu, H., Cheng, Y., Guo, Q., Jie, Z., Ye, F., Zhang, Y., Liu, Z., Mao, W., Zhang, L., Lu, J., Zhao, J., … Li, H. (2024). Plinabulin plus docetaxel versus docetaxel in patients with non-small-cell lung cancer after disease progression on platinum-based regimen (DUBLIN-3): A phase 3, international, multicentre, single-blind, parallel group, randomised controlled trial. *The Lancet Respiratory Medicine*, *12*(10), 775–786. https://doi.org/10.1016/s2213-2600(24)00178-4

Harvey, A. (2008). Natural products in drug discovery. *Drug Discovery Today*, *13*(19–20), 894–901. https://doi.org/10.1016/j.drudis.2008.07.004

Harvey, A. L., Edrada-Ebel, R., & Quinn, R. J. (2015). The re-emergence of natural products for drug discovery in the genomics era. *Nature Reviews Drug Discovery*, *14*(2), 111–129. https://doi.org/10.1038/nrd4510

Hirsch, S., Miroz, A., McCarthy, P., & Kashman, Y. (1989). Etzionin, a new antifungal metabolite from a red sea tunicate. *Tetrahedron Letters*, *30*(32), 4291–4294. https://doi.org/10.1016/S0040-4039(01)80713-9

Honda-Uezono, A., Kaida, A., Michi, Y., Harada, K., Hayashi, Y., Hayashi, Y., & Miura, M. (2012). Unusual expression of red fluorescence at M phase induced by anti-microtubule agents in HeLa cells expressing the fluorescent ubiquitination-based cell cycle indicator (Fucci). *Biochemical and Biophysical Research Communications*, *428*(2), 224–229. https://doi.org/10.1016/j.bbrc.2012.10.014

Hu, Y.-Q., Gao, C., Zhang, S., Xu, L., Xu, Z., Feng, L.-S., Wu, X., & Zhao, F. (2017). Quinoline hybrids and their antiplasmodial and antimalarial activities. *European Journal of Medicinal Chemistry*, *139*, 22–47. https://doi.org/10.1016/j.ejmech.2017.07.061

Hu, Y.-Q., Xu, Z., Zhang, S., Wu, X., Ding, J.-W., Lv, Z.-S., & Feng, L.-S. (2017). Recent developments of coumarin-containing derivatives and their anti-tubercular activity. *European Journal of Medicinal Chemistry*, *136*, 122–130. https://doi.org/10.1016/j.ejmech.2017.05.004

Hu, Y.-Q., Zhang, S., Xu, Z., Lv, Z.-S., Liu, M.-L., & Feng, L.-S. (2017). 4-Quinolone hybrids and their antibacterial activities. *European Journal of Medicinal Chemistry*, *141*, 335–345. https://doi.org/10.1016/j.ejmech.2017.09.050

Hu, Y.-Q., Zhang, S., Zhao, F., Gao, C., Feng, L.-S., Lv, Z.-S., Xu, Z., & Wu, X. (2017). Isoniazid derivatives and their anti-tubercular activity. *European Journal of Medicinal Chemistry*, *133*, 255–267. https://doi.org/10.1016/j.ejmech.2017.04.002

Huang, G.-J., Deng, J.-S., Liao, J.-C., Hou, W.-C., Wang, S.-Y., Sung, P.-J., & Kuo, Y.-H. (2012). Inducible Nitric Oxide Synthase and Cyclooxygenase-2 Participate in Anti-inflammatory Activity of Imperatorin from *Glehnia littoralis*. *Journal of Agricultural and Food Chemistry*, *60*(7), 1673–1681. https://doi.org/10.1021/jf204297e

Huang, H.-C., Lee, C.-R., Weng, Y.-I., Lee, M.-C., & Lee, Y.-T. (1992). Vasodilator effect of scoparone (6,7-dimethoxycoumarin) from a Chinese herb. *European Journal of Pharmacology*, *218*(1), 123–128. https://doi.org/10.1016/0014-2999(92)90155-W

Huang, R.-M., Yi, X.-X., Zhou, Y., Su, X., Peng, Y., & Gao, C.-H. (2014). An Update on 2,5-Diketopiperazines from Marine Organisms. *Marine Drugs*, *12*(12), 6213–6235. https://doi.org/10.3390/md12126213

Huryn, D. M., & Wipf, P. (2008). Natural product chemistry and anticancer drug discovery. In *Cancer Drug Design and Discovery* (pp. 107–130). Elsevier. https://doi.org/10.1016/B978-012369448-5.50008-2

Ibrahim, M. E., Hamama, W. S., Metwalli, A. E., & Zoorob, H. H. (2016). Chemoselective Synthesis of Enamino-Coumarin Derivatives Identified as Potent Antitumor Agents. *Journal of Heterocyclic Chemistry*, *53*(4), 1318–1323. https://doi.org/10.1002/jhet.2367

Ibrar, A., Zaib, S., Khan, I., Jabeen, F., Iqbal, J., & Saeed, A. (2015). Facile and expedient access to bis-coumarin–iminothiazole hybrids by molecular

hybridization approach: Synthesis, molecular modelling and assessment of alkaline phosphatase inhibition, anticancer and antileishmanial potential. *RSC Advances*, *5*(109), 89919–89931. https://doi.org/10.1039/C5RA14900B

Jeedigunta, S., Krenisky, J. M., & Kerr, R. G. (2000). Diketopiperazines as Advanced Intermediates in the Biosynthesis of Ecteinascidins. *Tetrahedron*, *56*(21), 3303–3307. https://doi.org/10.1016/S0040-4020(00)00249-0

Jelsch, C., Ejsmont, K., & Huder, L. (2014). The enrichment ratio of atomic contacts in crystals, an indicator derived from the Hirshfeld surface analysis. *IUCrJ*, *1*(2), 119–128. https://doi.org/10.1107/S2052252514003327

Jia, J.-M., Ma, X.-C., Wu, C.-F., Wu, L.-J., & Hu, G. (2005). Cordycedipeptide A, a New Cyclodipeptide from the Culture Liquid of Cordyceps sinensis (BERK.) SACC. *Chemical and Pharmaceutical Bulletin*, *53*(5), 582–583. https://doi.org/10.1248/cpb.53.582

Jordan, M. A., & Wilson, L. (2004). Microtubules as a target for anticancer drugs. *Nature Reviews Cancer*, *4*(4), 253–265. https://doi.org/10.1038/nrc1317

Joshi, D., Field, J., Murphy, J., Abdelrahim, M., Schönherr, H., Sparrow, J. R., Ellestad, G., Nakanishi, K., & Zask, A. (2013). Synthesis of Antioxidants for Prevention of Age-Related Macular Degeneration. *Journal of Natural Products*, *76*(3), 450–454. https://doi.org/10.1021/np300769c

Kamath, P. R., Sunil, D., Ajees, A. A., Pai, K. S. R., & Das, S. (2015). Some new indole–coumarin hybrids; Synthesis, anticancer and Bcl-2 docking studies. *Bioorganic Chemistry*, *63*, 101–109. https://doi.org/10.1016/j.bioorg.2015.10.001

Kamiyama, H., Kubo, Y., Sato, H., Yamamoto, N., Fukuda, T., Ishibashi, F., & Iwao, M. (2011). Synthesis, structure–activity relationships, and mechanism of action of anti-HIV-1 lamellarin α 20-sulfate analogues. *Bioorganic & Medicinal Chemistry*, *19*(24), 7541–7550. https://doi.org/10.1016/j.bmc.2011.10.030

Kanakkanthara, A., H. Teesdale-Spittle, P., & H. Miller, J. (2013). Cytoskeletal Alterations that Confer Resistance to Anti-tubulin Chemotherapeutics. *Anti-Cancer Agents in Medicinal Chemistry- Anti-Cancer Agents)*, *13*(1), 147–158. https://doi.org/10.2174/187152013804487263

Kanakkanthara, A., Northcote, P. T., & Miller, J. H. (2016). Peloruside A: A lead non-taxoid-site microtubule-stabilizing agent with potential activity against cancer, neurodegeneration, and autoimmune disease. *Natural Product Reports*, *33*(4), 549–561. https://doi.org/10.1039/C5NP00146C

Kanoh, K., Kohno, S., Katada, J., Takahashi, J., & Uno, I. (1999). (-)-Phenylahistin Arrests Cells in Mitosis by Inhibiting Tubulin Polymerization. *The Journal of Antibiotics*, *52*(2), 134–141. https://doi.org/10.7164/antibiotics.52.134

Kelland, L. (2005). Targeting Established Tumor Vasculature: A Novel Approach to Cancer Treatment. *Current Cancer Therapy Reviews*, *1*(1), 1–9. https://doi.org/10.2174/1573394052952456

Khan, I., Ibrar, A., Ahmed, W., & Saeed, A. (2015). Synthetic approaches, functionalization and therapeutic potential of quinazoline and quinazolinone skeletons: The advances continue. *European Journal of Medicinal Chemistry*, *90*, 124–169. https://doi.org/10.1016/j.ejmech.2014.10.084

Kharrngi, B., Dhar, E. D., Basumatary, G., Das, D., Deka, R. C., Yadav, A. K., & Bez, G. (2021). Developing a highly potent anthelmintic: Study of catalytic application of l-proline derived aminothiourea in rapid synthesis of biscoumarins and their *in vitro* anthelmintic essay. *Journal of Chemical Sciences*, *133*(1), 16. https://doi.org/10.1007/s12039-020-01881-3

Kilian, G., Jamie, H., Brauns, S. C. A., Dyason, K., & Milne, P. J. (2005). Biological activity of selected tyrosine-containing 2,5-diketopiperazines. *Die Pharmazie - An International Journal of Pharmaceutical Sciences*, *60*(4), 305–309.

Knowles, L. M., & Milner, J. A. (2001). Possible Mechanism by Which Allyl Sulfides Suppress Neoplastic Cell Proliferation. *The Journal of Nutrition*, *131*(3), 1061S-1066S. https://doi.org/10.1093/jn/131.3.1061S

Kong, Y., Liu, S., Wang, S., Yang, B., He, W., Li, H., Yang, S., Wang, G., & Dong, C. (2023). Design, synthesis and anticancer activities evaluation of novel pyrazole modified catalpol derivatives. *Scientific Reports*, *13*(1). https://doi.org/10.1038/s41598-023-33403-9

Kontogiorgis, C. A., & Hadjipavlou-Litina, D. J. (2005). Synthesis and Antiinflammatory Activity of Coumarin Derivatives. *Journal of Medicinal Chemistry*, *48*(20), 6400–6408. https://doi.org/10.1021/jm0580149

Kossuga, M. H., Lira, S. P., McHugh, S., Torres, Y. R., Lima, B. A., Gonçalves, R., Veloso, K., Ferreira, A. G., Rocha, R. M., & Berlinck, R. G. S. (2009). Antibacterial modified diketopiperazines from two ascidians of the genus Didemnum. *Journal of the Brazilian Chemical Society*, *20*(4), 704–711. https://doi.org/10.1590/S0103-50532009000400014

Kozlovsky, A. G., Vinokurova, N. G., Adanin, V. M., Burkhardt, G., Dahse, H.-M., & Gräfe, U. (2001). New Diketopiperazine Alkaloids from *Penicillium fellutanum* . *Journal of Natural Products*, *64*(4), 553–554. https://doi.org/10.1021/np010005p

Kraljević, T. G., Harej, A., Sedić, M., Pavelić, S. K., Stepanić, V., Drenjančević, D., Talapko, J., & Raić-Malić, S. (2016). Synthesis, *in vitro* anticancer and antibacterial activities and *in silico* studies of new 4-substituted 1,2,3-triazole–coumarin hybrids. *European Journal of Medicinal Chemistry*, *124*, 794–808. https://doi.org/10.1016/j.ejmech.2016.08.062

Kumar, P., Bhatia, R., & Rangra, N. K. (2025). Scaffolds imparting anthelmintic activity: Recent advancements and SAR studies. *Molecular Diversity*, *29*(1), 783–816. https://doi.org/10.1007/s11030-024-10869-x

Küpeli Akkol, E., Genç, Y., Karpuz, B., Sobarzo-Sánchez, E., & Capasso, R. (2020). Coumarins and Coumarin-Related Compounds in Pharmacotherapy of Cancer. *Cancers*, *12*(7), 1959. https://doi.org/10.3390/cancers12071959

Kurek, J. (2019). Introductory Chapter: Alkaloids - Their Importance in Nature and for Human Life. In J. Kurek (Ed.), *Alkaloids—Their Importance in Nature and Human Life*. IntechOpen. https://doi.org/10.5772/intechopen.85400

Laohapaisan, P., Reamtong, O., Tummatorn, J., Thongsornkleeb, C., Thaenkham, U., Adisakwattana, P., & Ruchirawat, S. (2023). Discovery of N-methylbenzo[d]oxazol-2-amine as new anthelmintic agent through scalable protocol for the synthesis of N-alkylbenzo[d]oxazol-2-amine and N-alkylbenzo[d]thiazol-2-amine derivatives. *Bioorganic Chemistry*, *131*, 106287. https://doi.org/10.1016/j.bioorg.2022.106287

Lee, K.-H., Chai, H.-B., Tamez, P. A., Pezzuto, J. M., Cordell, G. A., Win, K. K., & Tin-Wa, M. (2003). Biologically active alkylated coumarins from Kayea

assamica. *Phytochemistry*, *64*(2), 535–541. https://doi.org/10.1016/S0031-9422(03)00243-7

Li, B., Pai, R., Di, M., Aiello, D., Barnes, M. H., Butler, M. M., Tashjian, T. F., Peet, N. P., Bowlin, T. L., & Moir, D. T. (2012). Coumarin-Based Inhibitors of Bacillus anthracis and Staphylococcus aureus Replicative DNA Helicase: Chemical Optimization, Biological Evaluation, and Antibacterial Activities. *Journal of Medicinal Chemistry*, *55*(24), 10896–10908. https://doi.org/10.1021/jm300922h

Li, N.-G., Song, S.-L., Shen, M.-Z., Tang, Y.-P., Shi, Z.-H., Tang, H., Shi, Q.-P., Fu, Y.-F., & Duan, J.-A. (2012). Mannich bases of scutellarein as thrombin-inhibitors: Design, synthesis, biological activity and solubility. *Bioorganic & Medicinal Chemistry*, *20*(24), 6919–6923. https://doi.org/10.1016/j.bmc.2012.10.015

Li, W., Sun, H., Xu, S., Zhu, Z., & Xu, J. (2017). Tubulin Inhibitors Targeting the Colchicine Binding Site: A Perspective of Privileged Structures. *Future Medicinal Chemistry*, *9*(15), 1765–1794. https://doi.org/10.4155/fmc-2017-0100

Liao, S., Qin, X., Li, D., Tu, Z., Li, J., Zhou, X., Wang, J., Yang, B., Lin, X., Liu, J., Yang, X., & Liu, Y. (2014). Design and synthesis of novel soluble 2,5-diketopiperazine derivatives as potential anticancer agents. *European Journal of Medicinal Chemistry*, *83*, 236–244. https://doi.org/10.1016/j.ejmech.2014.06.030

Liao, S.-R., Qin, X.-C., Wang, Z., Li, D., Xu, L., Li, J.-S., Tu, Z.-C., & Liu, Y. (2016). Design, synthesis and cytotoxic activities of novel 2,5-diketopiperazine derivatives. *European Journal of Medicinal Chemistry*, *121*, 500–509. https://doi.org/10.1016/j.ejmech.2016.06.002

Lin, J. H., Yamazaki (2003). M. Role of P-Glycoprotein in Pharmacokinetics. *Clin Pharmacokinet, 42*, 59–98. https://doi.org/10.2165/00003088-200342010-00003

Lin, M.-H., Cheng, C.-H., Chen, K.-C., Lee, W.-T., Wang, Y.-F., Xiao, C.-Q., & Lin, C.-W. (2014). Induction of ROS-independent JNK-activation-mediated apoptosis by a novel coumarin-derivative, DMAC, in human colon cancer

cells. *Chemico-Biological Interactions*, *218*, 42–49. https://doi.org/10.1016/j.cbi.2014.04.015

Liu, G.-L., Hu, Y., Chen, X.-H., Wang, G.-X., & Ling, F. (2016). Synthesis and anthelmintic activity of coumarin–imidazole hybrid derivatives against Dactylogyrus intermedius in goldfish. *Bioorganic & Medicinal Chemistry Letters*, *26*(20), 5039–5043. https://doi.org/10.1016/j.bmcl.2016.08.090

Liu, G.-L., Liu, L., Hu, Y., & Wang, G.-X. (2021). Evaluation of the antiparasitic activity of coumarin derivatives against Dactylogyrus intermedius in goldfish (Carassius auratus). *Aquaculture*, *533*, 736069. https://doi.org/10.1016/j.aquaculture.2020.736069

Liu, J., Zhang, K., Cheng, L., Zhu, H., & Xu, T. (2020). Progress in Understanding the Molecular Mechanisms Underlying the Antitumour Effects of Ivermectin. *Drug Design, Development and Therapy*, *Volume 14*, 285–296. https://doi.org/10.2147/DDDT.S237393

Liu, M.-M., Chen, X.-Y., Huang, Y.-Q., Feng, P., Guo, Y.-L., Yang, G., & Chen, Y. (2014). Hybrids of Phenylsulfonylfuroxan and Coumarin as Potent Antitumor Agents. *Journal of Medicinal Chemistry*, *57*(22), 9343–9356. https://doi.org/10.1021/jm500613m

Liu, Y. N., Xue, J. H., Feng, N., Wu, P., Liu, X. Z., & Wei, X. Y. (2007). A new cyclodipeptide from the cultures of Geotrichum candidum. *Chinese Chemical Letters*, *18*(9), 1081–1083. https://doi.org/10.1016/j.cclet.2007.07.003

Lorenz, P., Jensen, P. R., & Fenical, W. (1998). Mactanamide, A New Fungistatic Diketopiperazine Produced By A Marine *Aspergillus* Sp. *Natural Product Letters*, *12*(1), 55–60. https://doi.org/10.1080/10575639808048871

Luo, G., Muyaba, M., Lyu, W., Tang, Z., Zhao, R., Xu, Q., You, Q., & Xiang, H. (2017). Design, synthesis and biological evaluation of novel 3-substituted 4-anilino-coumarin derivatives as antitumor agents. *Bioorganic & Medicinal Chemistry Letters*, *27*(4), 867–874. https://doi.org/10.1016/j.bmcl.2017.01.013

Ma, M., Zhao, J., Cheng, H., Deng, M., Ding, Z., Hou, Y., Li, F., Dou, G., & Li, W. (2018). *In vitro* and *in vivo* pharmacokinetic and pharmacodynamic study of MBRI-001, a deuterium-substituted plinabulin derivative as a potent anti-

cancer agent. *Bioorganic & Medicinal Chemistry*, *26*(16), 4687–4692. https://doi.org/10.1016/j.bmc.2018.08.009

Madari, H., Panda, D., Wilson, L., & Jacobs, R. S. (2003). Dicoumarol: A unique microtubule stabilizing natural product that is synergistic with Taxol. *Cancer Research*, *63*(6), 1214–1220.

Mahar, K. M., Enslin, M. B., Gress, A., Amrine-Madsen, H., & Cooper, M. (2018). Single- and Multiple-Day Dosing Studies to Investigate High-Dose Pharmacokinetics of Epelsiban and Its Metabolite, GSK2395448, in Healthy Female Volunteers. *Clinical Pharmacology in Drug Development*, *7*(1), 33–43. https://doi.org/10.1002/cpdd.363

Manolov, I., Maichle-Moessmer, C., Nicolova, I., & Danchev, N. (2006). Synthesis and Anticoagulant Activities of Substituted 2,4-Diketochromans, Biscoumarins, and Chromanocoumarins. *Archiv Der Pharmazie*, *339*(6), 319–326. https://doi.org/10.1002/ardp.200500149

Martins, M. B., & Carvalho, I. (2007). Diketopiperazines: Biological activity and synthesis. *Tetrahedron*, *63*(40), 9923–9932. https://doi.org/10.1016/j.tet.2007.04.105

Matts, R. L., Dixit, A., Peterson, L. B., Sun, L., Voruganti, S., Kalyanaraman, P., Hartson, S. D., Verkhivker, G. M., & Blagg, B. S. J. (2011). Elucidation of the Hsp90 C-Terminal Inhibitor Binding Site. *ACS Chemical Biology*, *6*(8), 800–807. https://doi.org/10.1021/cb200052x

Mead, J. A. R., Smith, J. N., & Williams, R. T. (1958). Studies in detoxication. 72. The metabolism of coumarin and of *o* -coumaric acid. *Biochemical Journal*, *68*(1), 67–74. https://doi.org/10.1042/bj0680067

Morita, H., Dota, T., & Kobayashi, J. (2004). Antimitotic activity of glaupalol-related coumarins from Glaucidium palmatum. *Bioorganic & Medicinal Chemistry Letters*, *14*(14), 3665–3668. https://doi.org/10.1016/j.bmcl.2004.05.015

Mukhopadhyay, T., Sasaki, J., Ramesh, R., & Roth, J. A. (2002). Mebendazole elicits a potent antitumor effect on human cancer cell lines both *in vitro* and *in vivo*. *Clinical Cancer Research: An Official Journal of the American Association for Cancer Research*, *8*(9), 2963–2969.

Narang, U., Kurian, N. K., & Bayram, S. (2024). Enigmatic secondary metabolites: Microbial melanins and their applications. In *Fungal Secondary Metabolites* (pp. 337–351). Elsevier. https://doi.org/10.1016/B978-0-323-95241-5.00017-4

Nasr, T., Bondock, S., & Youns, M. (2014). Anticancer activity of new coumarin substituted hydrazide–hydrazone derivatives. *European Journal of Medicinal Chemistry*, *76*, 539–548. https://doi.org/10.1016/j.ejmech.2014.02.026

Newman, D. J., & Cragg, G. M. (2020). Natural Products as Sources of New Drugs over the Nearly Four Decades from 01/1981 to 09/2019. *Journal of Natural Products*, *83*(3), 770–803. https://doi.org/10.1021/acs.jnatprod.9b01285

Newman, D. J., Cragg, G. M., & I. Kingston, D. G. (2008). Natural Products as Pharmaceuticals and Sources for Lead Structures. In *The Practice of Medicinal Chemistry* (pp. 159–186). Elsevier. https://doi.org/10.1016/B978-0-12-374194-3.00008-1

Neyts, J., Clercq, E. D., Singha, R., Chang, Y. H., Das, A. R., Chakraborty, S. K., Hong, S. C., Tsay, S.-C., Hsu, M.-H., & Hwu, J. R. (2009). Structure−Activity Relationship of New Anti-Hepatitis C Virus Agents: Heterobicycle−Coumarin Conjugates. *Journal of Medicinal Chemistry*, *52*(5), 1486–1490. https://doi.org/10.1021/jm801240d

Ng, K. T. P., Guo, D. Y., Cheng, Q., Geng, W., Ling, C. C., Li, C. X., Liu, X. B., Ma, Y. Y., Lo, C. M., Poon, R. T. P., Fan, S. T., & Man, K. (2012). A Garlic Derivative, S-allylcysteine (SAC), Suppresses Proliferation and Metastasis of Hepatocellular Carcinoma. *PLoS ONE*, *7*(2), e31655. https://doi.org/10.1371/journal.pone.0031655

Nicholson, B., Lloyd, G. K., Miller, B. R., Palladino, M. A., Kiso, Y., Hayashi, Y., & Neuteboom, S. T. C. (2006). NPI-2358 is a tubulin-depolymerizing agent: In-vitro evidence for activity as a tumor vascular-disrupting agent. *Anti-Cancer Drugs*, *17*(1), 25–31. https://doi.org/10.1097/01.cad.0000182745.01612.8a

Nogales, E. (2000). Structural Insights into Microtubule Function. *Annual Review of Biochemistry*, *69*(1), 277–302. https://doi.org/10.1146/annurev.biochem.69.1.277

Ntalli, N. G., & Caboni, P. (2012). Botanical Nematicides: A Review. *Journal of Agricultural and Food Chemistry*, *60*(40), 9929–9940. https://doi.org/10.1021/jf303107j

O' Connor, C. J., Laraia, L., & Spring, D. R. (2011). Chemical genetics. *Chemical Society Reviews*, *40*(8), 4332. https://doi.org/10.1039/c1cs15053g

Omokhefe Bruce, S. (2022). Secondary Metabolites from Natural Products. In R. Vijayakumar & S. Selvapuram Sudalaimuthu Raja (Eds.), *Secondary Metabolites—Trends and Reviews*. IntechOpen. https://doi.org/10.5772/intechopen.102222

Pan, L., Li, X.-Z., Sun, D.-A., Jin, H., Guo, H.-R., & Qin, B. (2016). Design and synthesis of novel coumarin analogs and their nematicidal activity against five phytonematodes. *Chinese Chemical Letters*, *27*(3), 375–379. https://doi.org/10.1016/j.cclet.2016.01.029

Patil, A. D., Freyer, A. J., Eggleston, D. S., Haltiwanger, R. C., Bean, M. F., Taylor, P. B., Caranfa, M. J., Breen, A. L., & Bartus, H. R. (1993). The inophyllums, novel inhibitors of HIV-1 reverse transcriptase isolated from the Malaysian tree, Calophyllum inophyllum Linn. *Journal of Medicinal Chemistry*, *36*(26), 4131–4138. https://doi.org/10.1021/jm00078a001

Paveley, R. A., & Bickle, Q. D. (2013). Automated Imaging and other developments in whole-organism anthelmintic screening. *Parasite Immunology*, *35*(9–10), 302–313. https://doi.org/10.1111/pim.12037

Pingaew, R., Saekee, A., Mandi, P., Nantasenamat, C., Prachayasittikul, S., Ruchirawat, S., & Prachayasittikul, V. (2014). Synthesis, biological evaluation and molecular docking of novel chalcone–coumarin hybrids as anticancer and antimalarial agents. *European Journal of Medicinal Chemistry*, *85*, 65–76. https://doi.org/10.1016/j.ejmech.2014.07.087

Pires, D. E., Blundell, T. L., & Ascher, D. B. (2015). pkCSM: predicting small-molecule pharmacokinetic and toxicity properties using graph-based signatures. *Journal of medicinal chemistry*, *58*(9), 4066-4072.

Pourgholami, M. H., Akhter, J., Wang, L., Lu, Y., & Morris, D. L. (2005). Antitumor activity of albendazole against the human colorectal cancer cell line HT-29: *In*

vitro and in a xenograft model of peritoneal carcinomatosis. *Cancer Chemotherapy and Pharmacology*, *55*(5), 425–432. https://doi.org/10.1007/s00280-004-0927-6

Pourgholami, M. H., Woon, L., Almajd, R., Akhter, J., Bowery, P., & Morris, D. L. (2001). *In vitro* and *in vivo* suppression of growth of hepatocellular carcinoma cells by albendazole. *Cancer Letters*, *165*(1), 43–49. https://doi.org/10.1016/S0304-3835(01)00382-2

Prota, A. E., Bargsten, K., Diaz, J. F., Marsh, M., Cuevas, C., Liniger, M., Neuhaus, C., Andreu, J. M., Altmann, K.-H., & Steinmetz, M. O. (2014). A new tubulin-binding site and pharmacophore for microtubule-destabilizing anticancer drugs. *Proceedings of the National Academy of Sciences*, *111*(38), 13817–13821. https://doi.org/10.1073/pnas.1408124111

Prota, A. E., Bargsten, K., Zurwerra, D., Field, J. J., Díaz, J. F., Altmann, K.-H., & Steinmetz, M. O. (2013). Molecular Mechanism of Action of Microtubule-Stabilizing Anticancer Agents. *Science*, *339*(6119), 587–590. https://doi.org/10.1126/science.1230582

Prota, A. E., Setter, J., Waight, A. B., Bargsten, K., Murga, J., Diaz, J. F., & Steinmetz, M. O. (2016). Pironetin Binds Covalently to αCys316 and Perturbs a Major Loop and Helix of α-Tubulin to Inhibit Microtubule Formation. *Journal of Molecular Biology*, *428*(15), 2981–2988. https://doi.org/10.1016/j.jmb.2016.06.023

Purushotham, M., & Paul, B. (2022). Iodinated Diketopiperazines: Synthesis and Biological Evaluation of Iodinated Analogues of Cyclo(L-Tyrosine-L-Tyrosine) Peptides. *ChemistrySelect*, *7*(16), e202201120. https://doi.org/10.1002/slct.202201120

Puttaraju, K. B., Shivashankar, K., Chandra, Mahendra, M., Rasal, V. P., Venkata Vivek, P. N., Rai, K., & Chanu, M. B. (2013). Microwave assisted synthesis of dihydrobenzo[4,5]imidazo[1,2-a]pyrimidin-4-ones; synthesis, *in vitro* antimicrobial and anticancer activities of novel coumarin substituted dihydrobenzo[4,5]imidazo[1,2-a]pyrimidin-4-ones. *European Journal of Medicinal Chemistry*, *69*, 316–322. https://doi.org/10.1016/j.ejmech.2013.07.015

Rahim, F., Samreen, Ullah, H., Fakhri, M. I., Salar, U., Perveen, S., & Choudhary, K. M. K. and M. I. (2017). Anti-Leishmanial Activities of Synthetic Biscoumarins. *Journal of The Chemical Society of Pakistan*, *39*(6), 79.

Ressurreição, A. S. M., Delatouche, R., Gennari, C., & Piarulli, U. (2011). Bifunctional 2,5-Diketopiperazines as Rigid Three-Dimensional Scaffolds in Receptors and Peptidomimetics. *European Journal of Organic Chemistry*, *2011*(2), 217–228. https://doi.org/10.1002/ejoc.201001330

Rodrigues, T., Reker, D., Schneider, P., & Schneider, G. (2016). Counting on natural products for drug design. *Nature Chemistry*, *8*(6), 531–541. https://doi.org/10.1038/nchem.2479

Saidu, N. E. B., Valente, S., Bana, E., Kirsch, G., Bagrel, D., & Montenarh, M. (2012). Coumarin polysulfides inhibit cell growth and induce apoptosis in HCT116 colon cancer cells. *Bioorganic & Medicinal Chemistry*, *20*(4), 1584–1593. https://doi.org/10.1016/j.bmc.2011.12.032

Salerno, L., Pittalà, V., Romeo, G., Modica, M. N., Marrazzo, A., Siracusa, M. A., Sorrenti, V., Di Giacomo, C., Vanella, L., Parayath, N. N., & Greish, K. (2015). Novel imidazole derivatives as heme oxygenase-1 (HO-1) and heme oxygenase-2 (HO-2) inhibitors and their cytotoxic activity in human-derived cancer cell lines. *European Journal of Medicinal Chemistry*, *96*, 162–172. https://doi.org/10.1016/j.ejmech.2015.04.003

Samadi, A. K., Zhang, X., Mukerji, R., Donnelly, A. C., Blagg, B. S., & Cohen, M. S. (2011). A novel C-terminal HSP90 inhibitor KU135 induces apoptosis and cell cycle arrest in melanoma cells. *Cancer Letters*, *312*(2), 158–167. https://doi.org/10.1016/j.canlet.2011.07.031

Sanduja, M., Gupta, J., Singh, H., Pagare, P. P., & Rana, A. (2020). Uracil-coumarin based hybrid molecules as potent anti-cancer and anti-bacterial agents. *Journal of Saudi Chemical Society*, *24*(2), 251–266. https://doi.org/10.1016/j.jscs.2019.12.001

Sasaki, J., Ramesh, R., Chada, S., Gomyo, Y., Roth, J. A., & Mukhopadhyay, T. (2002). The anthelmintic drug mebendazole induces mitotic arrest and apoptosis by depolymerizing tubulin in non-small cell lung cancer cells. *Molecular Cancer Therapeutics*, *1*(13), 1201–1209.

Sethna, S. M., & Shah, N. M. (1945). The Chemistry of Coumarins. *Chemical Reviews*, *36*(1), 1–62. https://doi.org/10.1021/cr60113a001

Sheldrick, G. M. (2015). Crystal structure refinement with *SHELXL*. *Acta Crystallographica Section C Structural Chemistry*, *71*(1), 3–8. https://doi.org/10.1107/S2053229614024218

Shen, B. (2015). A New Golden Age of Natural Products Drug Discovery. *Cell*, *163*(6), 1297–1300. https://doi.org/10.1016/j.cell.2015.11.031

Shi, Q. I. U., Hui, S. U. N., Ai-Hua, Z., Hong-Ying, X. U., Guang-Li, Y. a. N., Ying, H. a. N., & Xi-Jun, W. (2014). Natural alkaloids:basic aspects,biological roles,and future perspectives. *Chinese Journal of Natural Medicines*, *12*(6), 401–406.

Singh, A. V., Bandi, M., Raje, N., Richardson, P., Palladino, M. A., Chauhan, D., & Anderson, K. C. (2011). A novel vascular disrupting agent plinabulin triggers JNK-mediated apoptosis and inhibits angiogenesis in multiple myeloma cells. *Blood*, *117*(21), 5692–5700. https://doi.org/10.1182/blood-2010-12-323857

Singh, N., Sarkar, J., Sashidhara, K. V., Ali, S., & Sinha, S. (2014). Anti-tumour activity of a novel coumarin–chalcone hybrid is mediated through intrinsic apoptotic pathway by inducing PUMA and altering Bax/Bcl-2 ratio. *Apoptosis*, *19*(6), 1017–1028. https://doi.org/10.1007/s10495-014-0975-2

Singhal, S., Mehta, J., Desikan, R., Ayers, D., Roberson, P., Eddlemon, P., Munshi, N., Anaissie, E., Wilson, C., Dhodapkar, M., Zeldis, J., Siegel, D., Crowley, J., & Barlogie, B. (1999). Antitumor Activity of Thalidomide in Refractory Multiple Myeloma. *New England Journal of Medicine*, *341*(21), 1565–1571. https://doi.org/10.1056/nejm199911183412102

Soni, R., & Soman, S. S. (2018). Design and synthesis of aminocoumarin derivatives as DPP-IV inhibitors and anticancer agents. *Bioorganic Chemistry*, *79*, 277–284. https://doi.org/10.1016/j.bioorg.2018.05.008

Szwaczko, K. (2022). Coumarins Synthesis and Transformation via C–H Bond Activation—A Review. *Inorganics*, *10*(2), 23. https://doi.org/10.3390/inorganics10020023

Thakur, A., Singla, R., & Jaitak, V. (2015). Coumarins as anticancer agents: A review on synthetic strategies, mechanism of action and SAR studies. *European*

Journal of Medicinal Chemistry, *101*, 476–495. https://doi.org/10.1016/j.ejmech.2015.07.010

Tian, Z., Chu, Y., Wang, H., Zhong, L., Deng, M., & Li, W. (2018). Biological activity and interaction mechanism of the diketopiperazine derivatives as tubulin polymerization inhibitors. *RSC Advances*, *8*(2), 1055–1064. https://doi.org/10.1039/C7RA12173C

Tor, Y. S., Yazan, L. S., Foo, J. B., Wibowo, A., Ismail, N., Cheah, Y. K., Abdullah, R., Ismail, M., Ismail, I. S., & Yeap, S. K. (2015). Induction of Apoptosis in MCF-7 Cells via Oxidative Stress Generation, Mitochondria-Dependent and Caspase-Independent Pathway by Ethyl Acetate Extract of Dillenia suffruticosa and Its Chemical Profile. *PLOS ONE*, *10*(6), e0127441. https://doi.org/10.1371/journal.pone.0127441

Trescot, A. M. (2008). Opioid Pharmacology. *Pain Physician*, *2s;11*(3;2s), S133–S153. https://doi.org/10.36076/ppj.2008/11/S133

Vanden Broeck, A., McEwen, A. G., Chebaro, Y., Potier, N., & Lamour, V. (2019). Structural Basis for DNA Gyrase Interaction with Coumermycin A1. *Journal of Medicinal Chemistry*, *62*(8), 4225–4231. https://doi.org/10.1021/acs.jmedchem.8b01928

Walchshofer, N., Sarciron, M. E., Garnier, F., Delatour, P., Petavy, A. F., & Paris, J. (1997). Anthelmintic activity of 3,6-dibenzyl-2,5-dioxopiperazine, cyclo(L-Phe-L-Phe). *Amino Acids*, *12*(1), 41–47. https://doi.org/10.1007/BF01373425

Wender, P. A., & Miller, B. L. (2009). Synthesis at the molecular frontier. *Nature*, *460*(7252), 197–201. https://doi.org/10.1038/460197a

Wermuth, C. G. (2003). MOLECULAR VARIATIONS BASED ON ISOSTERIC REPLACEMENTS. In *The Practice of Medicinal Chemistry* (pp. 189–214). Elsevier. https://doi.org/10.1016/B978-012744481-9/50017-9

Wolff, S. K., Grimwood, D. J., McKinnon, J. J., Turner, M. J., Jayatilaka, D., & Spackman, M. A. (2012). *CrystalExplorer* (Version 3.1).

Wright, A. E., Forleo, D. A., Gunawardana, G. P., Gunasekera, S. P., Koehn, F. E., & McConnell, O. J. (1990). Antitumor tetrahydroisoquinoline alkaloids from the colonial ascidian Ecteinascidia turbinata. *The Journal of Organic Chemistry*, *55*(15), 4508–4512. https://doi.org/10.1021/jo00302a006

Wu, L., Wang, X., Xu, W., Farzaneh, F., & Xu, R. (2009). The Structure and Pharmacological Functions of Coumarins and Their Derivatives. *Current Medicinal Chemistry*, *16*(32), 4236–4260. https://doi.org/10.2174/092986709789578187

Wu, T., Li, T., Kang, Y.-N., Liu, L., Wang, X.-M., Lan, J.-S., Ding, Y., & Zhang, T. (2018). Synthesis and Biological Evaluation of Novel Alkyl Amine Substituted Icariside II Derivatives as Potential Anticancer Agents. *Molecules*, *23*(9), 2146. https://doi.org/10.3390/molecules23092146

Wu, X., Li, M., Qu, Y., Tang, W., Zheng, Y., Lian, J., Ji, M., & Xu, L. (2010). Design and synthesis of novel Gefitinib analogues with improved anti-tumor activity. *Bioorganic & Medicinal Chemistry*, *18*(11), 3812–3822. https://doi.org/10.1016/j.bmc.2010.04.046

Wu, X., Zhang, Y., Liu, S., Liu, C., Tang, G., Cao, X., Lei, X., & Peng, J. (2022). Applications of "linkers" in fragment-based drug design. *Bioorganic Chemistry*, *127*, 105921. https://doi.org/10.1016/j.bioorg.2022.105921

Xiang, W., Choudhary, S., Hamel, E., Mooberry, S. L., & Gangjee, A. (2018). Structure based drug design and *in vitro* metabolism study: Discovery of N-(4-methylthiophenyl)-N,2-dimethyl-cyclopenta[d]pyrimidine as a potent microtubule targeting agent. *Bioorganic & Medicinal Chemistry*, *26*(9), 2437–2451. https://doi.org/10.1016/j.bmc.2018.04.010

Xu, Y., Feng, J., Zhang, D., Zhang, B., Luo, M., Su, D., & Lin, N. (2014). S-allylcysteine, a garlic derivative, suppresses proliferation and induces apoptosis in human ovarian cancer cells *in vitro*. *Acta Pharmacologica Sinica*, *35*(2), 267–274. https://doi.org/10.1038/aps.2013.176

Xu, Z., Gao, C., Ren, Q.-C., Song, X.-F., Feng, L.-S., & Lv, Z.-S. (2017). Recent advances of pyrazole-containing derivatives as anti-tubercular agents. *European Journal of Medicinal Chemistry*, *139*, 429–440. https://doi.org/10.1016/j.ejmech.2017.07.059

Yamazaki, Y., Sumikura, M., Hidaka, K., Yasui, H., Kiso, Y., Yakushiji, F., & Hayashi, Y. (2010). Anti-microtubule 'plinabulin' chemical probe KPU-244-B3 labeled both α- and β-tubulin. *Bioorganic & Medicinal Chemistry*, *18*(9), 3169–3174. https://doi.org/10.1016/j.bmc.2010.03.037

Yamazaki, Y., Sumikura, M., Masuda, Y., Hayashi, Y., Yasui, H., Kiso, Y., Chinen, T., Usui, T., Yakushiji, F., Potts, B., Neuteboom, S., Palladino, M., Lloyd, G. K., & Hayashi, Y. (2012). Synthesis and structure–activity relationships of benzophenone-bearing diketopiperazine-type anti-microtubule agents. *Bioorganic & Medicinal Chemistry*, *20*(14), 4279–4289. https://doi.org/10.1016/j.bmc.2012.05.059

Yamazaki, Y., Tanaka, K., Nicholson, B., Deyanat-Yazdi, G., Potts, B., Yoshida, T., Oda, A., Kitagawa, T., Orikasa, S., Kiso, Y., Yasui, H., Akamatsu, M., Chinen, T., Usui, T., Shinozaki, Y., Yakushiji, F., Miller, B. R., Neuteboom, S., Palladino, M., … Hayashi, Y. (2012). Synthesis and Structure–Activity Relationship Study of Antimicrotubule Agents Phenylahistin Derivatives with a Didehydropiperazine-2,5-dione Structure. *Journal of Medicinal Chemistry*, *55*(3), 1056–1071. https://doi.org/10.1021/jm2009088

Yang, C.-P., & Horwitz, S. (2017). Taxol®: The First Microtubule Stabilizing Agent. *International Journal of Molecular Sciences*, *18*(8), 1733. https://doi.org/10.3390/ijms18081733

Yildirim, M., Unal, Z. N., Ersatir, M., Yetkin, D., Degirmenci, U., & Giray, E. S. (2022). Anti-Inflammatory Effects of Coumarin–Selenophene Derivatives on LPS-Stimulated RAW 264.7 Macrophage Cells. *Russian Journal of Bioorganic Chemistry*, *48*(6), 1209–1214. https://doi.org/10.1134/S1068162022060279

Zamani Taghizadeh Rabe, S., Iranshahi, M., & Mahmoudi, M. (2016). *In vitro* anti-inflammatory and immunomodulatory properties of umbelliprenin and methyl galbanate. *Journal of Immunotoxicology*, *13*(2), 209–216. https://doi.org/10.3109/1547691X.2015.1043606

Zengin Kurt, B., Sonmez, F., Ozturk, D., Akdemir, A., Angeli, A., & Supuran, C. T. (2019). Synthesis of coumarin-sulfonamide derivatives and determination of their cytotoxicity, carbonic anhydrase inhibitory and molecular docking studies. *European Journal of Medicinal Chemistry*, *183*, 111702. https://doi.org/10.1016/j.ejmech.2019.111702

Zhang, S., Xu, Z., Gao, C., Ren, Q.-C., Chang, L., Lv, Z.-S., & Feng, L.-S. (2017). Triazole derivatives and their anti-tubercular activity. *European Journal of*

Medicinal Chemistry, *138*, 501–513. https://doi.org/10.1016/j.ejmech.2017.06.051

Zhou, H. Y., Hong, J. L., Shu, P., Ni, Y. J., & Qin, M. J. (2009). A new dicoumarin and anticoagulant activity from Viola yedoensis Makino. *Fitoterapia*, *80*(5), 283–285. https://doi.org/10.1016/j.fitote.2009.03.005

BIO-DATA

1. NAME : Brilliant N. Marak

2. DATE OF BIRTH : 17th March 1995

3. FATHER'S NAME : Robinus T. Sangma

4. PERMANENT ADDRESS : Dobetkolgre, Williamnagar, East Garo Hills, Meghalaya-794111

5. EMAIL ADDRESS : brillymarak2@gmail.com

6. EDUCATIONAL QUALIFICATIONS :

Examination passed	Year of Passing	Board/University	Division	% of marks	Subjects
SSLC	2011	Meghalaya Board of School Education	I	77.0	Science, Mathematics, English, Garo, Social Science, Health Education
HSSLC	2013	Meghalaya Board of School Education	II	51.20	Physics, Chemistry, Mathematics Biology, English,
B.SC (Chemistry)	2016	North Eastern Hill University, Shillong	II	56.25	Chemistry, Physics, Mathematics
M.Sc (Chemistry)	2018	Mizoram University, Aizawl	I	71.25	Organic Chemistry (specialization), Physical Chemistry, Inorganic Chemistry, Analytical Chemistry

LIST OF PUBLICATIONS

1. **Brilliant N. Marak**, Jayanta Dowarah, Laldingluaia Khiangte, Ved Prakash Singh, A comprehensive insight on the development of Cyclic Dependent Kinase inhibitors as anticancer agents, **European Journal of Medicinal Chemistry** 203 (2020) 112571. https://doi.org/10.1016/j.ejmech.2020.112571.

2. **Brilliant N. Marak**, Jayanta Dowarah, Laldingluaia Khiangte, Ved Prakash Singh, Step toward repurposing drug discovery for COVID -19 therapeutics through in silico approach, **Drug Development Research** 82 (2021) 374–392. https://doi.org/10.1002/ddr.21757.

3. **Brilliant N. Marak**, F Nghakliana, Lalremruati, Zothansiama, Biswait Saha, Ved Prakash Singh, Design, Synthesis, and Multifaceted Exploration of Novel 2,5-Diketopiperazine Derivatives: Supramolecular framework, Anticancer Activity, ctDNA Binding, and Antioxidant Properties, Journal of Molecular Structure 1363 (2026) 145733 https://doi.org/10.1016/j.molstruc.2026.145733.

4. **Brilliant N. Marak**, F Nghakliana, Lalremruati, Zothansiama, Ved Prakash Singh, Design, Synthesis, and Evaluation of Novel Linker-Modulated 2,5-Diketopiperazines as Apoptosis-Inducing Anticancer Agents, Drug Development Research. (communicated).

5. Jayanta Dowarah, **Brilliant N. Marak**, Lalhruaizela, Balkaran Singh Sran, Ved Prakash Singh, Design, Synthesis, In Silico Analysis, and Structural Study of 4,6-Dimethyl-2-(3-(*p* -tolyloxy)propoxy)nicotinonitrile Fleximer, **Crystal Research and Technology** 55 (2020) 2000100. https://doi.org/10.1002/crat.202000100.

6. Jayanta Dowarah, Devanshi Patel, **Brilliant N. Marak**, Umesh Chand Singh Yadav, Pramod Kumar Shah, Pradeep Kumar Shukla, Ved Prakash Singh, Green synthesis, structural analysis and anticancer activity of

dihydropyrimidinone derivatives, **RSC Adv.** 11 (2021) 35737–35753. https://doi.org/10.1039/D1RA03969E.

7. Jayanta Dowarah, **Brilliant N. Marak**, Umesh Chand Singh Yadav, Ved Prakash Singh, Potential drug development and therapeutic approaches for clinical intervention in COVID-19, **Bioorganic Chemistry** 114 (2021) 105016. https://doi.org/10.1016/j.bioorg.2021.105016.

8. Ved Prakash Singh, Jayanta Dowarah, **Brilliant N. Marak**, Balkaran Singh Sran, A.K. Tewari, Study of the structure-bioactivity of fleximers: synthesis, crystal structure, Hirshfeld surface analysis, and anti-inflammatory assays, **Journal of Molecular Structure** 1239 (2021) 130513. https://doi.org/10.1016/j.molstruc.2021.130513.

9. Lalhruaizela, **Brilliant N. Marak**, Dipanta Gogoi, Jayanta Dowarah, Balkaran Singh Sran, Zodinpuia Pachuau, Ved Prakash Singh, Study of supramolecular self-assembly of pyridone and dihydropyridone co-crystal: Synthesis, crystal structure, Hirshfeld surface, DFT and molecular docking studies, **Journal of Molecular Structure** 1235 (2021) 130214. https://doi.org/10.1016/j.molstruc.2021.130214.

10. Lalhruaizela, **Brilliant N. Marak**, Balkaran Singh Sran, Ved Prakash Singh, Multicomponent Synthesis, Crystal Structure, Hirshfeld Surface Analysis, and Molecular Docking of 4H-Pyrans, **ChemistrySelect** 6 (2021) 11249–11260. https://doi.org/10.1002/slct.202103182.

11. Ved Prakash Singh, Jayanta Dowarah, **Brilliant N. Marak**, A.K. Tewari, Design, synthesis, in silico analysis with PPAR -γ receptor and study of non-covalent interactions in unsymmetrical heterocyclic/phenyl fleximer, **Journal of Chinese Chemical Society** 68 (2021) 150–158. https://doi.org/10.1002/jccs.202000215.

12. Jayanta Dowarah, **Brilliant N. Marak**, Balkaran Singh Sran, Pramod Kumar Shah, Pradeep Kumar Shukla, Ved Prakash Singh, Synthesis of a Pyridone-Based Phthalimide Fleximer and Its Characterization and Supramolecular

Property Evaluation, **ACS Omega** 7 (2022) 24485–24497. https://doi.org/10.1021/acsomega.2c02095.

13. Lalhruaizela, Devanshi Patel, **Brilliant N. Marak**, Jayanta Dowarah, Balkaran Singh Sran, Umesh Chand Singh Yadav, Ved Prakash Singh, Supramolecular architectures in dihydropyridones: Synthesis, crystal structure, Hirshfeld analysis, cytotoxicity and in silico studies, **Journal of Molecular Structure** 1250 (2022) 131671. https://doi.org/10.1016/j.molstruc.2021.131671.

14. Lalhruaizela, **Brilliant N. Marak**, B. Hazarika, S.K. Pandey, R. Kataria, Ved Prakash Singh, Study of self-assembly features in 4H-pyrans: Synthesis, Hirshfeld surface, and energy framework analysis, **Journal of Molecular Structure** 1265 (2022) 133361. https://doi.org/10.1016/j.molstruc.2022.133361.

15. Chuckles Ch Marak, **Brilliant N. Marak**, Ved Prakash Singh, G. Gurusubramanian, Vikas Kumar Roy, Phytochemical analysis, in silico study and toxicity profile of *Cycas pectinata* Buch.-Ham seed in mice, **Drug and Chemical Toxicology** 46 (2023) 330–342. https://doi.org/10.1080/01480545.2022.2033258.

16. Chuckles Ch Marak, **Brilliant N. Marak**, Ved Prakash Singh, G. Gurusubramanian, Vikas Kumar Roy, Effect of Cycas pectinata Seed Extract on Testicular Steroidogenesis in a Mouse Model, **Andrologia** 2023 (2023) 1–15. https://doi.org/10.1155/2023/5446928.

17. Lalhruaizela, Zothansiama, Lalfakawmi, **Brilliant N. Marak**, Biki Hazarika, Ramesh Kataria, Nachimuthu Senthil Kumar, Balkaran Singh Sran, Ved Prakash Singh, Non-Covalent Interactions in the Self-Assembly of Dihydropyridone Supramolecules and In Vitro Anti-Cancer Assessment in Human Lung Adenocarcinoma Cell Line (A549), **ChemPlusChem** 88 (2023) e202200444. https://doi.org/10.1002/cplu.202200444.

18. Lalhruaizela, **Brilliant N. Marak**, Laldingluaia Khiangte, Biki Hazarika, Ramesh Kataria, Ved Prakash Singh, Synthesis of Spirooxindoles and Study

of their Self-Assembly features; Hirshfeld Surface, Energy Framework and *In Silico* analysis, **ChemistrySelect** 8 (2023) e202300169. https://doi.org/10.1002/slct.202300169.

Book Chapter

Saurabh Chetia, Lalremruati**, Brilliant N Marak**, Ved Prakash Singh, Chemistry and Pharmacological Applications of 1,3-Oxazoles, *Five Membered Bioactive N and O-Heterocycles: Models and Medical Applications*, 2025, 1-54, IGI Global Scientific Publishing, Editors: Shrikaant Kulkarni, Hemantkumar Akolkar, Bapurao B. Shingate, Vijay M. Khedkar, ISBN13: 9798369372678.

CONFERENCES AND SEMINAR

1. Presented paper "*Design, Synthesis and Anti-cancer Activity of Novel Diketopiperazine Analogues*" in International Conference on Chemical Advances in Chemical Science Research and Education (CACSRE-2024) & National Convention of Chemistry Teachers (NCCT-2024), jointly organised by the Department of Chemistry, Industrial Chemistry, Chemistry (PUC), Mizoram University and the Association of Chemistry Teachers (ACT) during 6th-8th November, 2024 at Mizoram University.
2. Presented paper "*Synthesis and Analysis of the Energy Framework in the supramolecular Self-Assembly of Spirooxindoles*" at the International Conference on Science and Technology for Innovative and Sustainable Development (STISD-2023) jointly organized by Department of Chemistry and Department of Industrial Chemistry, Mizoram University, Aizawl during 28^{th}-30^{th} June 2023.
3. Presented paper "*Investigation of the Energy Framework of Self-Assembled Spirooxindoles*" at International Conference on conference on Recent Advances in Mathematical, Physical, and Chemical Sciences (ICRAMPC-2024) organized by School of Physical Sciences, Mizoram University, Aizawl during February 21-23, 2024.
4. Presented paper "*In silico Study of Anti-Parasitic and Anti-inflamtory Drugs Against SARS-Cov-2 Receptors: An Approach for Drug Repurposing*, in the 3^{rd} National Conference on Recent Adcancement in Physical Sciences, jointly organized by Department of Chemistry, Department of Physics, Department of Mathematics, NIT, Uttarakhand during Dec 19^{th}-20^{th}.
5. Presented paper "*Repurposing drug development through in silico approach as COVID-19 therapeutics*" in 2^{nd} Annual Convention of North East (India) Academy of Science and Technology (NEAST) & International Seminar on Recent Advances in Science and Technology (ISRAST) in 18^{th} November 2020.

PARTICULARS OF THE CANDIDATE

NAME OF CANDIDATE : Brilliant N. Marak

DEGREE : Doctor of Philosophy (Ph.D.)

DEPARTMENT : Chemistry

TITLE OF THESIS : Design, Synthesis, and Study of Bioactive Natural Product Congeners

DATE OF ADMISSION : 9th August 2018

APPROVAL OF RESEARCH PROPOSAL:

1. DRC : 16.04.2019

2. BOS : 23.04.2019

3. SCHOOL BOARD : 8.05.2019

MZU REGN. NO. 1600457 of 2017

Ph.D. REGISTRATION NO. & DATE : MZU/Ph.D./1253 of 09.08.2018

EXTENSION : No. 16-2/MZU(Acad)/24/14-15 Dated 3rd July, 2024

Head

Department of Chemistry

ABSTRACT

DESIGN, SYNTHESIS, AND STUDY OF BIOACTIVE NATURAL PRODUCT CONGENERS

AN ABSTRACT SUBMITTED IN PARTIAL FULFILLMENT OF THE REQUIREMENTS FOR THE DEGREE OF DOCTOR OF PHILOSOPHY

BRILLIANT N. MARAK
MZU REGISTRATION NO.: 1600457
Ph.D. REGISTRATION NO.: MZU/Ph.D./1253 of 09.08.2018

DEPARTMENT OF CHEMISTRY
SCHOOL OF PHYSICAL SCIENCES
NOVEMBER, 2025

DESIGN, SYNTHESIS, AND STUDY OF BIOACTIVE NATURAL PRODUCT CONGENERS

BY

BRILLIANT N. MARAK

Department of Chemistry

Under the supervision of

Prof. VED PRAKASH SINGH

Submitted

In partial fulfillment of the requirement of the Degree of Doctor of Philosophy in Chemistry of Mizoram University, Aizawl.

Abstract

Natural products have served as a cornerstone of drug discovery and development for many years. They offer remarkable structural diversity and inherent bioactivity, which have inspired the design of many therapeutic agents. Many of these agents remain in clinical use today. A large proportion of modern pharmaceuticals derive directly or indirectly from secondary metabolites made by plants, microorganisms, marine organisms, and other natural sources. These compounds often provide unique molecular frameworks. These frameworks serve as templates for the design of new chemical entities with enhanced potency, selectivity, and improved pharmacological profiles.

Despite advances in modern therapeutics, cancer and helminthic infections remain major global health challenges. Cancer is life-threatening and ranks second only to cardiovascular disorders in global mortality. Colorectal cancer makes up about 9.6% of all cases and is the third leading cause of cancer-related deaths, contributing to roughly 9.3% of total cancer mortality. Conventional chemotherapeutic drugs primarily act cytotoxically. They lack specificity and affect both malignant and healthy cells, leading to severe side effects and, over time, resistance. Therefore, there is a pressing need for safer, more effective, and selective anticancer agents.

Helminthic infections also pose a major global health concern, especially in impoverished regions. Poor sanitation and limited access to healthcare allow parasitic worms to spread. These infections affect billions of people and lead to malnutrition, impaired cognitive development, and economic hardship. Helminths can infect both humans and animals through ingestion of eggs or larvae or through skin penetration. Infection can involve various tissues, organs, and organ systems. Soil-transmitted helminths alone affect about 1.5 billion people worldwide. Current anthelmintic drugs have limits, and increasing drug resistance highlights the need for new therapies.

Among naturally derived molecules, 2,5-diketopiperazines (DKPs) and coumarins are important and structurally versatile classes with broad

pharmacological relevance. DKPs are pharmacologically diverse and exhibit a range of biological activities, including anticancer, anticoagulant, antitumor, anti-inflammatory, antiviral, antioxidant, and antimicrobial properties. They are valued in medicinal chemistry because they can interact with many biological targets. DKPs exhibit conformational rigidity, favorable properties, and drug-like characteristics, making them valuable templates for molecular design. Coumarins and bis-coumarins also have a broad range of biological activities, including anticancer, anthelmintic, anticoagulant, antitumor, anti-inflammatory, antiviral, antioxidant, and antimicrobial effects.

In this context, the present thesis, entitled "**Design, Synthesis, and Study of Bioactive Natural Product Congeners**" focuses on the rational design, synthesis, and biological evaluation of structurally novel analogues inspired by naturally occurring molecules. Three main classes of compounds were designed, synthesized, and investigated:

1. Plinabulin-based 2,5-diketopiperazine (DKP) analogues,
2. DKP–based coumarin hybrids, and
3. Bis-4-hydroxycoumarin hybrids.

The research presented in this thesis is organized into four chapters:

Chapter 1: Introduction.

Chapter 2: Design, Synthesis and Anti-Cancer Activity of Novel Plinabulin-Based 2,5-Diketopiperazine Analogues.

Chapter 3: Synthesis and Anti-Cancer Activity of Novel 2,5-Diketopiperazine Based Coumarin Analogues.

Chapter 4: Design and Development of Novel Hybrids of Bis-4-Hydroxycoumarin Derivatives as Anthelmintic Agents.

Chapter 5: Summary and Conclusion

A brief account of each chapter is provided below:

Chapter 1 provides a general introduction to the role of natural products in drug discovery and a comprehensive literature review on the medicinal chemistry of DKP, coumarin, and bis-coumarin derivatives.

Chapter 2 describes the design, synthesis, and anticancer evaluation of Plinabulin-based DKP analogues. A total of 24 novel analogues, inspired by the natural product phenylahistin and its potent derivative Plinabulin, were synthesized and fully characterized. Single-crystal X-ray diffraction (SCXRD) analysis of compound **2.31f** revealed key features of molecular conformation, crystal packing, and intermolecular interactions. Hirshfeld surface and energy framework analyses further elucidated the molecular self-assembly features of the compound. Compounds **2.31b, 2.31d, 2.32f**, and **2.32q** showed significant cytotoxicity against the HepG2 and HCT116 cell lines, with activity comparable to that of the standard drug 5-fluorouracil (5-FU). Apoptosis studies revealed that compound **2.32q** induced dose-dependent apoptosis in HCT116 cells and significantly enhanced caspase-6 activity by 93.04%, approximately 1.2-fold higher than 5-FU. Molecular docking studies revealed strong binding affinities for β-tubulin and c-Met, stabilized by hydrogen bonding and hydrophobic interactions. Phthalimide-containing derivatives achieved greater stabilization within the binding site through π–π stacking interactions involving the phthalimide rings, which likely contributed to the superior anticancer activity observed for compounds **2.32f** and **2.32q**.

Chapter 3 presents the design, synthesis, and anticancer evaluation of DKP–based coumarin hybrids. Considering the promising anticancer potential of DKP analogues reported in Chapter 2, a total of 18 novel DKP–based coumarin hybrids were synthesized by integrating coumarin moieties with the DKP core via flexible alkyl linkers. Twelve compounds were screened against A549 (human non-small cell lung cancer) cells, among which compound **3.12b** exhibited the highest potency, with IC_{50} values of 52.21 ± 4.14 μM and 22.02 ± 3.98 μM after 24 and 48 hours, respectively.

Chapter 4 describes the design and development of bis-4-hydroxycoumarin hybrids as potential anthelmintic agents. A library of 24 novel bis-4-hydroxycoumarin hybrids functionalized by amino moieties via flexible alkyl linkers was synthesized, and the *in vitro* anthelmintic activity was evaluated against *R. echinobothrida*. Among the series, derivatives functionalized with imidazolo and morpholino moieties exhibited six- to seven-fold greater potency than the standard drug albendazole. Morphological examinations by scanning electron microscopy (SEM) confirmed extensive, irreversible structural alterations in the parasites, and molecular docking revealed strong binding affinity within the taxane-binding pocket of β-tubulin.

Chapter 5 provides a concise summary and conclusion of the research findings.

Overall, these studies highlight the versatility of natural product frameworks as templates for medicinal chemistry exploration and present promising leads for the development of next-generation anticancer and anthelmintic agents.